ARCTIC AND MIDLATITUDE STRATOSPHERIC TRACE GAS MEASUREMENTS USING GROUND-BASED UV-VISIBLE SPECTROSCOPY

by

Annemarie Catherine Fraser

A thesis submitted in conformity with the requirements
for the degree of Doctor of Philosophy
Graduate Department of Physics
University of Toronto

Abstract

Arctic and Midlatitude Stratospheric Trace Gas Measurements Using Ground-based
UV-visible Spectroscopy

Annemarie Catherine Fraser

Doctor of Philosophy

Graduate Department of Physics

University of Toronto

2008

A ground-based, zenith-sky, UV-visible triple grating spectrometer was installed at the Polar Environment Atmospheric Research Laboratory (PEARL) in the Canadian High Arctic during polar springtime from 2004 to 2007 as part of the Canadian Arctic ACE (Atmospheric Chemistry Experiment) Validation Campaigns. From the solar spectra, ozone, NO_2, and BrO vertical column densities (VCDs) have been retrieved using the DOAS (Differential Optical Absorption Spectroscopy) technique. This spectrometer, the UT-GBS (University of Toronto Ground-Based Spectrometer), was also deployed as part of the fourth Middle Atmosphere Nitrogen TRend Assessment (MANTRA) campaign in Vanscoy, Saskatchewan in August and September 2004.

A near-identical spectrometer, the PEARL-GBS, was permanently installed at PEARL in August 2006 as part of the refurbishment of the laboratory by CANDAC (Canadian Network for the Detection of Atmospheric Change). Since then, the instrument has been making continuous measurements, with the exception of during polar night. Vertical columns of ozone and NO_2 can be retrieved year-round. During the 2007 sunrise campaign, differential slant column densities (DSCDs) of OClO and VCDs of BrO were also retrieved.

Ozone and NO_2 DSCDs and VCDs from the UT-GBS were compared to the DSCDs and VCDs from three other UV-visible, ground-based, grating spectrometers that also participated in the MANTRA and Eureka campaigns. Two methods developed by the UV-visible Working Group of the NDACC (Network for the Detection of Atmospheric Composition Change) were followed. During MANTRA, the instruments were found to partially meet the NDACC standards. The comparisons from Eureka were an improvement on the MANTRA comparisons, and also partially met the NDACC standards. In 2007, the columns from the UT-GBS and PEARL-GBS were compared, and were found to agree within the NDACC standards for both species.

Ozone and NO_2 VCDs from the ground-based instruments were also compared to integrated partial columns from the ACE-FTS (ACE-Fourier Transform Spectrometer) and ACE-MAESTRO (ACE-Measurements of Aerosol Extinction in the Stratosphere and Troposphere Retrieved by Occultation) on board the ACE satellite. ACE-FTS partial columns were found to agree with the ground-based total columns, while the ACE-MAESTRO partial columns were found to be smaller than expected for ozone and larger than expected for NO_2.

Acknowledgements

No work can be done in isolation, and many people have helped me produce this thesis, both directly with useful discussions or providing data and indirectly through a combination of distraction, Sunday brunch, coffee breaks, and Tuesday nights at the Pour House.

Kim Strong took me on as a summer NSERC student more years ago than I would like to admit, and I haven't left her alone since. Thank you for your continued encouragement and guidance.

I owe Elham Farahani thanks for graciously letting me take over her spectrometer and putting up with thousands of my questions. I hope I have left it in a state you can still feel proud of, despite the fact that I broke its first CCD.

Jennifer Walker worked with me for two summers helping with in-lab tests and other spectrometer-y affairs. I was also fortunate to have the help of summer student Hristina Popova in commissioning the PEARL-GBS. Thanks also to Cristen Adams, for taking over the instruments and saving them from an uncertain future.

I spend a lot of time working with data that is not my own. Thanks to all of you who share and allow me to manipulate your data in ways you might prefer I didn't. Sorry for constantly pestering you. Thanks to Florence Goutail for the SAOZ data, Tom McElroy and Clive Midwinter for the MAESTRO data, Tom, Hongjiang Wu, Jennifer, and Tobias Kerzenmacher for the SPS data, Debra Wunch for the U of T FTS data, Pierre Fogal for the DU-FTS data, Dejian Fu and Kaley Walker for PARIS-IR data, Jonathan Davies for the ozonesondes, and the ACE-FTS and ACE-MAESTRO teams for the ACE data. Hans Fast downloaded all the PV maps in the Eureka chapter. Thanks to Richard Mittermeier, Hans and Jonathan for at various times throughout this work providing both ozonesonde and Brewer data from the secret computers at Environment Canada. Gloria Manney and William Daffer provided the sPV calculations used in the Eureka analysis. Thanks to Yves Rochon for providing cloud data, William Burrows for the lightning data, and Tom

Ostry and Peter Rodriguez for the radar data, all used in the lightning chapter. Dmitry Ionov performed the calculations for the location of the slant column measurements in the Eureka chapter. I'm sure I have forgotten some people, and if this includes you, I owe you a beer.

Chris McLinden provided the radiative transfer model and photochemical box models used throughout this work, and has been wonderful in answering my questions about them. Caroline Fayt and Michel Van Roozendael provided WinDOAS, and have also provided advice in how to run it successfully. Michel also provided the O_4 AMFs in Chapter 5.

My thanks to the many people who have traveled with me to the Arctic. The love I have for that remote part of the world is at least partially a result of the wonderful people who were my traveling companions. Thank you for the sometimes late Arctic nights of movies (both watching and making), Oscar viewing, confluence hunting, mountain climbing, (ice) hockey, and shuffleboard (go fluffy pink bunnies!). Thanks to the station staff for graciously allowing us to invade their home, especially the cooks, who always made sure more of me left Eureka than arrived. Special thanks to Keith MacQuarrie, Paul Loewen, Oleg Mikhailov, Suzi Bingham, Bec Batchelor, Pierre Fogal, Alexei Khmel, and Matt Okraszewski for taking care of my spectrometer(s) and hardly complaining about their fiddlyness. Paul gets the gold star award for replacing shutters more times than I can count.

I also have to thank everyone who traveled with me to Saskatoon for MANTRA. You are all wonderful too, and Saskatoon is ... flat. Thanks to Jennifer, Stella Melo, Matt Toohey, Tobias, Debra, and everyone else who re-filled the loaner CCD with liquid nitrogen, or who packed up the spectrometer for me after I had gone home. Thanks for the BBQs and the GW beer.

I'd like to thank all the people who have made my days in MacLennan more interesting. Special mention to the TRIAD - from the darkness of the Month Of Hell to the joys of TRIAD Does San Francisco, you two have been there to make the whole experience much more fun than it would have been otherwise.

My thanks as well to my friends who for some odd reason chose not to identify as physicists. Thank you for convincing me to leave the building, for keeping me updated on the world outside physics, and for occasionally pretending to be interested in what I do. I would be a horrible person if I didn't make extra super special mention of Melissa. Thank you for cooking me dinner, taping embarrassing TV shows while I was away, discussing colonial chutney, and generally being the best room mate ever.

I'd like to close by thanking my family. The four of you have been nothing but supportive these long years at UofT. Thank you for being the kind of family that happily discusses science over Christmas dinner.

Contents

List of Tables

List of Figures

List of Acronyms

ACE	Atmospheric Chemistry Experiment
ACE-FTS	ACE-Fourier Transform Spectrometer
ACE-MAESTRO	ACE-Measurements of Aerosol Extinction in the Stratosphere and Troposphere Retrieved by Occultation
AMF	air mass factor
AStrO	Arctic Stratospheric Ozone Observatory
CANDAC	CAnadian Network for the Detection of Atmospheric Change
CAPPI	constant altitude plan position indicator
CCD	charged coupled device
CFC	chlorofluorocarbon
CG	cloud-to-ground
CLDN	Canadian Lightning Detection Network
DOAS	Differential Optical Absorption Spectroscopy
DOD	differential optical depth
DSCD	Differential slant column density
DU FTS	University of Denver Fourier Transform Spectrometer
EC	Environment Canada
ECMWF	European Centre for Medium-Range Weather Forecasts
FWHM	full width at half maximum
FTS	Fourier transform spectrometer
GEOS-4	Goddard Earth Observing System-4

GOES Geostationary Operational Environmental Satellite

GPIB General Purpose Interface Bus

HITRAN HIgh-resolution TRANsmission database

IC intra-cloud

InSb indium antimonide

LLG liquid light guide

MAESTRO Measurements of Aerosol Extinction in the Stratosphere and Troposphere Retrieved by Occultation

MAESTRO-G Measurements of Aerosol Extinction in the Stratosphere and Troposphere Retrieved by Occultation-Ground

MANTRA Middle Atmosphere Nitrogen TRend Assessment

MAX-DOAS Multi-AXis DOAS

MCT mercury cadmium telluride

MSIS-2000 Mass-Spectrometer-Incoherent-Scatter

NAD nitric acid dihydrate

NAM nitric acid monohydrate

NAT nitric acid trihydrate

NCEP National Centers for Environmental Prediction

NCAR National Center for Atmospheric Research

NDACC Network for the Detection of Atmospheric Composition Change

NIWA National Institute for Water and Atmospheric Research

NOAA National Oceanic and Atmospheric Administration

PARIS-IR Portable Atmospheric Research Interferometric Spectrometer for the Infrared

PEARL Polar Environment Atmospheric Research Laboratory

PEARL-GBS PEARL-Ground-Based Spectrometer

PSC Polar stratospheric cloud

PV potential vorticity

RCD reference column density

RMS root-mean-square

SAGE II Stratospheric Aerosol and Gas Experiment II

SCISAT SCIentific SATellite

SESAME Second European Stratospheric Arctic and Mid-latitude Experiment

SAOZ Système d'Analyse par Observations Zénitales

SNR signal-to-noise ratio

SPS SunPhotoSpectrometer

sPV scaled potential vorticity

STS supercooled ternary solutions

SZA solar zenith angle

TAO Toronto Atmospheric Observatory

TOMS Total Ozone Mapping Spectrometer

U of T FTS University of Toronto Fourier Transform Spectrometer

UT-GBS University of Toronto Ground-Based Spectrometer

VCD vertical column density

VMR volume mixing ratio

Chapter 1

Introduction

The ozone layer is a region of high ozone concentration in the stratosphere, extending between approximately 10 and 50 km, with a maximum density at roughly 25 km. Ozone absorbs ultraviolet light from the Sun, a process which is essential to all life on the surface of the Earth. Ultraviolet light can damage skin in humans and animals, leading to sunburns and skin cancer. It can also damage the cell walls of plants (Makhijani and Gurney, 1995).

In the mid-1980s, Farman et al. (1985) made the unexpected discovery that severe ozone depletion was occurring over Halley Bay, Antarctica. They examined total ozone data recorded at the station from 1957 onwards, and found that not only was severe depletion occurring, but that it was occurring seasonally in the spring, and not at other times of the year. Further examination of ground- and satellite-based data showed that ozone depletion was occurring throughout the Antarctic stratosphere, always in the spring, a phenomenon that came to be known as the ozone hole (Stolarski et al., 1986; Komhyr and Grass, 1986; Farmer et al., 1987; Mount et al., 1987). Stolarski and Cicerone (1974) had previously shown that chlorine could react catalytically with ozone to destroy it. Also in that year, Molina and Rowland (1974) showed that chlorofluorocarbons (CFCs) were photodissociated in the stratosphere, and were thus a significant source of stratospheric chlorine. As CFCs are well-mixed, chlorine-caused ozone depletion was thought to happen over the entire globe, and at a constant rate through the year. Molina and Rowland (1974) predicted that chlorine reactions would result in a 10% reduction of the stratospheric column by the middle of the twenty-first century. Thus it was a surprise that ozone depletion was happening in one particular location at one particular time of year.

In the two decades following the work of Farman et al. (1985), the processes that cause polar ozone depletion and the ozone hole have become well understood. It is now known that the Antarctic ozone hole is caused by a combination of the natural dynamics of the polar atmosphere, increased amounts of ozone-depleting substances in the atmosphere, and heterogeneous chemistry that takes place on the surface of polar stratospheric clouds. The list of substances that catalytically react with ozone has been expanded and includes the hydroxyl radical, nitrogen, chlorine, bromine, and iodine. Chlorine and bromine species are referred to as ozone-depleting substances. Ozone depletion occurs over the Arctic as well as the Antarctic, although due to increased topography in the Northern Hemisphere, which increases planetary wave activity, the depletion over the Arctic is not as severe. Ozone depletion is also occurring at midlatitudes, with total losses since 1980 of 3% in the Northern Hemisphere and 6% in the Southern Hemisphere (WMO, 2007).

1.1 Motivation and Goals

With the study of ozone depletion in the Canadian Arctic as one motivation, a ground-based, portable, UV-visible grating spectrometer, the University of Toronto Ground-Based Spectrometer (UT-GBS), was assembled at the University of Toronto in 1998. As part of my research, the instrument was deployed at the Polar Environment Atmospheric Research Laboratory (PEARL) in Eureka, Nunavut (80°N, 86°W) during polar sunrise in 2004-2007 for the Canadian Arctic ACE validation campaigns. Total columns of ozone, NO_2, and BrO were retrieved from the spectra recorded by the instrument. The Atmospheric Chemistry Experiment (ACE) is a Canadian satellite, launched in 2003, to investigate the chemical and dynamical processes that are involved in the distribution of ozone in the atmosphere, with a focus on the Canadian Arctic.

In 2005, a consortium of Canadian universities, the CAnadian Network for the Detection of Atmospheric Change (CANDAC), began to refurbish PEARL, formally Environment Canada's Arctic Stratospheric Ozone Observatory (AStrO). As part of this refurbishment, a second UT-GBS, the PEARL-Ground-Based Spectrometer (PEARL-GBS), was permanently installed at PEARL. This new instrument provides year-long measurements, except during polar night. In addition to the above species, slant column densities of OClO have also been retrieved from the spectra recorded by this instrument.

In addition to providing validation data for the ACE satellite, the measurements from the GBSs also allow for the characterization of the chemical composition of the stratosphere over Eureka during both chemically perturbed and unperturbed conditions. The measurements extend the record of the UT-GBS at Eureka, which date back to 1999. With the PEARL-GBS measuring year-round, both the seasonal and interannual variability of the Arctic ozone budget can be investigated. The measurements of BrO can also help to understand the ozone budget: bromine chemistry is not as well understood as that of other halogens. A lack of measurements of BrO, specifically at the high latitudes, means that most of the current understanding of bromine chemistry comes from model calculations (Tørnkvist et al., 2002).

The UT-GBS was also deployed as part of the ground-based instrument suite of the fourth Middle Atmosphere Nitrogen TRend Assessment (MANTRA) campaign in Vanscoy, Saskatchewan (52°N, 107°W) in August 2004. The ground-based instruments were able to measure the day-to-day variability of some of the trace gases to be measured by the instruments on board the balloon.

The goals of this Ph.D. project were the deployment of the UT-GBS at Eureka during the first four Canadian Arctic ACE validation campaigns and at Vanscoy during the MANTRA 2004 campaign, the installation and commissioning of the PEARL-GBS at Eureka, the retrieval of ozone, NO_2, and BrO total columns and OClO slant columns from the spectra, the optimization of the retrievals for these four species, the comparison of the data from the GBSs to other UV-visible grating spectrometers, and validation of the ACE satellite measurements.

1.2 Homogeneous Chemistry

1.2.1 The Chapman Cycle

The Chapman Cycle was proposed by Chapman (1930) as a mechanism for the creation and destruction of ozone. Ozone is produced when molecular oxygen is photodissociated into atomic oxygen by ultraviolet radiation with a wavelength of 40 – 240 nm:

$$O_2 + h\nu \longrightarrow 2O. \tag{1.1}$$

The atomic oxygen then combines with molecular oxygen in the presence of another molecule, such as nitrogen, to form ozone. Ozone is destroyed by absorbing ultraviolet radiation of 240 – 320 nm (Jacob, 1999; Dessler, 2000):

$$\begin{aligned} O_2 + O + M &\longrightarrow O_3 + M && (1.2)\\ O_3 + h\nu &\longrightarrow O_2 + O(^1D) && (1.3)\\ O(^1D) + M &\longrightarrow O + M. && (1.4) \end{aligned}$$

There is a rapid cycling between atomic oxygen and ozone through these reactions of the Chapman Cycle, and so they are often referred to as odd-oxygen, or O_x. Loss of ozone to atomic oxygen is not a permanent loss, as atomic oxygen will be quickly transformed back to ozone via Equation 1.2. Ozone can be permanently removed from the atmosphere by reacting with atomic oxygen (Jacob, 1999; Dessler, 2000):

$$O_3 + O \longrightarrow 2O_2. \tag{1.5}$$

In the 1950s, with more frequent and more accurate measurements of the vertical profile and total column amounts of ozone, it became clear that the Chapman Cycle predicted twice as much ozone as there was in the stratosphere (Rowland, 2006). It is now known that ozone reacts catalytically with the hydrogen (Bates and Nicolet, 1950), nitrogen (Crutzen, 1970), chlorine (Stolarski and Cicerone, 1974; Molina and Rowland, 1974), bromine (Wofsy et al., 1975; Yung et al., 1980), and iodine (Solomon, 1994) families. It is the increase of the stratospheric concentrations of chlorine and bromine that causes anthropogenic ozone depletion.

1.2.2 Hydrogen

The reactive hydrogen family, or $\mathrm{HO_x}$, is composed of the hydroxyl radical (OH), the hydroperoxy radical ($\mathrm{HO_2}$), and atomic hydrogen. Since atomic hydrogen reacts very quickly with oxygen to form $\mathrm{HO_2}$, its concentration in the stratosphere is minimal, and it is often omitted from $\mathrm{HO_x}$. The main source of $\mathrm{HO_x}$ into the stratosphere is the transport of water vapour. Once there, water is oxidized by atomic oxygen to form the hydroxyl radical (Jacob, 1999):

$$H_2O + O(^1D) \longrightarrow 2OH. \tag{1.6}$$

$\mathrm{HO_x}$ can also formed in the stratosphere by water reacting with $\mathrm{N_2O_5}$ and $\mathrm{BrONO_2}$, atomic oxygen reacting with methane ($\mathrm{CH_4}$), the methyl radical ($\mathrm{CH_3}$), and molecular hydrogen, OH reacting with carbon monoxide (CO), and, at high solar zenith angles, photodissociation of $\mathrm{HO_2NO_2}$ (Dessler, 2000). The hydroxyl radical then reacts catalytically with ozone:

$$OH + O_3 \longrightarrow HO_2 + O_2 \tag{1.7}$$

$$HO_2 + O_3 \longrightarrow OH + 2O_2 \tag{1.8}$$

$$net: 2O_3 \longrightarrow 3O_2. \tag{1.9}$$

A second reaction pathway for the $\mathrm{HO_2}$ radical is the reaction with atomic oxygen (Rowland, 2006):

$$OH + O_3 \longrightarrow HO_2 + O_2 \tag{1.10}$$

$$HO_2 + O \longrightarrow HO + O_2 \tag{1.11}$$

$$net: O_3 + O \longrightarrow 2O_2. \tag{1.12}$$

Odd-oxygen is also removed through the following reaction pathway, which is most effective in the upper stratosphere, above 40 km (Lary, 1997):

$$H + O_2 + M \longrightarrow HO_2 + M \tag{1.13}$$

$$HO_2 + O \longrightarrow OH + O_2 \tag{1.14}$$

$$OH + O \longrightarrow H + O_2 \tag{1.15}$$

$$net: 2O \longrightarrow O_2. \tag{1.16}$$

All three of these reactions convert odd-oxygen into molecular oxygen and result in a net loss of $\mathrm{O_x}$. The hydroxyl radical is removed from the atmosphere by reacting with the hydroperoxy radical (Jacob, 1999):

$$OH + HO_2 \longrightarrow H_2O + O_2. \tag{1.17}$$

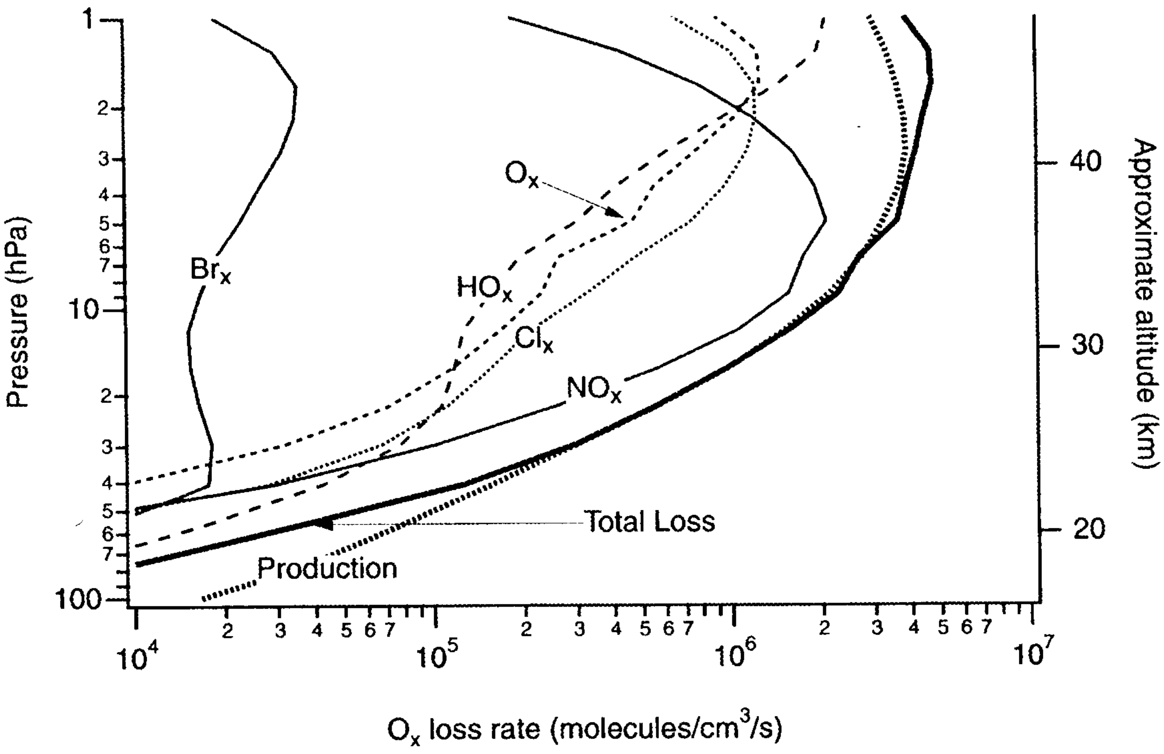

Figure 1.1: O_x loss rates for the catalytic cycles involving hydrogen, nitrogen, chlorine, and bromine. Also shown is the production rate. These are the twenty-four hour averages calculated for 35°N in September. This is Figure 3.7 from Dessler (2000).

In the lower stratosphere, HO_x can also be removed through reactions with nitrogen dioxide (NO_2), nitric acid (HNO_3), peroxynitric acid (HNO_4), and hydrogen chloride (HCl) (Dessler, 2000). In the lower stratosphere, below 15 km, and in the upper stratosphere, above 40 km, HO_x is the dominant sink for ozone, as seen in Figure 1.1 (Jacob, 1999; Dessler, 2000).

1.2.3 Nitrogen

Reactive nitrogen, or NO_x, is composed of nitric oxide (NO) and nitrogen dioxide (NO_2). Stratospheric nitrogen chemistry also involves longer-lived nitrogen species known as reservoirs: nitrate (NO_3), dinitrogen pentoxide (N_2O_5), chlorine nitrate ($ClONO_2$), bromine nitrate ($BrONO_2$), nitric acid (HNO_3), and peroxynitric acid (HO_2NO_2). Together, reactive nitrogen and its reservoirs make up NO_y.

Reactive nitrogen is transported to the stratosphere by way of nitrous oxide (N_2O), which has a long lifetime in the troposphere. Once in the stratosphere, about 90% gets photolysed to molecular nitrogen and atomic oxygen. The remainder is mostly converted to nitric oxide by reaction with atomic oxygen (Jacob, 1999):

$$N_2O + O(^1D) \longrightarrow 2NO. \tag{1.18}$$

Other sources of stratospheric nitrogen are the dissociation of molecular nitrogen by solar protons and cosmic rays, transport from the mesosphere, and transport of lightning-produced NO_x from the upper troposphere (Solomon, 1999; Dessler, 2000). NO_x reacts catalytically with ozone (Dessler, 2000):

$$NO + O_3 \longrightarrow NO_2 + O_3 \tag{1.19}$$

$$NO_2 + O \longrightarrow NO + O_2 \tag{1.20}$$

$$net : O_3 + O \longrightarrow 2O_2. \tag{1.21}$$

These two reactions occur rapidly, and the nitrogen cycles between NO and NO_2 rapidly. Reactive nitrogen is removed from the atmosphere through two main pathways. During the day, nitric acid is formed through the reaction with the hydroxyl radical:

$$NO_2 + OH + M \longrightarrow HNO_3 + M. \tag{1.22}$$

At night, N_2O_5 is formed through the reaction with ozone:

$$NO_2 + O_3 \longrightarrow NO_3 + O_2 \tag{1.23}$$

$$NO_3 + NO_2 + M \longrightarrow N_2O_5 + M. \tag{1.24}$$

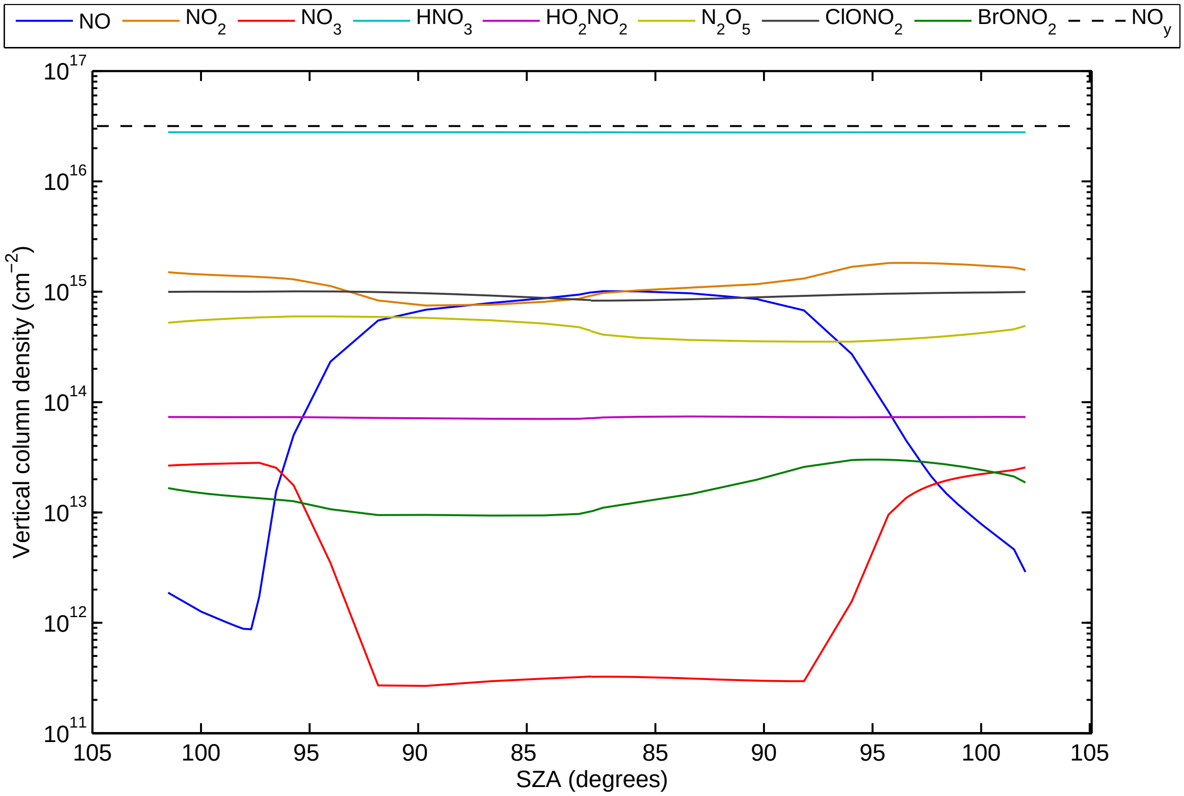

Figure 1.2: Diurnal variation of the total columns of the species that make up NO_y, calculated for mid-March at 80°N using the UCI photochemical box model.

These reactions cannot occur during the day because NO_3 is photolysed to NO_2 in a matter of seconds. NO_x can also be removed through reaction with ClO and BrO, which will be discussed below. The species that compose NO_y (other than NO and NO_2) are known as reservoir species for NO_x because they eventually can be turned back into reactive nitrogen. Reactive nitrogen is permanently removed from the stratosphere by transport of nitric acid to the troposphere, where it is rained out (Jacob, 1999). Between approximately 15 and 40 km, NO_2 is the dominant sink of ozone, as seen in Figure 1.1.

Figure 1.2 shows the diurnal variation of the total columns of the species that make up NO_y. These were calculated for mid-March at 80° N using the UCI (University of California at Irvine) photochemical box model (Prather, 1997; McLinden et al., 2000).

1.2.4 Chlorine

CFCs were first introduced in the 1930s, and were touted as being non-toxic and non-flammable. They quickly became widely used as a coolant in refrigerators and air conditioners (Rowland, 2006). In 1973, Lovelock et al. (1973) showed that CFC-11 ($CFCl_3$) was present at the surface at concentrations that decreased with latitude. The interest in CFCs was limited to its use as a tracer, as Lovelock et al. (1973) also showed that the abundance of CFC-11 in the atmosphere was roughly equal to the amount that had been produced up to that time. Stolarski and Cicerone (1974) proposed a catalytic cycle by which ozone is destroyed by chlorine. They proposed that chlorine could enter the stratosphere through transport of industrially produced HCl, or through powerful volcanic eruptions. Molina and Rowland (1974) showed that since CFCs have such long lifetimes in the troposphere (ranging from 50 to hundreds of years), they can easily be transported to the stratosphere. About 80% of the chlorine in the stratosphere is anthropogenic in origin (Dessler, 2000). Once there, CFCs photodissociate in a matter of days at altitudes between 20 and 40 km:

$$\text{CFC-11: } CFCl_3 + h\nu \longrightarrow CFCl_2 + Cl \tag{1.25}$$

$$\text{CFC-12: } CF_2Cl_2 + h\nu \longrightarrow CF_2Cl + Cl. \tag{1.26}$$

This reaction yields a free chlorine atom, which can then react catalytically with ozone:

$$Cl + O_3 \longrightarrow ClO + O_2 \tag{1.27}$$

$$ClO + O \longrightarrow Cl + O_2 \tag{1.28}$$

$$net : O_3 + O \longrightarrow 2O_2. \tag{1.29}$$

These two reactions occur rapidly, causing a cycling between Cl and chlorine monoxide (ClO), which are referred to together as the ClO_x family. When concentrations of ClO are high, such as at polar springtime (further discussed in Section 1.3), a second catalytic cycle can occur:

$$ClO + ClO + M \longrightarrow ClOOCl + M \tag{1.30}$$

$$ClOOCl + h\nu \longrightarrow ClOO + Cl \tag{1.31}$$

$$ClOO + M \longrightarrow Cl + O_2 \tag{1.32}$$

$$2 \times (Cl + O_3 \longrightarrow ClO + O_2) \tag{1.33}$$

$$net : 2O_3 \longrightarrow 3O_2. \tag{1.34}$$

Chlorine is also tied to the nitrogen family through the following catalytic reactions (Dessler, 2000):

$$ClONO_2 + h\nu \longrightarrow Cl + NO_3 \tag{1.35}$$

$$NO_3 + h\nu \longrightarrow NO + O_2 \tag{1.36}$$

$$NO + O_3 \longrightarrow NO_2 + O_2 \tag{1.37}$$

$$Cl + O_3 \longrightarrow ClO + O_2 \tag{1.38}$$

$$ClO + NO_2 + M \longrightarrow ClONO_2 + M \tag{1.39}$$

$$net : 2O_3 \longrightarrow 3O_2. \tag{1.40}$$

And also (Lary, 1997):

$$ClO + NO \longrightarrow Cl + NO_2 \tag{1.41}$$

$$NO_2 + O \longrightarrow NO + O_2 \tag{1.42}$$

$$Cl + O_3 \longrightarrow ClO + O_2 \tag{1.43}$$

$$net : O + O_3 \longrightarrow 2O_2. \tag{1.44}$$

Chlorine also reacts with the hydrogen family (Lary, 1997):

$$ClO + HO_2 \longrightarrow HOCl + O_2 \tag{1.45}$$

$$HOCl + h\nu \longrightarrow Cl + OH \tag{1.46}$$

$$Cl + O_3 \longrightarrow ClO + O_2 \tag{1.47}$$

$$OH + O_3 \longrightarrow HO_2 + 2O_2 \tag{1.48}$$

$$net : 2O_3 \longrightarrow 3O_2. \tag{1.49}$$

$\mathrm{ClO_x}$ is mainly removed by conversion to the reservoir species $\mathrm{ClONO_2}$ (Equation 1.39) and to HCl:

$$Cl + CH_4 \longrightarrow HCl + CH_3. \tag{1.50}$$

A small amount (10%) is also removed by reactions with $\mathrm{H_2}$, OH, and $\mathrm{HO_2}$ to form HCl. Analogously to the nitrogen family, reservoir chlorine species and reactive chlorine are grouped together into the chlorine family, $\mathrm{Cl_y}$. Chlorine is made up of $\mathrm{ClO_x}$, HCl, $\mathrm{ClONO_2}$, ClO, hydrogen chlorate (HOCl), and chlorine peroxide (ClOOCl). There are no chemical loss processes for $\mathrm{Cl_y}$. Concentrations will increase until all of the source CFCs are depleted (Dessler, 2000). $\mathrm{Cl_y}$ is removed from the stratosphere in the form of transport of HCl to the troposphere, which is water soluble and gets rained out (Solomon, 1999). In the middle stratosphere, $\mathrm{ClO_x}$ is the second most dominant loss process for $\mathrm{O_x}$, as seen in Figure 1.1.

Figure 1.3 shows the diurnal variation of the total columns of the species that make up $\mathrm{Cl_y}$. These were calculated for mid-March at 80° N using the UCI photochemical box model.

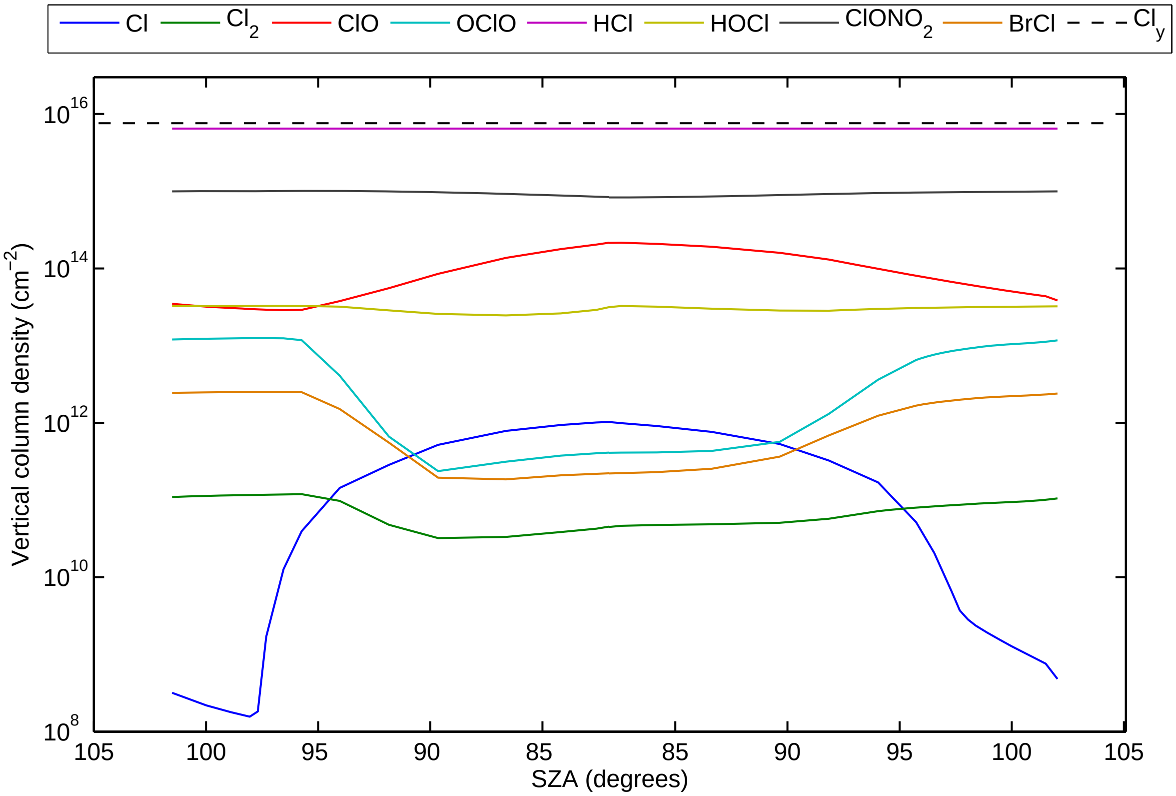

Figure 1.3: Diurnal variation of the total columns of the species that make up Cl_y, calculated for mid-March at 80°N using the UCI photochemical box model.

1.2.5 Bromine

Because the bromine atom is physically larger than the chlorine atom, the intramolecular bonds are weaker, and bromine species have shorter lifetimes than chlorine species. As a result, bromine is significantly more effective at removing ozone from the atmosphere than chlorine, but is a less important sink due to smaller concentrations in the atmosphere. However, bromine is less regulated than chlorine, meaning that its contribution to ozone depletion is expected to increase as chlorine levels decrease (Dessler, 2000). The primary source of bromine in the stratosphere is the transport of methyl bromide (CH_3Br) from the troposphere. Methyl bromide occurs naturally in the ocean, and is used as a fumigant and to sterilize soils (Makhijani and Gurney, 1995). Approximately two-thirds of stratospheric bromine is anthropogenic in origin (Dessler, 2000). Once in the stratosphere, it reacts with OH or atomic oxygen:

$$CH_3Br + OH + M \longrightarrow BrOH + M \tag{1.51}$$

$$CH_3Br + O + h\nu \longrightarrow BrO + CH_3. \tag{1.52}$$

Analogously to the chlorine catalytic cycle, bromine can react catalytically with ozone:

$$Br + O_3 \longrightarrow BrO + O_2 \tag{1.53}$$

$$BrO + O \longrightarrow Br + O_2 \tag{1.54}$$

$$net : O_3 + O \longrightarrow 2O_2. \tag{1.55}$$

Like the HO_x, NO_x, and ClO_x families, Br and BrO cycle rapidly between one another, and are grouped together in the BrO_x family. The above reactions do not contribute greatly to ozone depletion. The catalytic cycle most responsible for bromine-involving ozone loss also involves ClO:

$$Cl + O_3 \longrightarrow ClO + O_2 \tag{1.56}$$

$$Br + O_3 \longrightarrow BrO + O_2 \tag{1.57}$$

$$BrO + ClO \longrightarrow BrCl + O_2 \tag{1.58}$$

$$BrCl + h\nu \longrightarrow Br + Cl \tag{1.59}$$

$$net : 2O_3 \longrightarrow 3O_2. \tag{1.60}$$

The BrO and ClO reaction (Equation 1.58) has two other reaction pathways: either ClOO or OClO can be formed. If ClOO is formed, there is net ozone depletion:

$$Cl + O_3 \longrightarrow ClO + O_2 \tag{1.61}$$

$$Br + O_3 \longrightarrow BrO + O_2 \tag{1.62}$$

$$BrO + ClO \longrightarrow ClOO + Br \tag{1.63}$$

$$ClOO + M \longrightarrow Cl + O_2 + M \tag{1.64}$$

$$net : 2O_3 \longrightarrow 3O_2. \tag{1.65}$$

If OClO is formed in Equation 1.58, it is photolysed to ClO and atomic oxygen, and there is no net loss of odd oxygen (Dessler, 2000). The bromine family is linked to the hydrogen family via reactions with HOBr (Lary, 1996):

$$HO_2 + BrO \longrightarrow HOBr + O_2 \tag{1.66}$$

$$HOBr + h\nu \longrightarrow OH + Br \tag{1.67}$$

$$Br + O_3 \longrightarrow BrO + O_2 \tag{1.68}$$

$$OH + O_3 \longrightarrow HO_2 + O_2 \tag{1.69}$$

$$net : 2O_3 \longrightarrow 3O_2. \tag{1.70}$$

And also to the nitrogen family through reactions with $BrONO_2$ (Lary, 1996):

$$BrO + NO_2 + M \longrightarrow BrONO_2 + M \tag{1.71}$$

$$BrONO_2 + h\nu \longrightarrow Br + NO_3 \tag{1.72}$$

$$NO_3 + h\nu \longrightarrow NO + O_2 \tag{1.73}$$

$$NO + O_3 \longrightarrow NO_2 + O_2 \tag{1.74}$$

$$Br + O_3 \longrightarrow BrO + O_2 \tag{1.75}$$

$$net : 2O_3 \longrightarrow 3O_2. \tag{1.76}$$

There is roughly 20 ppt of bromine in the stratosphere, versus 3000 ppt of chlorine. Because bromine is much more reactive with ozone than chlorine, the bromine catalytic cycle is much more effective at removing ozone. Bromine is roughly 20–50 times more efficient at destroying ozone than chlorine (Rowland, 2006). The bromine family, $\mathrm{Br_y}$, is composed of $\mathrm{BrO_x}$, $\mathrm{BrONO_2}$, HBr, HOBr, and BrCl. $\mathrm{BrO_x}$ is removed from the atmosphere by conversion into the reservoir species HBr:

$$Br + HO_2 \longrightarrow HBr + O_2 \tag{1.77}$$

$$Br + HCHO \longrightarrow HBr + HCO. \tag{1.78}$$

Like chlorine, there are no loss processes for $\mathrm{Br_y}$ in the stratosphere. The concentration of bromine in the stratosphere will increase until all the source gases have been converted to $\mathrm{Br_y}$. Removal of bromine from the stratosphere most likely occurs via mixing into the troposphere (Dessler, 2000). Bromine is currently the smallest contributor to ozone loss in the midlatitudes, as seen in Figure 1.1, however its importance is enhanced at the poles, as will be discussed in Section 1.3.

Figure 1.4 shows the diurnal variation of the total columns of the species that make up $\mathrm{Br_y}$. These were calculated for mid-March at 80° N using the UCI photochemical box model.

1.3 Heterogeneous Chemistry

Sulphate aerosols are ubiquitously present in the stratosphere in the form of $\mathrm{H_2SO_4}$ at concentrations of approximately 1 $\mu\mathrm{m/cm^3}$ (Dessler, 2000). These aerosols provide a surface for the following reactions to occur (Solomon, 1999; Dessler, 2000):

$$N_2O_5 + H_2O \overset{aerosol}{\longrightarrow} 2HNO_3 \tag{1.79}$$

$$BrONO_2 + H_2O \overset{aerosol}{\longrightarrow} HOBr + HNO_3. \tag{1.80}$$

Both of these reactions occur at temperatures found throughout the stratosphere. Nitric acid is produced by both reactions. Since $\mathrm{HNO_3}$ is more stable in the atmosphere than

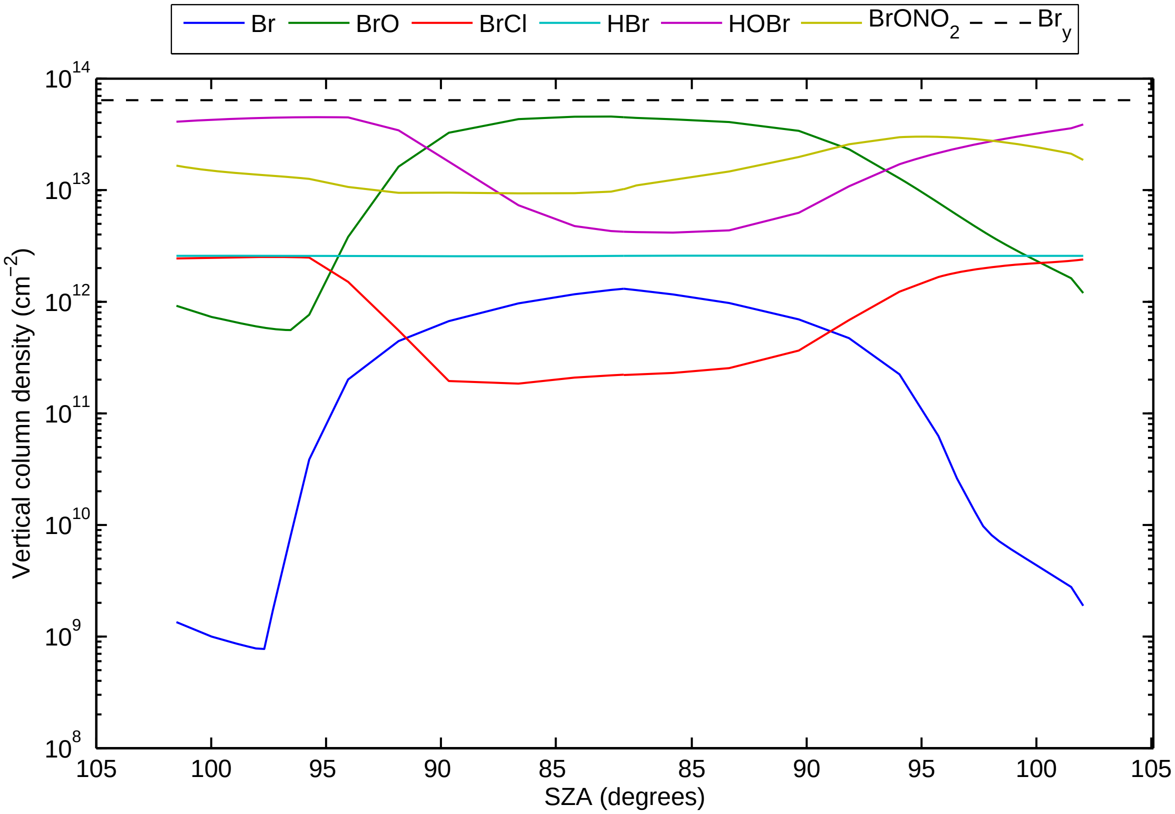

Figure 1.4: Diurnal variation of the total columns of the species that make up Br_y, calculated for mid-March at 80°N using the UCI photochemical box model.

either N_2O_5 or $BrONO_2$, creating more nitric acid has the effect of reducing the amount of NO_x in the stratosphere. This reduces nitrogen-fueled catalytic ozone destruction. However, less NO_x translates into more chlorine and bromine, since the NO_x is not available to form other nitrogen reservoirs such as $ClONO_2$ and $BrONO_2$. HO_x too is increased, because the nitric acid is photolysed to form OH. This increases ozone depletion by hydrogen, chlorine, and bromine. The net effect of these competing reactions depends on the relative concentrations of the ozone-depleting substances (Solomon, 1999; Jacob, 1999; Dessler, 2000). Equation 1.79 occurs more frequently at night, when concentrations of N_2O_5 are highest. An increase in aerosol density greatly increases the production of nitric acid. However, this reaction becomes saturated at roughly 5 μm/cm^3. Equation 1.80 occurs more frequently during the day, as $BrONO_2$ can be catalytically reformed through the following reactions (Dessler, 2000):

$$BrONO_2 + H_2O \overset{aerosol}{\longrightarrow} HOBr + HNO_3 \tag{1.81}$$

$$HOBr + h\nu \longrightarrow OH + Br \tag{1.82}$$

$$Br + O_3 \longrightarrow BrO + O_2 \tag{1.83}$$

$$BrO + NO_2 + M \longrightarrow BrONO_2 + M \tag{1.84}$$

$$net : NO_2 + H_2O + O_3 \longrightarrow HNO_3 + OH + O_2. \tag{1.85}$$

Unlike Equation 1.79, Equation 1.80 does not saturate with increasing aerosol concentrations (Dessler, 2000).

After the eruption of Mount Pinatubo in 1991, stratospheric aerosol concentrations were greatly increased (Thomason et al., 1997). More ozone loss was observed in the lower stratosphere, while less loss was observed in the mid-stratosphere (Mickley et al., 1997).

The following reactions also occur on the surface of aerosols, however they only become important at temperatures below 200 K (Solomon, 1999; Dessler, 2000):

$$ClONO_2 + H_2O \overset{aerosol}{\longrightarrow} HOCl + HNO_3 \tag{1.86}$$

$$ClONO_2 + HCl \overset{aerosol}{\longrightarrow} Cl_2 + HNO_3 \tag{1.87}$$

$$HOCl + HCl \overset{aerosol}{\longrightarrow} Cl_2 + H_2O \tag{1.88}$$

$$HOBr + HCl \overset{aerosol}{\longrightarrow} BrCl + H_2O. \tag{1.89}$$

These reactions have the effect of converting the long-lived species of chlorine, HCl and $\mathrm{ClONO_2}$, into more reactive HOCl, $\mathrm{Cl_2}$, and BrCl. These species are quickly converted to $\mathrm{ClO_x}$. The first two reactions also produce nitric acid, which, as discussed above, reduces the amount of $\mathrm{NO_x}$ (Dessler, 2000). The ramifications of the chlorine enhancement will be discussed in Section 1.4.

1.4 The Antarctic Ozone Hole

The Antarctic ozone hole, discovered in the mid-1980s (Farman et al., 1985), is caused by a combination of the natural dynamics of the Antarctic winter and early spring and the increase of ozone-depleting chemicals in the stratosphere.

1.4.1 Polar Vortex

When ozone absorbs ultraviolet light from the Sun, energy is transferred to the stratosphere, and it warms. This is balanced by the cooling effect of infrared radiation emission of carbon dioxide. In the polar regions, when the Sun sets in the fall, the warming due to ozone absorption stops. The stratosphere continues to cool due to CO_2 emission. The midlatitude stratosphere continues to be illuminated by the Sun, and so a temperature and pressure gradient is established between the pole and the midlatitudes. This induces flow towards the pole, which, because of the rotation of the Earth, creates a westerly circulation about the pole (Schoeberl and Hartmann, 1991). This flow is known as the polar night jet, and occurs in both hemispheres. The area polewards of the night jet is the polar vortex. The jet has a maximum near 60°, and extends upwards from ∽15 km (Dessler, 2000). This strong flow isolates the pole from the midlatitudes. When the Sun returns in the spring, ozone absorption resumes and the stratosphere warms, weakening the polar night jet. This causes the vortex to be less stable, and eventually it is broken apart by upward-propagating planetary waves from the troposphere. There is a quick transition to the summer circulation: a weak easterly flow (Schoeberl and Hartmann, 1991).

1.4.2 Polar Stratospheric Clouds

Polar stratospheric clouds (PSCs) are clouds that form in the cold polar stratosphere. PSCs are divided into two main groups: type I PSCs are composed of mainly nitric acid particles and type II PSCs are composed of mainly water ice particles. For type I clouds to form, temperatures in the stratosphere need to be below the condensation point of nitric acid: around 195 K. Similarly, temperatures need to be below the frost point of ice, around 188 K, for type II clouds to form (Koop et al., 1997). Both these temperatures are regularly reached in the winter Antarctic stratosphere (Toon et al., 1990).

Type I PSCs can be further divided depending on their constituent particles. Nitric acid exists in both the solid and liquid states in the stratosphere. As a liquid, it is in the form of supercooled ternary solutions (STS) of nitric acid, water, and sulphuric acid. These particles are spherical and small. There are three solid phases of nitric acid particles in the atmosphere: nitric acid trihydrate (NAT) - $HNO_3 \cdot 3H_2O$, nitric acid dihydrate (NAD) - $HNO_3 \cdot 2H_2O$, and nitric acid monohydrate (NAM) - $HNO_3 \cdot H_2O$ (Jacob, 1999; Biele et al., 2002). Type Ia clouds are composed of a small number of large aspherical solid particles. These clouds are observed at temperatures between the frost point of ice and the condensation point of NAT ($188\text{ K} < T < 195\text{ K}$) (Salawitch et al., 1989). Type Ia-enh (enhanced) clouds are a subset of type I clouds, and are thought to contain more and larger solid particles than type Ia (Tsias et al., 1998). In both type Ia and Ia-enh, the particles are thought to be NAT and NAD, as they are the most stable phases of nitric acid under polar conditions (Voigt et al., 2000). Type Ib clouds are composed of a large number of small liquid STS particles, and solid particles at a very low density. These clouds are observed at temperatures as low as 191 K, 4 K below the condensation point of NAT (Toon et al., 2000; Biele et al., 2002). Type M (mixed) clouds are a combination of type Ia and Ib clouds (Biele et al., 2002).

1.4.3 Polar Ozone Depletion

The polar vortex and polar stratospheric clouds are naturally occurring phenomena in the Antarctic stratosphere. They both play an important role in the formation of the ozone hole due to their effect on nitrogen, chlorine, and bromine chemistry. The polar vortex creates a cold, isolated stratosphere. Temperatures below 188 K are common in the Antarctic, and PSCs of all varieties form regularly. Polar stratospheric cloud particles can act as the aerosols discussed in Section 1.3. This has the effect of converting reservoir species of chlorine into reactive species, following Equations 1.86 to 1.89. This process is known as chlorine activation (Solomon, 1999; Dessler, 2000; Rowland, 2006). Bromine is also released into a more reactive form, but as chlorine accounts for most of the ozone depletion in the Antarctic, this discussion will focus on chlorine. PSCs exist for time periods of hours to days, and air masses inside the vortex are only occasionally exposed to the constituent aerosols. However, the heterogeneous reactions occur so quickly on the surface of the PSC particles that even short, irregular exposure to them can lead to almost complete chlorine activation (Dessler, 2000).

PSCs have another important role in the formation of the ozone hole in that the formation of PSCs removes both nitric acid and water from the gas phase in the stratosphere. These processes are known as denitrification and dehydration. Type I clouds remove both nitric acid and water, though the dehydration caused by their formation is small. The denitrification is significant (Dessler, 2000). Type II PSCs deplete water and nitric acid (since ice particles often grow on STS or NAT particles), leading to both denitrification and dehydration (Carslaw et al., 1998). As discussed in Section 1.3, the removal of reactive nitrogen from the gas phase, known as denoxification, enhances the depletion caused by hydrogen, chlorine, and bromine. However, the nitric acid and water in the PSC particles can be returned to the stratosphere when the PSC particles return to the gas phase. This process leads to the deactivation of chlorine, as the nitric acid provides $\mathrm{NO_x}$, which can then form $\mathrm{ClONO_2}$ and other reservoir species with the halogens (Tabazadeh et al., 2001). If the PSC particles grow to large sizes, they can sediment out of the stratosphere, carrying nitric acid and water to lower levels of the atmosphere. Type II particles (ice) are larger than type I particles, and often sediment. Type Ia particles (solid nitric acid) can grow to large sizes, known as “NAT rocks”, and can sediment as well (Tabazadeh et al., 2000). This leads to denitrification without dehydration. When particles sediment, they permanently remove nitric acid and water from the stratosphere.

When permanent denitrification does not occur, the nitric acid is returned to the stratosphere when PSC particles sublimate to the gas phase. Since PSC lifetimes range from hours to days, this occurs all winter long in the vortex. During the polar night, the chlorine species created by the reactions on the surface of the PSCs build up in the isolated polar vortex. When the Sun returns in the spring, the chlorine activation that takes place is mitigated by the release of NO_x from nitric acid (Dessler, 2000).

When permanent denitrification does occur, the chlorine remains activated when the PSC particles return to the gas phase. When the Sun returns in the spring, Cl_2, HOCl, and BrCl are all photodissociated into ClO_x. The elevated amounts of chlorine allow the ClO/ClO catalytic cycle (Equations 1.30 to 1.33) to dominate ozone destruction, accounting for two thirds of the ozone depletion (Dessler, 2000; Rowland, 2006). The ClO/BrO (e.g. Equations 1.56 to 1.59) and ClO/O (Equations 1.27 to 1.28) catalytic cycles also occur during chlorine activation, with the ClO/BrO cycle accounting for most of the remaining one third of ozone depletion, and the ClO/O cycle accounting for a few percent (Dessler, 2000).

Ozone depletion stops when the chlorine is deactivated. This can either occur when PSC particles return to the gas phase, or, in the case of denitrification, when the vortex breaks apart. At this point, the isolated polar air mixes with nitrogen-rich midlatitude air, and chlorine returns to its reservoir species. Ozone depletion can also stop when all the ozone has been depleted, which can occur over several kilometers in the Antarctic vortex (Dessler, 2000).

1.5 Arctic Ozone Depletion

The same processes occur in the Arctic to produce ozone depletion in the boreal spring. However, the Arctic vortex is not as strong as its southern counterpart. In both polar regions, the polar night jet forms at around 60°. In the Southern Hemisphere, this is over the ocean surrounding Antarctica. In the Northern Hemisphere, this is over the landmass of northern Canada, Europe, and Asia. The topography of the Northern Hemisphere creates planetary waves that propagate upwards, weakening the polar vortex. The weaker vortex means that the air is not as isolated as in the Southern Hemisphere, and so the vortex is warmer (Schoeberl and Hartmann, 1991). Because of this weakened vortex, the vortex often breaks up earlier than in the Antarctic, so some years there is no overlap of the cold temperatures required for PSC formation and sunlight (Solomon, 1999). Because the vortex is warmer, the temperatures required for PSC formation are not reached as often (Solomon, 1999). Figure 1.5 shows the minimum temperatures at approximately 20 km between 50° and 90° for the Northern and Southern Hemispheres. The green horizontal lines indicate the temperatures required for type I and II cloud formation. Both temperatures are always reached in the Southern Hemisphere, and the temperature remains below this threshold for months. In the Northern Hemisphere, the temperatures are not always reached, and when they are it is for short periods of time. This results in more variable chlorine activation, and, since the PSCs last for shorter lengths of time, less denitrification and dehydration. All of this results in less severe ozone depletion in the Arctic (Seinfeld and Pandis, 1998).

However, strong vortices and polar stratospheric clouds do occur in the Arctic, as does ozone depletion. Figure 1.6 shows the annual average total ozone from 63° poleward in March and October for the Northern and Southern Hemispheres. In warm years (e.g., 1989, 1999), no ozone depletion occurs in the Arctic, however in cold years (e.g., 1993, 1997), significant amounts of ozone are lost. In the Southern Hemisphere, there is variability as well, however ozone depletion always occurs.

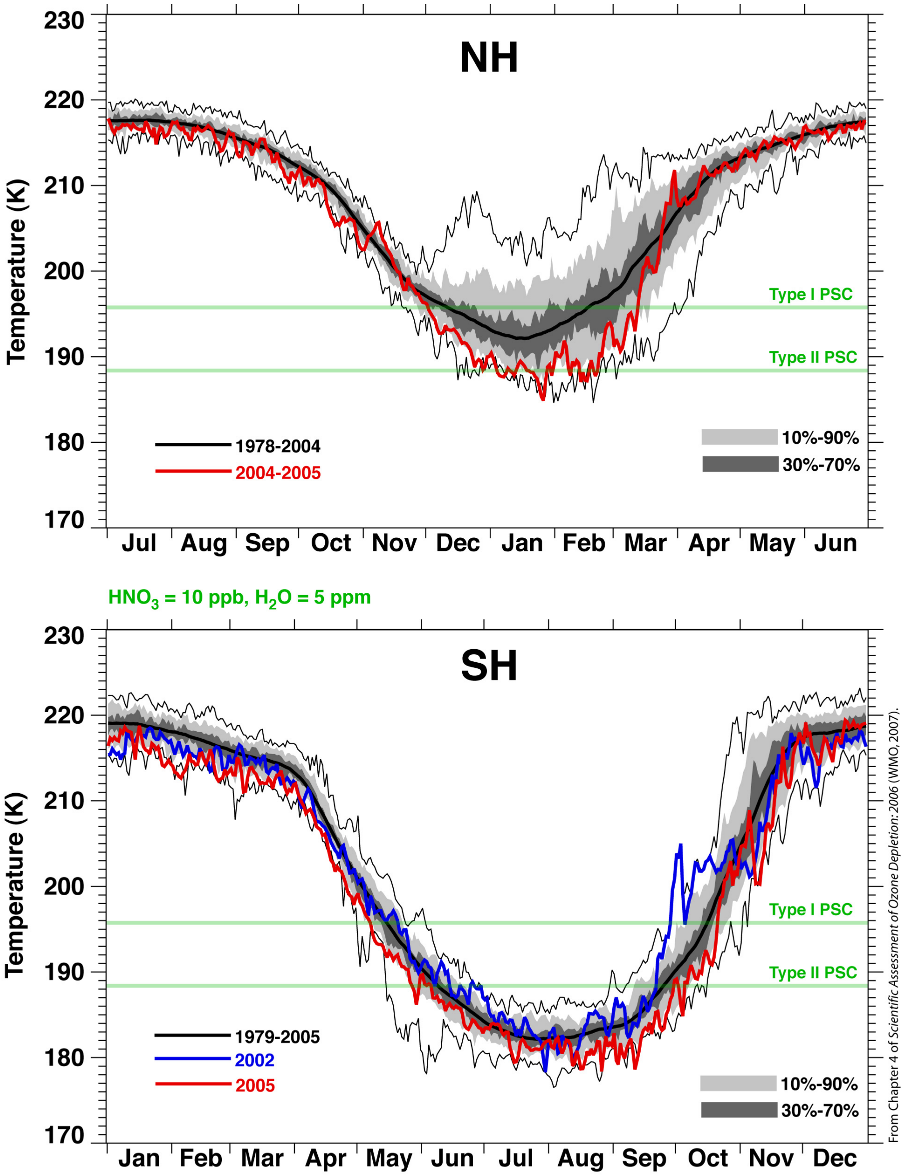

From Chapter 4 of *Scientific Assessment of Ozone Depletion: 2006* (WMO, 2007).

Figure 1.5: Annual temperature cycle and variability of the Northern (NH) and Southern (SH) Hemispheres at 50 hPa (∽ 20 km). The temperatures are the minimum temperatures between 50° and 90° in the hemisphere, from the National Centers for Environmental Prediction (NCEP)/National Center for Atmospheric Research (NCAR) reanalysis data. The thick black line shows the mean temperatures for 1978–2004 in the NH and 1979–2005 in the SH. The dark and light gray shading show the 30–70% and 10–90% probability of observations, respectively. The thin black lines show the extreme values. The green lines show the threshold temperatures for the formation of Type I and II PSCs, assuming 10 ppb of HNO_3 and 5 ppb of H_2O. This is Figure 4-1 from WMO (2007).

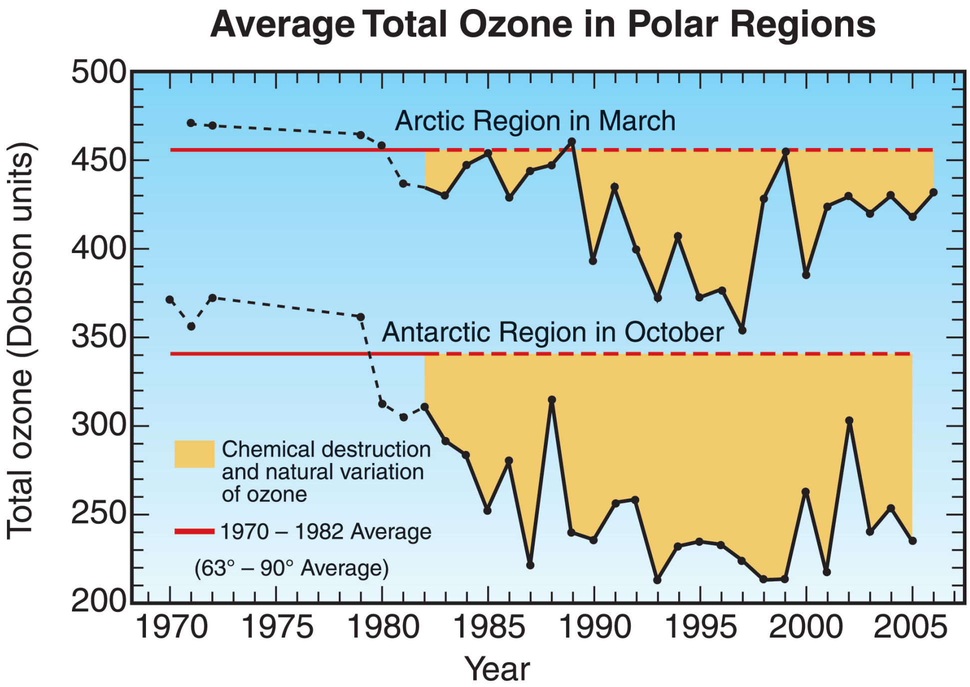

Figure 1.6: Annual average total ozone between 63° and 90° for March in the Northern Hemisphere and October in the Southern Hemisphere. The red line is the 1970–1982 average, while the shaded area indicates deviations from that average. The ozone data is taken from the Total Ozone Mapping Spectrometer (TOMS) instruments. This is Figure Q12-1 from WMO (2007).

1.6 Ozone Recovery

After the cause of ozone depletion became clear, an international treaty was signed in Montréal in 1987 to phase out the use of CFCs. The Montréal Protocol has been amended seven times, most recently in Beijing in 1999. The result of the treaty and its amendments is that concentrations of CFCs and chlorine are beginning to level off and decrease, as seen in Figure 1.7 (WMO, 2007).

As a result of the leveling-off and decrease of the effective stratospheric chlorine (which includes the effects of bromine), ozone concentrations are expected to begin recovering. Models suggest that this recovery should begin to occur during this decade. Observations of the Antarctic ozone hole show a stabilizing of the size and depth of the ozone hole, due to a saturation of loss caused by ozone-depleting substances. The inter-annual variability

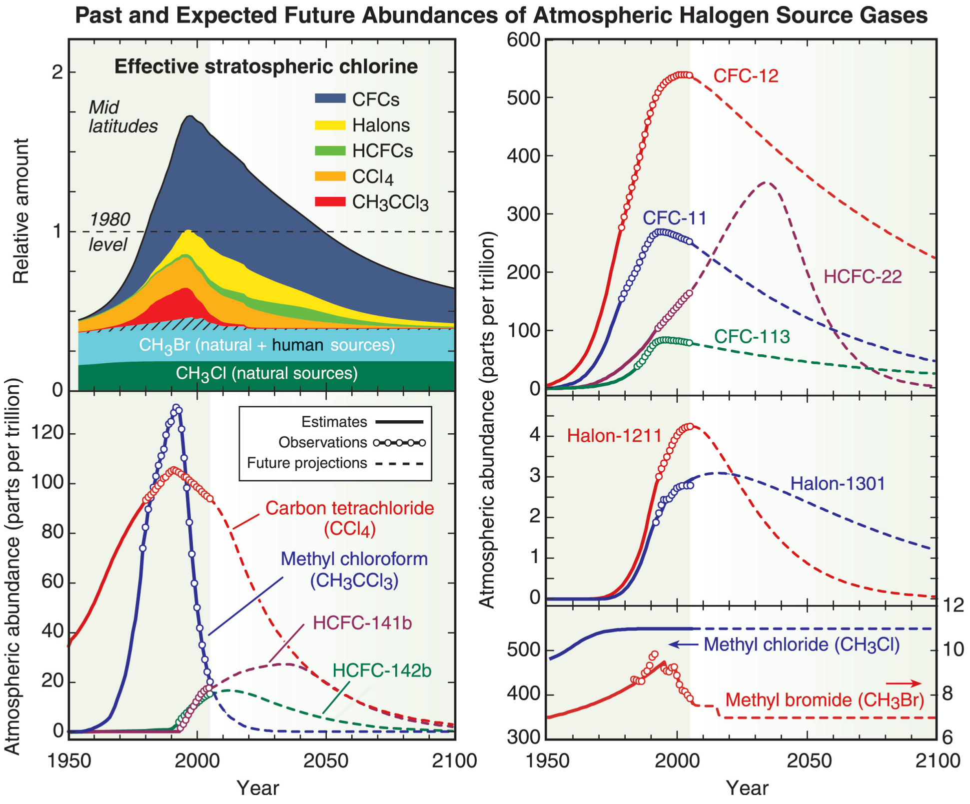

Figure 1.7: Concentrations of effective stratospheric chlorine and source gases for past observations and future predictions. Concentrations of CFCs are beginning to decrease following the regulations of the Montréal Protocol, while HCFC (Hydrochlorofluorocarbon, a less ozone-depleting CFC replacement) concentrations are expected to decrease near the middle of the century. This is Figure Q16-1 from WMO (2007).

of the ozone hole is thought to be masking the early stages of recovery. In the Arctic, there is much more inter-annual variability, making the recovery of the ozone layer much more difficult to detect (WMO, 2007).

Three stages are anticipated in ozone recovery, which are shown schematically in Figure 1.8. In stage one, the rate of change in the decrease of ozone is expected to slow down. In stage two, ozone concentrations will begin increasing. In stage three, ozone concentrations will return to pre-1980 levels (WMO, 2007). Chemical climate models have been used to predict when these stages will occur. In the midlatitudes and tropics, stage two is predicted to begin between 2000 and 2020. In the Antarctic, the maximum ozone hole is expected during the current decade (2000-2010), with an increase

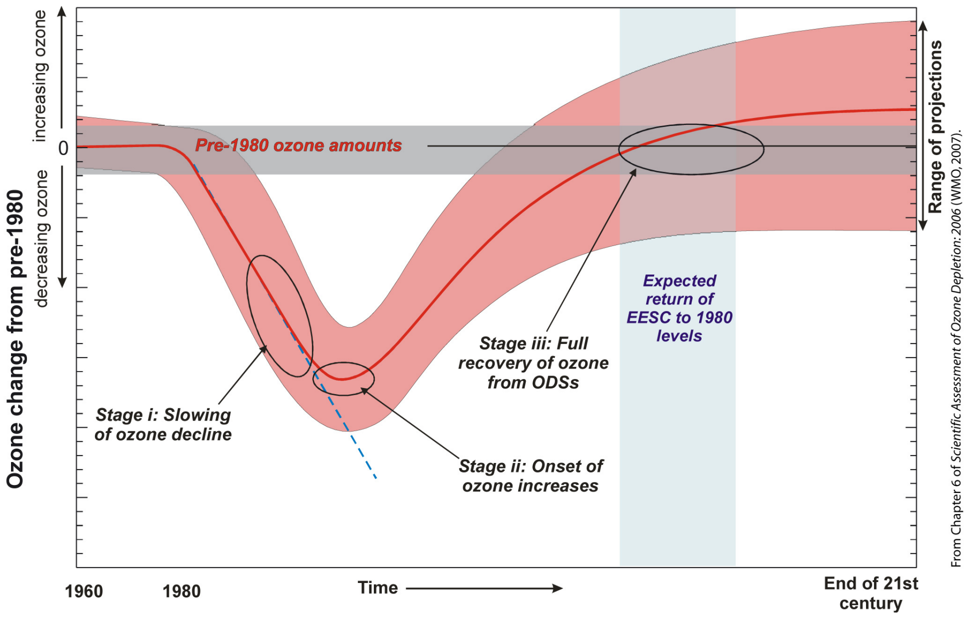

From Chapter 6 of *Scientific Assessment of Ozone Depletion: 2006* (WMO, 2007).

Figure 1.8: Schematic representation of the expected recovery of the ozone layer, based on global chemistry-climate models. The solid red line shows the observed and expected amounts of globally-averaged ozone. The red shaded region shows the range of observations and model results. The blue shaded region shows the time when ozone-depleting substances are predicted to return to pre-1980 values. This is Figure 6-1 from WMO (2007).

in ozone values between 2010 and 2020. In the Arctic, stages one and two are expected to occur between 2000 and 2020, with the large interannual variability masking the exact transitions (WMO, 2007; Austin et al., 2003).

1.7 Thesis Outline and Scientific Contributions

The remainder of this thesis is structured as follows. Chapter 2 describes the UT-GBS and PEARL-GBS, the primary instruments used in this work, as well as three other UV-visible instruments that were intercompared. The UT-GBS was assembled in 1998 by former postdoc Matt Bassford and Kim Strong and has since been deployed by them, former Ph.D. student Elham Farahani, and a series of summer students on the first three midlatitude MANTRA campaigns and the first five Arctic springtime campaigns. I took over primary responsibility for the UT-GBS in 2003, and deployed it at PEARL annually from 2004-2007 and in Vanscoy for the fourth MANTRA campaign in August and September 2004. The PEARL-GBS was assembled in July 2006 by myself and summer student Hristina Popova. I installed it permanently in Eureka in August 2006. This chapter also describes several instrument characterization tests that have been developed by myself, Elham, and Matt, with the help of many summer students. I have analysed all the results shown in this chapter.

Chapter 3 describes the Differential Optical Absorption Spectroscopy (DOAS) technique used to analyse the spectra from the instruments. The software package WinDOAS was used to analyse all the data in this work. The software was provided by Caroline Fayt and Michel Van Roozendael of the BIRA/IASB (Belgian Institute for Space Aeronomy), and I optimized it for each instrument and species. The sources of error are also discussed in this chapter.

In Chapter 4, the MANTRA 2004 campaign results are presented. Differential slant column densities (DSCDs) from the four UV-visible instruments are compared following the methods of the Network for the Detection of Atmospheric Composition Change (NDACC), also described in this chapter. To minimize the differences in analysis between instruments, and to ensure that differences seen in the results were due to actual differences in the spectra and not the analysis method, I analysed the spectra from the other three instruments using WinDOAS. The vertical column densities (VCDs) from the UV-visible instruments are compared as well, and the ozone columns are compared to columns from three Fourier transform spectrometers (FTSs) that also participated in the campaign.

Chapter 5 presents measurements of lightning-produced NO_2 during two thunderstorms in Vanscoy and in Toronto. I developed two new methods of separating the NO_2 into enhancements due to multiple scattering and due to lightning production. The differential slant column densities (DSCDs) are converted into vertical column densities (VCDs) and, using data from the Canadian Lightning Detection Network and radar data from Environment Canada, I calculated the amount of NO_2 produced by each lightning flash. The results are compared to previous measurements from other ground-based UV-visible instruments.

Chapter 6 presents the ozone, NO_2, BrO, and OClO results from the Eureka 2004-2007 campaigns from the UT-GBS and PEARL-GBS. The meteorological conditions of the four winters are discussed, and the results are discussed with consideration of the existence and location of the polar vortex. Comparisons of different methods of calculating the total columns of ozone and NO_2 are also performed. The data from the PEARL-GBS from its installation in 2006 to the beginning of polar night in 2007 are also discussed.

Chapter 7 presents the ozone and NO_2 results from the Eureka 2004-2007 campaigns obtained with the five participating UV-visible instruments. NDACC comparisons are again performed. As in Chapter 4, the spectra from the other instruments were reanalysed using WinDOAS. vertical column densitys (VCDs) are also compared to partial column measurements from the ACE-Fourier Transform Spectrometer (ACE-FTS) and ACE-Measurements of Aerosol Extinction in the Stratosphere and Troposphere Retrieved by Occultation (ACE-MAESTRO) instruments on board the ACE satellite.

Finally, Chapter 8 provides a summary of the main points of the thesis and suggestions for future work.

Chapter 2

Instrumentation

The primary instrument used in this work is the UT-GBS. The data from this instrument have been compared to three other UV-visible zenith-sky-viewing spectrometers: Système d'Analyse par Observations Zénitales (SAOZ), Measurements of Aerosol Extinction in the Stratosphere and Troposphere Retrieved by Occultation-Ground (MAESTRO-G), and the SunPhotoSpectrometer (SPS). In 2006, a second, near-identical spectrometer was obtained: the PEARL-GBS. All five instruments are described in this chapter.

In the course of this work, several tests were developed to determine and monitor the performance of the UT-GBS and PEARL-GBS. This allows for more confidence in the continuity of the measurements from location to location, as well as over time. These properties are also described herein.

2.1 The University of Toronto Ground-Based Spectrometer

Assembled in 1998, the UT-GBS has been used to measure concentrations of ozone, NO_2, BrO, and OClO. It has participated in many field campaigns, including the four MANTRA campaigns in Vanscoy, Saskatchewan, biennially from 1998 to 2004 (Bassford

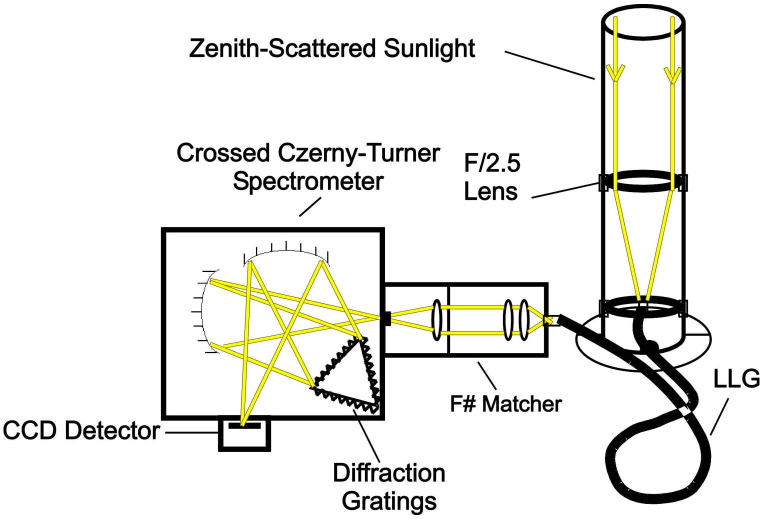

Figure 2.1: Schematic of the University of Toronto Ground-Based Spectrometer.

et al., 2001, 2005; Fraser et al., 2007a). It has been to PEARL (formerly AStrO) in Eureka, Nunavut eight times, from 1999-2001 and 2003-2007, and once to the Solar Winds Observatory in Resolute Bay, Nunavut in 2002 (Farahani, 2006; Farahani et al., 2008; Fraser et al., 2008). While not traveling, it is generally installed at the Toronto Atmospheric Observatory (TAO) in Toronto, Ontario.

2.1.1 The Spectrometer and Input Optics

The instrument is a crossed Czerny-Turner diffraction grating imaging spectrometer (model TRIAX 180, Instruments S.A. Inc.). A schematic is shown in Figure 2.1. Ultraviolet-visible light from the Sun is gathered by a fused silica lens of 40 mm diameter (f-number 2.5) and a 2° field-of-view. It is then focused onto a one-metre-long liquid light guide (LLG) with an inner-core diameter of 3 mm (f-number 0.85). The LLG depolarizes the light, while bringing it into the f-number matcher, a series of lenses that first collimates the light, and then focuses it onto the slit of the spectrometer (f-number 3.9). The instrument can also be operated at night, using the Moon or stars as a light source. In this case, an 11-inch Schmitt-Cassegrain telescope substitutes for the lens.

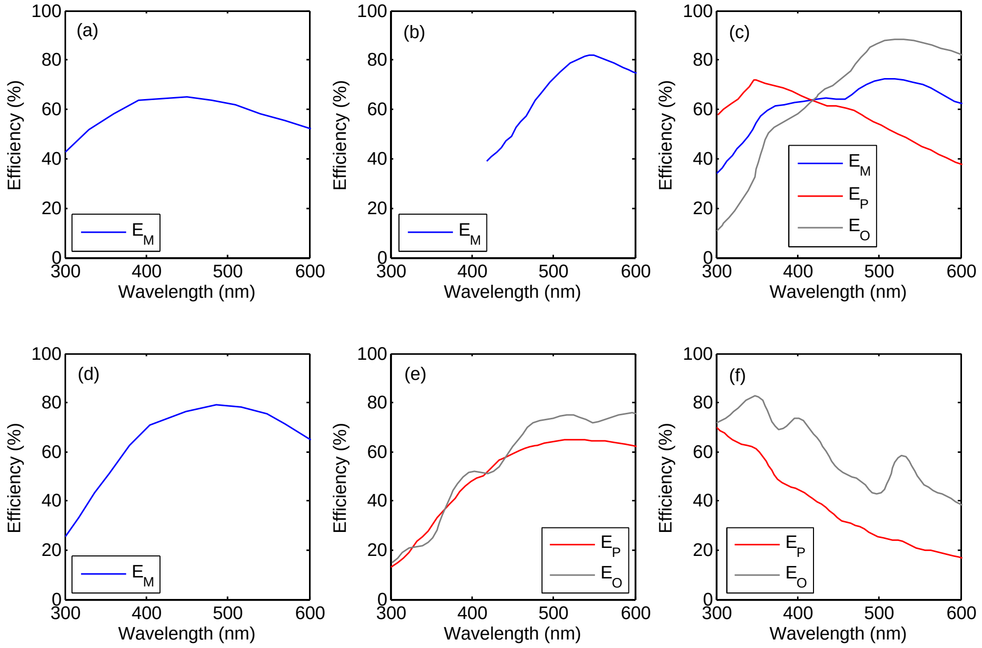

Figure 2.2: Grating efficiencies for the UT-GBS: (a) 400 gr/mm (blazed at 400 nm), (b) 600 gr/mm (blazed at 500 nm), (c) 1800 gr/mm (blazed at 400 nm), and for the PEARL-GBS: (d) 300 gr/mm (blazed at 500 nm), (e) 600 gr/mm (blazed at 500 nm), and (f) 1200 gr/mm (blazed at 330 nm). In all figures, E_M is the efficiency for unpolarized light, E_P is for light polarized parallel to the grooves of the grating, and E_O is for light polarized perpendicular to the grooves of the grating. Adapted from ISA documentation.

The spectrometer consists of two aspherical mirrors and three holographic or ruled plane gratings. The internal optics of the spectrometer are aspherical, which corrects astigmatism, provides point-to-point imaging, and generates a flat field output. The light passes through an adjustable, motorized slit and mechanical shutter, and then is collimated by one mirror onto one of the three gratings (400 gr/mm (ruled), 600 gr/mm (holographic), and 1800 gr/mm(holographic)). The efficiency of the gratings is shown in Figure 2.2 (a)-(c). A second mirror focuses the dispersed light onto the charged coupled device (CCD) detector. Changing the position of the grating varies the spectral range of the instrument, whereas changing the grating alters the resolution. A higher density grating gives higher resolution, but smaller spectral range. The focal length of the instrument is 0.190 m, with a focal plane of 30 mm × 12 mm.

2.1.2 The Detectors

Over the course of this work, the instrument has had three detectors: the original detector, the loaner detector, and the new detector. All three detectors have been two-dimensional array CCDs manufactured by Instruments S.A. The original detector used a back-illuminated chip, with 2000 × 800 pixels and a physical size of 30 mm × 12 mm, which is the same size as the focal plane of the spectrometer. The pixels were each 15 μm × 15 μm. Back-illuminated CCDs are illuminated from the silicon side of the chip, as opposed to the electrode side. This, plus the thinned silicon layer, increases the quantum efficiency of the CCD. The cooling system was triple-stage Peltier thermo-electric cooler. When new, it could reach temperatures as cold as 230 K (Bassford et al., 2005). At the end of its working life, during the Eureka 2004 campaign, it was reaching a minimum of 250 K. The quantum efficiency of this CCD, a measure of the detection efficiency of the pixels as a function of wavelength, is shown in Figure 2.3(a).

Shortly before the MANTRA 2004 campaign, the original detector began recording only saturated spectra. As it could not be repaired in time for the campaign, and was later found to be irreparable, a similar CCD was acquired on loan from the manufacturer. This CCD, known as the loaner CCD, was chosen based on availability and ability to integrate with the existing hardware and software of the instrument. This CCD was not ideal for the measuring conditions, but was the best solution available at the time. It used a front-illuminated chip, with 1024 × 128 pixels, and a physical size of 26.6 mm × 3.3 mm. The pixels were each 26 μm × 26 μm. The chip was cooled by liquid nitrogen, and could reach temperatures as cold as 140 K. Due to the fact that it was front-illuminated, this detector was more sensitive to the visible and near-IR than the ultraviolet, as illustrated by its quantum efficiency curve in Figure 2.3(b). The smaller number of pixels reduced the sampling over the features of the spectra, which reduced the sensitivity of the instrument to absorption features (Roscoe et al., 1996).

After the MANTRA 2004 campaign, a replacement CCD was acquired for the instru-

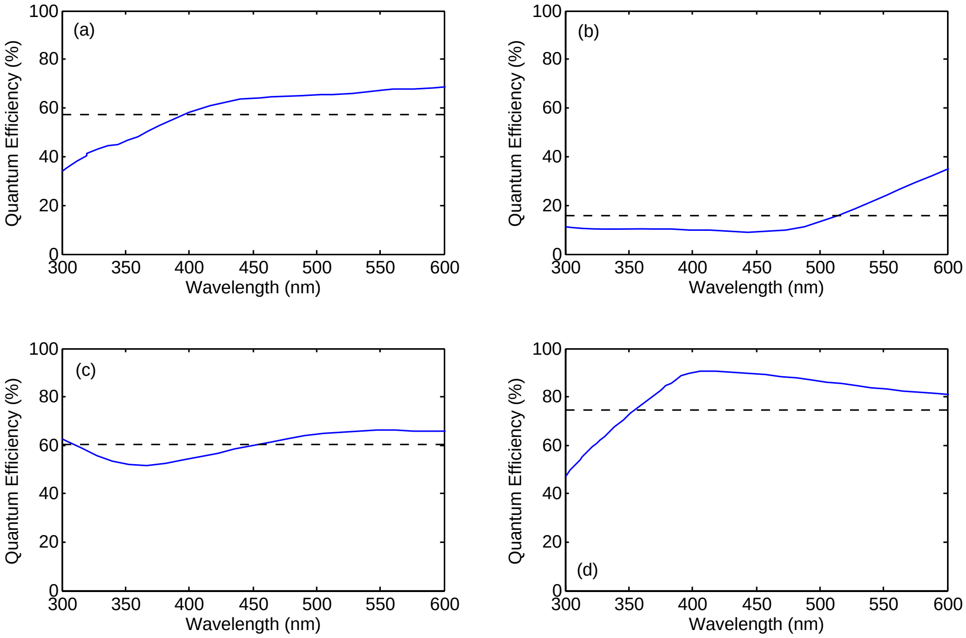

Figure 2.3: Quantum efficiencies of (a) the original CCD detector, (b) the loaner CCD detector, (c) the replacement CCD detector, and (d) the PEARL-GBS CCD detector. The dotted horizontal line indicates the average quantum efficiency between 300 and 600 nm. Adapted from ISA documentation.

ment. This CCD is also back-illuminated, and has 2048 × 512 pixels, and a physical size of 27.6 mm × 6.9 mm. Each pixel is 13.5 μm × 13.5 μm. It is has a four-stage Peltier thermo-electric cooling system and operates at a constant temperature of 201 K, provided the ambient temperature is less than 35°C. Above this temperature, the CCD temperature can increase, although this is outside the suggested operating range of the instrument. The CCD is coated with a UV-enhancing coating, allowing high quantum efficiency in the UV, as shown in Figure 2.3(c).

2.1.3 The Controllers and Software

The instrument is controlled with a computer via interface cables. All three detectors required slightly different setups, but the process of taking a measurement is the same. The spectrometer and detector are controlled by LabVIEW software, allowing for the recording of data automatically. This allows the instrument to be left virtually unattended during extended field campaigns. The physical parameters of the instrument, such as the the slit width or the grating used, are set in the LabVIEW window. A series of spectra recorded at short exposure times is taken by the instrument to determine the light levels available. If there is enough light, and the maximum number of counts is high enough, a parameter controlled by the software, the LabVIEW code then calculates the ideal exposure time to accumulate an ideal signal level (also set by the user). A spectrum is created by binning pixels along the vertical axis of the chip. The chip can also be divided into several vertical bands. A series of spectra is then recorded, and averaged. This is output as one spectrum, and this average of spectra is considered to be one measurement. If it is determined that there is not enough light to take a measurement, the spectrometer records a dark spectrum, at a user-determined exposure time with the shutter closed.

The original detector was controlled by two additional units: the CCD2000 and the CCD3000. The CCD2000 provided power to the cooling system of the CCD detector. The CCD3000 controlled power, clocking signals, and biases, as well as amplifying and digitizing the signal from the spectrometer. The CCD3000 and the spectrometer were controlled by the LabVIEW software via General Purpose Interface Bus (GPIB) cables. The loaner detector was also controlled by the CCD3000, but the CCD2000 was not required. The new detector is controlled by the Symphony controller, which performs the same function as the CCD2000 and CCD3000 combined. It is controlled by the LabVIEW software, and communicates with the computer via an ethernet cable.

When operating in Eureka, Nunavut, the instrument is located inside a hatch on the roof, with a UV-transmitting plexiglas window to view the zenith-sky. In this case, the computer is located on a table beneath the hatch, with the Symphony controller on a platform just below the spectrometer. When operating in Vanscoy and Toronto, and prior to 2003 in Eureka, the instrument is installed inside a weather-proof box located outside. The Symphony or CCD3000 controllers are placed inside the box, which is temperature-regulated by both an air conditioner and heating pads. Both are required year-round, with the exception of extreme temperature days in the summer or winter. The controlling computer is located inside. The computer can be controlled remotely with pcAnywhere software.

2.2 PEARL Ground-Based Spectrometer

The PEARL-GBS was acquired in 2006 and is a near replica of the UT-GBS. It was installed permanently at PEARL in August 2006, after being tested and compared to the UT-GBS in Toronto. The spectrometer itself is identical to the UT-GBS, with the exception of the gratings. While operating in zenith-sky mode, the input optics and configuration of the instrument is shown in Figure 2.4. The input optics are the same as the UT-GBS, however there is a filter wheel installed in front of the slit in the PEARL-GBS. The filter wheel is controlled by the LabVIEW software and contains four filters: blue green (band pass 350–600 nm), long wave (band pass $>$ 575 nm), black (band pass 250–400 nm), and neutral density (0.1% transmission). The position of the lenses in the f-number matcher is different due to the filter wheel. The other difference is that the slit of the PEARL-GBS is fixed to ensure reproducibility, and can be either 0.05 mm or 0.25 mm. Generally, the 0.05 mm slit is used. The gratings of the PEARL-GBS are 300 gr/mm (ruled), 600 gr/mm (holographic), and 1200 gr/mm (holographic). The grating efficiencies are shown in Figure 2.2(d)-(f). The detector of the PEARL-GBS is identical to the UT-GBS's detector, but the CCD is coated with an enhanced broadband coating, allowing for improved detection of the UV wavelengths. The quantum efficiency of the detector is shown in Figure 2.3(d). The instrument is controlled by a Symphony controller, and is installed in a hatch at PEARL.

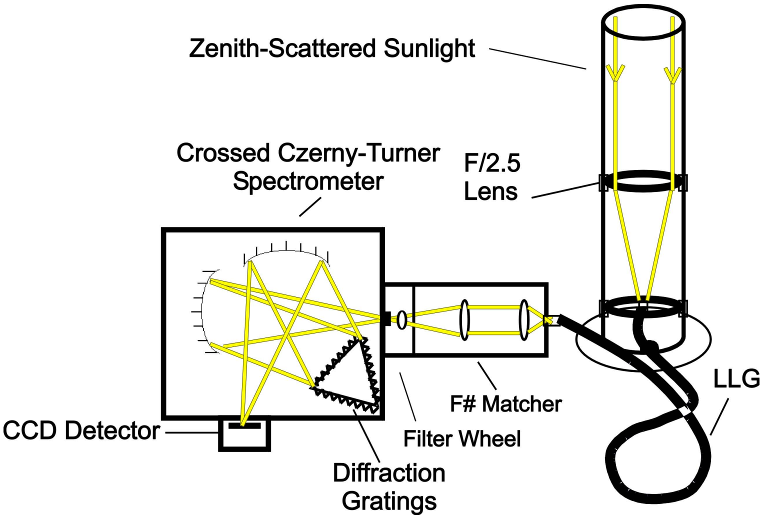

Figure 2.4: Schematic of the PEARL Ground-Based Spectrometer.

2.3 Other Instrumentation

2.3.1 Système d'Analyse par Observations Zénitales

The SAOZ instrument was constructed in the late 1980s, and is now deployed in a global network for measurements of stratospheric concentrations of trace gases important to ozone loss (Pommereau and Goutail, 1988). SAOZ records spectra between 270 and 620 nm, with a resolution of 1.0 nm. The detector is an uncooled 1024-pixel linear diode array. SAOZ records zenith-sky spectra with a 10° field-of-view. Spectra are recorded every thirty minutes throughout the day (fifteen minutes in the Arctic), and continuously during twilight, defined as when the solar zenith angle (SZA) is between 80° and 95°. Immediately after taking a solar spectrum, SAOZ records a dark spectrum of the same exposure time to remove the effects of dark current and bias of the detector. A schematic of the instrument is shown in Figure 2.5. During MANTRA, SAOZ is operated outside, in a weather-proof box. During the Eureka campaigns, it is installed inside PEARL, underneath a UV-transmitting plexiglas window.

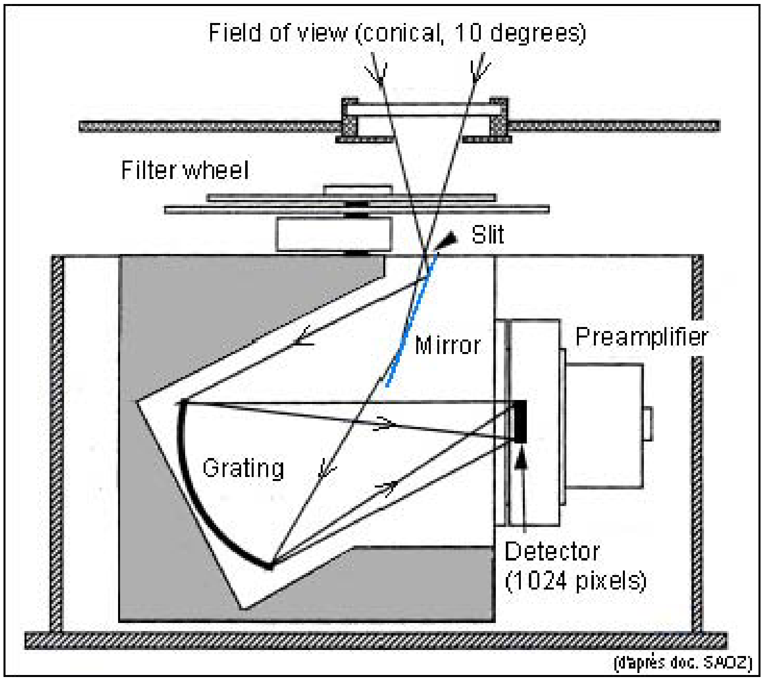

Figure 2.5: Schematic of the Système d'Analyse par Observations Zénitales (courtesy of Florence Goutail).

2.3.2 Measurements of Aerosol Extinction in the Stratosphere and Troposphere Retrieved by Occultation

MAESTRO-G (hereafter MAESTRO) is the ground-based clone of the grating spectrometer on board ACE (McElroy et al., 2007). Measurements of Aerosol Extinction in the Stratosphere and Troposphere Retrieved by Occultation (MAESTRO) is a double spectrometer, with two independent input optics, gratings, and detectors. The UV spectrometer has a spectral range from 260 to 560 nm and a resolution of 1.0 nm. The visible spectrometer has a spectral range from 525 to 1010 nm and a resolution of 2.0 nm. Both detectors are uncooled 1024-pixel linear diode arrays. The field-of-view is 0.1° by 6.5°. A schematic of the instrument is shown in Figure 2.6. Only data from the UV spectrometer are used in this work.

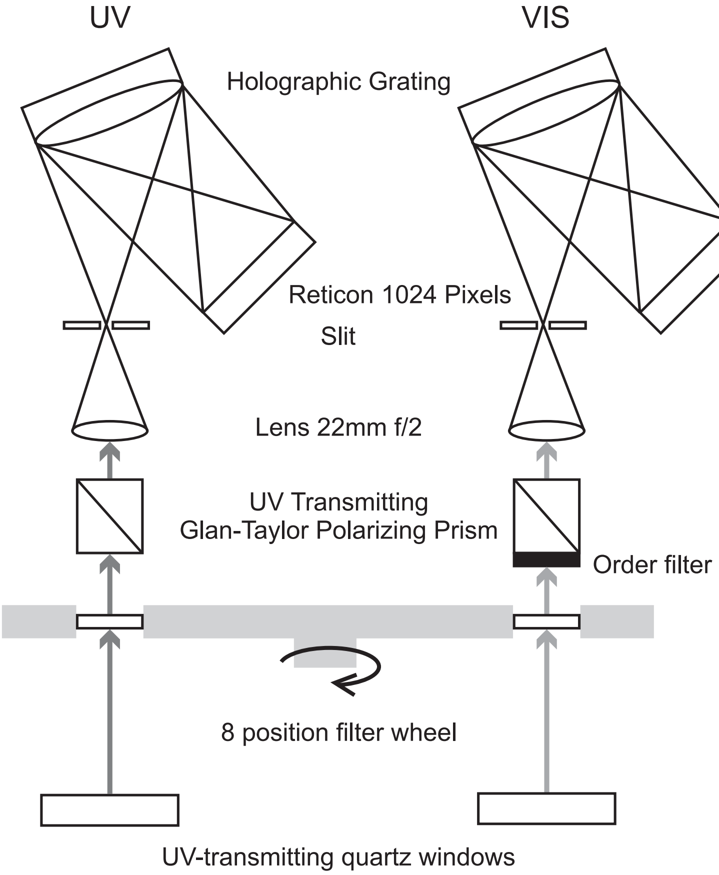

Figure 2.6: Schematic of MAESTRO instrument. Adapted from Figure 2 of McElroy et al. (2007).

2.3.3 SunPhotoSpectrometer

The SPS is the heritage instrument to MAESTRO. It is a photodiode array grating spectrometer that has been flown aboard the NASA ER-2 aircraft as the Composition and Photodissociative Flux Measurement (CPFM) experiment (McElroy, 1995). Zenith-sky spectra are recorded between 375 and 775 nm, with a resolution of 1.5 nm in both the NO_2 and ozone regions. The detector is an uncooled 1024-pixel linear photodiode array. Sunlight is collected by an achromatic lens, providing a 0.1° by 10° field-of-view. A schematic of the instrument is shown in Figure 2.7. Although both MAESTRO and the SPS are operated in direct Sun mode as well as zenith-sky mode, these direct Sun measurements will not be discussed. MAESTRO and SPS are mounted on a suntracker,

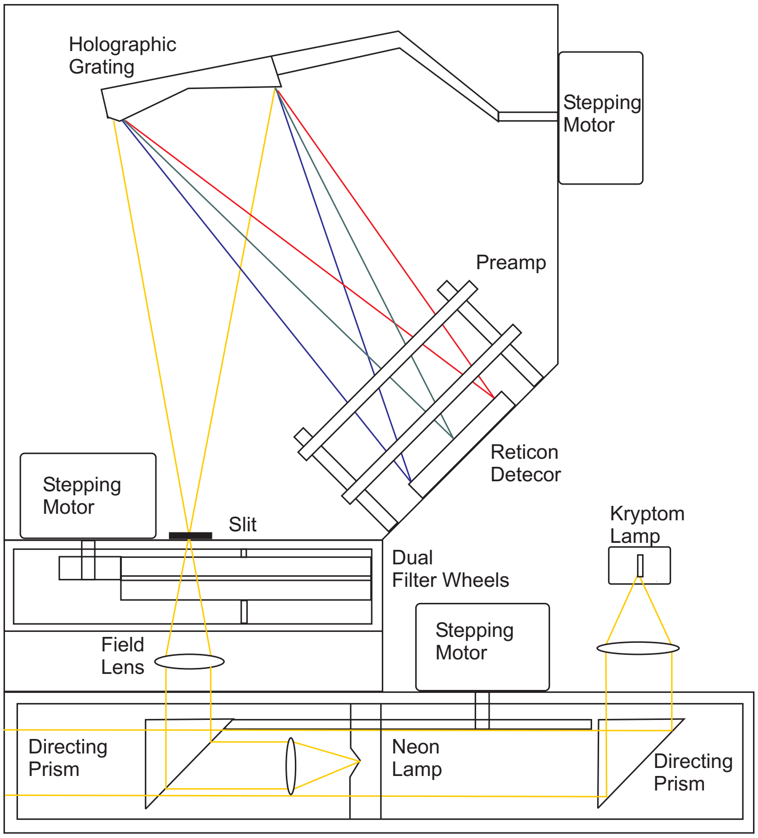

Figure 2.7: Schematic of the SunPhotoSpectrometer (courtesy of Clive Midwinter).

which tracks the Sun in azimuth during zenith-sky viewing and in elevation and azimuth during direct Sun viewing. During MANTRA, the two instruments were installed inside a commercial freezer, and only zenith-sky spectra were taken. During the Eureka campaigns, the two instruments are installed on the roof of PEARL, and operate at near ambient temperature (generally between -30°C and -40°C).

2.4 Characterization of the Spectrometers

2.4.1 Dark Current and Bias

When the shutter is closed and no light is entering the spectrometer, the signal that is recorded on the CCD is called the dark signal. This is made up of two components: the dark current and the bias. The bias is an electronic offset, added to the signal by the controller, to avoid negative counts. It should be constant with each spectrum. The dark current is a result of thermal emission of the CCD itself, and increases with exposure time (t), as well as temperature of the CCD (T), as in Equation 2.1 (Mackay, 1986):

$$\text{dark current(t,T)} = At \exp\left(\frac{-B}{T}\right). \tag{2.1}$$

A and B are constants unique to the detector. For the UT-GBS and PEARL-GBS CCDs, the dark current is thought to double with a 7°C increase in temperature, though the exact relationship has not been derived.

Both dark current and bias are found by taking a series of dark signal measurements with exposure times ranging over those used during zenith-sky measurements. The dark current and bias are found for each individual pixel by taking the linear fit to this line. The ordinate is the bias, and the slope is the dark current for a one-second exposure time. Figure 2.8 shows the bias of the four CCDs, while Figure 2.9 shows the dark current. The dark current is much lower for the loaner and new CCDs than for the original CCD. This is due to the lower operating temperature of both of these detectors. The bias and dark current for the two new CCDs are also less scattered than those of the older and loaner CCDs, due an error in the spectral acquisition code used in 2004 with these CCDs. Instead of averaging a series of spectra, as described in Section 2.1.3, only one spectrum was taken.

The dark current and bias are measured at the beginning of each field campaign, and where possible, overnight. The LabVIEW code can automatically record the set of exposure times overnight. In this way, any changes in the dark signal can be monitored. With the exception of the original CCD, both have been found to be constant to within a few counts.

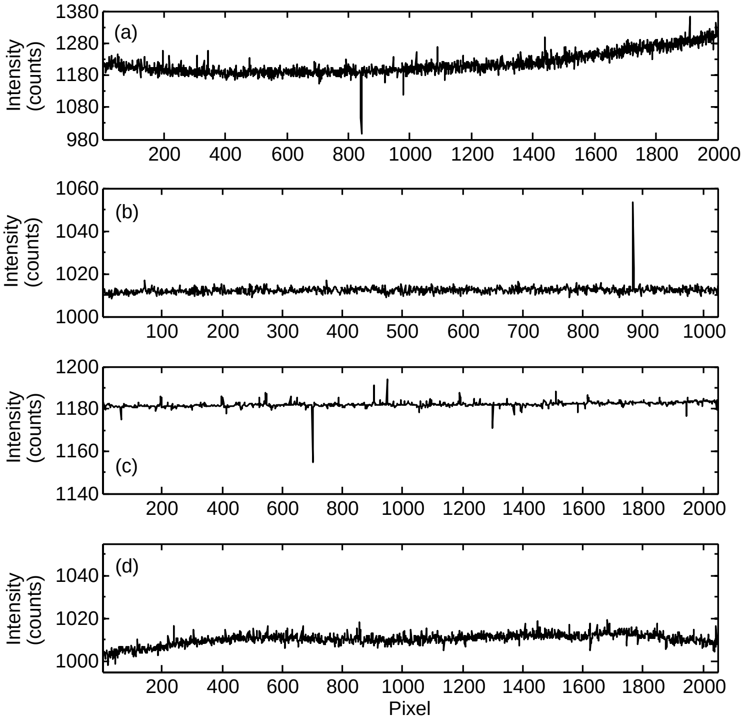

Figure 2.8: Bias measurements for (a) the original UT-GBS CCD, Eureka, February 2004, T=255 K, (b) the loaner CCD, MANTRA 2004, T=148 K, (c) the new CCD, Eureka, February 2005, T=201 K, and (d) the PEARL-GBS CCD, Eureka, August 2006, T=205 K.

2.4.2 Resolution

The spectral resolution of the instrument is dependent on the width of the entrance slit, grating, and the focus of the CCD. The narrower the slit, the higher the resolution of the instrument. However, a narrow slit reduces the amount of light entering the spectrometer, meaning that measurements cannot be made at very high solar zenith angles when the Sun is low in the sky. How well the CCD is focused is the most important factor in the resolution of the instrument. If the detector is not at the imaging plane of the spectrometer, the resolution is degraded.

Before and after each field campaign, the resolution of the instrument is measured using a set of three calibration lamps: mercury, xenon, and neon. The resolution is taken as the full width at half maximum (FWHM) of the spectral lines, Figure 2.10 shows the

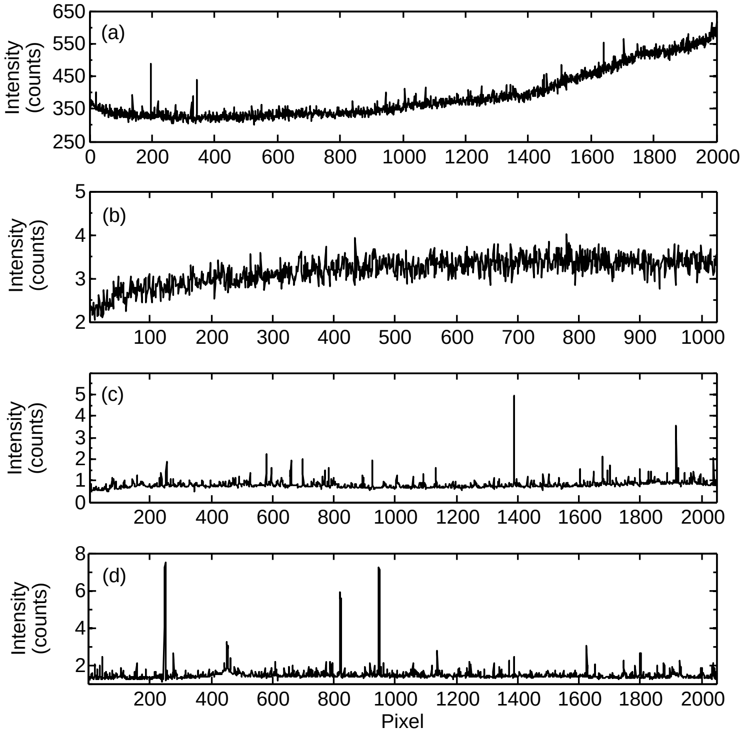

Figure 2.9: One-second dark current measurements for (a) the original UT-GBS CCD, Eureka, February 2004, T=255 K, (b) the loaner CCD, MANTRA 2004, T=148 K, (c) the new CCD, Eureka, February 2005, T=201 K, and (d) the PEARL-GBS CCD, Eureka, August 2006, T=205 K.

lineshape for the six gratings of the two instruments for the 435.8 nm emission line of the mercury lamp. The resolution varies across the detector, as shown in Figure 2.11. The resolution is expected to vary across the CCD due to the effects of coma. Coma, or comatic aberration, occurs when light is not perpendicular to the axis of the optics. This occurs in the spectrometer due to its off-axis design. Beams further away from the axis will have a different magnification than those that enter perfectly on axis. This causes a blurring effect, shown in Figure 2.12 (Wolfe, 1998). In addition to the resolution, the sampling of these lines is also important. A lower sampling can lead to larger errors introduced when the spectra are interpolated onto the wavelength grid of the reference spectrum (Roscoe et al., 1996). The loaner detector, although having a similar resolution to the new and old detectors, had a much smaller sampling, due to the smaller number

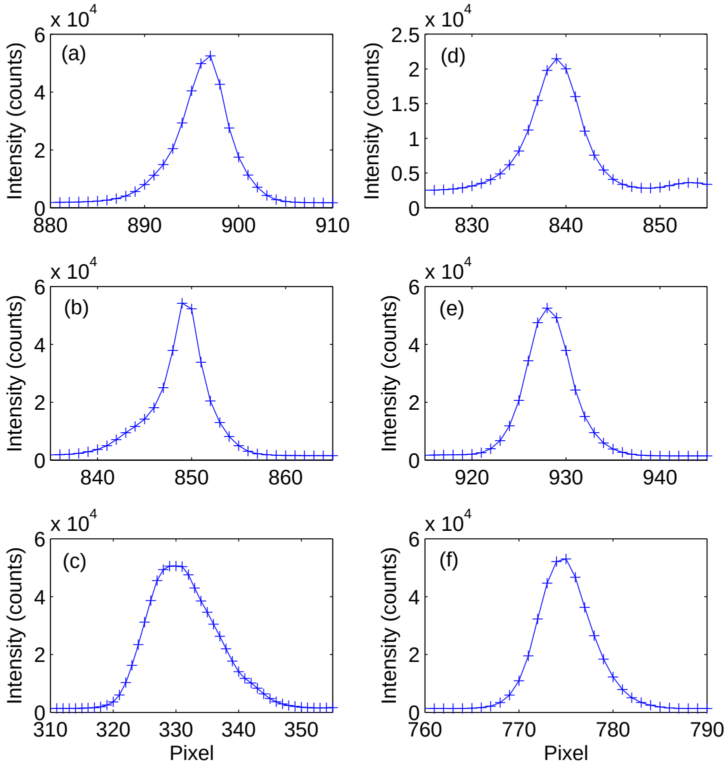

Figure 2.10: Line shape measurements of the 435.8 nm mercury emission line for the UT-GBS, Eureka, February 2007: (a) 400 gr/mm grating, (b) 600 gr/mm grating, and (c) 1800 gr/mm grating. Also measurements for the PEARL-GBS, Eureka, February 2007: (d) 300 gr/mm grating, (e) 600 gr/mm grating, and (f) 1200 gr/mm grating.

of pixels, meaning that the quality of the spectra was reduced. Table 2.1 gives the range of sampling across the detectors for the four detectors and six gratings.

2.4.3 Stray Light

Stray light is light detected by the CCD that did not travel along the instrument's optical axis to get to the detector. Light can enter the spectrometer at other angles and be scattered towards the detector, causing spurious signals, which tend to be more problematic at short wavelengths where the signals are weaker. Stray light increases with increasing exposure time.

To determine the stray light of the instrument, a long-wave pass filter (band pass >

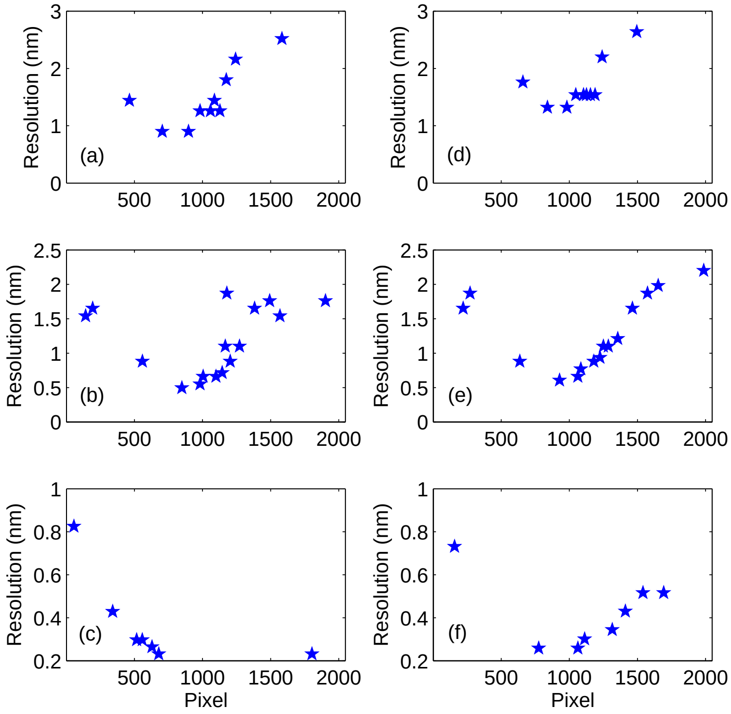

Figure 2.11: Resolution measurements for the UT-GBS, Eureka, February 2007: (a) 400 gr/mm grating, (b) 600 gr/mm grating, and (c) 1800 gr/mm grating. Also measurements for the PEARL-GBS, Eureka, February 2007: (d) 300 gr/mm grating, (e) 600 gr/mm grating, and (f) 1200 gr/mm grating.

575 nm) is placed inside the f-number matcher or, for the PEARL-GBS, the filter wheel is rotated to this filter. A desktop quartz-halogen lamp is used as light source. Keeping a constant exposure time, three spectra are taken: one without the filter, one with the filter, and a dark spectrum with the shutter closed. The stray light is then the difference between the spectrum taken with the filter and the dark spectrum. Stray light ratioed to the spectrum with no filter, corrected for dark current, for the two instruments is shown in Figure 2.13. The stray light has been found to be consistent with time. The signal is also similar when measured with different gratings. This test is repeated at the beginning and end of every field campaign. The stray light is not generally removed by taking the ratio in the DOAS technique.

The UV-visible Working Group of the NDACC has determined that if the stray light

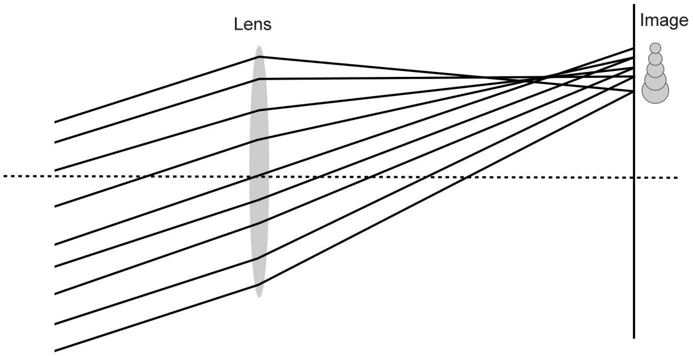

Figure 2.12: Coma in a single lens optical system. Adapted from Wolfe (1998).

Table 2.1: Range of sampling of spectral lines for the four detectors and six gratings of the UT-GBS (400, 600, and 1800 gr/mm) and PEARL-GBS (300, 600, and 1200 gr/mm). Sampling is given in pixels/FWHM.

CCD		Grating	
	400/300 gr/mm	600 gr/mm	1800/1200 gr/mm
original	7–20	6–20	7–16
loaner	3–19	3–18	3–12
new	5–14	4.5–16	7–25
PEARL-GBS	6–12	5.5-20	7–12

levels are less than 0.2% of the signal without the filter no significant error is introduced to the Differential slant column densitys (DSCDs) derived from the instrument. If the signal is larger than 0.5%, the error begins to become important (Johnston et al., 1999). For the ozone and NO_2 regions (larger than pixel 650), the stray light for both instruments is below 0.5%. For the BrO and OClO regions, the stray light is larger than 0.5%, and is approximated by fitting to the spectra (see Chapter 3).

2.4.4 Polarization

As will be discussed in Chapter 3, scattered sunlight is polarized. If the effects of polarization are not taken into account when performing the DOAS analysis, spurious signals

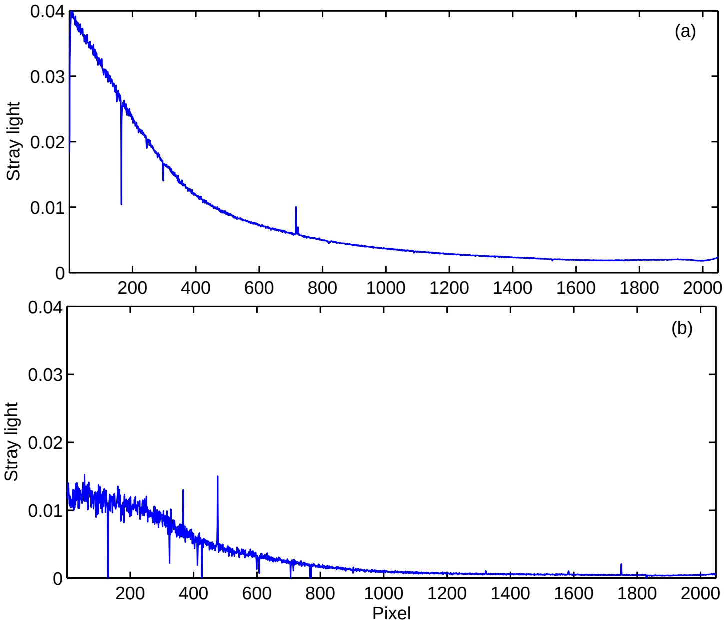

Figure 2.13: Stray light measurements as a fraction of the spectrum with no filter using a long-wave pass filter for (a) the UT-GBS, Eureka, February 2005, and (b) the PEARL-GBS, Eureka, August 2006. The approximate wavelength range is 340–560 nm.

appear in the differential optical depths that can be mistaken for absorption by trace gases. The six gratings of the UT-GBS and PEARL-GBS are all sensitive to the polarization of the incoming light, as seen in Figure 2.2. The liquid light guide is used to depolarize the light. The SAOZ instrument uses a grating that is not sensitive to polarization, while SPS and MAESTRO are mounted on a solar tracker, so that the instruments remain in the same position relative to the Sun.

To measure the effects of polarization after use of the LLG, a camera polarizer was placed in front of the input optics. Using a quartz-halogen lamp as a light source, spectra are taken with the polarizer in four positions with the polarizer's axis of polarization shifted in 45° increments. These spectra are then ratioed to each other. If the liquid light guide is completely successful in removing the effects of polarization, the spectra should not differ from one another and the ratios should be unity. Figure 2.14 shows the results of these tests for the UT-GBS and the PEARL-GBS for two spectra with the

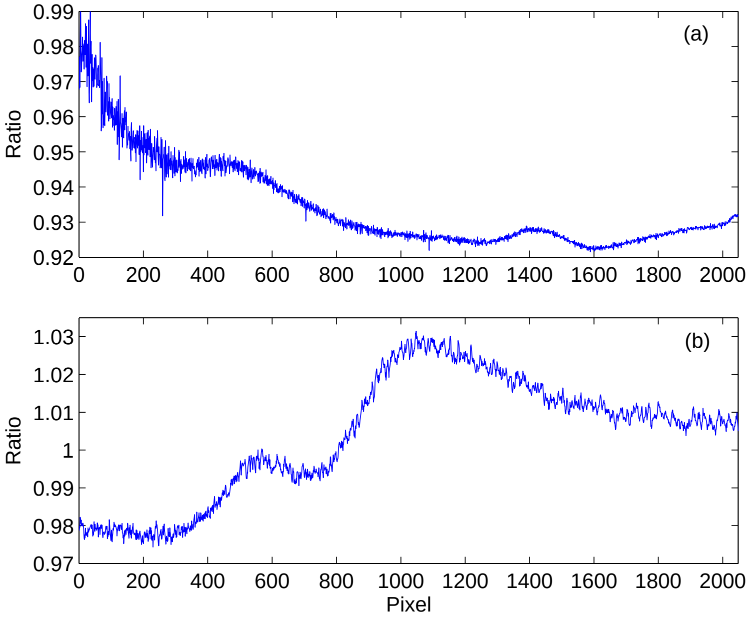

Figure 2.14: Ratio of the spectra with the polarizer rotated by 90° for the 600 gr/mm grating for (a) the UT-GBS, Toronto, April 2006, and (b) the PEARL UT-GBS, Toronto, July 2006. The approximate wavelength range is 340–560 nm.

polarizer rotated by 90° with respect to the original orientation. This orientation gives the largest variation with pixel. When the polarizer is rotated by 45° with respect to the original orientation, the shape of the signal is similar, with a smaller amplitude. The results are similar with different gratings.

The UV-visible Working Group of the NDACC has determined that if the variation of the ratio of the polarizer parallel to the entrance slit to the polarizer perpendicular to the entrance slit is less than 20% over the preferred NO_2 region (425–450 nm, approximately pixels 600-1000 in Figure 2.14), no significant error is introduced in the DSCDs (Johnston et al., 1999). Since the UT-GBS and PEARL-GBS use a liquid light guide as part of the input optics it is not possible to align the polarizer to the entrance slit. However, the maximum variation seen over the entire wavelength range is no greater than 7%, which is smaller than the 20% required by NDACC.

Chapter 3

Measurement Technique

Differential Optical Absorption Spectroscopy (DOAS) was first developed in the 1970s by J. F. Noxon and U. Platt (Noxon, 1975; Noxon et al., 1979; Platt et al., 1979). The core of the technique is the use of the ratio between two spectra: one taken with the Sun high in the sky (the reference spectrum) and one taken with the Sun close to the horizon, during twilight. This ratio leaves only the changes that occur in the spectra as the atmospheric path length increases with the Sun low on the horizon. In this way, accurate measurements of trace gases with very small optical depths can be found, and this is the strength of the DOAS technique.

In this chapter, the analysis of the spectra to retrieve slant and vertical column densities of the atmospheric constituents is described. The software package used to perform the analysis is also described. Finally, the sources of error in the measurements are explored.

3.1 Radiation in the Atmosphere

Energy is transfered from the Sun to the Earth by electromagnetic radiation, which travels in the form of electromagnetic waves. Figure 3.1 shows the electromagnetic spectrum. This thesis deals with UltraViolet-visible (UV-visible) light, which is at the peak of the

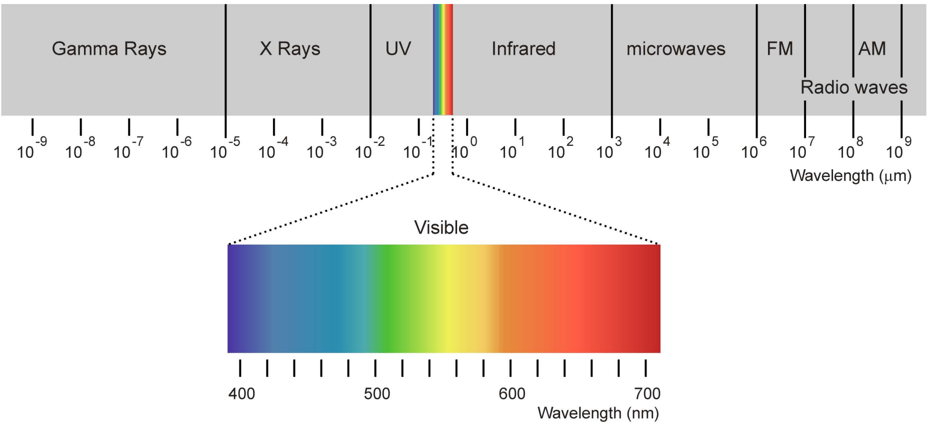

Figure 3.1: The electromagnetic spectrum. Adapted from Figure 1.1 in Liou (2002).

solar output. This is light between 300 and 400 nm (UV) and 400 and 700 nm (visible). Visible light can be seen by humans with the naked eye, while ultraviolet light is most commonly known as being responsible for sunburn in humans. The atmosphere can absorb and scatter sunlight as it travels to the Earth, and it is because of this that trace gases in the atmosphere can be detected by observing solar spectra.

3.1.1 Absorption

UV-visible light is absorbed in the atmosphere through interaction with molecules. Figure 3.2 shows a potential energy curve for a diatomic molecule. The x-axis represents the distance between the two atoms, while the y-axis represents the amount of potential energy stored in the molecule. The two curves marked ground and excited state represent the first and second electronic state of the molecule. The minimum in potential energy is known as a potential well, and represents the bound state of the atoms in the molecule. The horizontal lines in the potential well represent the vibrational states of the molecule. When energy in the form of sunlight is absorbed, it acts to increase the electronic state of the molecule. The transition lines 1, 2, and 3 in Figure 3.2 represent such absorption. Line 1 is a purely electronic transition, with the molecule being raised

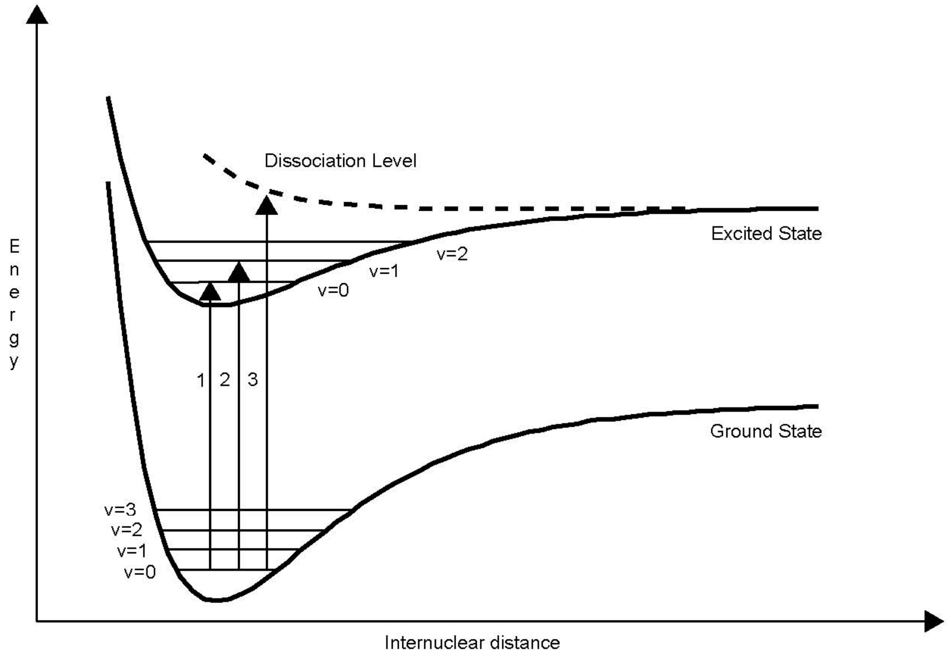

Figure 3.2: Potential energy curves for a diatomic molecule. The horizontal lines represent vibrational energy levels. Adapted from Figure 3.4 of Liou (2002).

from the first vibration level in the ground state to the first vibration level in the first excited state. A purely vibrational transition would increase the vibration level while remaining in the same electronic state. A combination of the two can occur, for example if the molecule transitioned from the ground state in the first vibration level to the first excited state in the second vibration level, shown as line 2. Transitions such as these are quantized: they require an exact amount of energy to be absorbed. Transition 3 in Figure 3.2 represents a transition that is not quantized - the molecule is increased to a state above the dissociation level - above this level the atoms can dissociate. A quantized transition occurs at discrete wavelengths, while non-quantized transitions occur at a smooth continuum of wavelengths. The strength of the absorption of a molecule is represented by an absorption cross section. Figure 3.3 shows the absorption cross section of ozone. Those transitions in the Huggins band are mainly quantized, while those in the Chappuis band are mainly not quantized (Liou, 2002).

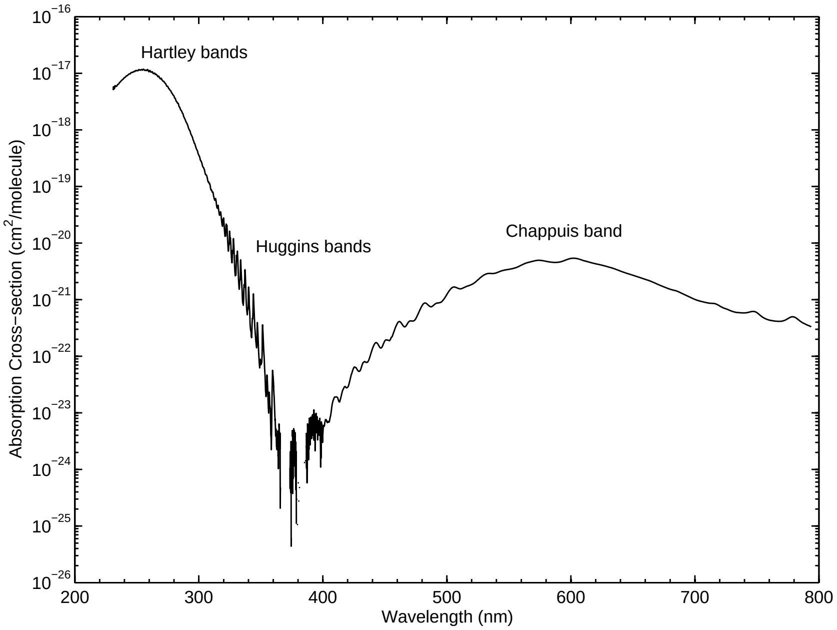

Figure 3.3: Ozone absorption cross section at 221 K (Burrows et al., 1999).

3.1.2 Scattering

Atmospheric scattering occurs when a particle in the atmosphere reradiates energy in all directions. Depending on the relative sizes of the wavelength of the light and the particle, different scattering regimes apply. For particles of radius much smaller than the wavelength of light, Rayleigh scattering occurs. The most familiar example of Rayleigh scattering is the blue sky. Rayleigh scattering is caused by the electrical field of the incident radiation inducing a dipole moment in the scattering particle. The scattered intensity varies with the wavelength of the incident radiation as in Equation 3.1:

$$I_\lambda \backsim 1/\lambda^4. \tag{3.1}$$

λ is the wavelength of the radiation, and I_λ is the intensity of the scattered radiation. Figure 3.4(a) shows the angular pattern of the scattered intensity for Rayleigh scattering of unpolarized incident sunlight. Extending this figure into three dimensions yields a solid of rotation about the horizontal axis. Light polarized perpendicular to the induced dipole moment is scattered equally in all directions, while light polarized parallel to the induced dipole moment is scattered preferentially forward and backward (with an angular dependence of $\cos^2\theta$). For unpolarized light, the resultant angular dependence is a combination of these two patterns: the intensity of the scattered light is equal in the forward and backward directions (parallel to the incoming beam), with minima towards the sides (perpendicular to the incoming beam). Light scattered forward and backward is composed equally of light of both polarizations, while light scattered towards the sides is composed of only one polarization. In all other directions, the scattered light is partially polarized (Liou, 2002).

For particles of radius of the same order of magnitude as the wavelength of light, Lorenz-Mie scattering occurs. Lorenz-Mie scattering is responsible for clouds appearing white. The intensity of the scattered light varies with the size of the particle. Figure 3.4(b) shows the angular pattern of the scattered intensity for Lorenz-Mie scattering. Light is preferentially scattered in the forward direction, with only a small amount scattered backwards in the direction of the incident beam (Liou, 2002).

For particles of radius much larger than the wavelength of light, geometrical scattering occurs. This scattering is most familiar in the form of rainbows, caused by geometrical scattering of sunlight through rain drops. Figure 3.4(c) shows the angular pattern of the scattered intensity for geometrical scattering (Liou, 2002). The lobes are caused by the incident beam of light being reflected, refracted, and diffracted around and through the particle.

In the above discussions of scattering, the scattered light had the same wavelength as the incident radiation. Raman scattering is scattering that changes the wavelength of the scattered light. The intensity of the wavelength-shifted light is weak, though it becomes significant in differential optical absorption spectroscopy. Raman-scattered light can fill

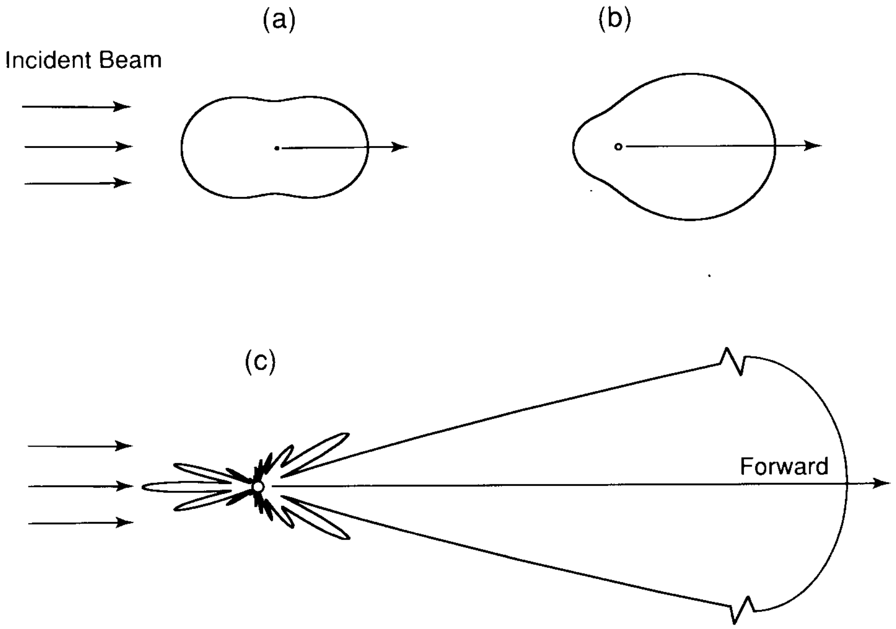

Figure 3.4: Angular patterns of the scattered intensity from a spherical aerosol illuminated by 500 nm unpolarized light: (a) particle radius 10^{-4} μm, Rayleigh scattering, (b) particle radius 0.1 μm, Lorenz-Mie scattering, and (c) particle radius 1 μm, geometrical scattering (scaled for presentation purposes). This figure is Figure 1.4 in Liou (2002).

in the Fraunhofer lines of the Sun in solar spectra. As the magnitude of the scattered light varies over twilight, ratioing two spectra leaves a signal from the changing Raman scattering. This signal is known as the Ring effect after Grainger and Ring (1962).

3.2 Differential Optical Absorption Spectroscopy

3.2.1 Beer-Bouguer-Lambert Law

The derivation of DOAS in this section follows Platt (1994). The underlying principle behind DOAS is the Beer-Bouguer-Lambert Law, hereafter Beer's Law (Perrin, 1948). In its simplest form, Beer's Law is given by:

$$dI(\lambda) = -\sigma(\lambda)\rho(\lambda)I(\lambda)dz \tag{3.2}$$

where $I(\lambda)$ is the intensity of the radiation at a particular wavelength, $\sigma(\lambda)$ is the absorption cross section of the absorber, $\rho(\lambda)$ is the density of the absorber, and z is the path length (Liou, 2002). This expression can be integrated provided that the cross section is independent of temperature and pressure, and therefore height. After integration, Equation 3.2 becomes:

$$I(\lambda) = I_0(\lambda)C(\lambda)\exp(-\sigma(\lambda)u) \tag{3.3}$$

where $I_0(\lambda)$ is the incident intensity (for this application, the solar intensity at the top of the atmosphere), and u is the slant column density, defined as the amount of absorber in the path. $C(\lambda)$ has been added to represent the instrument function. This form of Beer's Law is valid for one absorber, but can be generalized to include the absorption of many chemical species, as well as for extinction by aerosols and scattering. Including these sources of extinction, Equation 3.3 now becomes:

$$I(\lambda) = I_0(\lambda)C(\lambda)\exp\left[-\sum_i(\sigma(\lambda)u_i) + \varepsilon_R(\lambda) + \varepsilon_M(\lambda)\right] \tag{3.4}$$

where the sum over i is over the different absorbers being considered, $\varepsilon_R(\lambda)$ is the optical depth due to Rayleigh scattering, and $\varepsilon_M(\lambda)$ is the optical depth due to Mie scattering.

In order to retrieve the differential slant columns of the desired species, Equation 3.4 must be solved. $I(\lambda)$ is the spectrum measured by the instrument, after being corrected for dark current and bias. The absorption cross sections are measured in a laboratory, and for this work have been taken from the literature. The other terms in the equation are unknown. The radiation incident at the top of the atmosphere, $I_0(\lambda)$, and the instrument function can be removed by taking the negative natural logarithm of the ratio of two spectra, one at high Sun, the reference spectrum, and one during twilight:

$$-\,ln\left(\frac{I_1(\lambda)}{I_2(\lambda)}\right) = \sum_i \sigma_i(\lambda)(u_{i,1} - u_{i,2}) + \Delta\varepsilon_R(\lambda) + \Delta\varepsilon_M(\lambda); \tag{3.5}$$

The subscripts 1 and 2 indicate the twilight and high Sun spectra, respectively. Note that the scattering optical depths are now differential. The absorption cross section can be divided into two parts: one that varies smoothly $(\sigma_0(\lambda))$ and one that varies rapidly $(\sigma'(\lambda))$ with wavelength:

$$-\mathit{ln}\left(\frac{I_1(\lambda)}{I_2(\lambda)}\right) = \left[\sum_i \sigma_i'(\lambda)(u_{i,1}-u_{i,2})\right] + \left[\sum_i \sigma_{i0}(\lambda)(u_{i,1}-u_{i,2}) + \Delta\varepsilon_R(\lambda) + \Delta\varepsilon_M(\lambda)\right]. \tag{3.6}$$

In Equation 3.6, the term to the far right contains only terms that vary smoothly with wavelength, while the leftmost sum contains only terms that vary rapidly with wavelength. By fitting a polynomial to this equation and subtracting it, the smoothly varying part can be removed, leaving only the rapidly varying part:

$$-\mathit{ln}\left(\frac{I_1'(\lambda)}{I_2'(\lambda)}\right) = \left[\sum_i \sigma_i'(\lambda)(u_{i,1}-u_{i,2})\right]. \tag{3.7}$$

The primed terms on the left above are the measured intensities with the fitted polynomial removed. The cross sections are known, leaving only the difference in slant column densities unknown. This DSCD is found by performing a simultaneous fit of the differential absorption cross sections to Equation 3.7. Depending on the species sought, different wavelength regions and species are fit.

3.2.2 Choice of the Reference Spectrum

Analysis can be performed using either a daily or a single reference spectrum. In this work, in either case the spectrum is generally chosen to be at solar noon. A single reference spectrum is chosen uniquely for each instrument and for each measuring period or campaign. The spectrum from one instrument is not used for another instrument because this would eliminate one of the benefits of DOAS: when the ratio of two spectra are taken in Equation 3.5, the instrument function is eliminated. Combining spectra from more than one instrument would introduce features to the spectra from differing instrument functions, which could then be fit, wrongly, as atmospheric absorption. Reference spectra are chosen unique to each campaign to avoid complications arising from small differences in the instrument after shipment. Generally, after being dismantled and shipped, the calibration of the instrument is slightly different: the gratings are not positioned in exactly the same way as before. Complications can also arise due to temperature fluctuations during the campaign that slightly change the optical path through the instrument. Daily reference spectra have the advantage that daily variations in this calibration are relatively small and do not have as much influence on the analysis. For this reason, daily reference spectra are often used in instrument comparisons, such as in Chapter 7.

The wavelength shifts determined by WinDOAS for the Eureka spectra (Chapter 7), analysed with daily reference spectra are generally small, between 0 and 0.2 pixels through one twilight period, while the shifts determined by WinDOAS for the MANTRA spectra (Chapter 4), analysed with a single reference spectrum, vary between 0 and 3 pixels, depending on the day. Over one twilight period during MANTRA, the variation can be as high as 0.8 pixels. The wavelength calibration of the instrument changes more over the course of a campaign than over the course of one day.

3.3 Vertical Column Densities

In normal operation, the spectrometer collects zenith-scattered sunlight. Figure 3.5 shows the path of zenith-scattered and direct sunlight from the Sun to the spectrometer at high Sun and at twilight. For zenith-scattered light, the path through the troposphere remains approximately constant throughout the day, whereas the stratospheric path increases greatly with increasing SZA. Because of this, zenith-sky spectroscopy is ideal

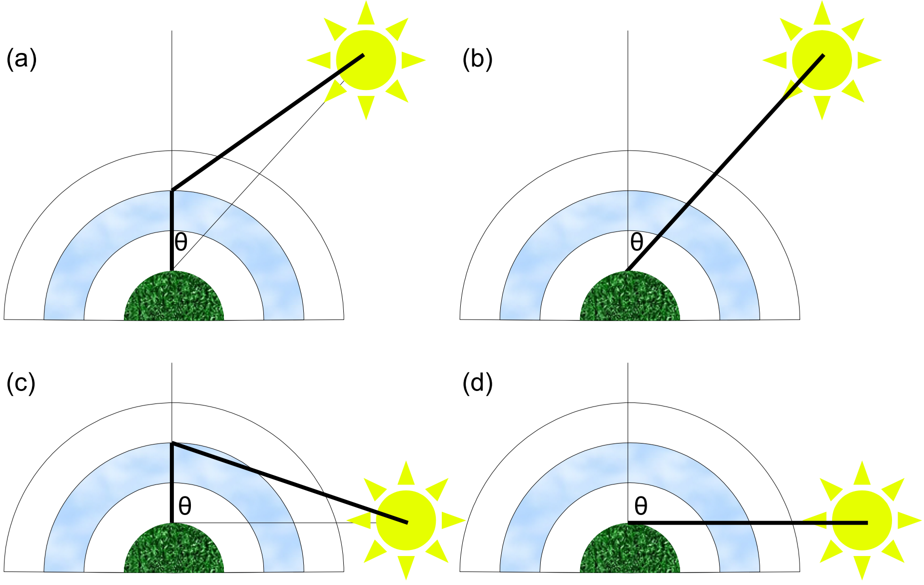

Figure 3.5: Path of sunlight through the atmosphere: (a) zenith-scattered, noon, (b) direct Sun, noon, (c) zenith-scattered, SZA=90°, (d) direct Sun, SZA=90°. In all figures, the thick line represents the average path of the sunlight and θ indicates the SZA. This figure is adapted from Fish (1994).

for measuring stratospheric concentrations. By taking the ratio of the two spectra, the tropospheric contribution is virtually eliminated, with the exception of species that have a large diurnal cycle. The DSCDs that are derived from the DOAS technique are the difference in total concentrations of the trace gases along these paths. In order to retrieve the VCDs, these paths must be modeled, which requires the use of a radiative transfer model.

The model used in this work is a one-dimensional vector radiative transfer model for a spherical-shell atmosphere that includes the effects of polarization (McLinden et al., 2002). Included in the model are vertical profiles of ozone, NO_2, BrO, aerosols, temperature, and density. The model solves the radiative transfer equation using successive orders of scattering in an inhomogeneous atmosphere. Both the NO_2 and BrO profiles are allowed to vary along the path of the light, following the diurnal variation of the UCI photochemical box model. The air mass factor (AMF) is calculated by applying a 5%

perturbation to the entire profile and from the following equation:

$$AMF(\lambda,\theta) = -\frac{ln(I(\lambda,\theta)/I_0(\lambda,\theta))}{\sigma(\lambda) \times \Delta VCD(\theta)}. \tag{3.8}$$

$I_0(\lambda,\theta)$ is the calculated incident radiance on the instrument at wavelength λ and SZA(θ), $I(\lambda,\theta)$ is the radiance after the perturbation to the absorber profile, $\sigma(\lambda)$ is the absorption cross-section, and ΔVCD(θ) is the change in the absorber column density. AMFs are calculated at 505 nm for ozone, 425 nm for NO_2, and 350 nm for BrO. The model has been previously compared to other radiative transfer models (Wagner et al., 2007), and has been found to agree within 5% at both UV and visible wavelengths.

For the MANTRA and Eureka field campaigns, density, temperature, and ozone profiles are taken from ozonesondes flown during the campaign. For MANTRA, a mean of all the sonde profiles is used; for Eureka, daily sonde profiles are used. For Toronto the density, temperature, and ozone profiles are taken from the UCI chemical box model at 45°. When no sonde was flown, the sonde from the closest day is used. The aerosol profile is taken from a Stratospheric Aerosol and Gas Experiment II (SAGE II) aerosol profile recorded in 1997. The NO_2 and BrO profiles are taken from the chemical box model at 45° for Toronto, 55° for MANTRA, and 75° for Eureka. One mean profile is used for each month. The ozone and NO_2 AMFs at 90° are approximately 17 for Toronto in May and for MANTRA. In Eureka, the value ranges between 13 and 18 for ozone and 11 and 18 for NO_2 between February and October. The BrO AMF at 90° for Eureka ranges between 10 and 12 between February and April.

Depending on the species in question, there are several ways of transforming zenith-sky DSCDs into VCDs using the calculated AMFs. For ozone, which does not have a large diurnal cycle, there are two methods, both of which are based on the following relationship:

$$DSCD(SZA) = VCD(SZA) \times AMF(SZA) - RCD \tag{3.9}$$

where reference column density (RCD) is the amount of absorber in the reference spectrum. In the first method, a Langley plot of DSCD versus AMF is made for each twilight period, and the VCD is found by performing a straight line fit to the data. The slope of the line is the VCD, as can be seen in Equation 3.9 and Figure 3.6. In the second method, Langley plots are again made for each twilight period, however the RCD is now retrieved from the ordinate of the plot (see Figure 3.6). In the case of a single reference spectrum, an average RCD for the whole campaign is found. In the case of a daily reference, an average RCD for each day is found from the morning and afternoon values. Each DSCD is then converted into a VCD using Equation 3.9, and the VCD for a twilight period is taken as the average of all these VCDs. Both methods rely on there being no strong diurnal variation of ozone. For either method, generally only DSCDs from solar zenith angles between 86° and 91° are used (Sarkissian et al., 1997).

For NO_2, there are again two methods for finding the VCD. The averaging method described above can be used, although since NO_2 does have a strong diurnal variation, the VCD found is now an average of the VCDs over the twilight period. In the other method, the DSCD at a solar zenith angle of 90° is interpolated from each set of twilight measurements, and the VCD at 90° is found by inverting Equation 3.9. BrO VCDs are found using this method.

3.4 Sources of Error

Measurement errors for the DSCD and VCD measurements are calculated for each campaign as a percentage of the column amount from the root-mean-square (RMS) of individual sources of random and systematic error, after Bassford et al. (2005). Table 3.1 gives the estimated values of the individual sources of error for the UT-GBS during the Eureka

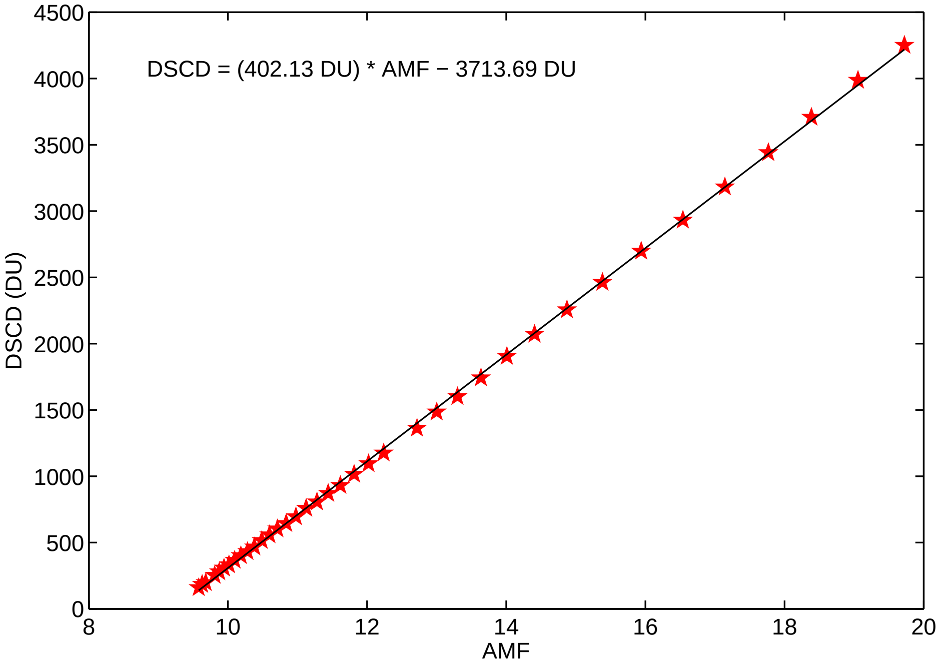

Figure 3.6: Ozone Langley plot for the UT-GBS for March 5, 2005. By Equation 3.9, the slope of the line is the VCD and the negative of the ordinate of the plot is the RCD.

2005-2007 campaigns. Those errors that are independent of the campaign are shown in bold type. When the value represents a best estimate taken from the literature, a reference is given in the table. All other values are calculated from the measurements. Table 3.2 summarizes the DSCD and VCD errors for the different campaigns and instruments discussed in this work.

Errors in the DSCDs stem from random noise on the spectra, instrument error, pseudo-random errors, errors in the absorption cross sections, the temperature dependence of the cross sections, and the effects of multiple Raman scattering. Instrument errors arise from uncertainties in the bias and dark current of the instrument, as well as the effects of stray light. These instrument errors add an offset to the spectra. Pseudo-random errors result in unaccounted-for structure in the spectra, and are a result of errors in the characterization of the slit function, interpolation, and the wavelength calibration of the spectra and the effects of polarization. If not properly corrected for, these errors add an additional signal containing spectral structure to the spectra that is not included in the DOAS fitting. NO_2, BrO, and OClO cross-sections are all sensitive to the temperature of the atmosphere. A single cross-section for each species was chosen at a reasonable temperature for the stratosphere, which introduces uncertainties into the fitted DSCDs. No correction has been made for the filling-in of absorption features by multiple Raman scattering. Pfeilsticker et al. (1999b) show that this effect can result in an underestimation of NO_2 columns by 5% and ozone columns by 1%. The NO_2 value is taken here for BrO and OClO.

VCD errors combine the DSCD errors, uncertainties in the AMF, and uncertainty in determining the RCD. Uncertainties in the AMF were derived by Bassford et al. (2001) for ozone and NO_2. The BrO AMF uncertainty given here is derived from the variation of the BrO AMFs over the course of the Eureka campaigns. The uncertainty in the RCD is derived by varying the RCD from the smallest to largest value derived for the campaign and observing the variation caused in the VCD.

3.5 Data Analysis Software

WinDOAS is a programme written by Carolyn Fayt and Michel Van Roozendael at BIRA/IASB (Belgian Institute for Space Aeronomy). There are many different options available in WinDOAS; here only those that are most commonly used are described. The inputs to the programme are the corrected spectra to be fitted, a reference spectrum, cross sections of the absorbing species, the variation in the slit function across the detector, and a first guess of the wavelength calibration. The spectra have been corrected for bias and dark current, but have not been wavelength calibrated. The pre-processing of the spectra in WinDOAS performs a non-linear least-squares fit, using the Marquardt-Levenberg algorithm (Bevington, 1992), to the reference spectrum to determine the wavelength calibration and the slit function, using the Fraunhofer lines. The variable slit function is

Table 3.1: Measurement errors for the UT-GBS for the Eureka 2005 campaign. When the value represents a best estimate taken from the literature, the reference is given in the table. All other values were calculated from the measurements. Those errors that are independent of the campaign are shown in bold type. The total error is found by taking the root-mean-square of the individual sources of error.

Source of error	O_3 (%)	NO_2(%)	BrO(%)	OClO(%)
Random errors on DSCD				
Random noise	1	2	5	7.5
Systematic errors on DSCD				
Instrument error	1	1	1	1
Pseudo-random errors	**1-2**[a]	**4-6**[a]	**10**	**10**
Absolute cross sections	**2.6**[b]	**5**[c]	**8**[d]	**7**[e]
Temperature dependence of cross section	-	**<8**[f]	**2**[g]	**7**[e]
Filling in of absorption lines by Raman scattering	**1**[h]	**5**[h]	**5**[h]	**5**[h]
Total random error DSCD	1.0	2.0	5.0	5.0
Total systematic error DSCD	3.3	11.8	13.9	15.0
Total rms error DSCD	3.5	12.0	14.8	16.7
Random errors on VCD				
AMF error	**2**[a]	**5**[a]	**8**	-
Systematic errors on VCD				
Uncertainty in RCD	1	10	7	-
Total random error VCD	2.2	5.4	9.4	-
Total systematic error VCD	3.5	15.5	15.6	-
Total rms error VCD	4.1	16.4	18.2	-

---

[a] Bassford et al. (2005)
[b] Burrows et al. (1999)
[c] Vandaele et al. (1998)
[d] Wilmouth et al. (1999)
[e] Wahner et al. (1987)
[f] Pfeilsticker et al. (1999b)
[g] Harder et al. (2000)
[h] Fish and Jones (1995); Pfeilsticker et al. (1999b)

Table 3.2: Total DSCD and VCD percentage errors for the campaigns and instruments discussed in this work.

Campaign	Instrument	O_3 Error (%)		NO_2 Error (%)	
		DSCD	VCD	DSCD	VCD
Eureka 2004	UT-GBS (original CCD)	4.6	5.0	12.6	16.6
	MAESTRO	4.2	4.8	12.2	20.0
	SPS	3.5	5.0	12.2	20.0
MANTRA 2004	UT-GBS (loaner CCD)	4.6	5.0	12.3	15.0
	SAOZ	3.5	4.1	12.0	14.8
	MAESTRO	4.5	5.0	-	-
	SPS	4.5	5.0	-	-
Eureka 2005–2007	UT-GBS (new CCD)	3.5	4.1	12.0	16.4
	PEARL-GBS	3.5	4.1	12.0	16.4
	SAOZ	3.5	4.1	12.0	16.4
	MAESTRO	4.2	4.8	12.2	20.0
	SPS	3.5	5.0	12.2	20.0

then applied to the cross sections, smoothing them to the resolution of the instrument. In the processing step, the differential slant column densities are fitted using the same non-linear fitting technique as used in the wavelength calibration. The cross sections are first high-pass filtered to produce differential cross sections, the twilight spectra are wavelength calibrated using the same method as the reference spectrum, and an offset fitting is performed. The offset accounts for stray light and dark current that may not have been properly corrected for. The offset is defined as follows:

$$I(\lambda) - \text{offset}(\lambda) \cdot \bar{I} = I_0(\lambda) \exp(-OD(\lambda)) \tag{3.10}$$

where $\bar{I}$ is the mean intensity of the spectrum over the fitting window and OD is the optical depth. The offset can be further defined as:

$$\text{offset}(\lambda) = a + b(\lambda - \lambda_0) + c(\lambda - \lambda_0)^2 \tag{3.11}$$

Table 3.3: Wavelength regions and species fit.

Species	Wavelength Region (nm)	Other Species Fit
Ozone	450–550	NO_2, O_4, H_2O, Ring
NO_2	425–450	O_3, O_4, H_2O, Ring
BrO	345–360	O_3, NO_2, O_4, OClO, Ring
OClO	365–390	O_3, NO_2, O_4, BrO, Ring

where λ_0 is the central wavelength of the fitting window, and a, b, and c are fitted parameters. This definition, with the scaling by the mean intensity, means that the offset can be interpreted as a percentage of the intensity of the spectrum (Fayt and Van Roozendael, 2001).

The offset is used only for the SAOZ and SPS instruments, and for the UT-GBS and PEARL-GBS for BrO and OClO. The PEARL-GBS also uses an offset when fitting NO_2 from the 1200 gr/mm grating. For the GBSs, offsets are used when the fitting window includes wavelengths less than 400 nm, as stray light becomes larger at these wavelengths (see Figure 2.12). For the other instruments, stray light measurements were not performed, and the offset was only fit when it improved the quality of the differential optical depth (DOD) fits. The GBSs' offset is between 0 and 5%; for SAOZ and SPS it is between 0 and 5% for ozone and 0 and 10% for NO_2. A non-linear least-squares fit is then performed with all the cross sections to determine the DSCDs for that spectrum. The residual of the fit, the DSCDs, and the standard deviations in the fits are all output (Fayt and Van Roozendael, 2001). Figures 3.7 and 3.8 show a schematic representation of the sequence of the processing of spectra by WinDOAS.

3.6 Wavelength Regions and Cross Sections

The cross sections used and wavelength regions fit depend on the gas being retrieved, and are summarized in Table 3.3. Ozone (T=221 K or 241 K, resolution=0.2–0.4 nm)

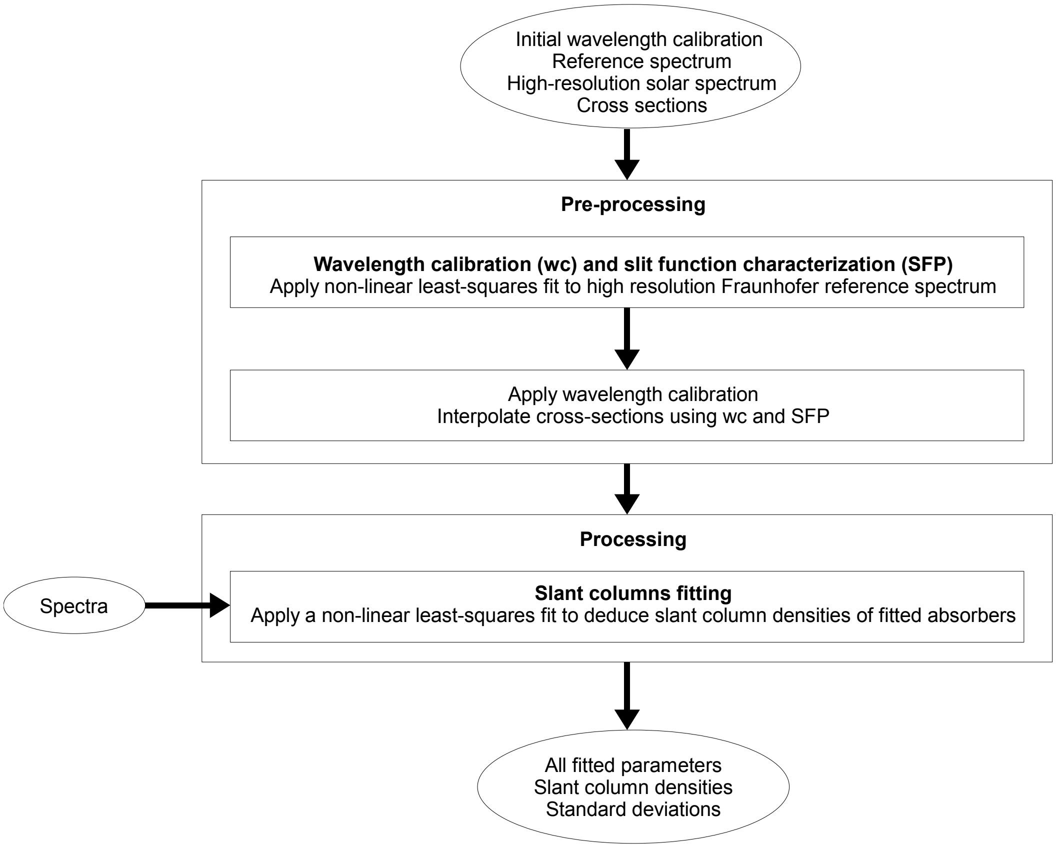

Figure 3.7: Overview of the WinDOAS programme. Adapted from Fayt and Van Roozendael (2001).

(Burrows et al., 1999), NO_2 (T=220 K, resolution=0.01–0.2 nm) (Vandaele et al., 1998), O_4 (T=298 K, resolution=0.6 nm) (Greenblatt et al., 1990), H_2O (converted from the line parameters given in Rothman et al., 2003), BrO (T=228 K, resolution=0.40 nm) (Wilmouth et al., 1999), OClO (T=204 K, resolution=0.22 nm) (Wahner et al., 1987), and the Ring cross section (Chance and Spurr, 1997) are all fit. The Ring cross section is calculated by convolving a high resolution solar spectrum with rotational Raman spectra of O_2 and N_2. Figure 3.9 shows the absorption cross sections in the regions in which the gases are retrieved. Figure 3.10 shows examples of typical differential optical depth fits for ozone, NO_2, BrO, and OClO for the UT-GBS and PEARL-GBS.

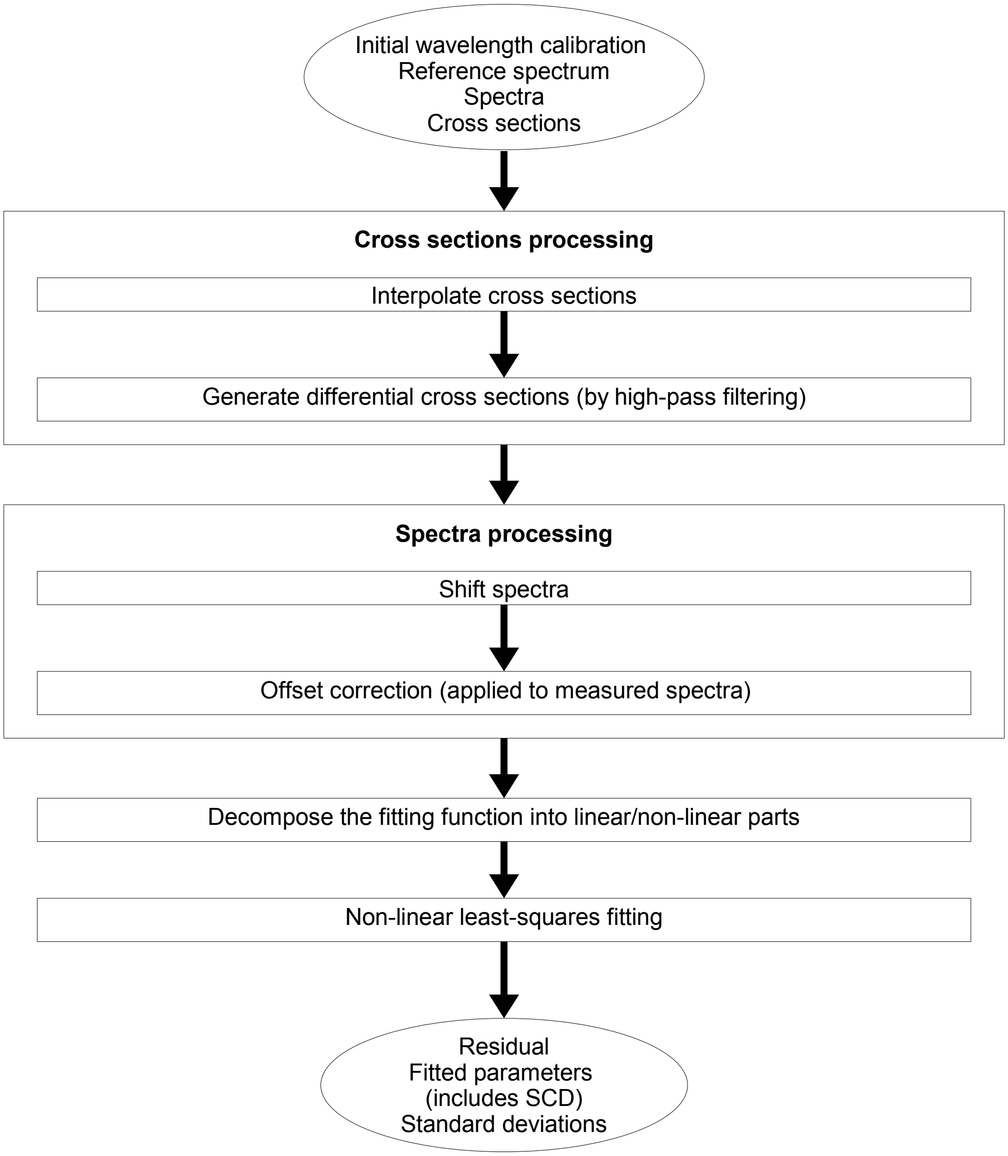

Figure 3.8: Schematic of the WinDOAS slant column density fitting. Adapted from Fayt and Van Roozendael (2001).

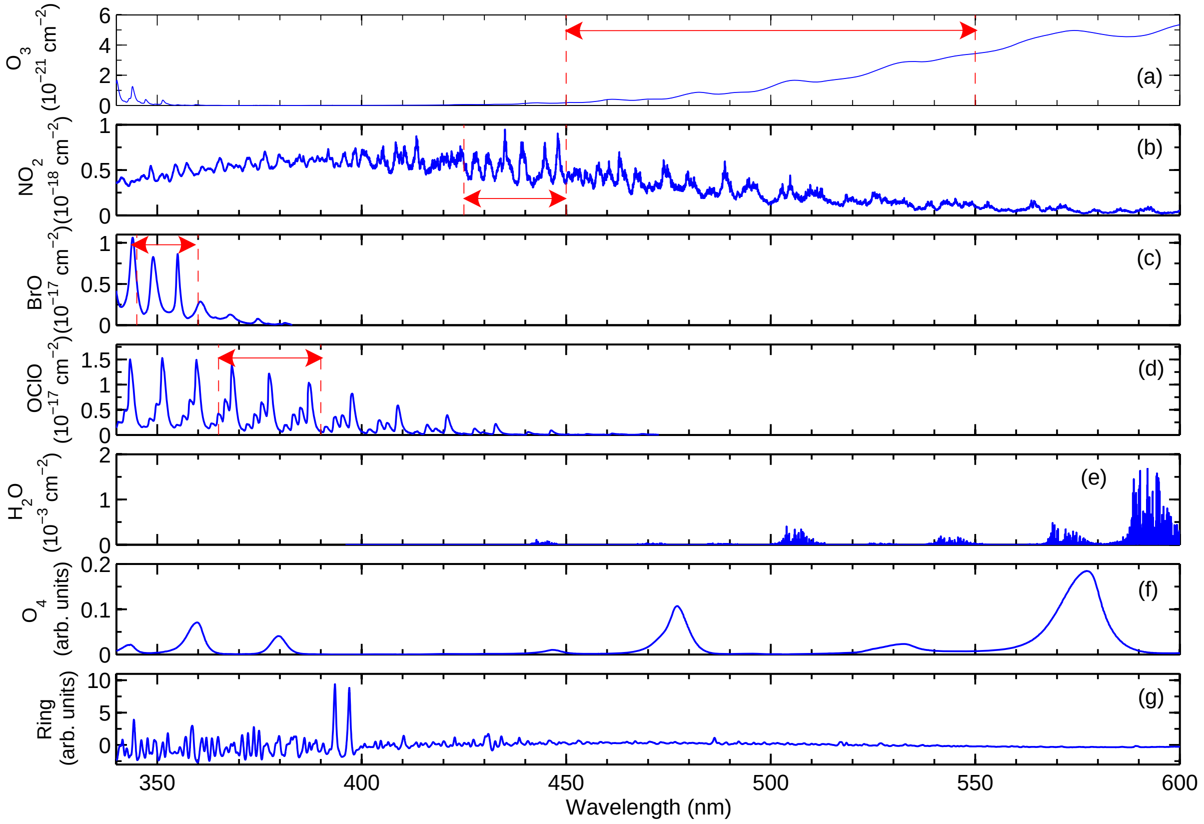

Figure 3.9: (a) Ozone, (b) NO$_2$, (c) BrO, (d) OClO, (e) H$_2$O, (f) O$_4$, and (g) Ring absorption cross sections. All are shown at the original resolution at which they were recorded, as noted in the text. The Ring cross section is shown at 0.5 nm resolution. The red lines in (a)–(d) show the regions in which the species are generally retrieved.

3.6.1 The Solar I$_0$ Effect

The solar I$_0$ effect arises from the fact that the absorption cross sections used in the DOAS analysis are measured at higher spectral resolutions and using a different light source than the zenith-sky spectra (Aliwell et al., 2002). The zenith-sky spectra contain the highly structured Fraunhofer lines caused by the Sun's atmosphere. These lines are removed by taking the negative logarithm of the ratio of two spectra: one taken at twilight and one taken when the Sun is high in the sky, as discussed in Section 3.2.1. However, since these spectra are recorded by the instrument, the solar spectra have been filtered by the instrument's line shape, and the complete removal of the Fraunhofer lines is not

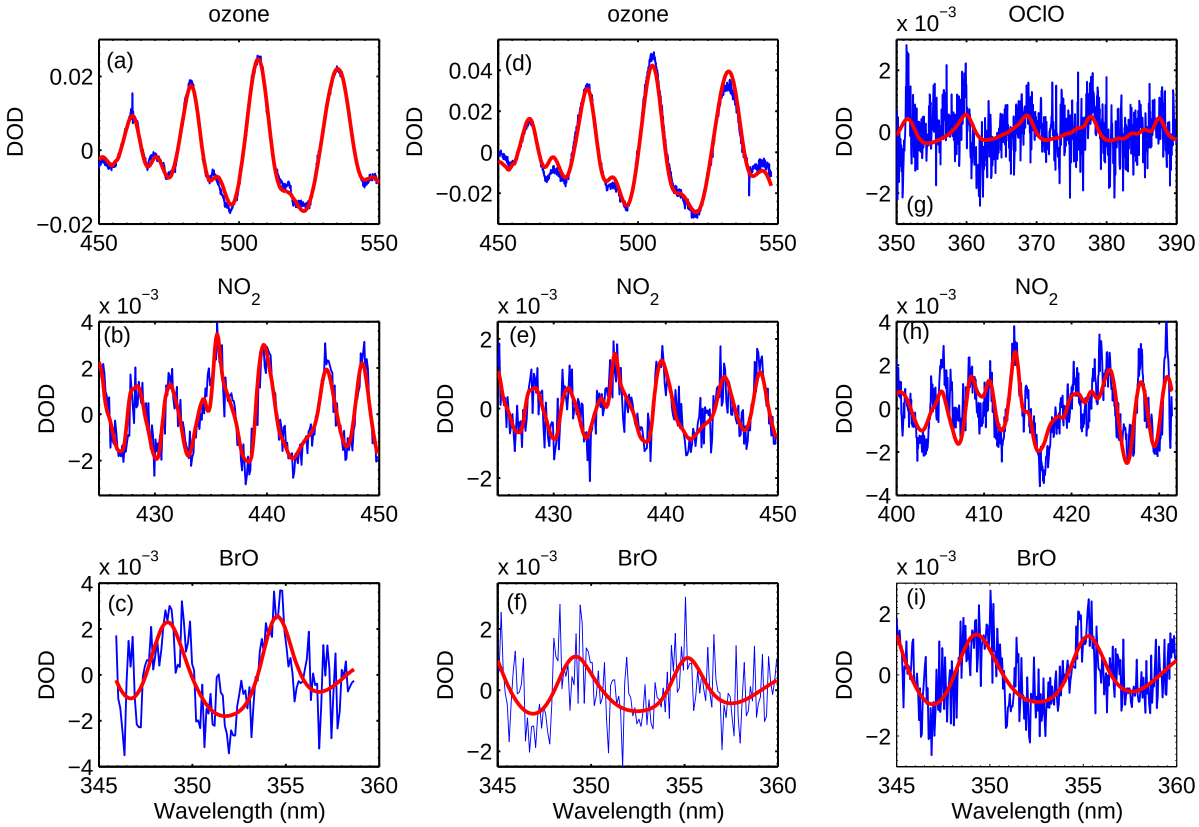

Figure 3.10: Differential Optical Depth (DOD) fits for the UT-GBS for (a) ozone, (b) NO_2, and (c) BrO for March 5, 2007 at Eureka using the 600 gr/mm grating. DOD fits for the PEARL-GBS for (d) ozone, (e) NO_2, and (f) BrO for February 27, 2007 at Eureka using the 600 gr/mm grating. DOD fits for the PEARL-GBS for (g) OClO, (h) NO_2, and (i) BrO for March 5, 2007 at Eureka using the 1200 gr/mm grating. All fits are for a SZA of approximately 90° in the afternoon. In all figures, the blue line is the recorded DOD while the red line is the fit to the data.

possible. In the simplest terms, and neglecting absorption in the reference spectrum, the spectra recorded by the spectrometer can be described as:

$$I_{REF}(\lambda') = \int I_0(\lambda) W(\lambda - \lambda') d\lambda \tag{3.12}$$

$$I_{TWI}(\lambda') = \int I_0(\lambda) \exp(-OD(\lambda)) W(\lambda - \lambda') d\lambda. \tag{3.13}$$

I_{REF} and I_{TWI} are the reference and twilight spectra, W is the instrument slit function, and OD is the optical depth. Taking the ratio of these spectra only eliminates I_0, the solar spectrum, if either the optical depth or I_0 are independent of wavelength over the integration interval. This effect can be corrected for by performing an I_0 correction of the absorption cross section (Aliwell et al., 2002). This can be performed by WinDOAS, where the corrected cross section is calculated to be:

$$\sigma_{corrected}(\lambda) = -\frac{1}{X} ln \left(\frac{synth(\lambda)}{sol(\lambda)} \right). \tag{3.14}$$

sol is the high-resolution solar spectrum, smoothed to the resolution of the instrument, *synth* is a synthetic absorption spectrum, generated using high-resolution cross sections and filtered by the instrument's resolution, and X is the expected column amount of the absorber (Fayt and Van Roozendael, 2001). In this work, I_0 corrections are performed for ozone and NO_2 cross sections, assuming columns of 10^{20} and 10^{17} molecules/cm^2, for analysis of NO_2, BrO, and OClO, as recommended by Aliwell et al. (2002). For BrO retrievals, not correcting the cross sections for the I_0 effect can lead to overestimation of the DSCDs of 35% (Aliwell et al., 2002).

Chapter 4

The MANTRA 2004 Campaign

Middle Atmosphere Nitrogen TRend Assessment (MANTRA) was a series of balloon campaigns conducted in Vanscoy, Saskatchewan (52°N, 107°W, see Figure 4.1) to measure stratospheric trace gases that impact midlatitude stratospheric ozone chemistry (Strong et al., 2005). Balloons were flown in late summer during the reversal of the stratospheric flow. This is the period when the atmosphere is closest to photochemical equilibrium and dynamics do not have a large influence (Wunch et al., 2005, and references therein). MANTRA field campaigns were held biennially from 1998 to 2004.

In 2004, a suite of five UV-visible ground-based instruments operated through the duration of the campaign, measuring the day-to-day variability of some of the trace gases in question. Three Fourier transform spectrometers (FTSs) were part of the main balloon payload and, in preparation for the launch, made sporadic ground-based measurements. Ozonesondes were also launched, on average, every other day. The campaign took place between 3 August and 15 September, with 40 days of measurements.

Ozone and NO_2 differential slant column densities and vertical column densities were determined for the duration of the campaign from the four zenith-viewing UV-visible instruments and are discussed and compared in this chapter. The ozone vertical column densities are also compared to measurements from a direct-Sun-viewing Brewer

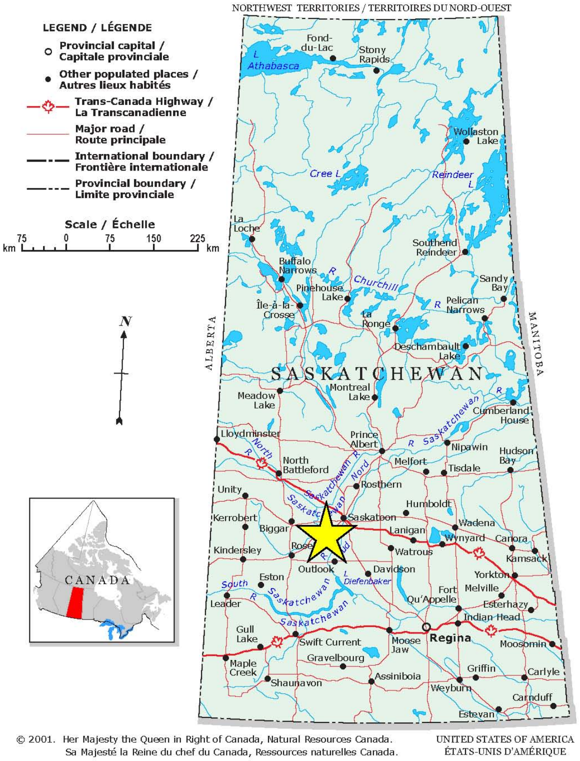

Figure 4.1: The yellow star indicates the location of Vanscoy, Saskatchewan, the launch site for the MANTRA balloon campaigns. (Map ©Natural Resources Canada.)

spectrophotometer, the three FTS instruments, and integrated ozone profiles from the ozonesonde flights. The results in this chapter have been published in Fraser et al. (2007a).

4.1 NDACC Intercomparison Campaigns

The UV-visible instruments are compared following the protocols established by the UV-visible Working Group of the NDACC (formerly the Network for the Detection of Stratospheric Change – NDSC) (Kurylo and Zander, 2000). In order to maintain the uniformity of measurements made throughout the NDACC, intercomparison campaigns between UV-visible instruments are periodically held. Although the MANTRA campaign was not an NDACC intercomparison campaign, it did meet the requirements of an instrument intercomparison: the measurement site was reasonably free from tropospheric pollution (Vanscoy is upwind from Saskatoon, which is 30 km to the north-west), measurements were made for at least ten days, measurements were taken over the the course of the entire day, and the measurements were coincident in time. Three NDACC campaigns have been held to date: in 1992 at Lauder, New Zealand (Hofmann et al., 1995), in 1996 at the Observatoire de Haute Provence, France (Roscoe et al., 1999), and in 2003 at the Andøya Rocket Range in Andenes, Norway (Vandaele et al., 2005). A non-NDACC comparison was held in 1994 in Camborne, United Kingdom (Vaughan et al., 1997). The results of these four campaigns will be discussed in chronological order.

4.1.1 Lauder, New Zealand

The first formal NDACC intercomparison took place in Lauder, New Zealand (45°S, 170°E) between May 12 and 23, 1992 (Hofmann et al., 1995). Seven instruments took part in the campaign; six of them use the DOAS technique to retrieve trace gas data. One of these instruments was an earlier version of SAOZ. Only NO_2 results are discussed in Hofmann et al. (1995). At the beginning of the campaign, the instruments all made measurements of three gas cells containing three known amounts of NO_2. Each instrument was then assigned a correction factor, derived from the difference between the measured amount of NO_2 in one of the cells and the known amount, to apply to the slant column measurements of NO_2. Instruments were analysed with their standard software packages and cross sections. Both daily and single reference spectra were used. Whether one of these made for better or worse comparisons was dependent on the instrument. The agreement between the instruments was found to be, in general, good, with the seven instruments agreeing to within 20% at a SZA of 90° on all days, and to within 10% at 90° on most days. The best agreement was found at a SZA of 90°. Measurements at SZA smaller than this (high Sun) showed significant divergence for most instruments, due to the decreasing path length and slant column of NO_2. Measurements at SZAs larger than 90° (low Sun) showed divergence due to the decreasing amount of signal as the Sun set. Two instruments: those from the National Institute for Water and Atmospheric Research (NIWA) (of New Zealand) and from the National Oceanic and Atmospheric Administration (NOAA) (of the United States) were found to agree very well on all days of the campaign at all solar zenith angles.

4.1.2 Camborne, United Kingdom

An intercomparison took place in Camborne, United Kingdom (50°N, 5°E) between September 12 and 23, 1994 in preparation for the Second European Stratospheric Arctic and Mid-latitude Experiment (SESAME) campaign (Vaughan et al., 1997). The purpose of the intercomparison exercise was to ensure the consistency of the instruments. Eleven instruments from nine institutions took part, all of them using the DOAS technique. Four SAOZ instruments took part, three of them the older model with a 512-pixel detector, and one of them a newer model with the current 1024-pixel detector. Analyses with both ozone and NO_2 slant column and vertical columns were compared. Analysis was done with the instruments' own analysis software and cross sections of choice. Similar, though not identical, wavelength regions were used for all of the instruments. Both daily reference spectra and a single reference spectrum were compared. For ozone slant columns, the four SAOZ instruments agreed with one another to generally within 4%, though differences as high as 10% were seen. For NO_2, the SAOZ slant columns were generally within 5%, with differences up to 15%. Comparisons between the other instruments showed mean differences of up to 10% for ozone and 30% for NO_2. For vertical columns, similar agreement was found, with the calculation of the reference column density being the greatest source of the uncertainty in the vertical column.

4.1.3 Observatoire Haute Provence, France

The second NDACC intercomparison campaign took place at the Observatoire Haute Provence in Southern France (44°N, 6°E) between June 11 and 21, 1996. Sixteen instruments from eleven institutions participated, fourteen of which used the DOAS analysis technique. Of these, four were SAOZ instruments, three of them using a 1024-pixel detector and one using the older 512-pixel detector. Both ozone and NO_2 slant column densities are compared in Roscoe et al. (1999). In all cases, the spectra were analysed with the instruments' own analysis code. Comparisons were done using both daily reference spectra and a single reference spectrum. Comparisons were also made using the instruments' preferred cross sections and a set of common cross sections. The instruments' preferred wavelength range was also used, although one day was analysed with a prescribed wavelength region for NO_2. Two formal methods of comparison were introduced: regression analysis and fractional differences.

For regression analysis, the DSCDs from two instruments for a single twilight are transformed onto a common SZA grid. Only SZAs larger than 70° were used in this work. A linear regression is then performed, as in Equation 4.1.

$$Y = Intercept + Slope \times X \tag{4.1}$$

X and Y are the DSCDs of the two instruments being compared. The slope of the regression fit represents how well the two data sets agree: a non-unity slope indicates the DSCDs do not vary with SZA in the same way. Note that if different wavelength regions are used for the DOAS analysis, the DSCDs may not be expected to agree, due to the differences in air mass factors for the wavelength regions. A non-zero intercept represents a systematic offset between the two data sets. Residuals are also calculated from the fit parameters, as in Equation 4.2.

$$R_i = (Intercept + Slope \times X_i) - Y_i \tag{4.2}$$

Residuals that increase or decrease with SZA are a sign of non-linear error in at least one of the data sets. The goal of these comparisons is to identify a pair of instruments with unity slope and intercepts and residuals that are very close to zero. These measurements can then be taken to be of high quality. Comparisons of the other instruments with these "reference instruments" can then be examined to identify biases. In this campaign, the instruments from the Belgian, Bremen, and New Zealand groups were identified as reference instruments (none of these are of the SAOZ design). For ozone, most of the instruments' slopes agreed within 5%, regardless of cross sections used. The average slopes over the whole campaign, using a single reference spectrum, were between 0.52 and 1.77, when compared to one of the reference instruments. The slopes from the modern 1024-pixel SAOZ instruments were between 0.96 and 1.04. The intercepts range from between 15 and 3740 DU; for the SAOZ instruments the range was between 15 and 160 DU. The residuals ranged between 30 and 200 DU, and for SAOZ between 50 and 70 DU. For NO_2, the slopes agreed to within 5% only when the same cross sections and wavelength intervals are used. The DSCDs from instruments that do not track the Sun or have a fibre to depolarize the sunlight were also scaled by a factor of 1.035 (Fish and Jones, 1995). In this case, the slopes for one twilight period ranged from between 0.79 and 1.18, with the SAOZ slopes ranging between 1.01 and 1.18. The intercepts ranged between $(0.02\text{–}1.85)\times10^{16}$ molecules/cm^2, with the SAOZ intercepts ranging between $(0.46\text{–}1.85)\times10^{16}$ molecules/cm^2. The residuals ranged between $(0.028\text{–}1.53)\times10^{16}$ molecules/cm^2, with SAOZ residuals between $(0.226\text{–}0.545)\times10^{16}$ molecules/cm^2.

The second method of comparing DSCDs is to calculate the fractional difference compared to one of the reference instruments. For these comparisons a limited SZA range is used: 85° to 91°, which is similar to the range used to calculate vertical column densities. The DSCDs of one instrument are interpolated onto the SZA of the reference instrument. For ozone, using daily reference spectra and the instruments' preferred cross sections and wavelength region, the campaign-mean fractional differences are within 2.5% for most instruments, though the values range between -30% and 8%. The SAOZ instruments range between 0 and 3%. For NO_2 using daily reference spectra and the instruments' preferred cross sections and wavelength region, most of the instruments are within 7%, with a range of -8% and 15%. The campaign-mean fractional differences for the SAOZ instruments are between -5% and 10%.

4.1.4 Andenes, Norway

The third NDACC intercomparison campaign was held at the Andøya Rocket Range in Andenes, Norway (69°N, 16°E) from February 21 to March 6, 2003 (Vandaele et al., 2005). Nine instruments participated, including one SAOZ instrument. All the instruments used the DOAS technique. Only NO_2 slant column densities were compared. The regression analysis and fractional differences comparisons presented by Roscoe et al. (1999) were used to compare the instruments. Comparisons were performed with both daily and single reference spectra. Comparisons were also done using the instruments' preferred cross sections and wavelength regions, as well as prescribed cross sections and wavelength regions. The reference instruments were identified as being from the Belgian, New Zealand, and Spanish groups.

For the regression analysis comparisons, using a daily reference spectrum and the instruments' own choice of cross sections and wavelength regions, the instruments agree to within 7% in the slope, and all instruments meet the intercept and residual standards (to be discussed in Section 4.1.5). The SAOZ slope values are 1.013 and 1.008 in the morning and afternoon, respectively. The SAOZ intercepts are 0.1×10^{13} molecules/cm^2 in the morning and 2.3×10^{13} molecules/cm^2 in the afternoon. The residuals from SAOZ are 6.6×10^{13} molecules/cm^2 in the morning and 8.9×10^{13} molecules/cm^2 in the afternoon. All of these values are averaged over the whole campaign. Using the wavelength region 425–450 nm, the agreement is improved to 5% in the slope values. The average morning and afternoon slope from SAOZ is 0.946 in this region. The degradation is most likely due to the reduced signal-to-noise ratio of the SAOZ in this region due to smaller sampling. In both wavelength regions, SAOZ showed the largest differences from the reference instruments. Using a single reference spectrum did not affect the slope or residual values, but the intercepts were always larger. The results were an improvement over the previous comparisons at the Observatoire Haute Provence. This was likely due to a combination of factors: (1) improvements in instrument design and data retrievals, (2) the limited SZA range and shorter days of the polar spring, (3) small tropospheric NO_2 columns, and (4) small Ring effect contribution due to the small SZA range. The fractional differences showed larger variability in the morning versus the afternoon comparisons. During the campaign, the difference between SAOZ and the reference instruments' DSCDs varied between -37 and 4%, with an average of -4.3% in the morning and -2% in the afternoon.

4.1.5 NDACC Certification

Following the intercomparison campaign at the Observatoire Haute Provence, the NDACC established standards that instruments should meet to be considered for NDACC certification (Johnston et al., 1999). Two categories of certification are possible: Type 1 instruments are certified for global studies and trend measurements, while Type 2 instruments are certified for process studies and satellite validation. For both comparison types, the targets set by NDACC are for campaign-averaged values.

Type 1 comparisons follow the regression analysis described in Section 4.1.3, using SZAs between 70° and 91°. In this work, the regression is performed using a least-squares estimation method, and errors in the fit parameters are calculated (York et al., 2004). The NDACC target standards are given in Table 4.1.

Table 4.1: NDACC Type 1 comparison targets (Johnston et al., 1999).

Species	Slope	Intercept	Residual
Ozone	1.00±0.03	± 56 DU	< 37 DU
NO_2	1.00±0.05	$\pm 1.50 \times 10^{15}$ molecules/cm^2	$< 1.00 \times 10^{15}$ molecules/cm^2

Table 4.2: NDACC Type 2 comparison targets (Johnston et al., 1999).

Species	Ratio	Standard Deviation	Standard Deviation of the Offset
Ozone	1.00±0.05	< 0.03	
NO_2	1.00±0.10	< 0.05	$<2.50\times10^{15}$molec/cm^2

Type 2 comparisons are similar to the fractional differences comparisons described in Section 4.1.3, but for VCDs rather than DSCDs. In this comparison, the VCDs over the course of a twilight are transformed onto a common SZA grid ranging from 85° to 91° and the ratio of the data from the two instruments is taken. The target campaign-averaged values are given in Table 4.2. Since NO_2 concentrations increase throughout the day, the offset value between the morning and afternoon VCDs can be calculated by finding the y-intercept of a plot of the afternoon DSCDs against the morning DSCDs. The standard deviation in this offset should be less than 2.50×10^{15} molecules/cm^2. This offset value is only valid if the diurnal variation in NO_2 is similar during the campaign.

4.2 Instrumentation

The UT-GBS, SAOZ, MAESTRO, and SPS, all described in Chapter 2, took part in the campaign. Shortly before the beginning of the campaign, the CCD detector of the UT-GBS began malfunctioning and could not be repaired. The loaner detector was obtained from the manufacturer. As discussed in Chapter 2, this detector was not ideal. Despite this, good data was obtained from August 7 to September 15 (days 220–259).

SAOZ was operated between August 6 and September 15 (days 219–259); due to a problem with the shutter of the instrument, no data was obtained between August 13 and 16 (days 226–229). SPS measured between August 16 and September 14 (days 229–258). MAESTRO was primarily a balloon instrument during the MANTRA campaign, and so only eight days of zenith-sky data were taken, from August 16 to 23 (days 229–236).

The Brewer spectrophotometer (hereafter Brewer) was designed in the early 1980s to provide automated measurements of ozone and SO_2 (Savastiouk and McElroy, 2005). Brewers operate at twelve stations in Canada, as part of the Canadian Stratospheric Ozone and UV Monitoring Network, and at numerous locations throughout the world. The Brewer records direct Sun UV spectra at five discrete wavelengths: 306.3 nm, 310.1 nm, 313.5 nm, 316.7 nm, and 320.0 nm. A photomultiplier tube is used as the detector. Brewer # 007 was used at Vanscoy, and operated between August 6 and September 15 (days 219–259).

The University of Toronto Fourier Transform Spectrometer (U of T FTS) is an ABB Bomem DA5 instrument that has a 50-cm maximum optical path difference, and records single-sided interferograms along a linear mirror path. The instrument measures simultaneously on indium antimonide (InSb) and mercury cadmium telluride (MCT) detectors. Both detectors are photovoltaic in order to ensure a linear response to signal intensity. The U of T FTS has a spectral range spanning 1200–1500 cm^{-1} (2–8 μm) that is constrained by the detectors, the cadmium fluoride (CaF_2) beamsplitter, and a germanium solar filter. The instrument was extensively refurbished for the MANTRA 2004 campaign: new electronics and software were installed so that it could participate in both the balloon flight and the ground-based campaign. The refurbishment is described in Wunch et al. (2006). Only data from the MCT detector is discussed here, due to poor alignment of the InSb detector for the ground-based measurements. Ground-based data was recorded on six days: August 10–12, 19, and 27 and September 7 (days 223–225, 232, 240, and 251).

The Portable Atmospheric Research Interferometric Spectrometer for the Infrared

(PARIS-IR) is a compact, portable Fourier transform spectrometer built by ABB Bomem for performing atmospheric remote sensing measurements from balloon-borne platforms and the ground (Fu et al., 2007). It records double-sided interferograms and has the same spectral resolution (0.02 cm^{-1}) and spectral coverage (750–4400 cm^{-1}) as the satellite-borne ACE-FTS (Bernath et al., 2005). This is due to their similar design, and the use of components such as the beamsplitter that were flight spares for the satellite instrument. PARIS-IR recorded ground-based data on August 13 (day 226).

The University of Denver Fourier Transform Spectrometer (DU FTS) is an early ABB Bomem model with an extensive flight history. For the MANTRA 2004 flight, it was configured with a pair of MCT detectors. It has a maximum optical path difference of 50 cm and at flight time was operating at a resolution of 0.03 cm^{-1}. The spectrometer control and acquisition electronics have been updated several times, and this configuration uses a pair of digital filtering processors, providing two bandpasses of approximately 718–1438 and 1438–2154 cm^{-1}. The data acquisition control hardware and software were upgraded for the 2004 campaign, and are described in Fogal et al. (2005). The major difference between the 1998 flight configuration described therein and this campaign is the improved detectors and control and acquisition electronics. Ground-based data were obtained on August 25 and September 13 (days 238 and 257). All three FTSs measure direct sunlight through the use of three independent solar trackers.

4.3 Data Analysis

4.3.1 UV-visible Instruments

As described in Chapter 3, the programme WinDOAS is used to analyse the spectra from the UT-GBS, SAOZ, MAESTRO, and SPS. The details of the WinDOAS analysis are given in Table 4.3. These settings are chosen to optimize the wavelength calibration and spectra fits of the instruments. A Gaussian line shape is fit to the slit functions of the instruments. Ozone was fit between 450 and 500 nm, and NO_2 between 400 and 450 nm. A single reference spectrum for each instrument from day 247 (September 3, SZA=44.8°) was used as the reference spectrum. As a result of the common reference spectrum and analysis procedure, any differences seen in the differential slant column densities should be a result of the original spectra, and not an artifact of the analysis method. Since MAESTRO was not operating on day 247, and because there were no clear sky days during the period when it was operating, a reference spectrum from day 233 (August 20, SZA =44.7°) was used for the MAESTRO analysis. The DSCDs of the other instruments at the time of the MAESTRO reference spectrum are within 6 DU of the DSCD measured by MAESTRO. It is expected that the impact of using a reference spectrum from this day is negligible. VCDs were calculated using both the averaging and Langley plot methods, and are found to agree within error bars. As such, only the results from the averaging method are shown here. The AMF was calculated from the radiative transfer model initialized with temperature, pressure, and ozone profiles taken from the average of all ozonesondes flown during the campaign and an NO_2 profile taken from the UCI chemical box model at 55°N in August (McLinden et al., 2002). The campaign-mean ozone RCD and standard deviations are 307±178 DU for the UT-GBS, 388±150 DU for SAOZ, 486±182 DU for MAESTRO, and 356±147 DU for SPS. For NO_2, the mean RCDs and standard deviations are $(1.13\pm0.68)\times10^{16}$ molecules/cm^2 for the UT-GBS and $(0.87\pm0.53)\times10^{16}$ molecules/cm^2 for SAOZ. The mean RCDs agree within the standard deviation, and the standard deviations are similar, showing the instruments display similar scatter in the RCD throughout the campaign. The percentage errors for the DSCDs and VCDs are given in Chapter 3.

The NO_2 DSCDs calculated using WinDOAS for MAESTRO and SPS are unreliable, with the fitting error being of the same order of magnitude as the fitted differential slant columns. As a result, no NO_2 from these instruments is available. Both MAESTRO and SPS have uncooled detectors, whose signal-to-noise ratios increase with colder tempera-

Table 4.3: Details of the WinDOAS analysis for the four UV-visible instruments. These settings are the same for the ozone and NO_2 analyses. The same polynomial degree is used in the calibration for both the wavelength shift and the slit function parameters, and is given in the column CDP (calibration polynomial degree). CWL (calibration window limit) is the range used for the wavelength calibration. CF (continuous functions) is the degree of polynomial fit to the optical depth in the DOAS analysis. The offset is the term fit to correct for stray light, discussed in Chapter 3.

Instrument	CPD	CWL (nm)	# of Subwindows	CF	Offset
UT-GBS	3	400–550	5	0, 1, 2, 3	none
SAOZ	3	400–550	4	0, 1, 2, 5	linear
MAESTRO	3	400–550	5	0, 1, 2	none
SPS	3	400–550	6	0, 1, 2, 3, 4, 5	linear

tures. In an effort to improve the quality of the recorded spectra, both instruments were installed inside a modified commercial freezer. This deployment was not ideal, as the viewing windows of both instruments often frosted over, decreasing the signal-to-noise ratio of the detectors. This decrease in signal affects the NO_2 retrievals more than the ozone retrievals due to the fact that the signal from NO_2 is much weaker than that from ozone. For MAESTRO, another possible problem is the direction of the polarizer, installed in the foreoptics. This polarizer was found to be in the wrong position at the beginning of the Eureka 2005 campaign. If the polarizer was in the wrong position during MANTRA, only the weak polarization would have been recorded, which could explain why the NO_2 signal is weak in the MAESTRO spectra.

Total columns of ozone from the Brewer are retrieved using an algorithm based on Beer's Law. Errors are calculated based on the standard deviation of the column measurements made over the course of a day and are generally less than 1% (Savastiouk and McElroy, 2005).

4.3.2 Fourier Transform Spectrometers

Retrievals for the U of T FTS and PARIS-IR were performed using SFIT2 (v.3.82beta3 for U of T FTS, v.3.81 for PARIS-IR) (Rinsland et al., 1998; Pougatchev et al., 1995), which employs the optimal estimation method of Rodgers (2000). SFIT2 retrieves the primary trace gas volume mixing ratio (VMR) vertical profile represented on an altitude grid. Total column amounts are retrieved by integrating the VMR profiles. Both instruments use the HIgh-resolution TRANsmission database (HITRAN) 2004 spectral database (Rothman et al., 2005a). For the U of T FTS, ozone was retrieved from the 3040 cm^{-1} microwindow (3039.90–3040.60 cm^{-1}) with H_2O and CH_4 fit as interfering species. Individual total columns are retrieved from spectra co-added over 20 minute time intervals. Daily averages are then computed from these individual total column amounts, and the error bars (7%) represent the maximum standard deviation of the individual total columns (Wunch et al., 2006). For PARIS-IR, ozone is retrieved from the 990 cm^{-1} microwindow (987.15–990.0 cm^{-1}), with the isotopologues of ozone, CO_2, H_2O, and solar lines fit as interfering species. The data analysis is described in detail in Fu et al. (2007). The uncertainty in the retrieved PARIS-IR results for ozone include contributions from the spectral noise, interfering molecules, uncertainties in the viewing geometry and uncertainties in the atmospheric temperature profiles. This value is estimated to be 2.7%. For both instruments, the *a priori* ozone profile was taken from ozonesondes flown during the campaign. For the U of T FTS, the pressure and temperature profiles are taken from the NCEP weather model (McPherson, 1994) and the U.S. Standard Atmosphere. For PARIS-IR, the pressure and temperature profiles are taken from NCEP and the Mass-Spectrometer-Incoherent-Scatter (MSIS-2000) model (Picone et al., 2002).

The columns from the DU FTS were generated using an optimal estimation retrieval based on the DU RADCO (RADiation COde) which is used as the spectral forward model, and from which the ray-tracing algorithm is adapted (Blatherwick et al., 1989;

Fogal, 1994). The model atmosphere (pressure, temperature, and ozone) was constructed based on radiosonde data from the ozonesondes flown during the campaign. The HITRAN 2004 spectral database was used. The spectra analysed for ozone are all from the longer wavelength channel (987.45–987.55 cm^{-1}) as the other channel (1438–2154 cm^{-1}) is dominated by water vapour at ground level. H_2O and CO_2 are fit as interfering species. Given the relatively low resolution of the spectrometer, little profile information is retrieved. Nonetheless, very good column determinations can be made. Uncertainty in the ozone columns is 15%, resulting primarily from the variance in the ozonesonde flights used in constructing the *a priori* VMR profile.

4.4 Differential Slant Column Density Comparisons

4.4.1 Type 1 Comparisons

Figure 4.2 shows the ozone and NO_2 DSCDs from the afternoon of August 20 (day 233) for the UT-GBS, SAOZ, MAESTRO, and SPS instruments. This was a relatively clear day, with all four instruments measuring. MAESTRO DSCDs are averaged over 0.25° intervals. The SPS and MAESTRO ozone agree up to a SZA of 91°, despite the scatter in the SPS DSCDs. UT-GBS ozone DSCDs are approximately 250 DU higher than the SPS and MAESTRO, however this is a constant offset. The SAOZ DSCDs at low SZAs agree with the UT-GBS DSCDs, but increase more rapidly with SZA than the UT-GBS DSCDs. SPS DSCDs become scattered above 91°, most likely due to the build-up of ice on the viewing window during unattended operation, which was worse for SPS than for MAESTRO. The low signal-to-noise ratio of the UT-GBS causes some scatter in the DSCDs, which is especially visible for NO_2. NO_2 absorption features are weaker and narrower than those of ozone, resulting in NO_2 retrievals being more sensitive to the quality of the spectra, as well as to the retrieval parameters used in the DOAS analysis. Despite this scatter, the NO_2 DSCDs show good agreement. In the case of NO_2, the

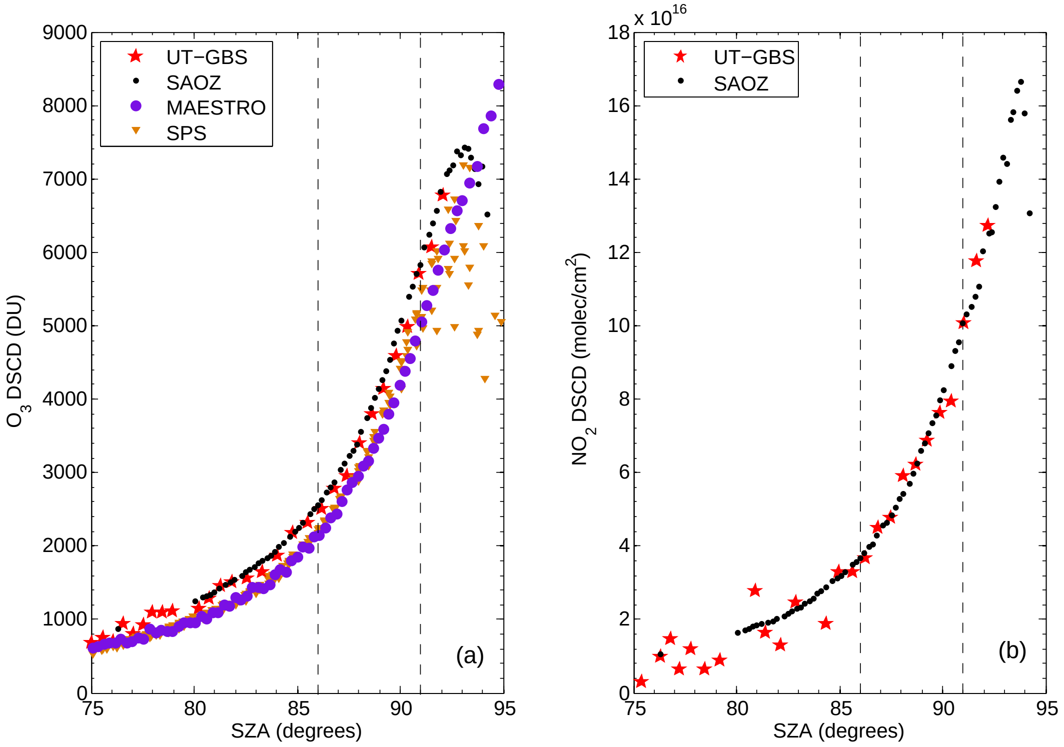

Figure 4.2: (a) Ozone differential slant column densities for the UT-GBS, SAOZ, MAESTRO, and SPS for sunset of August 20, 2004. (b) As (a), but NO_2 and for SAOZ and the UT-GBS. The dashed lines at 86° and 91° indicate the range of DSCDs used in the calculation of VCDs. For the Type 1 and 2 comparisons, DSCDs between 85° and 91° are used.

UT-GBS DSCDs are scattered about those from SAOZ. All of these observations are consistent throughout the campaign, with the exception of the SPS and MAESTRO agreement. The two datasets are not always in agreement at small SZAs: on some days the DSCDs are separated by a roughly constant value of up to 200 DU over all SZAs.

Figure 4.3 shows an example of the regression analysis for ozone and NO_2 for measurements taken at sunset on August 20 between the UT-GBS and SAOZ. Only the SZAs between 85° and 91° are considered, due to the large errors for small SZAs in the UT-GBS data. SAOZ data has been interpolated onto the UT-GBS SZA grid because of the smaller number of UT-GBS data points. The top panels show the regression fit of the two datasets, while the bottom panels show the calculated residual versus SZA. The results of the fits are also shown. Figure 4.4 shows the average results of the anal-

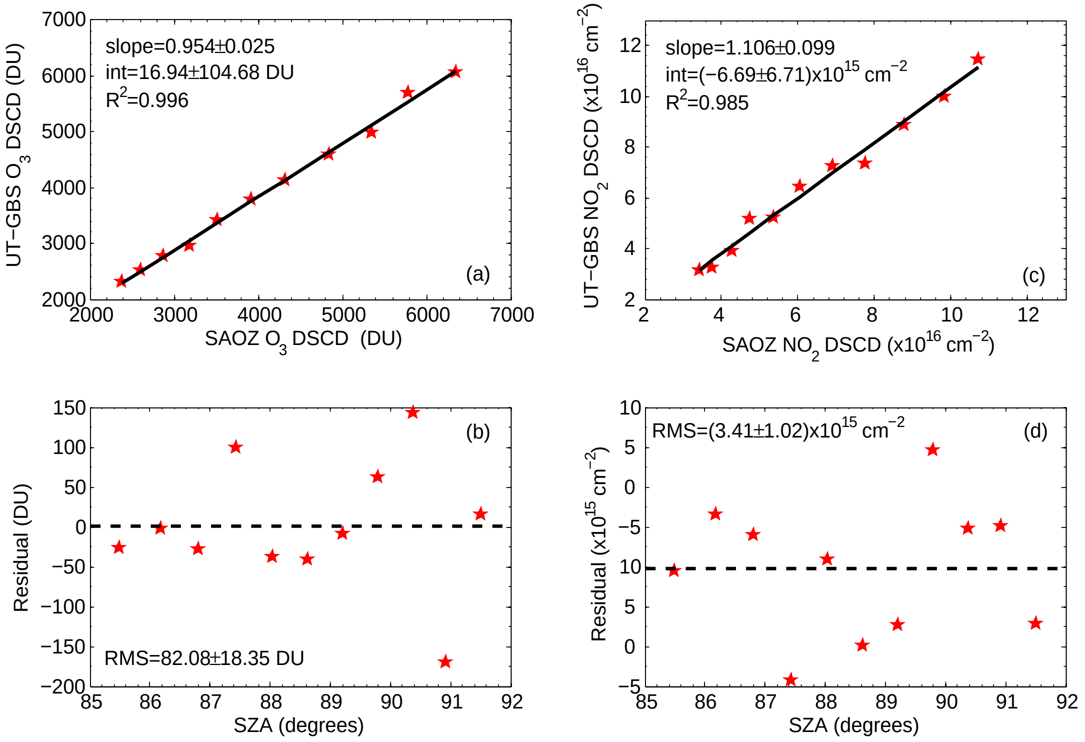

Figure 4.3: (a) Type 1 regression analysis for ozone between UT-GBS and SAOZ for sunset, August 20, (b) residuals of the fit in (a), (c) same as (a) but for NO_2, (d) same as (b) but for NO_2. The solid lines in (a) and (c) are the fitted lines to the data. The dashed lines in (b) and (d) are the average of the residuals.

ysis for ozone for the entire campaign for all pairs of instruments. Error bars are the standard errors ($\sigma/\sqrt{N}$, σ is the standard deviation, N is the number of comparisons) of the parameter throughout the campaign. The required accuracies to be considered a certified NDACC instrument for global trend studies are shown as dashed horizontal lines in Figure 4.4 (see Table 4.1). Only one regression analysis is shown for each pair of instruments (i.e., only UT-GBS vs. SAOZ and not SAOZ vs. UT-GBS); the results from the other analyses have been calculated, and are in agreement with the analysis shown.

The UT-GBS vs. SPS morning, MAESTRO vs. SAOZ morning, and MAESTRO vs. SPS morning and afternoon ozone comparisons all have average slopes that meet the NDACC standards. As noted above, the SAOZ ozone DSCDs diverge from those of the other instruments at higher SZAs. This is reflected in the slopes that are smaller than the

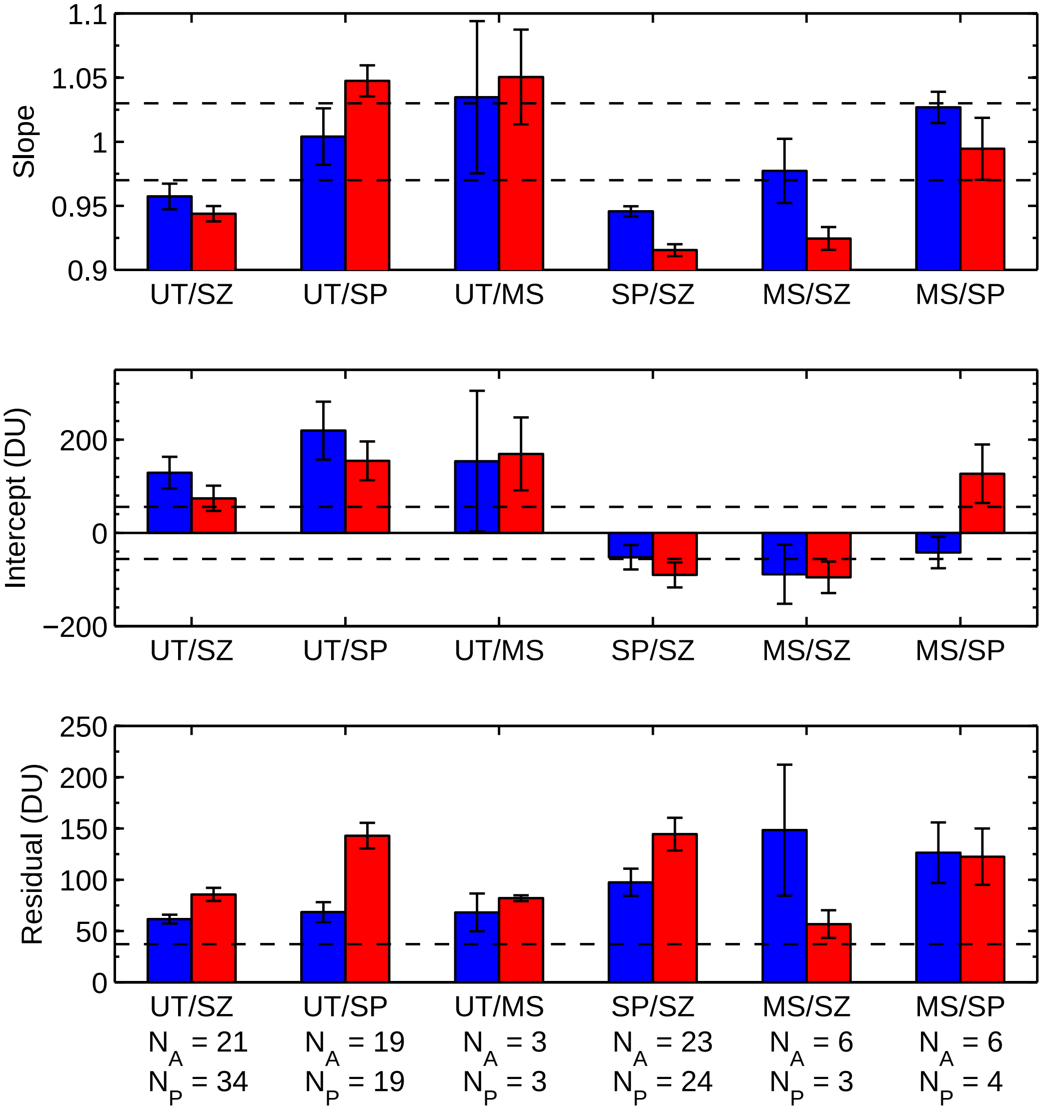

Figure 4.4: Type 1 regression analysis results for ozone for all pairs of UV-visible zenith-sky instruments. Dashed horizontal lines indicate the required accuracies set by the NDACC. Blue is for the morning comparisons, red is for the afternoon. The error bars indicate one standard error. UT indicates the UT-GBS, SZ is SAOZ, SP is SPS, and MS is MAESTRO. N_A and N_P are the number of days used in calculating the morning and afternoon averages.

NDACC standard. This may be a result of the larger field-of-view of SAOZ (10° vs. 2° for the UT-GBS). For all the comparisons with the UT-GBS, the morning standard errors on the slopes are larger than the afternoon standard errors. In general for the UT-GBS, there are more measurements in the afternoon than in the morning, extending to a larger SZA. This is a result of the general campaign trend of cloudier skies during sunrise than during sunset. Since the UT-GBS's loaned detector was not as sensitive to UV-visible light as would have been ideal, the cloudy, darker skies meant that the first UT-GBS measurement of the day was often not until a SZA of 90°. With the exception of the SPS vs. SAOZ and MAESTRO vs. SPS morning comparisons, the intercepts in Figure 4.4 do not meet the NDACC intercept standard. The large intercepts are consistent with the differences in the RCDs discussed in Section 4.3.1. The residuals are also all large and variable - indicating scatter in the DSCDs from all the instruments. In the case of the UT-GBS, this is partly due to the low signal-to-noise ratio of the spectra.

The campaign averages for the NO_2 regression parameters for the UT-GBS and SAOZ are shown in Table 4.4. The errors given are the standard errors. Both slopes fall within the required standards (see Table 4.1). The intercepts and residuals are approximately 1.25 to 3.5 times the standards. The error in the daily values of the parameters are all large, especially the sunrise values. This is again due, in part, to fewer measurements in the morning than in the afternoon. In addition, due to the lower columns of NO_2 present during sunrise, it is to be expected that the sunrise values would be more uncertain than the sunset values.

4.4.2 Type 2 Comparisons

The results from the Type 2 ozone comparisons are shown in Figure 4.5. The dotted horizontal lines indicate the required accuracy set by the NDACC. The error bars for the ratios are the standard errors. The UT-GBS vs. SAOZ morning, UT-GBS vs. MAESTRO, and MAESTRO vs. SAOZ morning comparisons have average results that meet the

Table 4.4: Type 1 regression analysis results for NO_2 for the UT-GBS and SAOZ. Values given are campaign averages for the regression parameters. Errors represent the standard error. Values that meet the NDACC standards are shown in bold. The intercept and residual are given in 10^{16} molecules/cm^2. N is the number of days used in calculating the average.

	NO_2 AM, N = 19	NO_2 PM, N = 33
Slope	**1.024±0.020**	**1.018±0.013**
Intercept	0.531±0.092	0.190±0.078
RMS of Residual	0.281±0.021	0.375±0.016

Table 4.5: Type 2 results for NO_2 for the UT-GBS and SAOZ. The offsets are given in 10^{16} molecules/cm^2. Values given are campaign averages. Values that meet the NDACC standards are shown in bold. The number of days used in the average is the same as for the Type 2 comparisons (Table 4.4).

	NO_2 AM	NO_2 PM
Ratio	**1.030**	**1.100**
Standard Deviation	0.071	0.058
NO_2 offset	UT-GBS: (0.34±**0.19**)	SAOZ: (0.29±**0.10**)

NDACC standards. As for the Type 1 comparisons, the comparisons with SAOZ have small values compared to the standards. The standard deviations are all smaller than the standards, with the exception of the UT-GBS vs. SAOZ morning comparison, a reflection of the smaller number of DSCDs for the UT-GBS in the morning.

The campaign averages for the NO_2 ratios, the standard deviation of the ratios, and the average offsets for the UT-GBS vs. SAOZ comparison are given in Table 4.5. The ratios meet the NDACC standards (see Table 4.2). The standard deviations of the ratios do not meet the standard. This is likely a result of the scattered UT-GBS DSCDs due to the low signal-to-noise ratio of the instrument. The standard deviation of the NO_2 offset (given as the error) for both instruments are well within the NDACC standards. The average value of the offset is similar for both instruments.

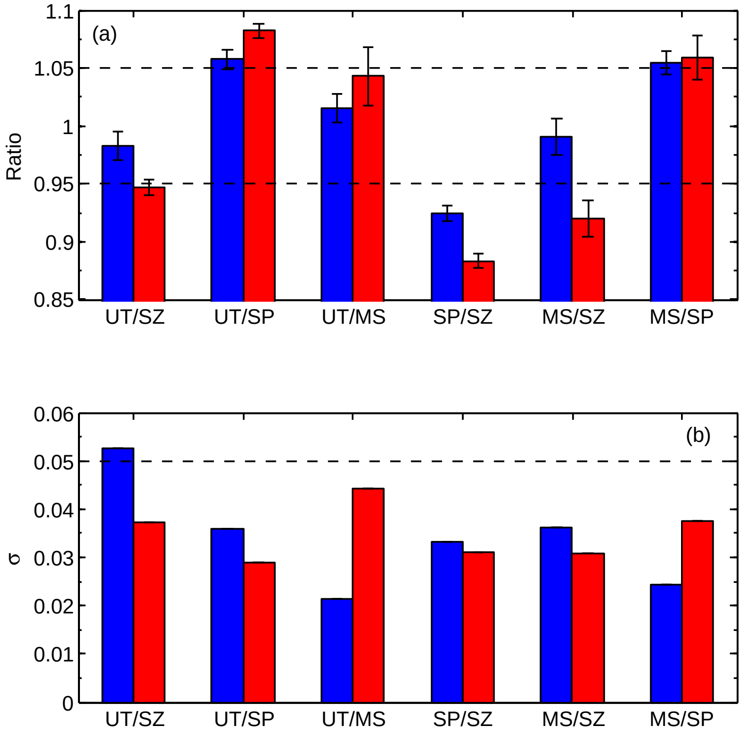

Figure 4.5: Type 2 (a) ratio and (b) standard deviation results for ozone for all pairs of UV-visible zenith-sky instruments. Dashed horizontal lines indicate the required accuracy set by the NDACC. Blue is for the morning comparisons, red is for the afternoon. The error bars indicate one standard error. The number of days used in the average is the same as for the Type 1 comparisons (Figure 4.4).

4.5 Vertical Column Density Comparisons

4.5.1 Ozone

Daily averaged vertical column densities of ozone, calculated using the averaging method, from the four zenith-sky viewing UV-visible instruments, the Brewer, the three FTSs, and the ozonesondes are shown in Figure 4.6. The ozonesonde profiles have been integrated, with a correction added to account for ozone above the burst height of the balloons. Errors on the ozonesonde columns are 5% (Tarasick et al., 2005). All instruments show a relatively constant ozone column throughout the campaign, varying between 280 and 340 DU.

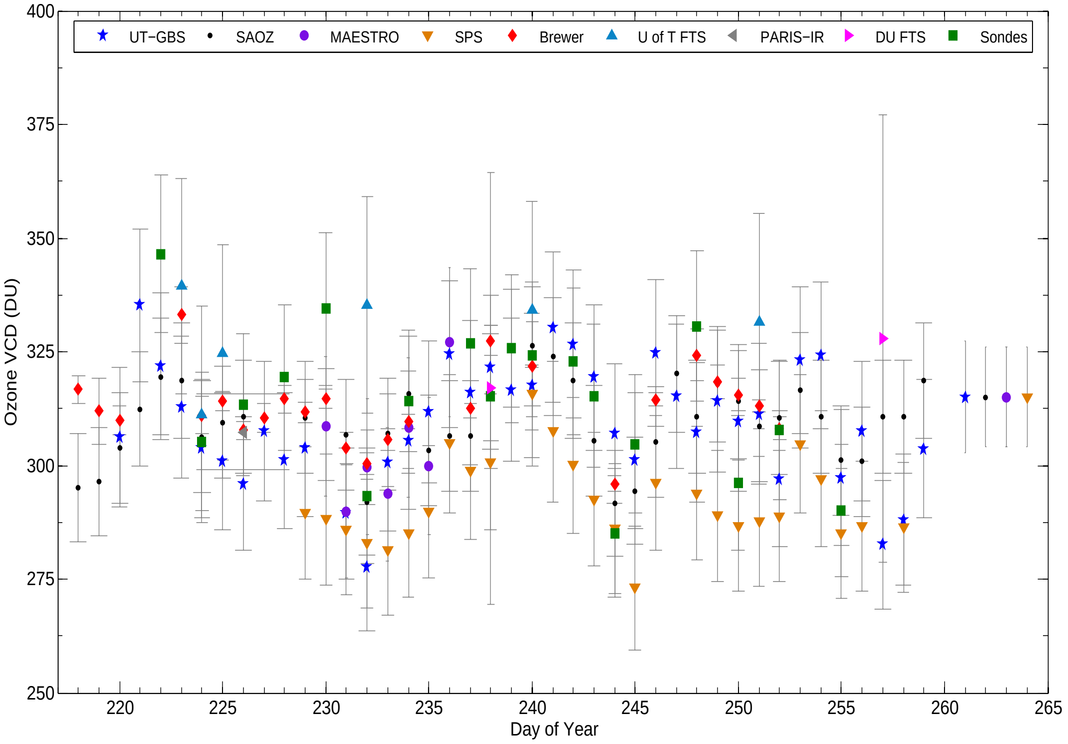

Figure 4.6: Daily-averaged ozone vertical column densities as measured by the UT-GBS, SAOZ, MAESTRO, SPS, Brewer, U of T FTS, DU FTS, PARIS-IR, and ozonesondes. For the UV-visible instruments, the error bars indicate the total errors given in Chapter 3. For the FTS instruments, the error bars reflect the error discussed in Section 4.3.2. For the ozonesondes, errors are 5%. For the UV-visible instruments, representative systematic error bars are shown at the right of the figure.

The ozone VCDs from the zenith-sky UV-visible instruments universally agree within their error bars, which represent both random and systematic errors. On average for the campaign, the SPS VCDs are 18 DU lower than those of the other instruments. The trends from the instruments are also consistent. The measurements from the direct-Sun-viewing Brewer agree with the other UV-visible instruments for the duration of the campaign. The measurements from the ozonesondes are scattered about the ground-based instruments, however the values agree within the combined random and systematic error of the instruments.

The primary role of the FTS instruments during MANTRA 2004 was to participate in the main balloon flight. Ground-based measurements were taken to test the performance of the instruments, when there were no flight tests being performed. As a result, the data for all three instruments is sporadic. The single PARIS-IR column of day number 226 agrees very well with the columns measured by the Brewer and the ozonesonde on that day, and is 11 DU (4%) higher than the UT-GBS column. The ozone columns from the U of T FTS agree with the other instruments within error bars except for day number 232. This is most likely due to a detector alignment error. The columns are 4–7% higher than the UV-visible instruments on the six days of measurements, or 3–6% if day 232 is omitted. The DU FTS ozone column on day number 238 is in good agreement with the other instruments and the ozonesonde, falling in the middle of the 27 DU measurement range. On day 257, the DU FTS ozone column is approximately 17 DU (6%) higher than the SAOZ and 45 DU (15%) higher than the UT-GBS. Disagreements between UV-visible and FTS instruments could be due to known issues with the cross sections of ozone in the infrared and the UV-visible (Rothman et al., 2005b), sensitivity to different layers of the atmosphere (Rodgers and Connor, 2003), differences in the time of day of the instruments are measuring, and differences in the viewing geometry of the instruments (zenith sky versus direct Sun).

4.5.2 NO_2

Vertical column densities of NO_2 from the UT-GBS and SAOZ, calculated using the averaging method, are shown in Figure 4.7. Both instruments show a general decrease in NO_2 as the days get shorter and the available sunlight decreases. As expected from the agreement in the DSCDs discussed in Section 7.2, the instruments agree within their error bars, which represent both random and systematic error. The UT-GBS columns are on average 4% and 6% smaller than the SAOZ columns in the morning and afternoon, respectively. The trend in both the morning and afternoon NO_2 VCDs is the same for both instruments. The columns from the UT-GBS decrease by 18% from day 230 to day 258, while the SAOZ columns decrease by 22% during this same period.

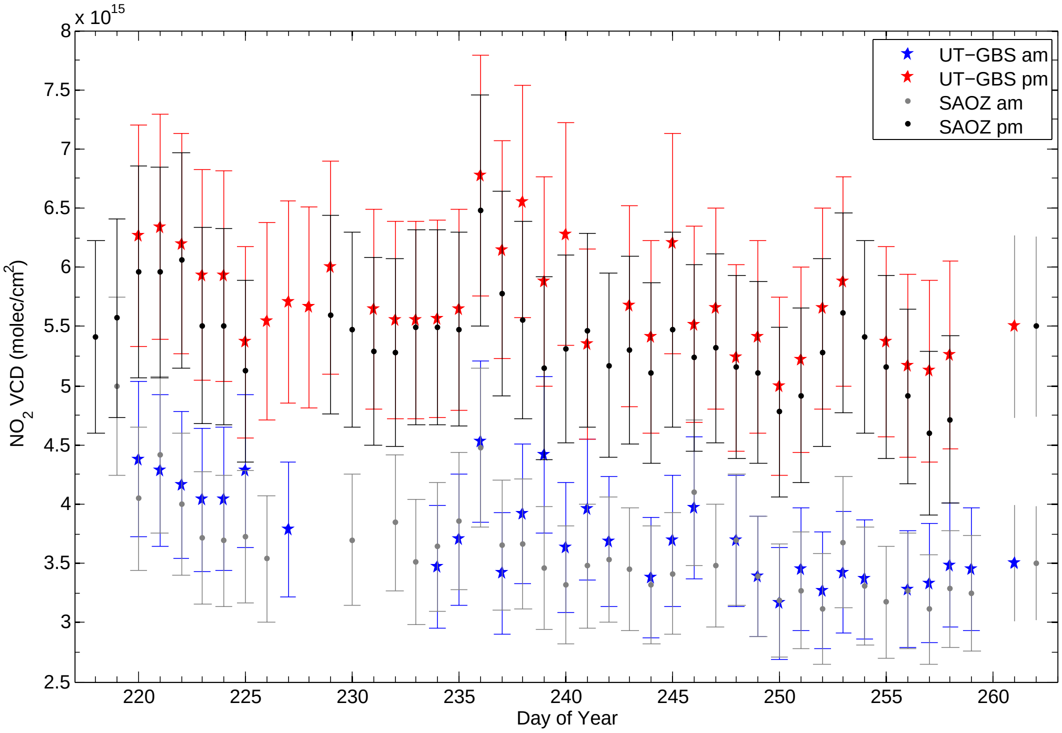

Figure 4.7: NO_2 vertical column densities as measured by the UT-GBS and SAOZ. Error bars represent the total errors given in Chapter 3. The error bars to the right of the plot indicate representative systematic error bars.

The campaign average of the ratio of the morning to the afternoon NO_2 VCDs for the UT-GBS is 0.66 with a standard deviation of 0.06. For SAOZ the average ratio is 0.68 with a standard deviation of 0.05. This is slightly lower than the 0.72 with a standard deviation of 0.06 calculated for the UT-GBS during the MANTRA 1998 campaign (Bassford et al., 2005). These values are in agreement with the 0.6 and 0.7 values measured during the summer in Japan at similar latitudes to Vanscoy (43.4° and 44.4°) by Koike et al. (1999).

4.6 Summary

The ozone DSCD comparisons from the four UV-visible zenith-sky-viewing instruments in general do not meet the NDACC standards for instruments certified for trend studies

(Type 1). Although some of the instrument comparisons yield intercepts that meet the standards within one standard error, almost all of the intercepts are larger than the requirements. The intercepts indicate variability in the agreement at small SZA, and an offset in the DSCDs. The residuals as well are large, indicating increased scatter on the DSCDs; in the case of the UT-GBS, this scatter is caused by the low signal-to-noise ratio of the instrument during this campaign.

The ozone DSCD comparisons partially meet the standards for instruments certified for process studies and satellite validation (Type 2). Some of the comparisons yield ratios that meet the standards. The standard deviations for all the comparisons are in the required range, with the exception of the UT-GBS vs. SAOZ morning comparison. This indicates consistency in the agreement between the instruments.

The NO_2 DSCD comparison between the UT-GBS and SAOZ partially meets the NDACC standards for an instrument certified for trend studies (Type 1). The required slope values are met, while the intercepts and the residuals are larger than required. This is a result of the low signal-to-noise ratio of the UT-GBS for the MANTRA 2004 campaign. The NO_2 DSCDs also partially meet the NDACC standards for an instrument certified for process studies and satellite validation (Type 2). The ratios of the DSCDs from the two instruments meet the standards, while the standard deviations are larger than required. This is also due to the low signal-to-noise of the UT-GBS during the campaign. The NO_2 offsets between the morning and afternoon DSCDs are consistent with the requirements of the NDACC.

Vertical column densities of ozone measured by the zenith-sky UV-visible instruments, Brewer spectrophotometer, PARIS-IR, the DU FTS, the U of T FTS, and ozonesondes agree within combined error bars (15%) for the duration of the campaign. NO_2 VCDs from the UT-GBS and SAOZ also agree within their combined random and systematic error (15%) during the campaign. All instruments observed a relatively constant ozone field, and slightly decreasing NO_2 columns over the course of the campaign.

Chapter 5

Lightning-Produced NO_2

During thunderstorms, NO_2 and NO are formed by lightning breaking the bonds of N_2. Enhanced NO_2 caused by lightning can be detected by ground-based UV-visible spectrometers. On the afternoons of August 28, 2004, during MANTRA 2004, and May 17, 2006, in Toronto, the UT-GBS measured elevated slant columns of ozone, O_4, and NO_2. The ozone and O_4 have been attributed to an enhanced path length in the troposphere due to the multiple-scattering effects of clouds. The NO_2 is partly attributed to enhanced path length, and also partly to lightning-produced NO_x. Two methods to estimate the NO_2 due to path enhancement have been developed, allowing an estimation of the amount of NO_2 produced by lightning to be found. Combining this result with radar data from Environment Canada and lightning flash data from the Canadian Lightning Detection Network (CLDN) allows an estimation of the amount of NO_2 produced by each lightning flash. The results of the MANTRA study are published in Fraser et al. (2007b) and are presented here in an updated form.

5.1 Lightning-Produced NO_x

In the troposphere, NO_x ($NO + NO_2$) can act as both an ozone source and sink, depending on the concentrations of ozone precursors (CO, CH_4, and volatile organic compounds) and

NO_x, as well as the amount of available sunlight. Sources of NO_x in the troposphere are numerous, and include ground-based fossil fuel burning (∼24 Tg N/year), biomass burning (∼8 Tg N/year), soil emissions (∼12 Tg N/year), NH_3 oxidation (∼3 Tg N/year), aircraft emissions (∼0.4 Tg N/year), and transport from the stratosphere (<0.4 Tg N/year) (Price et al., 1997, and references therein). Another source of NO_x in the middle and upper troposphere, with by far the largest uncertainty, is lightning. The large amounts of energy released by lightning flashes can break apart N_2 and O_2 molecules, which then recombine to form NO. This newly formed NO can then react with ozone to form NO_2 (Zel'dovitch and Raizer, 1966). Recent estimates of the global annual production rate due to lightning-produced NO_x lie between 1 and 20 Tg N/year, with a best estimate of 5–6 Tg N/year (Huntrieser et al., 2002; Tie et al., 2002; Ridley et al., 2004; Boersma et al., 2005; Beirle et al., 2006; Martin et al., 2007; Schumann and Huntrieser, 2007).

5.2 August 28, 2004

5.2.1 Thunderstorm

On the afternoon of 28 August, 2004, a thunderstorm passed over Vanscoy. Environment Canada (EC) meteorological observations in Saskatoon (30 km north of Vanscoy) showed thunderstorm conditions for three hours, from 17:00 to 20:00 LT (23:00 to 2:00 UTC). Figure 5.1 shows the cloud base heights and total cloud opacity recorded by EC in Saskatoon during the storms.

Figure 5.2 shows the constant altitude plan position indicator (CAPPI) radar reflectivity measured by the EC radar in Radisson, Saskatchewan (60 km north-west of Vanscoy). The CAPPI radar image shows the reflectivity at an altitude of 1.5 km. Images are shown for 30-minute intervals from 15:00 to 22:00 LT (21:00 to 4:00 UTC). Cells of heavy rain and hail (pink colour) are observed over Vanscoy (the orange arrow). The maximum radar reflectivity in the 5 km area around Vanscoy is shown in Figure 5.1. A se-

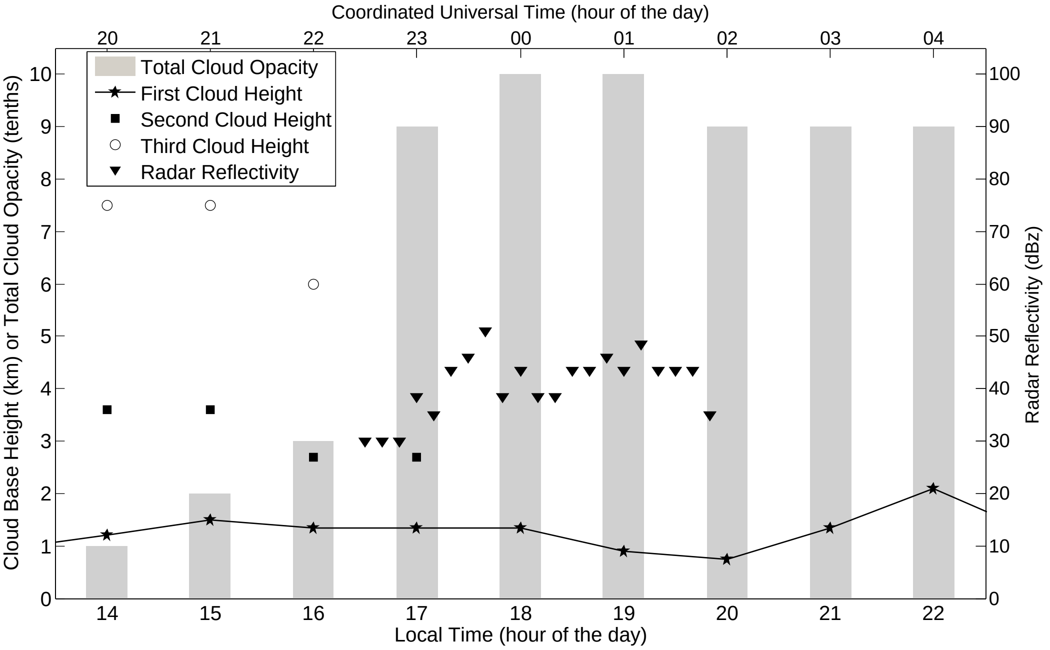

Figure 5.1: Cloud base heights (in km) and total cloud opacity (in tenths) recorded by Environment Canada at Saskatoon on August 28, 2004. First, second, and third heights are the base heights of the three layers of cloud. Also shown is the maximum radar reflectivity in the 5 km area around Vanscoy, recorded by the Environment Canada radar in Radisson, Saskatchewan.

ries of thunderstorm cells formed to the west of Vanscoy, near the Alberta-Saskatchewan border, and traveled to the east, eventually dissipating to the east of the measurement site. In total, three cells (or remnants of cells) passed over Vanscoy. The maximum area of the three cells was (61±10) km^2 (using the area with reflectivity greater than 40 dBZ (MacKeen et al., 1999)). Since Vanscoy was upwind of Saskatoon for the duration of the storm, it is unlikely the observed enhancements were due to the upward transport of anthropogenic NO$_2$.

The CLDN is a series of ground-based detectors that sense lightning using the time-of-arrival of radio pulses generated by lightning (Burrows et al., 2002). Figure 5.3 shows the lightning flashes detected by the CLDN over the Prairies for August 28. Images are available on an hourly basis; the colour-coding indicates in which 10-minute period the flash was detected. Each individual + and - represents a detected flash. The flashes are

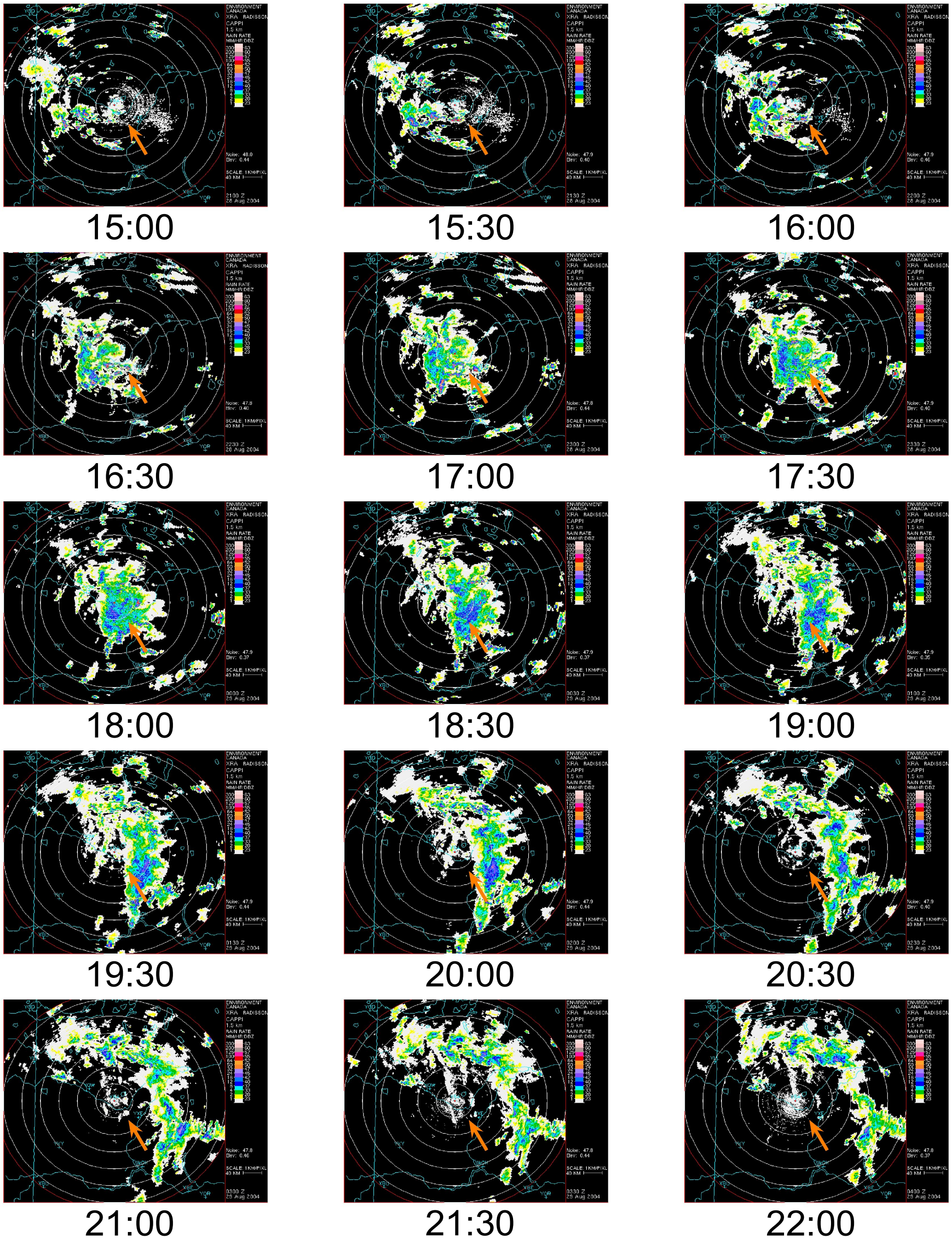
15:00
15:30
16:00
16:30
17:00
17:30
18:00
18:30
19:00
19:30
20:00
20:30
21:00
21:30
22:00

Figure 5.2: Precipitation rate calculated from the Environment Canada radar measurements in Radisson, Saskatchewan on August 28, 2004. Vanscoy is indicated by the orange arrow. Images are shown at 30-minute intervals, from 15:00 to 22:00 LT (21:00 to 4:00 UTC). The local time is indicated below each individual radar image.

overlaid on a visible Geostationary Operational Environmental Satellite (GOES) image for the beginning of the hour. The total number of flashes detected by the CLDN upwind of Vanscoy is (524±52). The detection efficiency of the CLDN is approximately 85-90% for cloud-to-ground (CG) and 1-4% for intra-cloud (IC) flashes at the latitude of Vanscoy, due to the lower amounts of energy released by the latter. Approximately 94.4% of the observed flashes were CG. Correcting these 494 flashes for the detection efficiency of the CLDN yields (565±59) CG flashes. This leaves (30±3) detected IC flashes. Correcting these flashes for the 1-4% detection efficiency yields 750-3000 IC flashes.

5.2.2 Differential Slant Column Densities

Figure 5.4(a)-(c) shows the ozone, NO_2, and O_4 DSCDs measured by the UT-GBS and SAOZ on August 28. Figure 5.4(d) shows the intensities measured by both instruments on the same day. Intensities were calculated by dividing the intensity at 450 nm (the peak of the spectrum) by the exposure time of the measurement. They were then referenced to the intensity per time at 450 nm and SZA=60° in the morning. Both instruments observed a maximum in all three species at SZA=77° (18:31LT), which is consistent with the occurrence of the thunderstorm. During the storm, the measured intensities fall to roughly 5% of the morning intensities, which is consistent with the heavy cloud cover observed in Figures 5.1 and 5.2.

At the ozone maximum, the DSCDs of both instruments are roughly double the morning values. Since ozone is generally constant during the day, it is expected that the afternoon and morning DSCDs at a particular SZA would be the same. At the peak of NO_2, the DSCDs have increased by a factor of 25 for the UT-GBS, and 20 for SAOZ 15 minutes before the peak. SAOZ had not begun continuous measurements at the peak of the storm, and thus did not capture the true maximum in the NO_2 columns. However, since the NO_2 columns between the instruments were in agreement for the rest of the campaign (see Chapter 4), it can be assumed that had SAOZ been measuring, it would

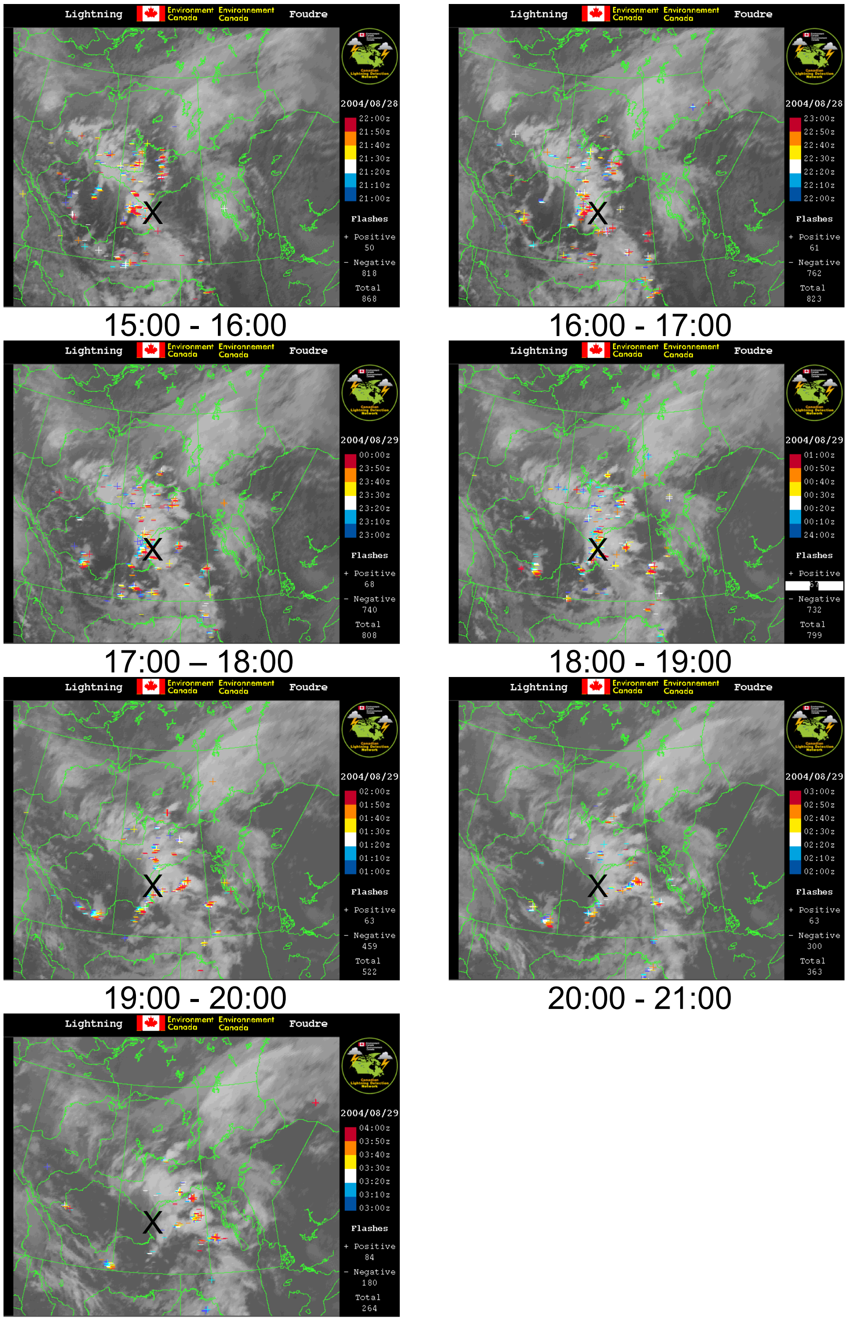

15:00 - 16:00

16:00 - 17:00

17:00 – 18:00

18:00 - 19:00

19:00 - 20:00

20:00 - 21:00

21:00 - 22:00

Figure 5.3: Lightning flash data for August 28 in Vanscoy (X) from the Canadian Lightning Detection Network (CLDN) superimposed on a visible GOES image. Each plus (+) and minus (-) represents an individual lightning flash. The local time of the image is displayed below each individual image.

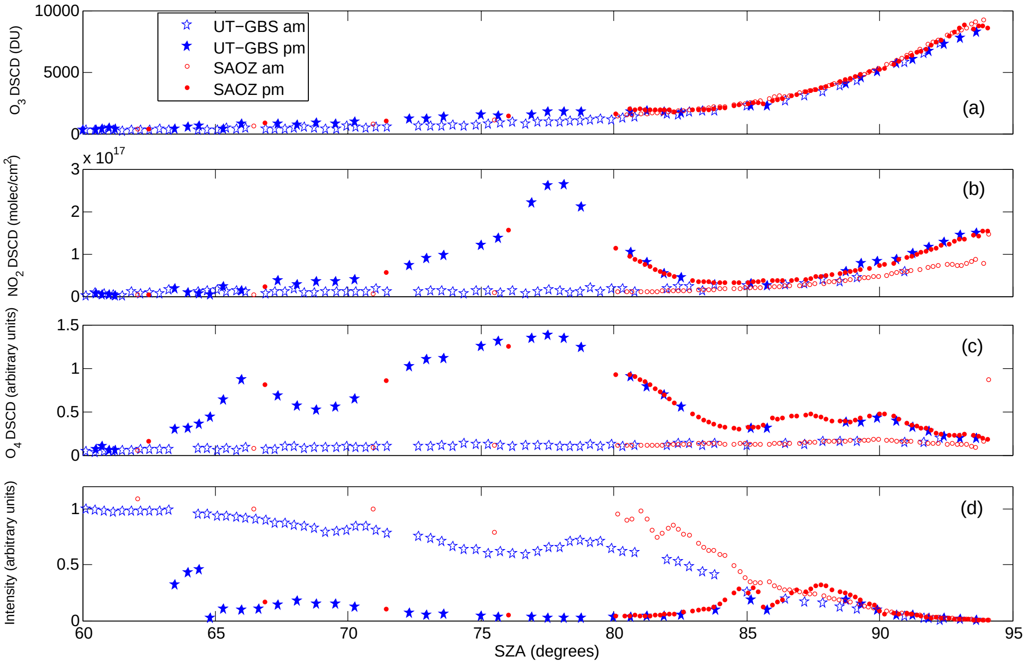

Figure 5.4: (a) Ozone, (b) NO_2, and (c) O_4 differential slant column densities, and (d) intensities measured by the UT-GBS and SAOZ in Vanscoy on August 28, 2004. Intensities are calculated by dividing the intensity at 450 nm by the exposure time of the measurement and are referenced to the intensity at 450 nm (in counts per second) at SZA=60° in the morning.

have agreed with the UT-GBS measurement. Since the lifetime of NO_x is several days, the decrease in NO_2 after the peak is most likely due to advection of less-NO_2-rich air masses as the thunderstorm passed over Vanscoy, and not to the decay of NO_2.

The increase in ozone is consistent with similar observations of ozone during thick cloud events in England, France, Sweden, and the tropical Atlantic (Erle et al., 1995; Wagner et al., 1998; Pfeilsticker et al., 1999a; Winterrath et al., 1999). The increase in NO_2 is roughly double that observed by Langford et al. (2004) during a thunderstorm in Colorado, though less than the 35-fold increase seen by Winterrath et al. (1999). The observed enhancements in ozone and part of the enhancements in NO_2 are caused by increased path length through the atmosphere. In the case of NO_2, the increase is also partly due to lightning-produced NO_x.

Pfeilsticker et al. (1998) describe two processes that combine to increase the path length, or air mass factor, in the presence of thick clouds. The “ping-pong” effect occurs when light is multiply reflected between layers of clouds. Photon diffusion inside a thick cloud also increases the path length. Other processes that could account for the enhanced ozone column include transport, in-cloud production, convection, transport from the stratosphere, and reaction with NO (Winterrath et al., 1999). To verify the influence of multiple scattering, the ratios of ozone and NO_2 to O_4 are examined. O_4 concentrations are related to concentrations of oxygen, and in the absence of an increase in the oxygen vertical column, O_4 vertical columns are expected to be constant (e.g., Wagner et al., 2002). A maximum in O_4 as seen in Figure 5.4(c) is evidence of multiple scattering through the atmosphere, in this case due to the thick clouds associated with the thunderstorm. O_4 DSCD measurements are an established method of inferring the path length through the atmosphere in the presence of clouds (Erle et al., 1995; Wagner et al., 1998, 2002). Figure 5.5 shows the ratios of ozone and NO_2 to O_4 for the afternoon of August 28. The O_3 to O_4 ratio is fairly constant until the start of twilight, indicating that the excess ozone is a result of increased path length through the clouds. In the case of NO_2 there is a clear maximum in the ratio at 77°, indicating additional NO_2 in the atmosphere, which is attributed here to lightning.

5.2.3 Derivation of Lightning-Produced NO_2

Two new methods have been used to separate the observed enhancement of the differential slant column of NO_2 into a portion due to path-enhancement and a portion due to lightning production. These methods, as well as the conversion of the lightning-produced DSCDs into VCDs are discussed in this section.

Method One: Ratios to O_4

The behaviour of the NO_2/O_4 ratio is fairly consistent between clear-sky days, however it can vary significantly between cloudy days, due to varying cloud cover. The ratio is also

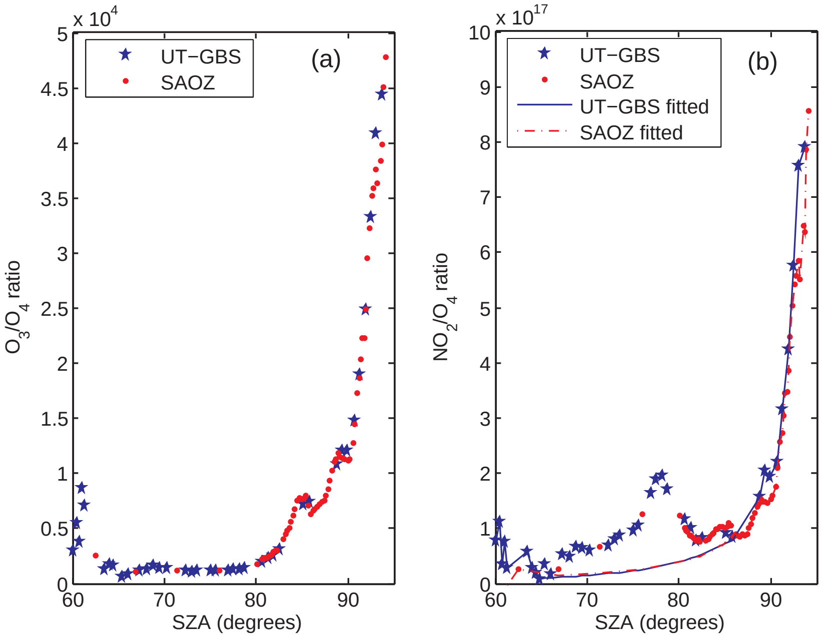

Figure 5.5: (a) Measured O_3/O_4 DSCD ratios, and (b) measured and fitted NO_2/O_4 DSCD ratios for the afternoon of August 28 in Vanscoy. The measured value of the ratio is plotted before and after the peak (before 65° and after 82°) in the NO_2/O_4 ratio (see text).

strongly dependent on the vertical profile of NO_2. It is therefore difficult to predict what the NO_2/O_4 ratio would have been on August 28 if no NO_2 were formed by lightning. However, on other days of the campaign, the ratio increases exponentially with solar zenith angle. To estimate what the NO_2 to O_4 ratio would have been with no lightning-produced NO_2, two independent exponential fits were made to the observed NO_2/O_4 ratios for the SAOZ and the UT-GBS, omitting the points between 65° and 82°, which correspond to the beginning and end of the observed maximum in the ratio. These fits for both the instruments are shown in Figure 5.5(b), along with the measured value of the ratio, which is used before and after the peak (before 65° and after 82°). From these fitted values of the NO_2/O_4 ratio during the storm, an estimate of the portion of the NO_2 differential slant column due to the enhanced path length can be derived:

$$DSCD'_{NO_2,PE}(SZA) = \left[\frac{DSCD_{NO_2}}{DSCD_{O_4}}(SZA)\right]_{\text{fit}} \times DSCD'_{O_4,meas}(SZA). \tag{5.1}$$

$DSCD'_{NO_2,\mathrm{PE}}$ is the path-enhanced NO_2, the subscript *"fit"* indicates the fitted NO_2/O_4 ratio, and $DSCD'_{O_4,\mathrm{meas}}$ is the measured O_4 column. This relationship is only valid if the vertical profiles of O_4 and NO_2 do not change. To find the portion of the observed enhanced NO_2 DSCD that is due to path enhancement, the assumption is made that the vertical profile does not change. Any change in profile is therefore attributed to the lightning-produced NO_2. The resulting NO_2 DSCDs are shown in Figure 5.6(a). The difference between the observed NO_2 differential slant column and the differential slant column calculated from the interpolated NO_2/O_4 ratio is the slant column of NO_2 attributed to production by lightning, shown in Figure 5.6(b). The results from both the UT-GBS and SAOZ are similar.

Method Two: Air Mass Factors

A second method of deriving the slant column of NO_2 caused by path enhancement is to use the measurements of O_4 to derive the enhanced air mass factor, or path length, for O_4 and NO_2. Generally, measured differential slant column densities of both species are related to the air mass factor by Equation 3.9. With no path enhancement, the afternoon O_4 DSCDs would follow the same trend as the morning DSCDs, increasing with SZA. Assuming no change in the VCD, the path-enhanced DSCD′ will be related to the enhanced AMF′ by:

$$DSCD'(SZA) = VCD \times AMF'(SZA) - RCD \tag{5.2}$$

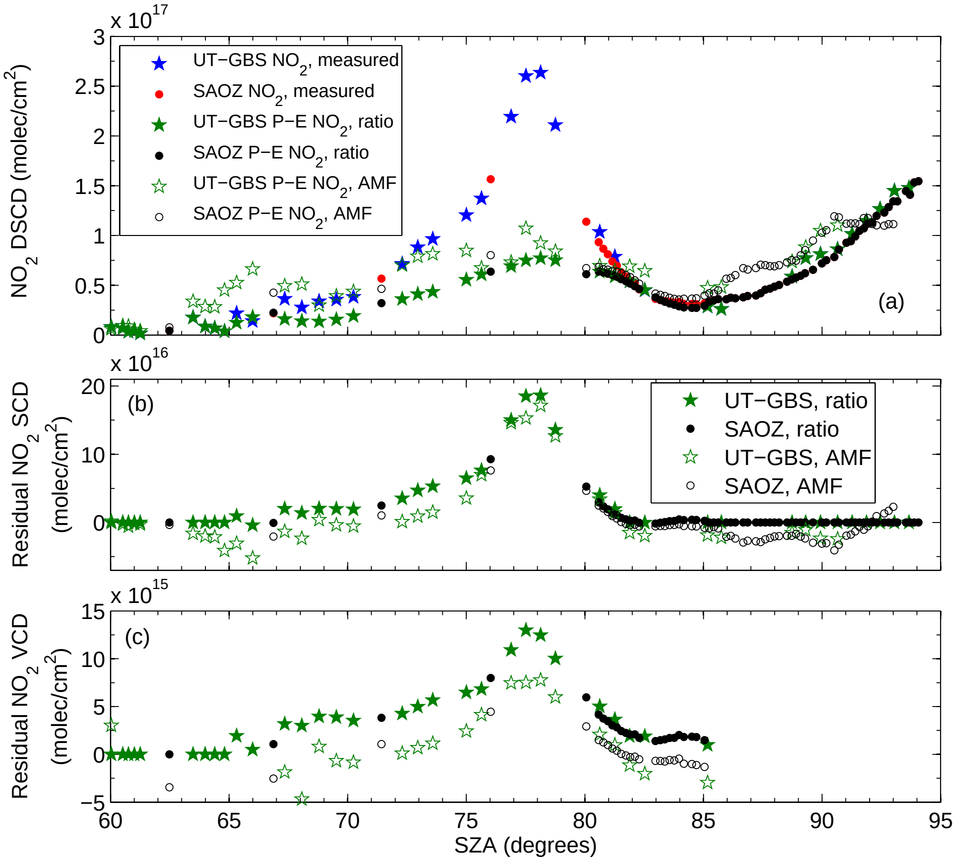

Figure 5.6: (a) Measured total NO_2 DSCDs as well as the derived contribution from path-enhancement (P-E) for methods one (ratios to O_4) and two (derived AMFs) discussed in the text. (b) Residual NO_2 SCDs attributed to lightning. (c) Lightning-produced NO_2 VCDs calculated from the residual in (b) and Equation 5.8.

where the primes indicate path enhancement. The enhanced AMF′ can be found by combining Equations 3.9 and 5.2:

$$AMF'(SZA) = AMF(SZA)\frac{DSCD'(SZA) + RCD}{DSCD(SZA) + RCD}. \tag{5.3}$$

The O_4 non-path-enhanced AMFs were calculated using the SCIATRAN radiative transfer model (Rozanov et al., 2005). NO_2 AMFs were calculated with the radiative transfer model of McLinden et al. (2002) initialized with temperature, pressure, and ozone profiles taken from the average of all ozonesondes launched during the campaign and a climato-

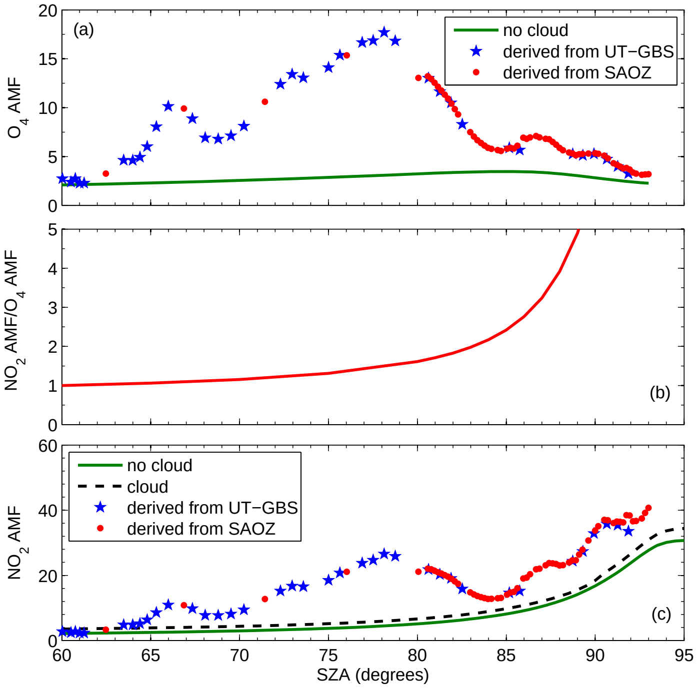

Figure 5.7: (a) O_4 air mass factors from SCIATRAN and derived from the measurements using Equation 5.3. (b) Ratio of NO_2-to-O_4 AMFs calculated using the radiative transfer models. (c) Same as (a), but for NO_2 and using Equation 5.4. Also shown is the AMF calculated for the case of a cloud of OD=70 from 1-10 km using a radiative transfer model (McLinden et al., 2002).

logical NO_2 profile. The RCDs for O_4 and NO_2 were found from Langley plots, of DSCD versus AMF, for the morning of August 28. Measured O_4 differential slant columns from the morning and afternoon were used as DSCD and DSCD′, respectively, in Equation 5.3. Figure 5.7(a) shows the enhanced O_4 AMF′ for both instruments, derived using Equation 5.3.

The AMFs for O_4 and NO_2 differ since they are retrieved in different wavelength regions and have different vertical profiles. In the radiative transfer model, the O_4 AMF is calculated at 477 nm, while the NO_2 AMF is calculated at 425 nm. O_4 is primarily a tropospheric species, and its AMF peaks at about 85°. NO_2 is primarily a stratospheric species, and its AMF peaks at about 94°. When the Sun is lower in the sky than 85°, the NO_2 AMF increases while the O_4 AMF decreases, which leads to the rapid increase in the ratio of the two modeled AMFs seen in Figure 5.7(b). The ratio of the two AMFs is a maximum for the cloud-free scenario. Without more detailed observations of the clouds and vertical profiles of the two species, it is difficult to predict what the ratio of the AMFs would have been during the storm, and even more difficult to quantify how it would change with SZA. Given this, a maximum NO_2 AMF can be found by assuming there are no clouds during the storm. Although this assumption is certainly false, it allows the calculation of an upper limit on the NO_2 due to path enhancement, and a lower limit on the NO_2 produced by lightning. Taking this cloud-free ratio, the estimated NO_2 AMF′ is found from:

$$AMF'_{NO_2}(SZA) = AMF'_{O_4}(SZA)\frac{AMF_{NO_2}(SZA)}{AMF_{O_4}(SZA)}. \tag{5.4}$$

Figure 5.7(c) shows this estimated NO_2 AMF for each instrument, as well as the calculated AMFs for cloudless and cloudy scenarios, calculated with the radiative transfer model (McLinden et al., 2002) assuming no clouds and assuming a thick cumulus cloud near the surface, of optical depth 70, extending between 1 and 10 km (e.g., Bassford et al., 2001). The same profiles were used to initialize the model in both the cloud-free and cloud cases.

Figure 5.6(a) shows the resulting upper limit for NO_2 DSCDs′ due to path enhancement calculated from Equation 5.3. The NO_2 differential slant columns measured in the morning were used as DSCDs, increased to account for the expected increase due to the diurnal variation of NO_2. The increase was calculated using a linear fit to the ratio of the NO_2 DSCDs observed in the afternoon to those observed in the morning, excluding the DSCDs measured during the thunderstorm. The upper limit of NO_2 DSCDs from both SAOZ and UT-GBS is similar. Prior to 67°, the upper limit exceeds the measured NO_2 DSCD, an indication that an assumption made in calculating the NO_2 AMFs is incorrect: most likely the ratio of the air mass factors is smaller than assumed. For all

SZAs the DSCDs from the AMF method are larger than those from the ratio method, which is expected given the use of the clear-sky ratio of AMFs.

Conversion to Vertical Column Densities

The difference between the measured NO_2 DSCD and the derived path-enhanced NO_2 DSCD′ in Figure 5.6(a) is the amount of NO_2 produced by lightning, which is shown in Figure 5.6(b). However, these residuals are slant columns: the above methods have calculated the path-enhanced NO_2 assuming no change in the vertical column. Lightning produces NO_2 beneath the cloud through cloud-to-ground flashes, which is transported into the cloud through the strong vertical updrafts present during thunderstorms. NO_2 is also produced within the cloud by intra-cloud flashes (Fehr et al., 2004). Therefore the path length through the lightning-produced NO_2 will also be increased by multiple scattering within the cloud.

The AMF will also be affected by the change in the NO_2 profile due to lightning-produced NO_2. The increase in NO_2 is expected to be on the order of 10% in the troposphere (Winterrath et al., 1999): such an increase causes a 0-10% change in the AMF. The NO_2 path-enhanced AMF′ calculated in the previous section at minimum doubles the AMF from the clear sky scenario. The AMF through the lightning-produced NO_2 can therefore be approximated by the AMF′ derived in the previous section. The observed DSCD will then be related to the enhanced VCD by the following equation:

$$DSCD_{obs} = VCD_{obs} \times AMF' - RCD, \tag{5.5}$$

where the subscript *obs* indicates the observed DSCD and VCD. This equation, together with Equation 5.2, can be expanded to consider the contributions from the stratosphere and troposphere. Since the path and lightning-produced NO_2 enhancements are confined to the troposphere, the stratospheric VCD and AMF are unchanged:

$$DSCD' = VCD_{strat} \times AMF_{strat} + VCD_{trop} \times AMF'_{trop} - RCD \tag{5.6}$$

$$DSCD_{obs} = VCD_{strat} \times AMF_{strat} + VCD_{obs,trop} \times AMF'_{trop} - RCD. \tag{5.7}$$

The subscripts *trop* and *strat* refer to the tropospheric and stratospheric contributions. Solving these two equations for the change in the NO_2 VCD due to production by lightning yields:

$$\Delta VCD_{lightning} = VCD_{obs,trop} - VCD_{trop} = \frac{DSCD_{obs} - DSCD'}{AMF'_{trop}}. \tag{5.8}$$

The enhanced tropospheric AMF is required to solve Equation 5.8 for the VCD of NO_2 produced by lightning. Since O_4 is primarily a tropospheric species, the AMF′ derived in the previous section approximates the AMF'_{trop} required. Since the AMF derived in method two is used to convert the DSCDs found using both methods, the two methods are no longer completely independent. The ratio method represents the best guess of the NO_2 ΔVCDs, while the AMF method produces an absolute minimum. The resulting ΔVCDs, shown in Figure 5.6(c), are attributed to lightning. Only values below 86° are shown, outside this range the difference in the numerator of Equation 5.8 is small, due to the fact the slant column of lightning-produced NO_2 is small or non-existent before and after the thunderstorm passes over Vanscoy. Since the AMF′ is a maximum of the enhanced AMF, the ΔVCDs are a minimum amount of NO_2 produced by lightning.

No attempt has been made to account for horizontal variations in the NO_2 concentrations. In addition, it has been implicitly assumed that the transport of NO_2 produced by lightning outside the thunderstorm cells is approximately balanced by the transport of NO_2 from other thunderstorms into the cells. Although this assumption is most likely false, the assumptions involved in calculating a correction term for the effects of transport would introduce further error into the NO_2 VCD. Instead, a 20% error is attributed to the VCDs in addition to the errors in the DSCDs as a result of these processes, and the uncertainties in calculating the AMF.

5.2.4 Flash Production Amount

Taking the lightning-produced VCDs derived in Section 5.2.3, the amount of NO_2 produced per CG flash can be calculated. Using the ratio method, the amount of excess NO_2 VCD, found by integrating under the curves between 64° and 86° for method one in Figure 5.6(c) is $(9.84\pm1.81)\times10^{16}$ molecules NO_2/cm^2 for the UT-GBS and $(7.73\pm1.42)\times10^{16}$ molecules NO_2/cm^2 for SAOZ. The error estimates on the total excess NO_2 are the root-sum-square of the DSCD error discussed in Chapter 2, the estimated errors in the methods used to obtain the lightning-produced NO_2 ΔVCD (20%) and the estimated integration error (10%). From Section 5.2.1, the size of the heavy-precipitation cell is $(61\pm10)\,km^2$. Using the corrected number of CG lightning flashes during the storm from the CLDN (565±59 flashes), the storm-averaged NO_2 production per CG flash of lightning can be calculated from:

$$NO_2 \text{ produced } = \frac{E \times A}{F} \tag{5.9}$$

where E is the residual NO_2 VCD derived from measurements, A is the area of the storm, and F is the number of lightning flashes (Noxon, 1976). The production amounts from this method are $(1.06\pm0.34)\times10^{26}$ molecules NO_2/CG flash from the UT-GBS and $(0.83\pm0.27)\times10^{26}$ molecules NO_2/CG flash from SAOZ. The values derived from both instruments agree within error bars.

Using the air mass factor method, the UT-GBS observed $(4.00\pm0.74)\times10^{16}$ excess molecules NO_2/cm^2 and SAOZ observed $(3.99\pm0.73)\times10^{16}$ excess molecules NO_2/cm^2. The minimum production amount is found to be $(0.43\pm0.14)\times10^{26}$ molecules NO_2/CG flash from both the UT-GBS and SAOZ. The two methods do not agree within their combined error bars. However, it should be noted that the values calculated are slightly different quantities. The values found using the air mass factor method of limiting the NO_2 due to lightning production are minimum values for the amount of NO_2 production by lightning, whereas the values found using the NO_2 to O_4 ratio are best estimates of the actual NO_2 production amount. For the ratio method, the production amounts calculated from the SAOZ measurements are slightly lower. This is a result of the Gaussian fit to SAOZ not capturing the peak of NO_2 for this method.

Noxon (1976) estimated an order of magnitude value of 10^{26} molecules NO_2/CG flash based on DOAS differential slant column measurements of NO_2 made during a thunderstorm in Colorado. Franzblau and Popp (1989) derived a rate of $(7\pm3)\times10^{26}$ molecules NO_2/CG flash using a similar method in New Mexico. Langford et al. (2004) measured $(5.8\pm2.9)\times10^{26}$ molecules NO_2/CG flash from a zenith-viewing UV-Visible spectrometer. The values calculated here are significantly smaller than the latter two estimates.

Ridley et al. (2005) suggest that the production of NO_2 from intra-cloud flashes is of the same order of magnitude as from cloud-to-ground flashes. No correction has been made to the flash frequency observed by the CLDN to account for intra-cloud flashes, and these flashes are not considered when applying Equation 5.9. As a result, the NO_2 flash production amounts derived here, and the previously reported values cited above, are for CG flashes only. Correcting for the detection efficiency of the CLDN, 750–3000 IC flashes occurred during the thunderstorm. The range of NO_2 produced per flash, from both methods and both instruments, is $(0.07\text{–}0.17)\times10^{26}$ molecules NO_2/(CG+IC) flash for 3000 IC flashes and $(0.19\text{–}0.46)\times10^{26}$ molecules NO_2/(CG+IC) flash for 750 IC flashes.

Schumann and Huntrieser (2007) compiled a list of 40 estimates of the NO_x production amount per flash (both CG and IC) found from theoretical calculations and ground, aircraft, and satellite-based observations. These values range between 0.04×10^{26}

molecules NO_x/flash to 6.7×10^{26} molecules NO_x/flash. Based on this list, Schumann and Huntrieser (2007) conclude that the best estimate of the NO_x produced per flash is 1.5×10^{26} molecules NO_x/flash, with a range of (0.2–4)×10^{26} molecules NO_x/flash. This result is not directly comparable with the NO_2 per flash amount derived in this work. The ratio of NO_2 to NO_x during a thunderstorm is uncertain and depends on the temperature, ozone profile, and actinic flux, and therefore altitude. Ridley et al. (1996), from in-situ aircraft measurements of NO and NO_2 during thunderstorms in New Mexico, find a ratio of NO_2 to NO_x of 14–20%. Applying the mean of this ratio (17%) to the range of production amounts per CG and IC flash derived here gives (0.41–2.71)×10^{26} molecules NO_x/flash (the range includes both instruments and both methods). Using the best estimate from the ratio method gives a range of (0.99–2.71)×10^{26} molecules NO_x/flash for the UT-GBS and (0.78–2.11)×10^{26} molecules NO_x/flash for SAOZ, where the lower estimates are for 3000 IC flashes and the upper estimates are for 750 IC flashes. These estimates agree with the lower values suggested by Schumann and Huntrieser (2007). It should be noted that the NO_2 to NO_x ratio is uncertain, and the value used here is an estimate. In addition, the values calculated here are minimum production amounts due to the use of the ratio of clear sky AMFs in deriving the path-enhanced AMF′.

The molecules NO_x per flash amounts can be converted to a global production rate of NO_x using the flash rate of 44 flashes/s observed by the Optical Transient Detector (OTD) satellite (Christian et al., 2003). The flash production amounts derived here yield a range of 1.3–8.7 Tg N/year, while the best estimate amounts (from the ratio method) yield a range of 6.1–8.7 Tg N/year. The ranges cover the values derived from both instruments and for both 750 and 3000 IC flashes. The estimates here are consistent with the current best estimate of the global production rate of lightning-produced NO_x, which is between 5 and 6 Tg N/year (Martin et al., 2007; Schumann and Huntrieser, 2007).

5.3 May 17, 2006

5.3.1 Thunderstorm

Thunderstorms were observed at Pearson International Airport, 20 km west of the Toronto Atmospheric Observatory between 15:00 and 17:00 LT (19:00 – 21:00 UTC) in the afternoon of May 17, 2006. Figure 5.8 shows the precipitation rate at 1.5 km altitude calculated from the EC radar at King City, Ontario, located 45 km to the north of TAO. Several cells of heavy rain (orange, red, and purple) form to the north-west of Toronto and travel to the south-east. The maximum total area of the storm cells is (38±10) km^2, using the radar reflectivity greater than 40 dBZ (MacKeen et al., 1999). Figure 5.9 shows the lightning flash data observed by the CLDN between 14:00 and 20:00 LT (19:00 and 24:00 UTC) over southern Ontario. The total number of flashes that occur upwind of TAO is (1151±115). Approximately half of the observed flashes, 550, are CG flashes. Correcting for the detection efficiency of the network, there are (612±61) CG flashes during the thunderstorm. Correcting the remaining IC flashes for the 4–5% efficiency of the CLDN in southern Ontario yields 1336±133 IC flashes.

5.3.2 Differential Slant Column Densities

Elevated DSCDs of ozone, O_4, and NO_2 were observed by the UT-GBS during the thunderstorm. Figure 5.10 shows the DSCDs and intensities measured on May 17. The intensities are calculated as in Section 5.2, and scaled to the intensity measured at SZA=33.9° in the morning. The UT-GBS does not make measurements when the temperature of the CCD is above 203 K, since this indicates that the ambient temperature of its operating environment is above 30°C, outside of the range in which the spectrometer is designed to work. As the storm began, it was too warm inside the instrument's box for the UT-GBS to measure. As a result, the UT-GBS was not measuring at the beginning of the thunderstorm. The air temperature dropped when the storm began, and the UT-GBS began

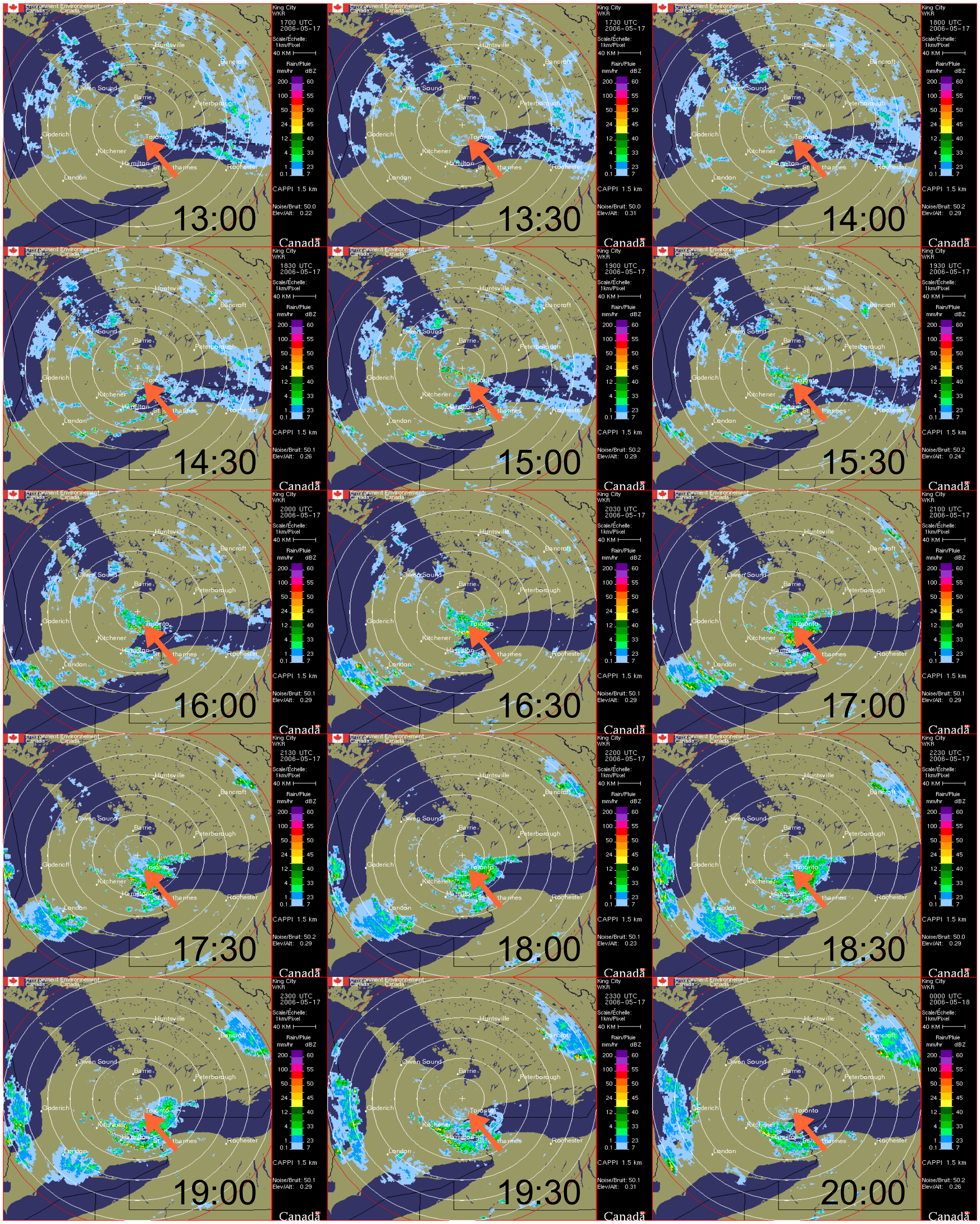

Figure 5.8: Precipitation rates at 1.5 km between 13:00 and 20:00 LT (17:00 and 24:00 UTC) calculated from the Environment Canada radar measurements in King City, Ontario on May 17, 2006. The local time is given in the bottom right corner of the images. The orange arrow indicates Toronto.

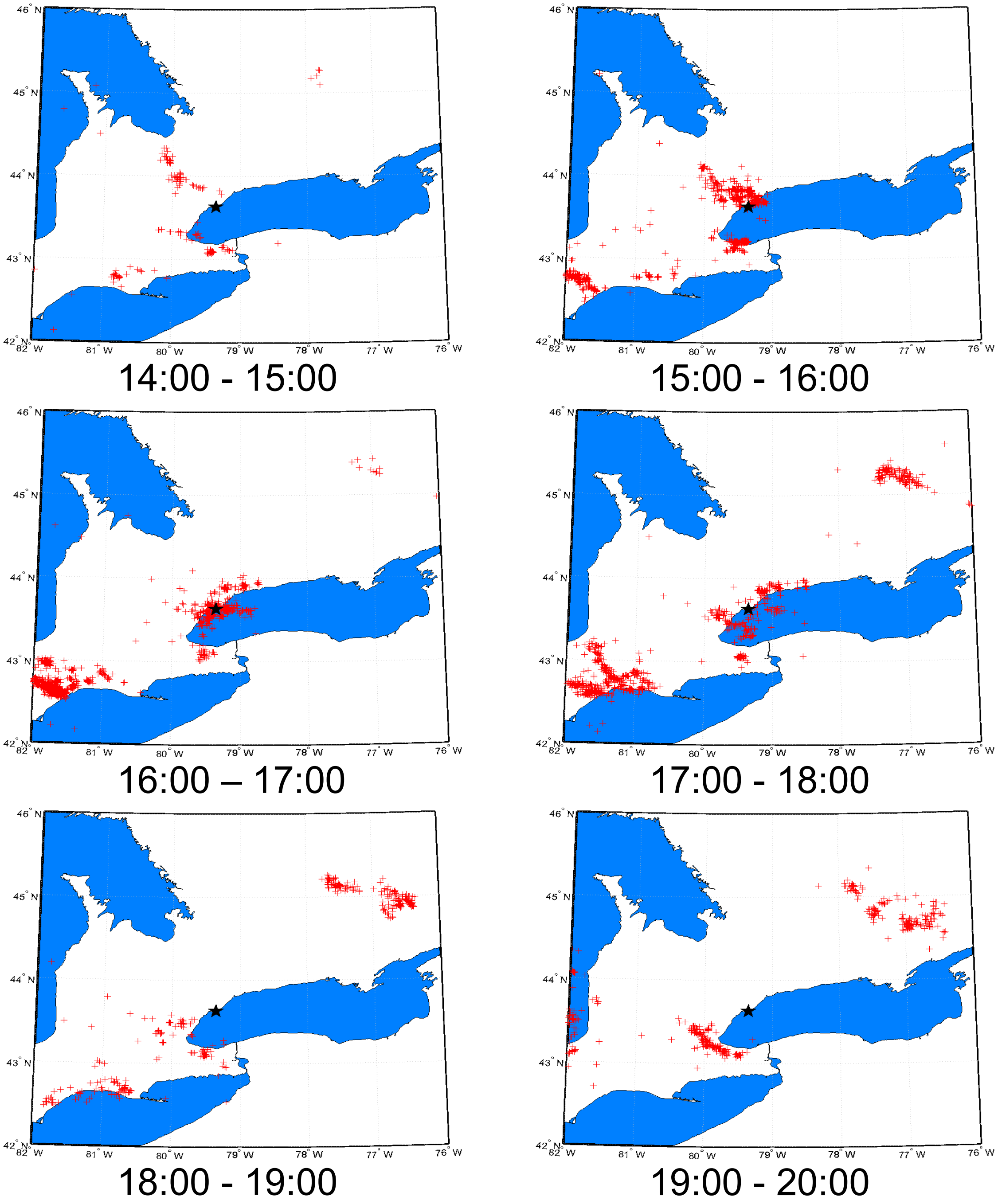

14:00 - 15:00

15:00 - 16:00

16:00 – 17:00

17:00 - 18:00

18:00 - 19:00

19:00 - 20:00

Figure 5.9: Lightning flash data from the CLDN for Southern Ontario for hourly periods between 14:00 and 20:00 LT (19:00 and 24:00 UTC). Each plus (+) represents an individual lightning flash. The local time is shown beneath the images. The location of Toronto is indicated by the black star.

measuring shortly before the peak in the observed gases.

The increases in the DSCDs measured in the afternoon are much larger than the increases seen during MANTRA. For ozone, the columns are 18 times larger during the storm than in the morning. For NO_2, the increase is 120 times. This thunderstorm took place at smaller SZAs than the storm observed during MANTRA: between 45° and 77° versus between 63° and 90°. Figure 5.11(a) and (c) show the air mass factors calculated from a radiative transfer model (McLinden et al., 2002) for ozone and NO_2 with and without a cloud of optical depth 70 extending from 1 to 10 km. The absolute value of the increase in AMF is similar to that calculated for MANTRA (Figure 5.7), however at these small SZAs the increase is a larger percentage increase of the AMF. For ozone, at 77°, the peak of the DSCD increase in Vanscoy, the modeled cloud increases the AMF by 4.4, or 105%. In Toronto, at 47°, the peak of the DSCD increase, the modeled AMF increases by 4.4, or 272%. As a result, larger column increases are seen during the Toronto storm than during the MANTRA storm.

Winterrath et al. (1999) observed a doubling of the ozone DSCDs and a 35-fold increase of the NO_2 DSCDs during a thunderstorm in southern France. This storm occurred between 60° and 85°, with a peak at 76°, more in line with the storm observed during MANTRA. Langford et al. (2004) observed a ten-fold increase of the NO_2 DSCDs during a thunderstorm in Colorado. The storm occurred between 56° and 66°, with a peak at 60°, also more in line with the storm observed during MANTRA.

5.3.3 Derivation of Lightning-Produced NO_2

The methods developed in Section 5.2 have been applied to the differential slant columns observed during this thunderstorm as well. Figure 5.12 shows the O_3/O_4 and NO_2/O_4 ratios observed by the UT-GBS during the Toronto storm. The O_3/O_4 ratio is fairly constant through the thunderstorm, indicating that the majority of the ozone enhancement is due to path enhancement. The NO_2/O_4 ratio shows a distinct peak at 47°, and is

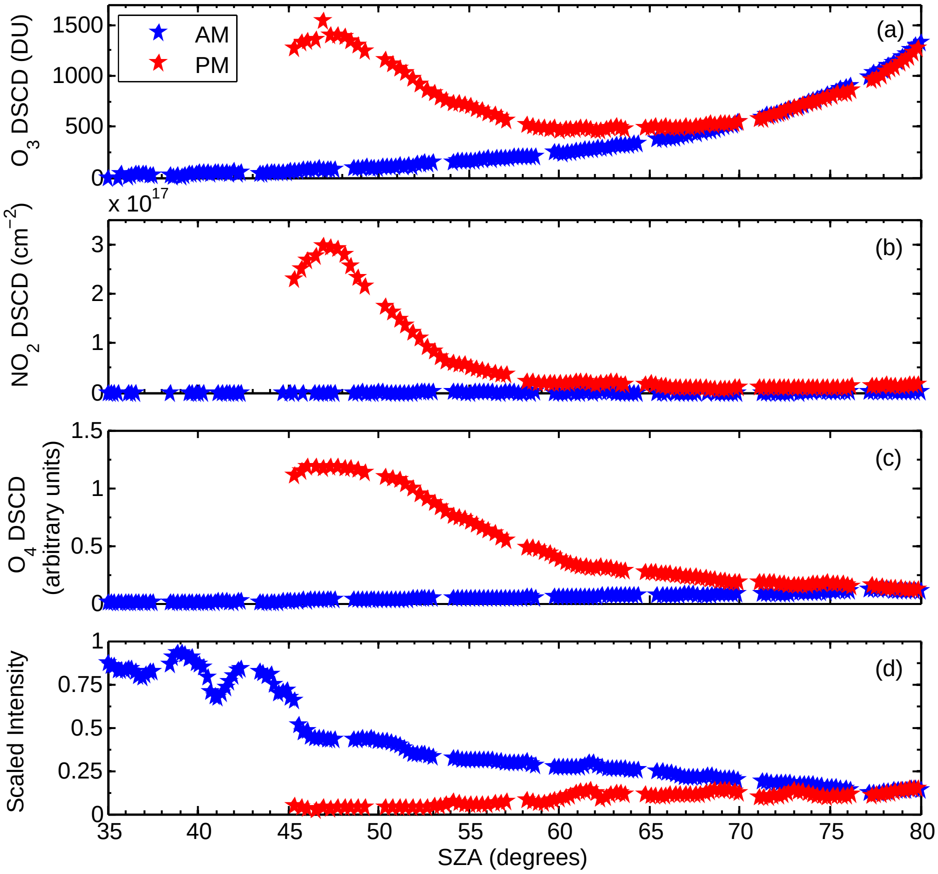

Figure 5.10: (a) Ozone, (b) NO_2, and (c) O_4 differential slant column densities, and (d) intensities measured by the UT-GBS on May 17, 2006 in Toronto. Intensities are calculated by dividing the intensity at 450 nm by the exposure time of the measurement and are referenced to the intensity at 450 nm (in counts per second) at SZA=33.9° in the morning.

elevated throughout the storm, indicating that there must be additional NO_2 produced during the storm. An exponential fit was made to this ratio, using SZAs higher than 66°, to approximate what the ratio would have been during the storm in the absence of lightning-produced NO_2. This fit is shown in Figure 5.12(b). The measured value of the ratio is used for SZAs larger than 66°. An estimate of the path-enhanced DSCD′s is found using the measured O_4 DSCDs and Equation 5.1. These estimated NO_2 DSCDs are shown in Figure 5.13(a).

The enhanced NO_2 AMF′s derived using method two (Section 5.2.3) are shown in Figure 5.11. The O_4 AMF′ is increased to a maximum of approximately 19 from 1.6,

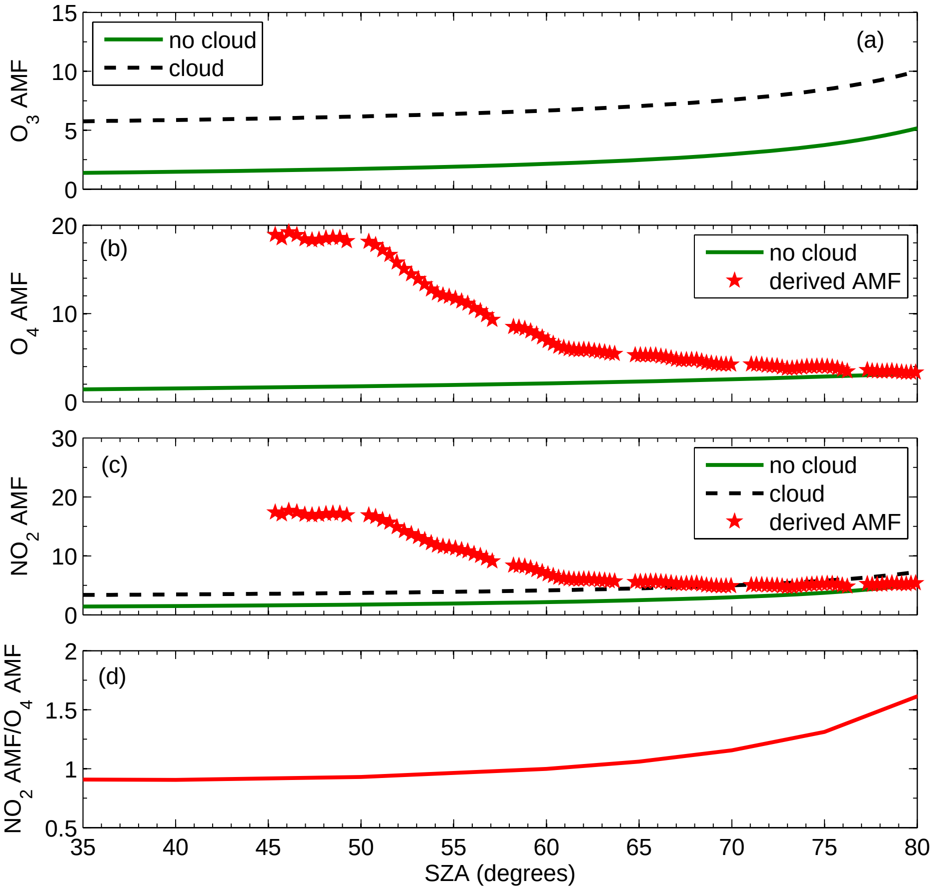

Figure 5.11: (a) Ozone AMFs calculated for the case of no clouds and for a cloud of OD=70 from 1–10 km using a radiative transfer model (McLinden et al., 2002). (b) O_4 AMFs from SCIATRAN and derived from the measurements using Equation 5.3. (c) Same as (a), but for NO_2 and also showing the calculated AMFs derived using Equation 5.4. (d) Ratio of modeled NO_2-to-O_4 AMFs.

while the NO_2 AMF is increased to a maximum of 18 from 1.6. The enhancements seen in MANTRA were from 3 to 18 and from 4.5 to 27 for O_4 and NO_2, respectively. This accounts for the much larger relative increases in the DSCDs seen in Toronto versus those seen during MANTRA. The path-enhanced DSCDs derived from this method are shown in Figure 5.13(a). For all SZAs, the path-enhanced DSCD′s derived from the ratio method are much smaller than those derived from the AMF method. This is an indication that the NO_2/O_4 ratio derived using method one is too large. This is most likely a result of the UT-GBS not measuring during the beginning of the storm, and so

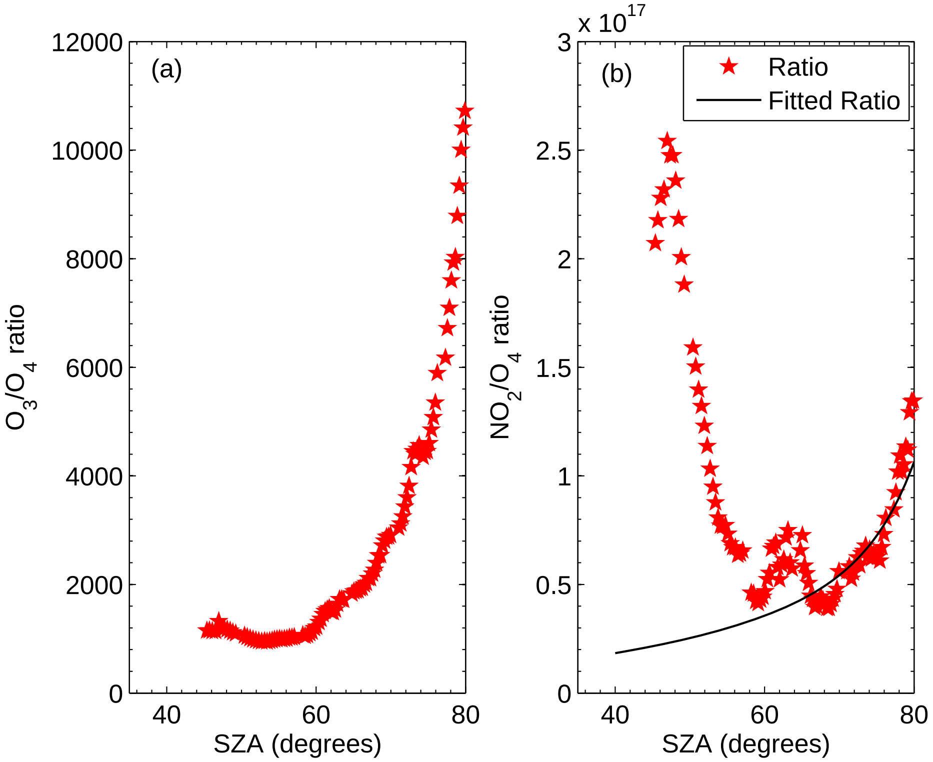

Figure 5.12: (a) Measured O_3/O_4 ratios, and (b) measured and fitted NO_2 ratios for the afternoon of May 17, 2006 in Toronto.

the initial value of the ratio is unknown.

Figure 5.13(b) shows the difference between the observed NO_2 DSCD′s and the path-enhanced NO_2 DSCDs. The values from both methods are similar to those seen during MANTRA. Figure 5.13(c) shows the lightning-produced NO_2 ΔVCDs, calculated from the residuals in Figure 5.13(b) and Equation 5.8. The maximum values of the VCDs are similar to those seen during MANTRA.

5.3.4 Flash Production Amount

The amount of excess NO_2, found by integrating under the curves in Figure 5.13(c), is $(1.03\pm0.31)\times10^{17}$ molecules NO_2/cm^2 for the ratio method and $(0.44\pm0.13)\times10^{17}$ molecules NO_2/cm^2 for the AMF method. A Gaussian is fit to the ΔVCDs to account

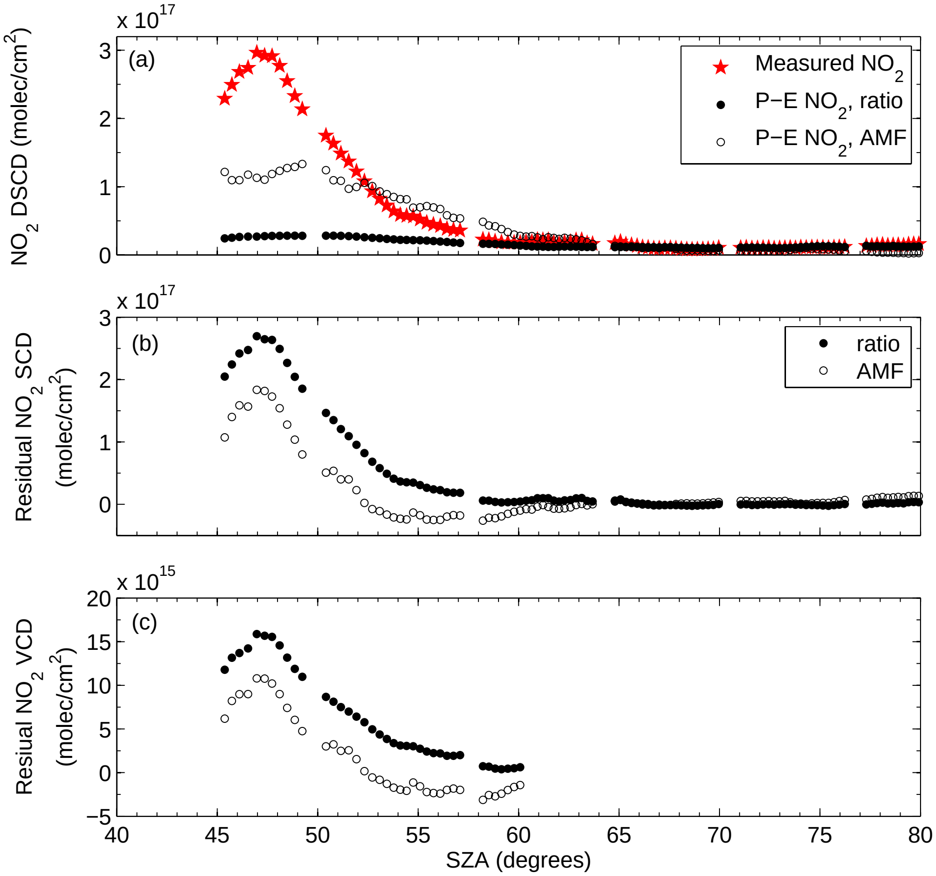

Figure 5.13: (a) Measured total NO_2 DSCDs as well the derived contribution from path-enhancement (P-E) for methods one (ratios to O_4) and two (derived AMFs) discussed in the text. (b) Residual NO_2 SCDs attributed to lightning. (c) Lightning-produced NO_2 VCDs calculated from the residual in (b) and Equation 5.8.

for the SZAs smaller than 45°. From Section 5.3.1, the maximum area of the storm was (38±10) km^2, with 612±61 CG flashes. From Equation 5.9, the amount of excess NO_2 produced by lightning is $(0.64\pm0.21)\times10^{26}$ molecules NO_2/CG flash from the ratio method and $(0.27\pm0.09)\times10^{26}$ molecules NO_2/CG flash from the AMF method.

These values agree within error with the values found using the same methods from the UT-GBS and SAOZ in MANTRA. Table 5.1 summarizes the CG flash production amounts found in this work. The values here are smaller than those found during MANTRA. The thunderstorm that took place during MANTRA had a greater number of flashes, covered a greater area, and had a higher radar reflectivity (indicating hail as well

Table 5.1: Lightning-produced NO_2 flash production amounts (FPA) found in this work. All values are in 10^{26}molecules NO_2/flash. The range of estimates for the FPA per (CG + IC) flash for the MANTRA thunderstorm accounts for the 750–3000 IC flashes.

Campaign/Method	FPA per CG flash	FPA per (CG+IC) flash
MANTRA/UT-GBS ratio	1.06±0.34	0.17–0.46
MANTRA/UT-GBS AMF	0.43±0.14	0.07–0.19
MANTRA/SAOZ ratio	0.83±0.27	0.13–0.36
MANTRA/SAOZ AMF	0.43±0.14	0.07–0.19
Toronto/UT-GBS ratio	0.64±0.21	0.20±0.07
Toronto/UT-GBS AMF	0.27±0.09	0.09±0.02

as heavy rain) than the storm that took place in Toronto. The smaller flash production rates found in Toronto are most likely a result of the less energetic storm.

The detection efficiency for the CLDN for IC flashes in southern Ontario is 4–5% (Burrows et al., 2002). Correcting the 601±60 flashes for this detection efficiency yields 1336±133 flashes. Taking these flashes into account, the amount of NO_2 produced per flash would be $(0.20\pm0.07)\times10^{26}$ molecules NO_2/flash from the ratio method and $(0.09\pm0.02)\times10^{26}$ molecules NO_2/flash from the AMF method. Converting these amounts to NO_x per flash, using the mean NO_2 to NO_x ratio (17%) found by Ridley et al. (1996), yields a minimum of $(0.53\pm0.17)\times10^{26}$ molecules NO_x/flash from the AMF method and a best estimate of $(1.18\pm0.39)\times10^{26}$ molecules NO_x/flash from the ratio method, in agreement with the range found by Schumann and Huntrieser (2007). This implies an annual global production rate of lightning-produced NO_x of 1.7 Tg N/year from the AMF method and a best estimate of 3.8 Tg N/year from the ratio method. This is in agreement with the best estimate of 5–6 Tg N/year (Martin et al., 2007; Schumann and Huntrieser, 2007).

5.4 Summary

Elevated columns of ozone, O_4, and NO_2 were observed by both SAOZ and UT-GBS during a thunderstorm that occurred during the 2004 MANTRA campaign and by the UT-GBS in May 2006 in Toronto. In the case of ozone and O_4, the enhancement is most likely due to increased path length in and between clouds. In the case of NO_2, the enhancement is due to increased path length and the production of NO_x by lightning. The amount of NO_2 due to lightning has been calculated, using two new methods to estimate the excess NO_2 due to path enhancement within the cloud. Lightning flash data from the CLDN and radar data from nearby Environment Canada radar stations were used to determine the amount of NO_2 produced per lightning flash. For the MANTRA storm, production values in the range of $(0.41–2.71)\times10^{26}$ molecules NO_x/flash calculated from both instruments agree with the best estimate range found by Schumann and Huntrieser (2007). For the Toronto storm, production values of $(0.53\pm0.17)\times10^{26}$ and $(1.18\pm0.39)\times10^{26}$ molecules NO_x/flash were derived, and are in agreement with the values derived during MANTRA and by Schumann and Huntrieser (2007). These production amounts yield a global lightning-produced NO_x production rate of 1.3–8.7 Tg N/year for the MANTRA storm and 1.7–3.8 Tg N/year from the Toronto storm, in agreement with the current best estimate of 5–6 Tg N/year (Martin et al., 2007; Schumann and Huntrieser, 2007). Error estimates for the production amounts are approximately 32% of the derived values, due to the difficulties in accurately representing the area of the NO_2-producing thunderstorms, the transport of NO_2 into and out of the measured air masses, and the separation of the observed NO_2 into contributions from lightning and path enhancement.

Chapter 6

The Eureka Campaigns 2004-2007

Four Canadian Arctic ACE validation campaigns (the "Eureka campaigns") have been held during polar sunrise at PEARL (known as AStrO in 2004/2005), 15 km from Eureka, Nunavut (80°N, 86°W) from 2004 to 2007. Figure 6.1 shows the location of Eureka. This chapter discusses the ozone, NO_2, BrO, and OClO measurements from the UT-GBS and PEARL-GBS during the four campaigns. Comparisons between the UV-visible instruments that participated in the campaigns will be discussed in Chapter 7. The ozone and NO_2 results from 2004 to 2006, as well as the comparison of vertical column density retrieval methods, have been published in Fraser et al. (2008).

The PEARL-GBS was installed at PEARL in August 2006 and has since recorded spectra continuously, with the exception of during polar night (late-October to mid-February). The results of the first year of measurements with this instrument are also discussed in this chapter.

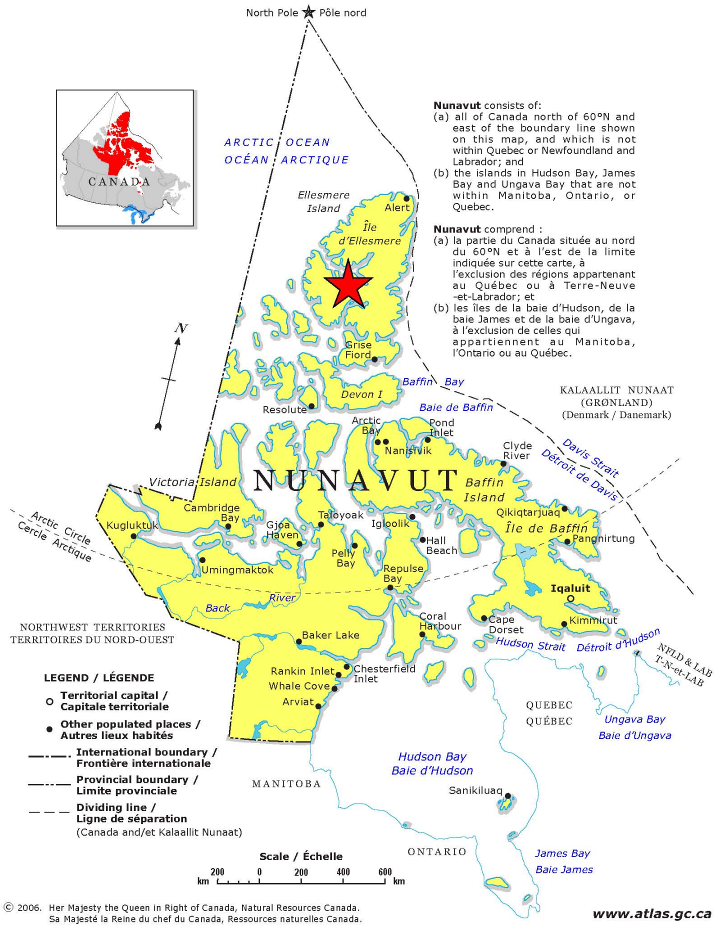

Figure 6.1: The red star indicates the location of Eureka, Nunavut, the site of the Canadian Arctic ACE validation campaigns. (Map ©Natural Resources Canada.)

6.1 Description of the Campaigns

6.1.1 2004

The 2004 Canadian Arctic ACE validation campaign took place from February 19 to April 15. Figure 6.2 shows the European Centre for Medium-Range Weather Forecasts (ECMWF) potential vorticity (PV) map at a potential temperature of 475 K ($\backsim$19 km) for selected days of the campaign. This level is in the lower stratosphere, where the peak in ozone mixing ratio is located. PV is a dynamical variable proportional to the inverse of the density of the atmosphere (ρ), the vertical gradient of the potential temperature

(θ), and the curl of the absolute wind velocity (known as the absolute vorticity, η) and is given by:

$$PV = \frac{1}{\rho}\eta\nabla\theta. \tag{6.1}$$

PV increases with latitude. The edge of the polar vortex is characterized by strong gradients in the PV, and so it is a useful quantity in determining the location of the vortex (Brasseur and Solomon, 2005). In Figure 6.2, high values of PV (red, yellow) indicate the polar vortex, while low values of PV (blue, green) are outside the vortex.

2004 was an unusual winter in the Arctic stratosphere, with a sudden stratospheric warming occurring in December 2003. The vortex began to recover in February, and reformed with a strong vortex in the middle and upper stratosphere. The vortex in the lower stratosphere did not recover substantially, as seen in Figure 6.2. The stratosphere did not undergo a final warming, breaking down the vortex, until late April (Manney et al., 2005, 2008). Eureka was inside the vortex at those altitudes where it had reformed. The vertical columns from the intensive phase of this campaign were discussed in Kerzenmacher et al. (2005).

6.1.2 2005

The 2005 Eureka campaign ran from February 18 to March 31. The 2005 Arctic winter was notable for having the lowest stratospheric temperatures on record. A major final warming of the stratosphere occurred on March 10 (Manney et al., 2008). Figure 6.3 shows ECMWF PV maps at 475 K for the campaign. Eureka was on the edge of the polar vortex until early March, when the vortex began to move away and break apart.

6.1.3 2006

The 2006 Eureka campaign took place from February 17 to March 31. 2006 was a warm winter in the polar stratosphere, with a sudden stratospheric warming occurring in

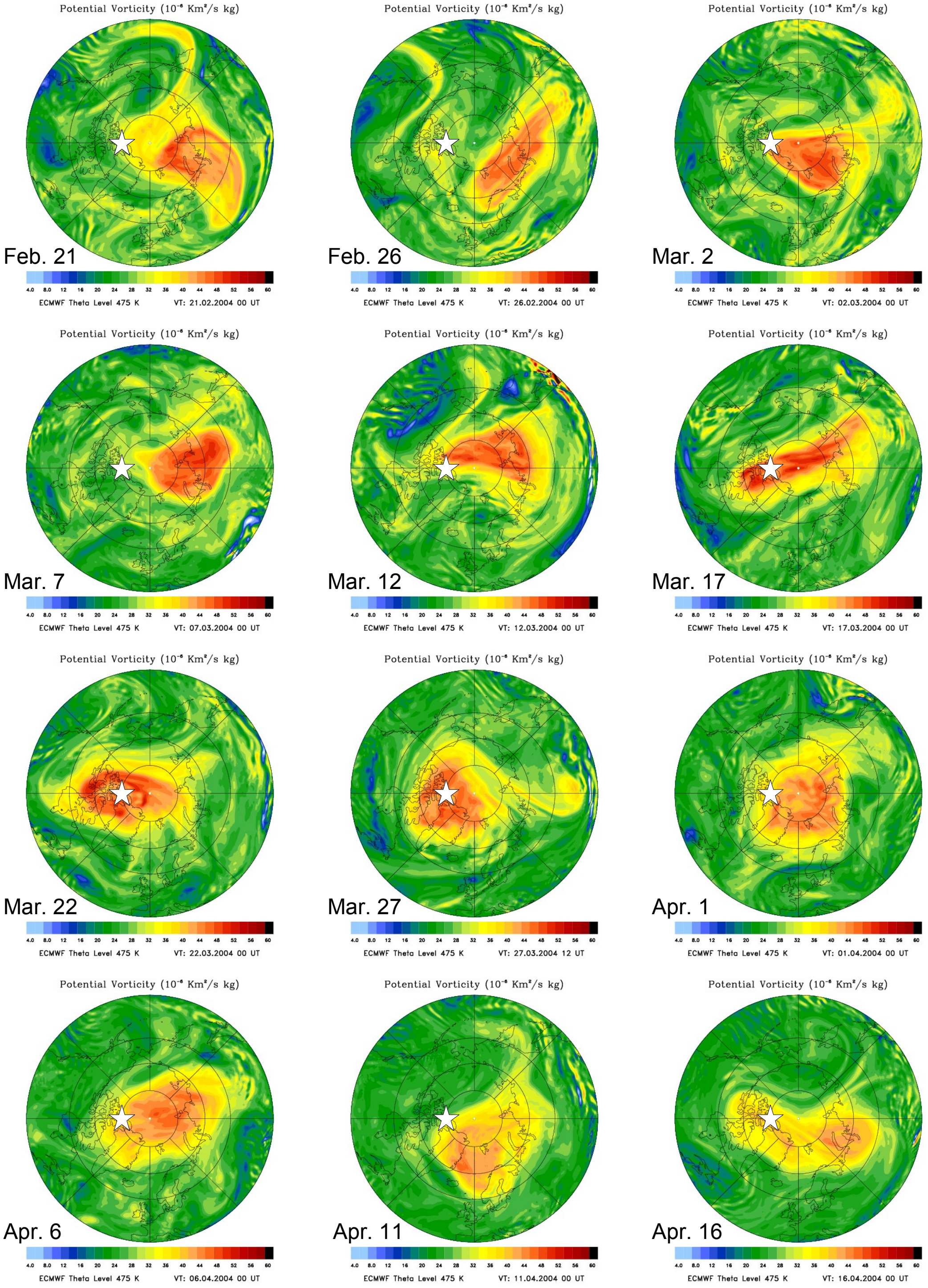

Figure 6.2: ECMWF potential vorticity on the 475 K potential temperature layer for 2004. The location of PEARL is indicated by the white star. The date of each map is indicated to the lower left of the map.

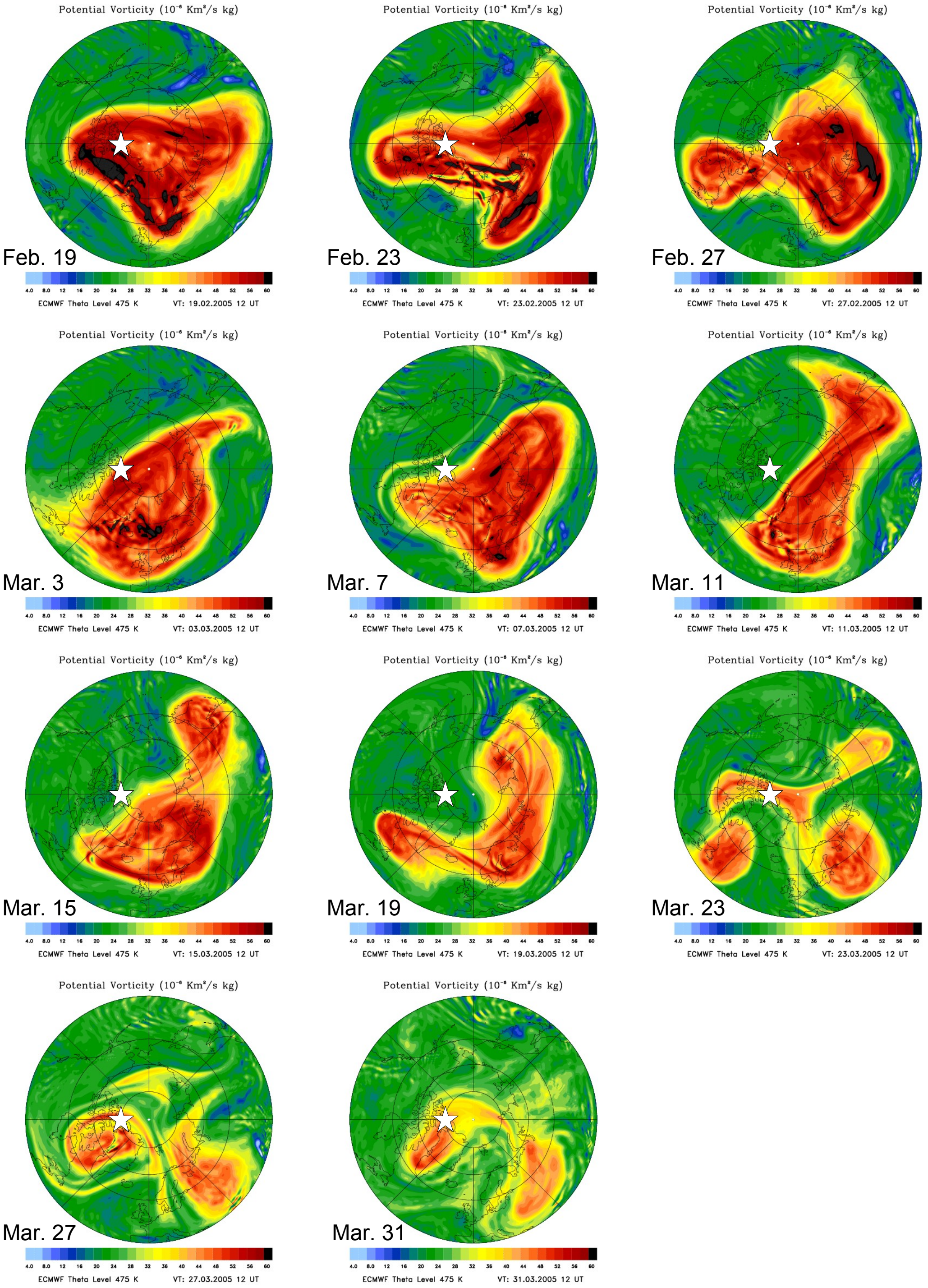

Figure 6.3: As Figure 6.2, but for 2005.

January. As in 2004, the vortex began to reform in February, with a strong vortex (though not as strong as in 2004) in the middle and upper stratosphere, with no substantial vortex in the lower stratosphere, as seen in Figure 6.4. The final warming of the stratosphere occurred in April (Manney et al., 2008). As in 2004, Eureka was inside the vortex at altitudes where it had reformed.

6.1.4 2007

The 2007 Eureka campaign took place from February 19 to April 3. The winter of 2007 had a strong polar vortex placed over the pole, with Eureka spending a lot of time inside the vortex. A region of high ozone was located to the west of Eureka during the beginning of the campaign, with Eureka moving in and out of the vortex into this region. In mid-March, the polar vortex moved over Eureka and remained until the final warming began at the end of March. Figure 6.5 shows the ECMWF PV for the campaign. The UT-GBS remained in Eureka beyond the end of the campaign, taking measurements until May 12.

A more complete view of the synoptic context of the first three campaigns can be found in Manney et al. (2008).

6.2 Data Analysis

The programme WinDOAS is used to analyse the data from the UT-GBS and PEARL-GBS, as described in Chapter 3. The details of the WinDOAS settings are given in Table 6.1. For ozone and NO_2, a daily reference spectrum from the smallest SZA available is used as a reference spectrum. For BrO and OClO, reference spectra are selected for each twilight period, with a SZA of 80°. When the Sun does not reach 80°, the smallest SZA is used. Daily AMFs are calculated using the radiative transfer model initialized with temperature, pressure, and ozone profiles taken from ozonesondes. When sondes were not launched, the sonde from the closest day is used.

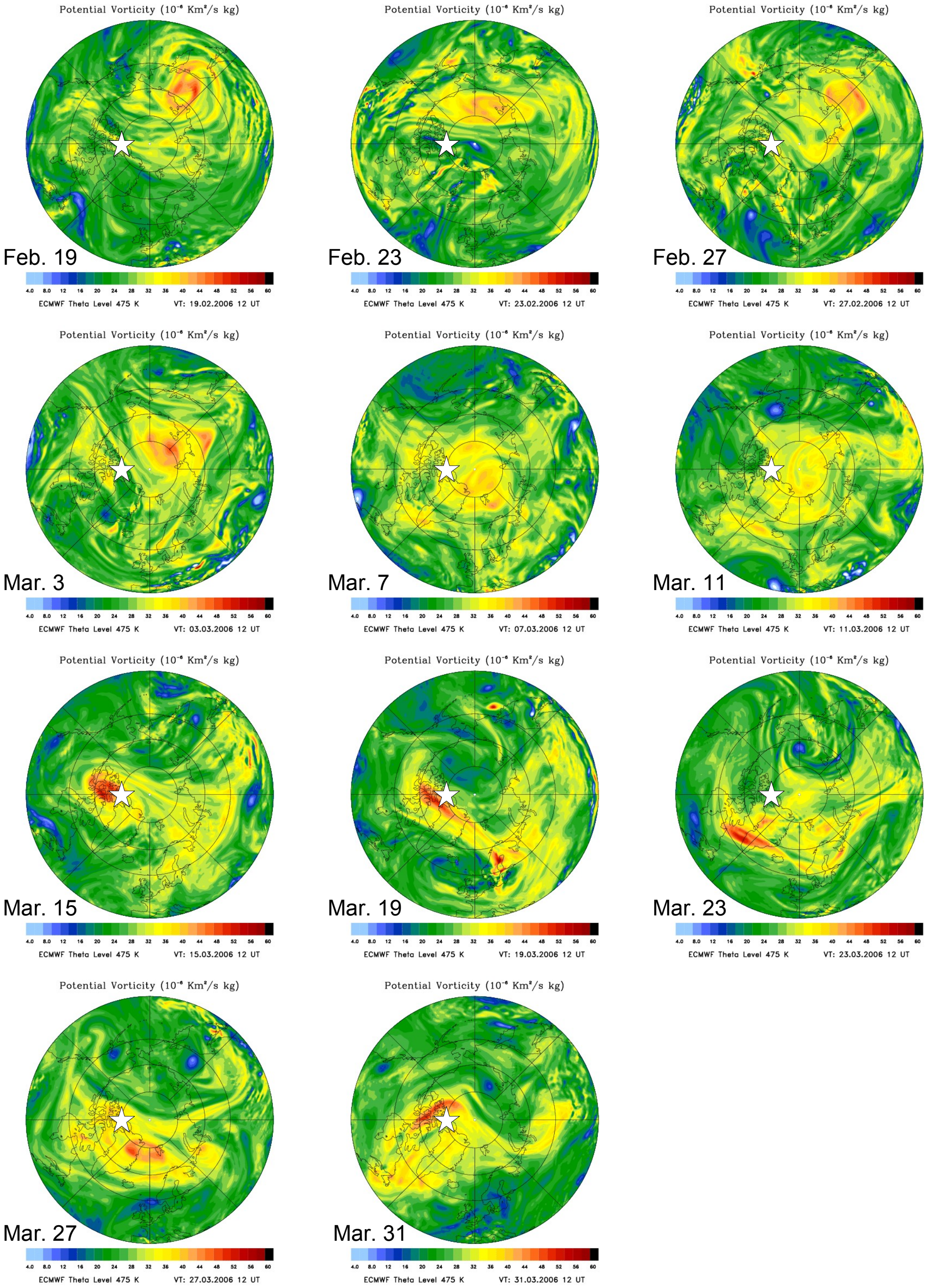

Figure 6.4: As Figure 6.2, but for 2006.

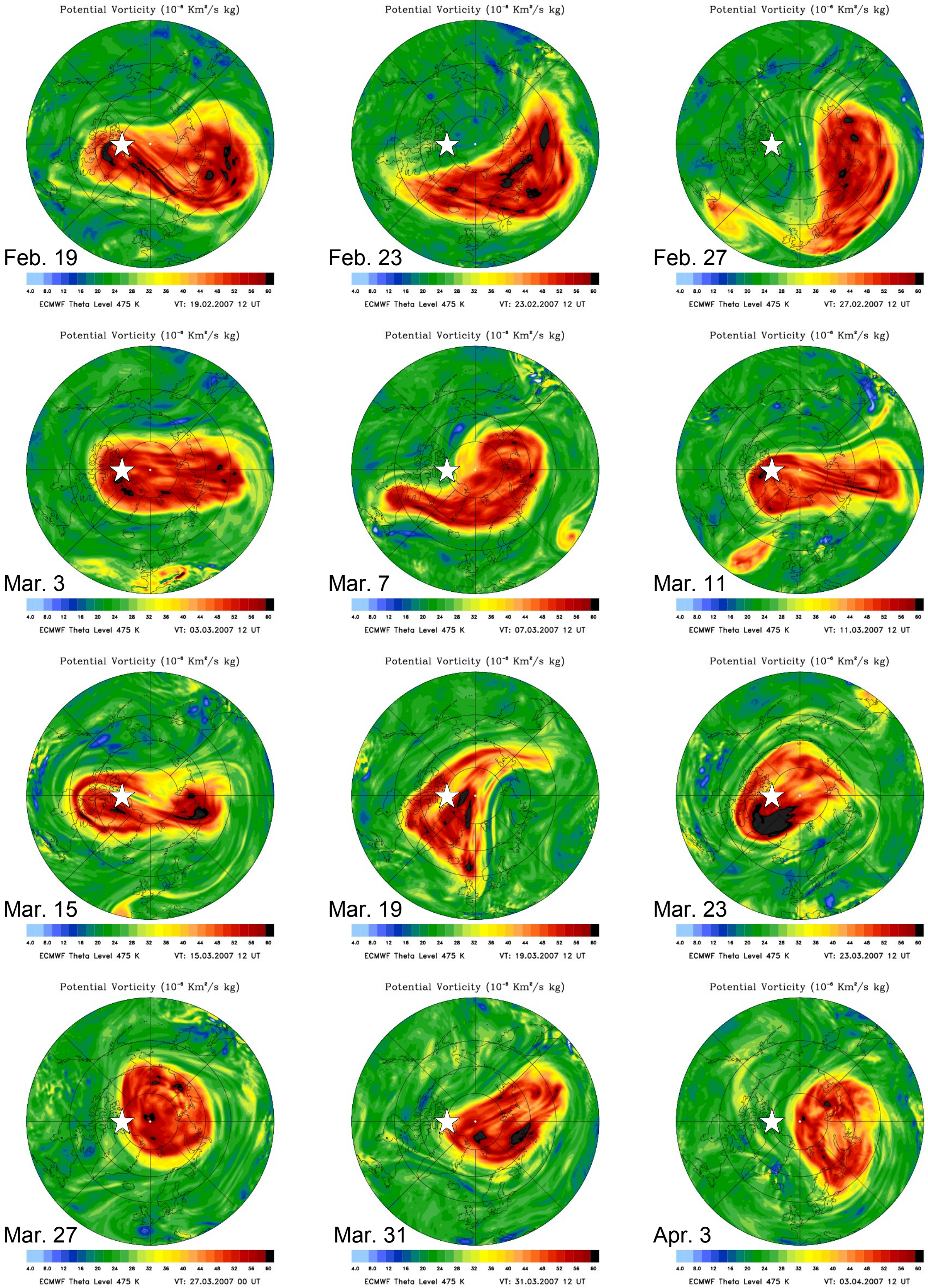

Figure 6.5: As Figure 6.2, but for 2007.

Table 6.1: Details of the WinDOAS analysis for the UT-GBS and PEARL-GBS. The same polynomial degree is used in the calibration for both the wavelength shift and the slit function parameters, and is given in the column CDP (calibration polynomial degree). CWL (calibration window limit) is the range used for the wavelength calibration. # of SW is the number of subwindows used in the wavelength calibration. CF (continuous functions) is the degree of polynomial fit to the optical depth in the DOAS analysis. The offset is the term fit to correct for stray light, discussed in Chapter 3.

Species	Grating (gr/mm)	CPD	CWL (nm)	# of SW	CF	Offset
Ozone	600 and 400	3	400–550	5	0,1,2,3	none
NO_2	600 and 400	3	400–550	5	0,1,2,3	none
NO_2	1200	3	380–420	5	0,1,2,3	quadratic
BrO	600	2	350–400	3	0,1,2,3	quadratic
BrO	1200	2	340–400	3	0,1,2,3	quadratic
OClO	1200	3	340–390	5	0,1,2,3	quadratic

6.3 Calculation of Vertical Column Densities

As discussed in Section 3.3, there are two methods of calculating the ozone and NO_2 VCDs. Figure 6.6 shows the results of both of these methods for both species in 2005 for the UT-GBS. This year is shown because Eureka spent the beginning of the campaign on the edge of the polar vortex. After March 8 (day 67), the vortex moved away from Eureka and began to break up (Manney et al., 2008).

The ozone results, shown in Figure 6.6(a), show poor agreement between the two methods to day 67, and good agreement between the VCDs after this day. The discrepancies between the methods can be as high as 50 DU (or ∽15% of the total column) during the first half of the campaign, while the differences are no greater than 20 DU (or ∽6% of the total column) during the second half. While Eureka was on the edge of the vortex, due to the viewing geometry of the instrument, the air masses sampled in the morning were towards the east into the vortex, while the air masses sampled in the afternoon were towards the west, out of the vortex (see Figure 6.3). The SZA range used for both methods is 86° to 91°. Both methods of finding the ozone VCD assume that the VCD does not change over the twilight period. This assumption is not valid for

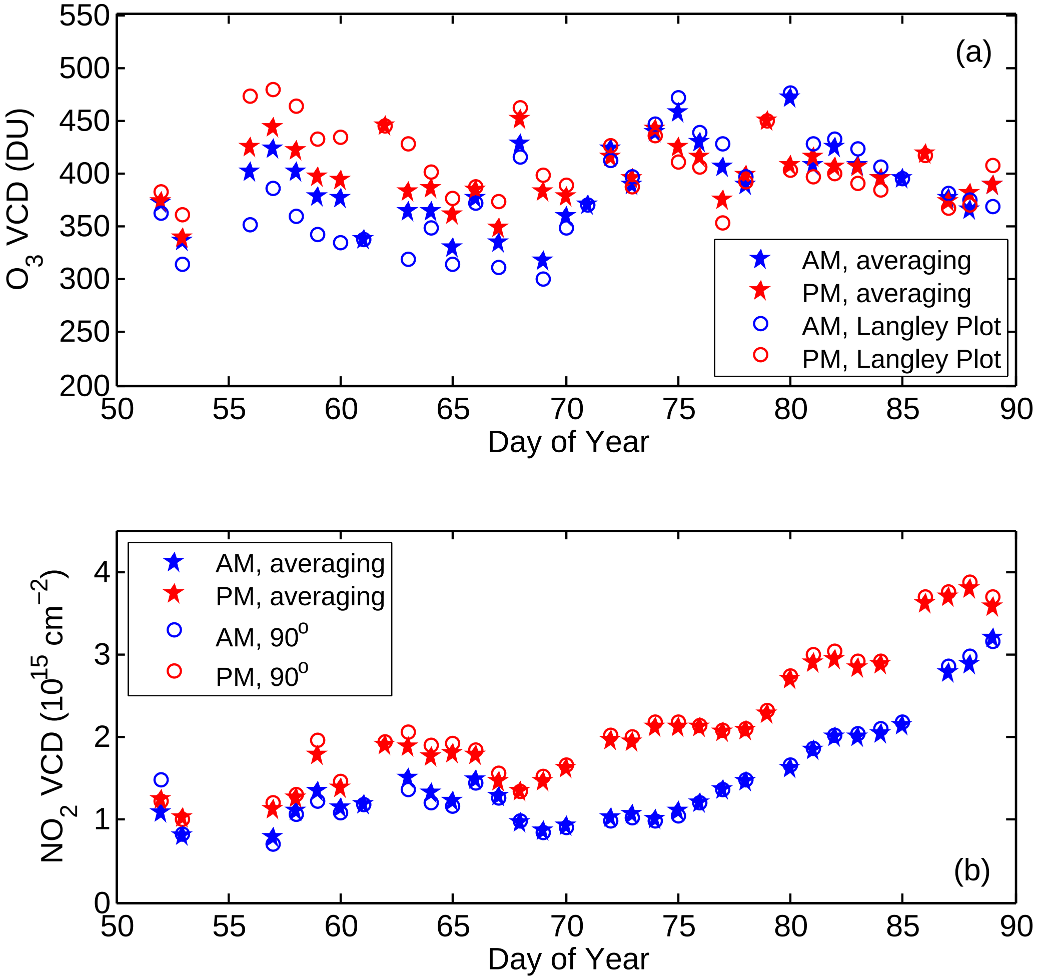

Figure 6.6: (a) Comparison of the averaging and Langley plot methods for finding the ozone VCD for the UT-GBS at Eureka in 2005. (b) Comparison of the averaging and 90° methods for NO_2.

the period when Eureka was on the edge of the vortex, because each DSCD is in fact sampled at a different physical location. The measurements closest to noon are south of Eureka, while those near a SZA of 90° are to the east or the west, either into the vortex in the morning or away from the vortex in the afternoon. Figure 6.7 shows the geometrical projection of the ozone maximum (taken to be 18 km) along the line of sight to the Sun for March 4, 2005. Because there are more measurements taken at solar noon, the averaging method weights the VCD towards these noontime measurements. For this

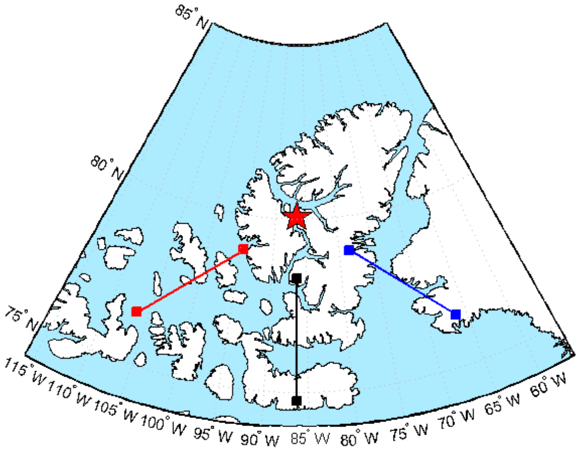

Figure 6.7: Spatial extent of the DSCD measurements for March 4, 2005, calculated as the geometrical projection of the ozone maximum (18 km) for 86° (noon) and 91°. The blue and red lines indicate the projection of the ozone maximum at 91° for sunrise and sunset, respectively. The black line indicates the projection at 86°, which is the solar maximum on this day. The red star indicates the location of PEARL.

period of the campaign, this results in larger VCDs in the morning and smaller VCDs in the afternoon. During the second part of the campaign, when the vortex had moved away from Eureka, the methods agree, as a result of the more homogenous ozone field.

Figure 6.8(a) and (b) show the morning ozone VCDs calculated directly from the DSCD for March 5 and 20, 2005, respectively. On March 5, Eureka was located on the edge of the vortex, while on March 20 it was located outside the vortex. The VCDs on March 5 span 40 DU between 86° and 91°, and are systematically decreasing. On March 20, the VCDs span 20 DU over the same SZA period, and are relatively constant between 87° and 92°. On both days, the VCD calculated from the averaging method is closer to the value at 86° than the VCD calculated from the Langley plot method. Despite the fact that only SZAs between 86° and 91° are used in both calculations, the VCDs calculated from the Langley plot method correspond to the VCD at SZAs above 91°.

The NO_2 results, shown in Figure 6.6(b), do not display the same dramatic differences between the methods as seen for ozone. Unlike the total ozone column, the NO_2 column has a diurnal cycle, and its concentrations are expected to vary throughout the twilight

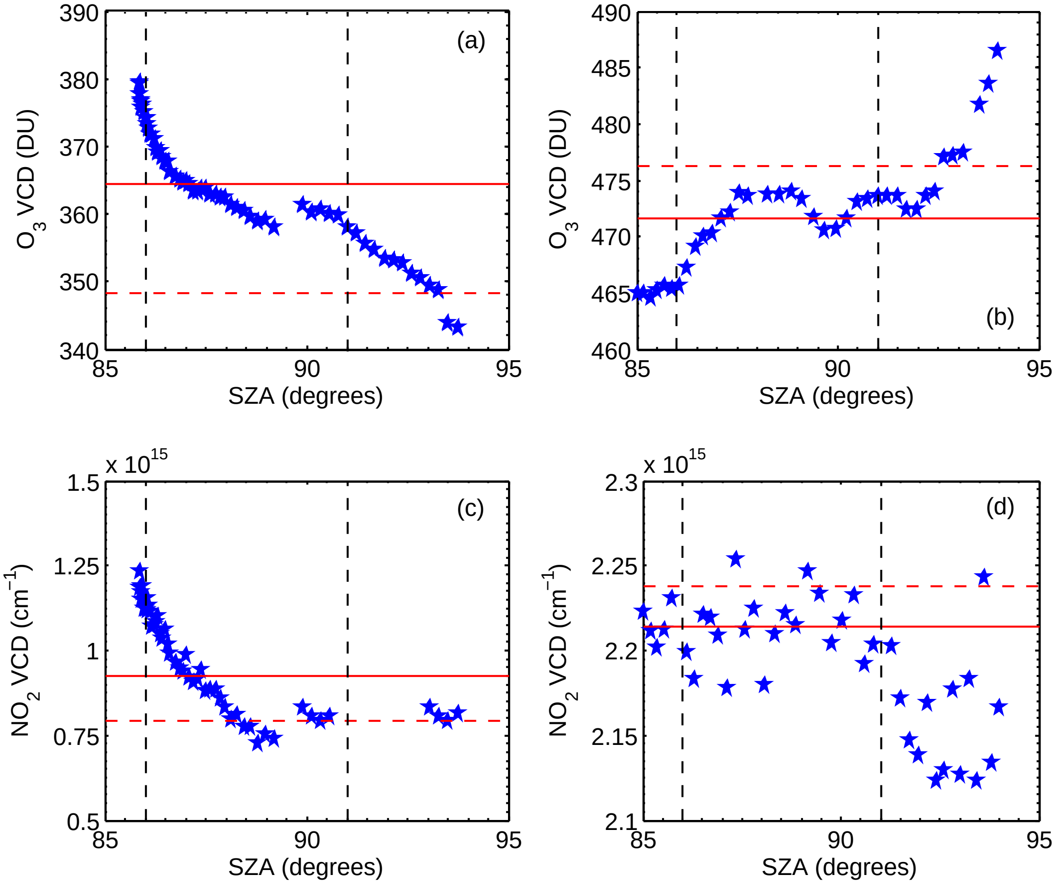

Figure 6.8: (a) Ozone morning VCDs with SZA for March 5, 2005, and (b) March 20, 2005. (c) as (a) but for NO_2, and (d) as (b) but for NO_2. The solid horizontal line indicates the VCD calculated using the averaging method, while the dotted horizontal line indicates the VCD calculated using the Langley plot method for ozone, and the 90° method for NO_2. The vertical dashed lines indicate the range of SZAs used in the averaging and Langley plot methods of calculating the VCD.

period. The 90° method takes this into account by finding the VCD at 90°, while the averaging method finds the average VCD between 86° and 91°. However, both methods assume that the same air mass is viewed throughout the twilight period, which is not the case in the first part of the campaign when Eureka was on the edge of the polar vortex. The fact that the two methods agree during the whole campaign is an indication that the NO_2 field is not as heterogeneous as the ozone field. The VCDs become less scattered after March 8, when the vortex moves away from Eureka. Figure 6.8(c) and

(d) show the morning NO_2 VCDs calculated from the DSCDs. The VCDs from March 5 span 0.5×10^{15} cm^{-2} between 86° and 91°, while those from March 21 span just 0.1×10^{15} cm^{-2} over the same SZA period. As for ozone, the VCD calculated from the averaging method is closer to the VCDs at noon. The 90° method gives a VCD that is closer to the VCD at 90°.

The averaging method is used for the calculation of the ozone VCDs for the Eureka campaigns, to minimize the morning and afternoon differences, due to the weighting towards noon. In addition, Sarkissian et al. (1997) find the averaging method to better agree with the ozonesondes. For consistency, the averaging method is also used for the NO_2 VCD calculations.

The 90° method is used for calculating the BrO VCDs. BrO has a strong diurnal cycle (see Figure 1.4). Because of this, calculations of the VCD and RCD are more difficult than for ozone and NO_2. This is further complicated by the small range of SZAs available in Eureka. BrO DSCD retrievals are performed using a morning or evening daily reference spectrum at 80°, or, when the Sun does not reach 80°, the closest available SZA. Each twilight period therefore has a unique RCD, and at most two RCD values can be averaged (when the Sun does not reach 80°). When possible, the RCD is calculated using Langley plots in the 80°-85° SZA range. Before the Sun reaches 85° (March 7, day 66) the highest five-degree range is used. This small SZA region is chosen to minimize the effects of the diurnal cycle when calculating the RCD, however, depending on the time of year, BrO amounts can vary during this period, leading to uncertainties in the calculated RCD.

Further complicating the retrieval of BrO VCDs is the potential presence of so-called "bromine explosions" in the troposphere. Bromine explosions are the occurrence of large amounts of BrO in the troposphere, the mechanism for which is thought to be the autocatalytic release of bromine from sea salt surfaces (Piot and von Glasgow, 2008). Bromine explosions have been observed in the springtime in both the Arctic (e.g. McElroy et al.,

1999) and the Antarctic (e.g. Schofield et al., 2006). The AMFs are calculated assuming a background amount of BrO (0.5 ppt), while during bromine explosions the tropospheric amount increases to roughly 15 ppt (Schofield et al., 2006). This large increase in the tropospheric column has a significant impact on the AMFs. In the radiative transfer model used in this work, increasing the tropospheric column to 7 ppt from 0.5 ppt reduces the AMF by half at 90°. In the presence of a bromine enhancement, the VCDs derived using an AMF calculated assuming no tropospheric enhancement will be smaller than the true VCDs. To date, no evidence of bromine explosions has been seen in the zenith-sky measurements from either instrument.

6.4 Campaign Results

6.4.1 2004

The ozone and NO_2 VCDs from the 2004 campaign are shown in Figure 6.9. The instrument was operated with the 400 gr/mm grating during this campaign. This, and the reduced signal-to-noise ratio (SNR) caused by an error in the data analysis code, discussed in Section 2.4.1, meant that the low resolution and noise of the spectra did not allow the retrieval of BrO and OClO.

Also shown is the scaled potential vorticity (sPV) calculated from Goddard Earth Observing System-4 (GEOS-4) reanalysis data for sunrise (SZA=90°) at Eureka (Bloom et al., 2005; Manney et al., 1994). A description of how sPV is calculated is given in Manney et al. (2007). sPV is shown on three potential temperature levels: 490 K (∽18 km, lower stratosphere), 850 K (∽30 km, middle stratosphere), and 1700 K (∽50 km, upper stratosphere). The values for sunset have also been calculated, and are similar to the sunrise values. To first order, sPV values below 1.2×10^{-4} s^{-1} indicate that Eureka is outside the vortex, while those above 1.6×10^{-4} s^{-1} indicate that Eureka is inside the vortex. In between these values, Eureka is on the edge of the vortex (Manney et al.,

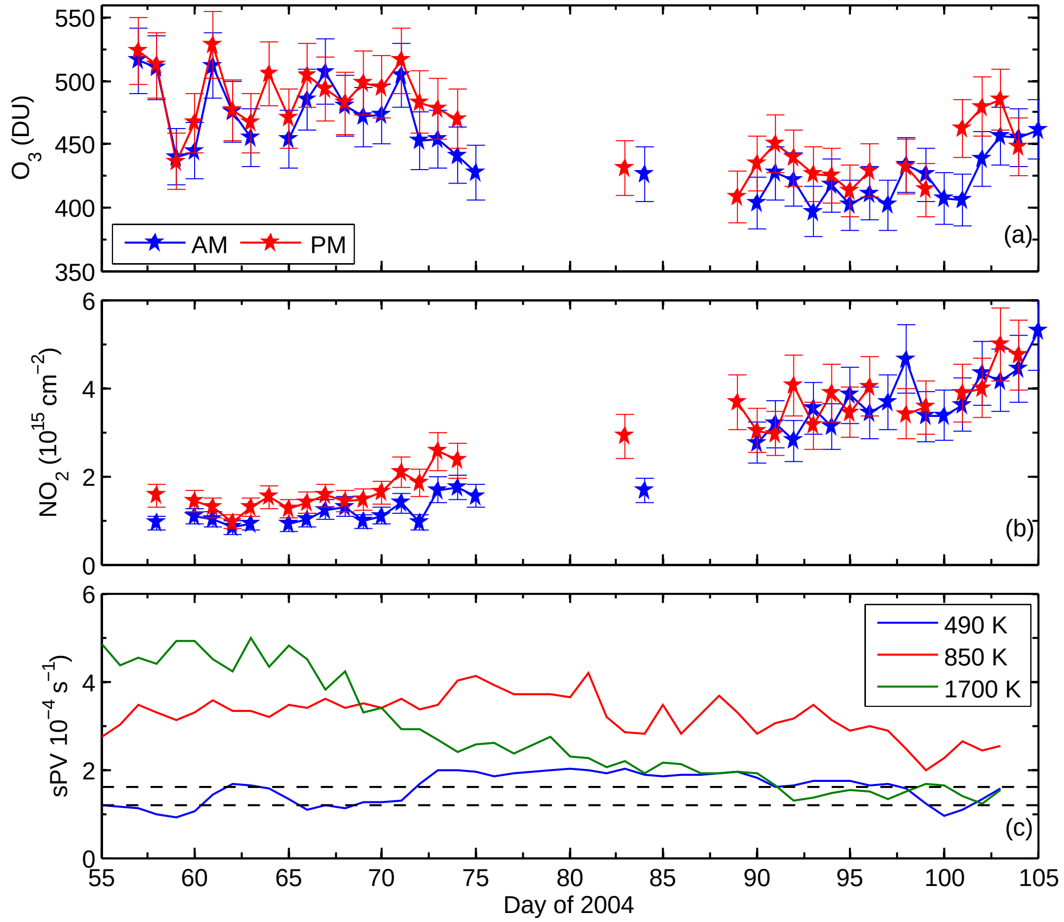

Figure 6.9: (a) Ozone and (b) NO_2 from the UT-GBS for polar sunrise 2004. (c) sPV on 490 K, 850 K, and 1700 K potential temperature levels (corresponding to altitudes of 18 km, 30 km, and 50 km). The dotted horizontal lines indicate 1.2 and 1.6×10^{-4} s^{-1}, approximately demarking the edges of the polar vortex region.

2008).

By the start of the 2004 campaign, the polar vortex had reformed over Eureka in the middle and upper stratosphere, with a weak vortex in the lower stratosphere. As can be seen in Figure 6.9(c), through much of the campaign, Eureka was well inside the vortex at higher altitudes. In the lower stratosphere, where the peak in ozone is found (∽15-20 km), Eureka is on the edge or outside the vortex until day 62 (March 2), when it briefly enters the vortex until day 65 (March 5). It then returns to the edge of the vortex until day 72 (March 12), where it stays until day 99 (April 9). On day 102 (April 11) it enters the vortex again.

The ozone columns drop as Eureka enters the vortex on day 62, and then returns to levels seen earlier in the campaign on day 66. The ozone remains fairly constant until day 72, when it begins to decrease as Eureka enters the vortex again. The ozone then levels off at the end of March, remaining so until day 99, when it begins to decrease. On day 102 (April 11) the ozone shows a slight recovery as the vortex moves over Eureka once again.

The behaviour of NO_2 during the campaign is dominated by the recovery of N_2O_5 being photolysed. Morning and afternoon columns begin to agree towards the end of the campaign as the Sun is continuously above the horizon after April 14 (day 105). The maximum in the NO_2 profile is between 25 and 35 km, with large contributions in the lower stratosphere as well. In the middle stratosphere, Eureka is inside the vortex for the whole campaign. The NO_2 and ozone columns are negatively correlated during the campaign (correlation coefficient, r, $\backsim$ -0.60), an indication of transport of relatively ozone-poor and nitrogen-rich air from lower latitudes. NO_2 is steadily increasing, with larger values from day 62–65. As the ozone decreases after day 72, the NO_2 steadily increases. At the end of the campaign, when the middle stratosphere is on the edge of the vortex, the two species are both increasing.

6.4.2 2005

The ozone, NO_2, and BrO VCDs as well as the sPV from 2005 are shown in Figure 6.10. The instrument was operated with the 600 gr/mm grating, with the new CCD and the corrected data acquisition code. This increased the SNR from that of the 2004 campaign, and allowed for the retrieval of BrO. The resolution of the 600 gr/mm grating is too coarse for OClO retrieval.

In 2005, Eureka was on the edge of, or outside, the vortex until March 8 (day 67), when the vortex moved away from Eureka and began to break apart. From Figure

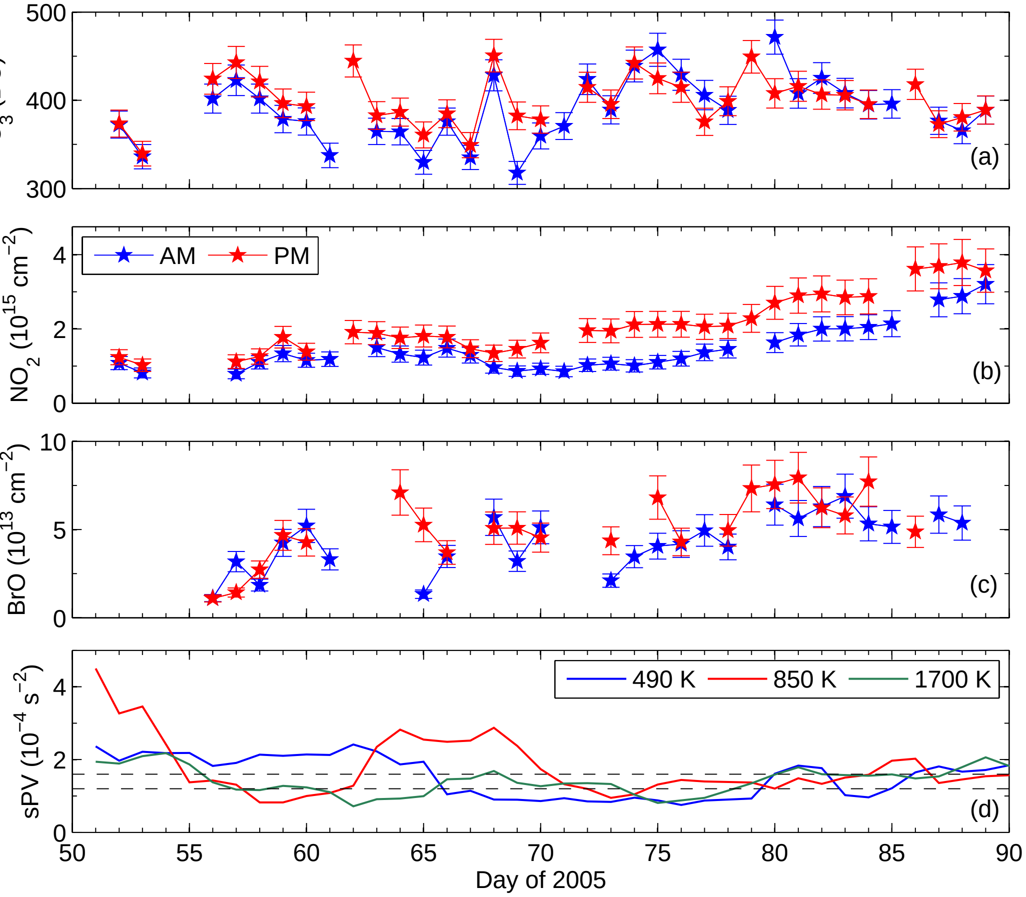

Figure 6.10: (a) Ozone, (b) NO_2, and (c) BrO from the UT-GBS for polar sunrise 2005. (d) sPV on 490 K, 850 K, and 1700 K potential temperature levels.

6.10(d), the lower stratosphere was inside the vortex until day 65 (March 6), on the edge of the vortex until day 67 (March 8), and then outside the vortex for the remainder of the campaign. The remnants of the vortex returned for two brief periods: day 80–82 (March 21–23) and day 86–91 (March 27–April 1). Until day 65, the ozone is decreasing. As the vortex moves away, the ozone concentrations begin to stabilize and increase, then begin to decrease again after day 75 (March 16). There is a slight increase as the vortex moves back to Eureka on day 80, and then the column decreases until the end of the campaign.

In the middle stratosphere, Eureka is inside the vortex until day 55 (February 24), from day 63 (March 4) to day 70 (March 11), and from day 83 (March 24) to day 86 (March 27). For the rest of the campaign, it is either outside or on the edge of the vortex.

The NO_2 columns increase until day 65, when they show a slight decrease, recovering by day 68, when they increase until day 82, when the columns begin to decrease again. On day 86 they have recovered and keep increasing until the end of the campaign. Until day 65, and after day 82, the NO_2 is increasing while the ozone columns are decreasing (correlation coefficient $\backsim$ -0.76). In between these days, both the ozone and NO_2 columns are generally increasing (correlation coefficient $\backsim$ 0.85).

The peak in BrO is between 10 and 20 km, in the lower stratosphere. Until day 65, while Eureka is inside the vortex, BrO VCDs increase. When Eureka moves outside the vortex, after day 68, the columns remain roughly stable, decreasing slightly. The columns increase again on day 79, when Eureka begins to enter the vortex again, and then generally decrease slightly until the end of the campaign. As observed by Tørnkvist et al. (2002), stratospheric BrO peaks during the winter and decreases through the spring. Until day 61, BrO is generally increasing while ozone is generally decreasing (correlation coefficient $\backsim$ -0.90), potentially indicating bromine and chlorine-driven catalytic destruction of ozone. After day 61, the two species are positively correlated (correlation coefficient $\backsim$ 0.67). Eureka is generally outside of the vortex after day 65, where ClO concentrations are expected to be small, and so no BrO/ClO depletion of ozone can occur (Equations 1.55–1.59).

There is no clear relationship between BrO and NO_2 until day 80, when they become negatively correlated (correlation coefficient $\backsim$ -0.55). Tørnkvist et al. (2002) observed a negative correlation between the two species for measurements taken at Ny-Ålesund, Norway (79°N) during two springtime campaigns and Andøya (69°N), Norway over the course of one year of measurements. Richter et al. (1999) also observed a negative correlation in measurements taken at Bremen, Germany (53°N) in 1994–1996. Model studies expect a negative correlation between BrO and NO_2. When concentrations of NO_2 increase, $BrONO_2$ is quickly formed, and BrO concentrations decrease (Fish et al., 1995; Danilin and McConnell, 1995).

The seasonal variation of BrO VCDs, generally increasing until mid-March and then decreasing to the end of the campaign is similar to the variation in DSCD seen at the Arctic sites of Ny-Ålesund, Andøya, and Kiruna, Sweden (68°N) by Sinnhuber et al. (2002) for the springs of 1998, 1999, and 2000. Tørnkvist et al. (2002) also observed the decrease of springtime BrO. The DSCDs used in the calculation of VCDs in this work range between -1 and 6×10^{14} molecules/cm^2, larger than the 0.5–4×10^{14} molecules/cm^2 observed by Tørnkvist et al. (2002) and larger than the 0.1-2×10^{14} molecules/cm^2 observed in Ny-Ålesund by Sinnhuber et al. (2002). The Tørnkvist et al. (2002) observations are generally inside the vortex, while Sinnhuber et al. (2002) do not provide the meteorology of the observing conditions. Tørnkvist et al. (2002) observed smaller BrO amounts outside the polar vortex, in agreement with the behaviour seen in Eureka.

6.4.3 2006

Ozone, NO_2, and BrO VCDs for 2006 are shown in Figure 6.11, along with the sPV. The instrument was operated with the 600 gr/mm grating, allowing the retrieval of ozone, NO_2, and BrO VCDs. From Figure 6.11(d), the upper and middle stratosphere were inside the vortex for the entire campaign. The vortex in the lower stratosphere did not reform substantially after the sudden stratospheric warming in January (Manney et al., 2008). The ozone field observed by all of the instruments is relatively constant throughout the campaign.

In the middle stratosphere, the sPV increases sharply on day 63 (March 2), and remains high until day 77 (March 18), indicating that Eureka moves further into the vortex at these altitudes. The NO_2 columns increase until day 63, when they start to decrease slightly. The columns continue to vary with the sPV, decreasing when Eureka moves further into the vortex, until day 77, when they increase uniformly until the end of the campaign. Generally, ozone and NO_2 columns follow opposite trends (correlation coefficient $\backsim$ -0.65).

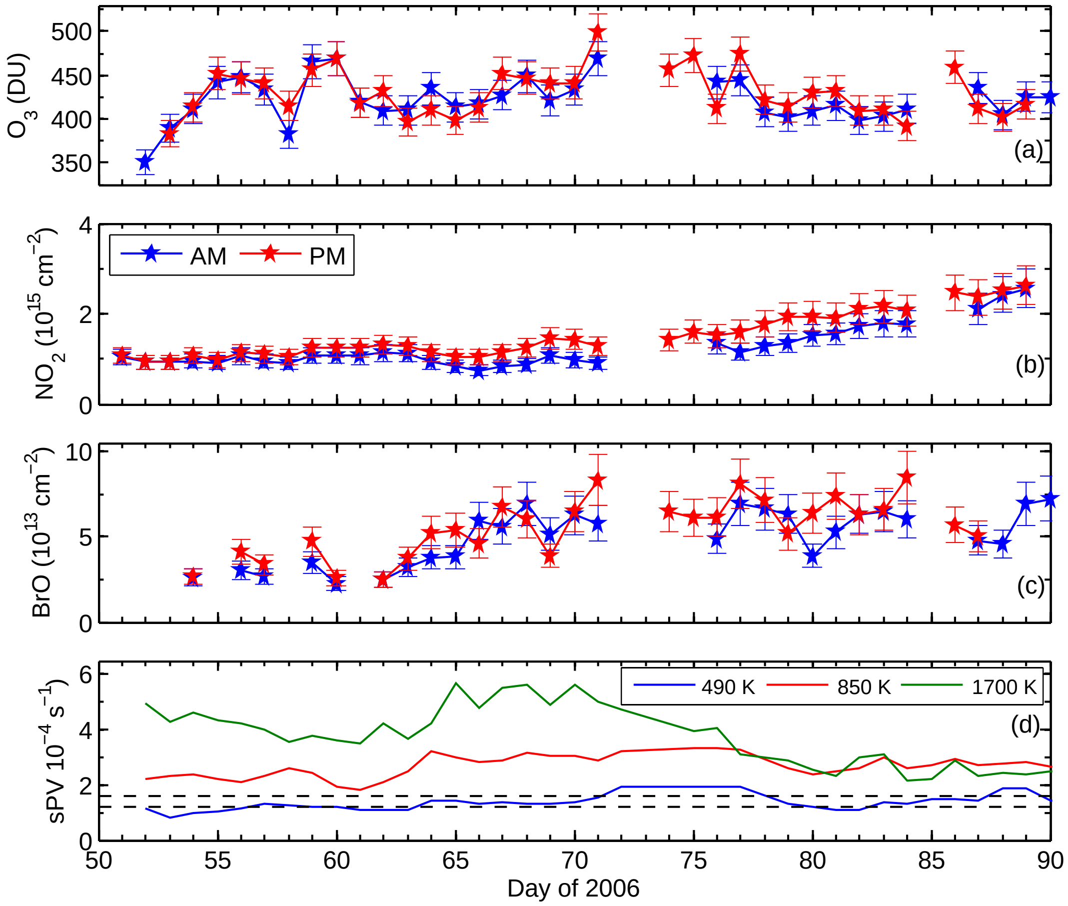

Figure 6.11: As Figure 6.10, but for 2006.

The BrO columns are generally increasing until day 70 (March 11), and then remain relatively constant for the remainder of the campaign. Throughout the campaign, ozone and BrO VCDs generally follow the same trends (correlation coefficient ∽ 0.61). BrO and NO_2 columns are both generally increasing until day 71. After this date, BrO columns decrease while NO_2 columns continue to increase (correlation coefficient ∽ -0.85). As observed in 2005, the BrO columns peak during the winter and decrease through the spring. The DSCDs vary between -1 and 6×10^{14} molecules/cm^2, again larger than the ranges observed by Tørnkvist et al. (2002) and Sinnhuber et al. (2002) at a similar latitude.

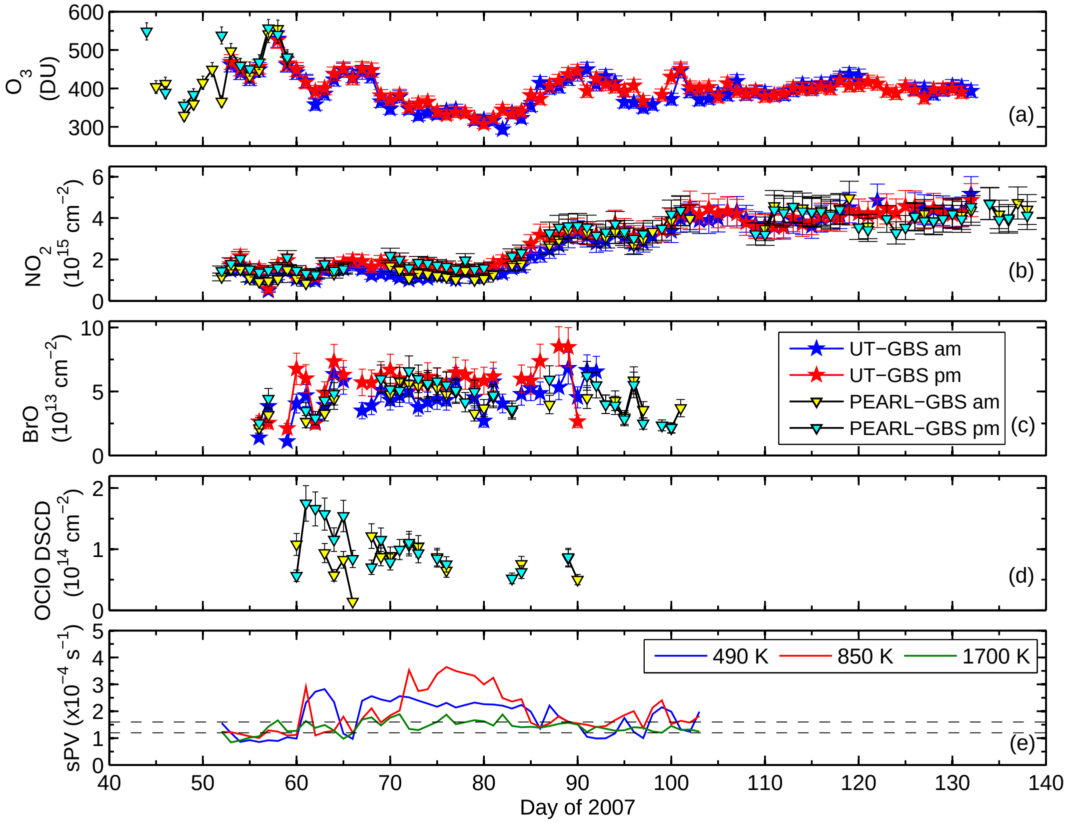

Figure 6.12: (a) Ozone, (b) NO_2, and (c) BrO VCDs from the UT-GBS and PEARL-GBS for polar sunrise 2007. (d) OClO DSCDs and (e) sPV on 490 K, 850 K, and 1700 K potential temperature levels. sPV was not calculated before day 52.

6.4.4 2007

Ozone, NO_2, and BrO VCDs, and OClO DSCDs are shown in Figure 6.12, along with the sPV. In 2007, the UT-GBS was operated with the 600 gr/mm grating, as in 2005 and 2006, and ozone, NO_2, and BrO VCDs are retrieved. The PEARL-GBS was operated with the 600 gr/mm grating until February 28, after which the 1200 gr/mm grating was used. This meant the two instruments were operating in the same configuration for one week. After this, the PEARL-GBS measured at a higher resolution, allowing for the recovery of NO_2, BrO, and OClO. The comparisons between the instruments will be discussed in Chapter 7.

In the lower stratosphere, Eureka is outside the vortex until day 60 (March 1), enters the vortex between day 61 and 64 (March 2 to 5), and briefly exits the vortex between day 65 and 66 (March 6 and 7). Eureka then enters the vortex on day 67 (March 8), and stays inside or on the edge of the vortex until day 90 (March 31). The vortex then moves back and forth over Eureka in April, with Eureka inside the vortex on day 95 (April 5), between day 98 and 100 (April 8 to 10), and again on day 103 (April 13). Ozone VCDs are higher outside and on the edge of the vortex. During the three-week period when Eureka remains in the vortex, ozone concentrations are seen to decrease. Once the vortex breaks apart in April, ozone columns are fairly constant through the rest of April and May.

In the middle stratosphere, Eureka is outside the vortex until day 62 (March 3), with the exception of day 61 (March 2) when it enters the vortex. Eureka then stays on the edge or inside the vortex for the remainder of the campaign. Between days 70 and 80, the sPV values become much larger, indicating that Eureka has moved further into the vortex. NO_2 VCDs are low at the beginning of the campaign and increase on day 63 when Eureka enters the vortex. When Eureka is deep inside the vortex between days 70 and 80, NO_2 concentrations decrease slightly. When Eureka moves to the edge of the vortex again, concentrations begin to increase, and generally increase for the remainder of the campaign. Ozone and NO_2 generally follow the same trends throughout the campaign (correlation coefficient $\backsim 0.59$).

BrO VCDs are generally increasing at the beginning of the campaign until Eureka enters the vortex on day 68 (March 9), when they begin to decrease slightly. They increase when Eureka moves out of the vortex at the end of March, and then decrease through April. Once the Sun no longer sets, in mid-April, the VCD at 90° can no longer be calculated. As seen in previous campaigns, the BrO columns peak in the middle of the campaign and decrease until the end of the observation period. Ozone and BrO generally follow the same trends throughout the campaign (correlation coefficient $\backsim 0.32$). NO_2 and BrO are not clearly related until the end of the campaign, after day 90, when NO_2

columns increase while BrO columns decrease (correlation coefficient ∽ -0.61). This year, the BrO DSCDs from both instruments vary between -2 and 4×10^{14} molecules/cm^2.

The vertical profile of OClO is not well known, and the AMFs cannot be calculated. The DSCDs in Figure 6.12 are at 90°, analysed with a daily reference spectrum at 80°, or, before the Sun rises to 80°, the highest SZA possible. The OClO DSCDs increase sharply when Eureka moves into the vortex on day 61, indicating chlorine activation inside the vortex, and steadily decrease during the three-week period when Eureka is inside the vortex in March. The decrease is an indication that active chlorine is being converted to inactive forms. Temperatures in the lower vortex, from the GEOS-4 reanalysis (not shown), are constantly above the temperatures required for PSC formation, indicating that chlorine activation occurred earlier in the winter. There is no strong relationship between OClO and the other species. When Eureka is in the vortex, ozone concentrations decrease from roughly 450 DU to 300 DU. During this period, all four species are decreasing. BrO concentrations remain relatively constant, falling by only 7% of their original value, which may indicate the occurrence of the BrO/ClO-driven catalytic destruction of ozone.

Table 6.2 shows OClO DSCDs observed by ground-based zenith-sky-viewing grating spectrometers operated in the Arctic during springtime; Farahani (2006) used the UT-GBS. Generally a reference spectrum at 80° was used, with the exception of Farahani (2006), which used 76°. The range of DSCDs observed during the Eureka 2007 campaign with the PEARL-GBS is consistent with the range of the other observations.

6.5 PEARL-GBS

The PEARL-GBS was permanently installed in Eureka in August 2006. The instrument has made continuous measurements since then, with the exception of during polar night, a few days in September 2006, and a period in June 2007, when instrument problems

Table 6.2: OClO DSCD range observed by ground-based zenith-sky spectrometers during Arctic springtime.

Location	OClO DSCD range (10^{14} molecules/cm^2)	Reference
Søndre Strømfjord, Greenland (67°N)	0.5–2.5	Grund et al. (1998)
Andøya, Norway (69°N)	0.4–1.3	Tørnkvist et al. (2002)
Ny-Ålesund, Norway (79°N)	0.5–1.5	Wittrock et al. (1998)
Ny-Ålesund, Norway (79°N)	0.5–2.0	Tørnkvist et al. (2002)
Eureka, Canada (80°N)	0.3–4.0	Farahani (2006)
Eureka, Canada (80°N)	0.1–2.0	this work

prevented measurements. During the majority of the Canadian Arctic ACE validation campaign in 2007, it was operated with the 1200 gr/mm grating, and ozone measurements were not possible. Except for these periods, there is a continuous ozone and NO_2 VCD record from the installation to the beginning of polar night in 2007. With the addition of the ozone data from the UT-GBS, the ozone record is extended during the 2007 Eureka campaign.

Figure 6.13(a) shows the ozone VCDs from the PEARL-GBS and UT-GBS. Also shown are the weekly (daily during the polar springtime campaigns) ozonesondes launched from the weather station. The PV on the 475 K potential temperature level ($\backsim$19 km) from the NCEP automailer is also shown in this figure. Because the Sun travels through a limited range of SZAs in the course of a day in Eureka, in the summer when the Sun is continuously above the horizon the preferred SZA range for calculating the VCD is not always available. During this time, all available SZAs are used. This period is denoted by open symbols in Figure 6.13(a), and runs between day 105 (April 15) and 230 (August 18). Figure 6.14 shows the maximum and minimum SZAs in Eureka throughout the year.

During springtime, the ozone concentrations are largely determined by the PV levels and the position of Eureka with respect to the vortex. Once the vortex breaks apart, the VCDs are constant for roughly a month, and then decrease throughout the summer

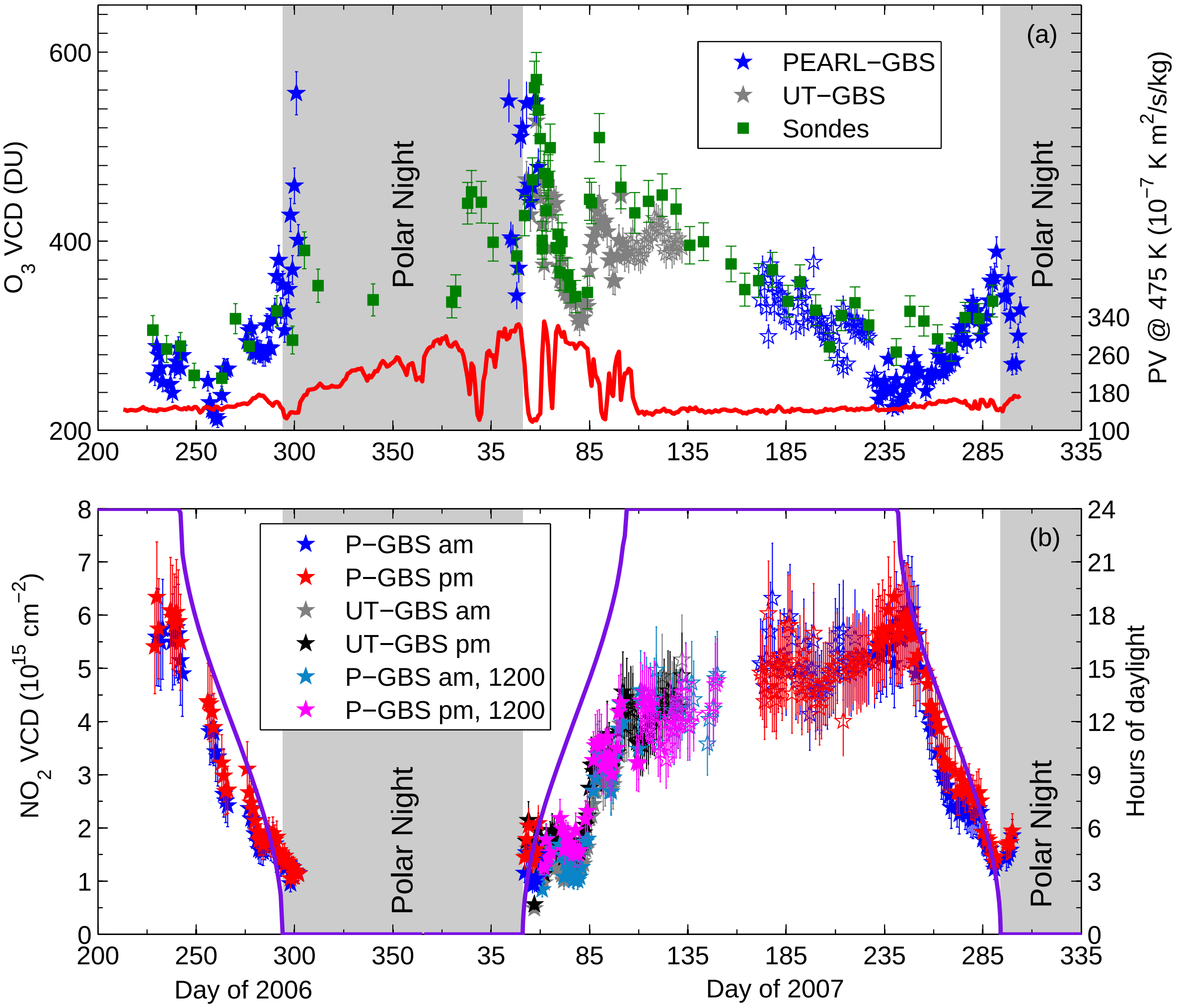

Figure 6.13: (a) Ozone VCDs from the PEARL-GBS, UT-GBS, and ozonesondes from August 2006 to October 2007. Also shown, as a solid red line, is the PV on the 475 K potential temperature level (∽19 km). (b) NO_2 VCDs from the PEARL-GBS (P-GBS in the legend) and UT-GBS from August 2006 to October 2007. Also shown are the total hours of daylight as the purple solid line. The open symbols indicate the days where VCDs are calculated using all available SZAs, because the Sun is not in the 86° to 91° range.

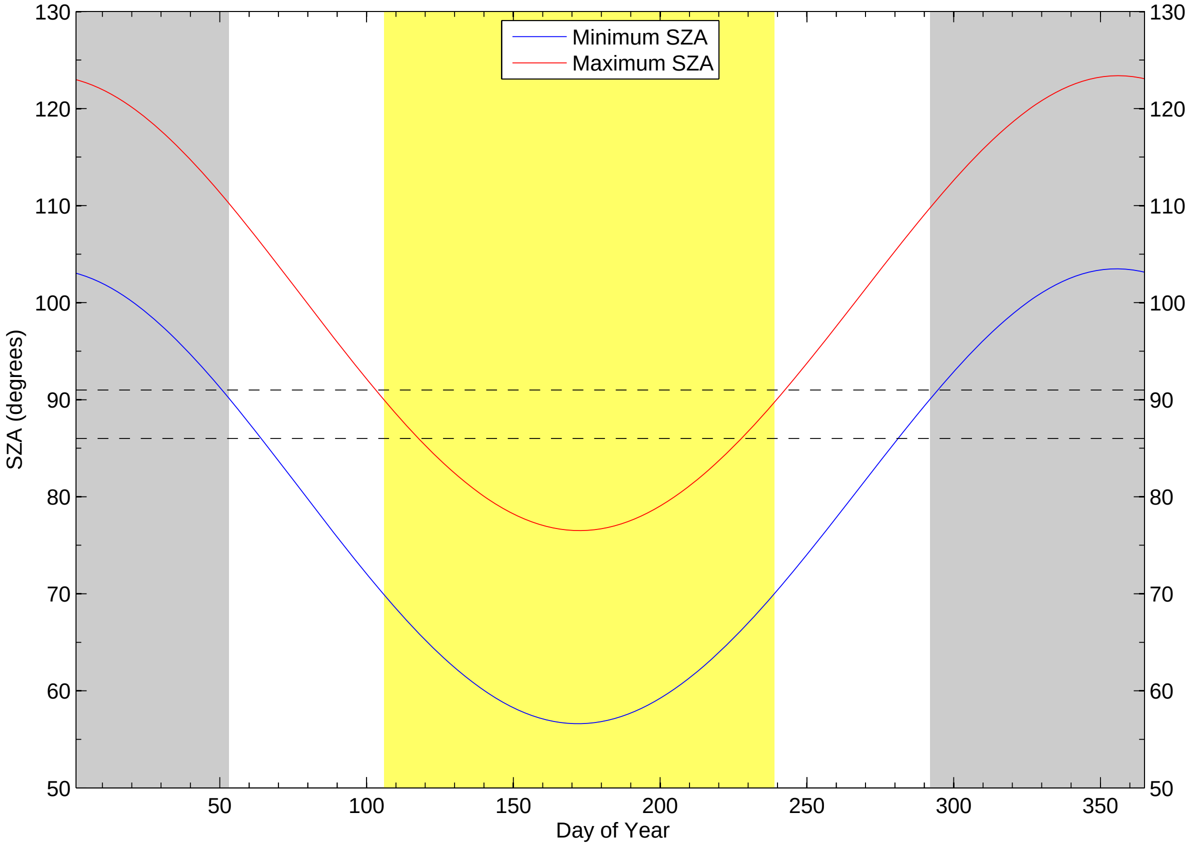

Figure 6.14: Maximum and minimum SZAs in Eureka throughout the year, calculated for 2007. The gray shaded region indicates polar night, when the Sun does not rise above the horizon, while the yellow shaded area indicates the time of year when the Sun is continuously above the horizon. The horizontal dotted lines indicate 86° and 91°, the preferred range of SZAs used in the calculation of VCDs

until the end of August. Ozone decreases through the summer for two reasons: transport of ozone into the polar regions is reduced in the summer, and with the Sun constantly above the horizon, photochemical destruction of ozone occurs continuously. In 2006, the start of the period of increasing ozone begins in mid-September, while in 2007 it begins in late August. In both years, ozone concentrations increase steadily through the fall until the beginning of polar night. In 2006, the VCDs continue to increase at the start of polar night as Eureka moves further away from the forming polar vortex. In 2007, the VCDs begin to decrease after the Sun sets, while the PV increases.

Figure 6.13(b) shows the NO_2 VCDs from the PEARL-GBS and UT-GBS from August 2006 to October 2007. As in Figure 6.13(a), open symbols are used when the Sun does not set below 86°. Also shown in this figure is the number of hours of daylight (defined as when the SZA is below 90°). NO_2 is formed throughout the day, as N_2O_5 is photolysed. The amount of daylight is the dominant factor in the NO_2 concentrations. As the amount of available sunlight decreases in the fall or increases in the spring, the concentrations of NO_2 quickly decrease and increase. In the spring, the recovery of NO_2 is complicated by the position of the vortex. Once the vortex breaks apart, the concentrations of NO_2 steadily increase, leveling off near the end of June to remain relatively constant over the summer. At the end of August, the Sun sets for the first time since April, and the concentrations quickly begin decreasing. In both years, the rapid decrease begins at the end of August, with the setting of the Sun. In both years, the NO_2 steadily decreases until the beginning of polar night. In 2006, concentrations continue to decrease. In 2007, concentrations start to increase. This behaviour corresponds to the behaviour of the ozone VCDs, and is related to the position of the newly forming polar vortex. Outside of polar springtime, ozone and NO_2 are negatively correlated (correlation coefficient $\backsim$ -0.56 for August to October 2006, -0.58 for May to October 2007).

Figure 6.15 shows the BrO DSCDs from the PEARL-GBS calculated at 90° and 75° using a daily reference spectrum from the highest possible SZA. Negative values indicate that the reference spectrum is taken at a SZA close to 90° or 75°, so the DSCD is not large. The 600 gr/mm grating is used until February 28 (day 59), after which the 1200 gr/mm grating is used. After June 1 (day 152), the instrument resumed using the 600 gr/mm grating, to allow for ozone measurements through the summer. BrO concentrations had decreased significantly from the maximum observed in March, and were too small to be measured accurately with the 600 gr/mm grating. Although BrO concentrations begin to increase in the fall, the concentration remains too small for accurate DSCDs. The 75° DSCDs show the continued decrease and leveling off of the BrO columns expected

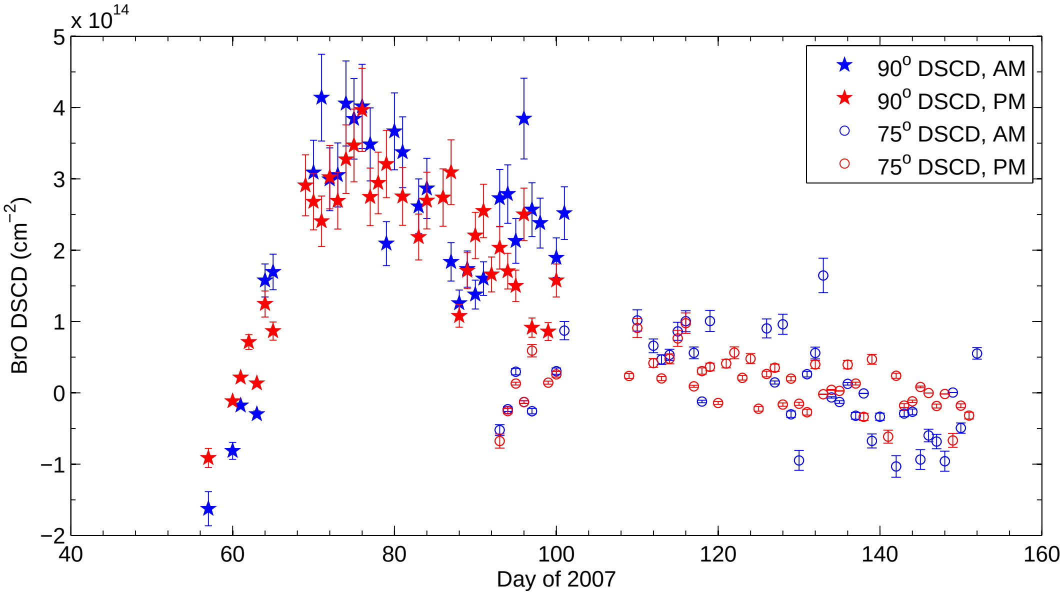

Figure 6.15: BrO DSCDs from the PEARL-GBS from February to June 2007. DSCDs at both 90° and 75° are shown.

through the summer. As observed during the springtime campaign, the BrO DSCDs show weak positive correlation with ozone (correlation coefficient ∽ 0.41) and weak negative correlation with with NO_2 (correlation coefficient ∽ -0.39).

6.6 Summary

Ozone and NO_2 VCDs have been measured at Eureka by the UT-GBS during polar sunrise as part of the Canadian Arctic ACE validation campaigns from 2004 to 2007, continuing the time series begun in 1999. BrO VCD measurements were made from 2005 to 2007. In August 2006, the PEARL-GBS was permanently installed at PEARL, and has made continuous measurements of ozone and NO_2 VCDs. During the 2007 Eureka campaign, the PEARL-GBS was operated with the 1200 gr/mm grating, giving a finer resolution and allowing for the retrieval of OClO DSCDs. BrO VCD measurements with the finer grating were also made during the Eureka campaign. The four campaigns took place during four winters with very different meteorology: in 2004 and 2006, the polar vortex had undergone a sudden stratospheric warming earlier in the winter, and a weakened vortex had reformed prior to the start of the campaign. In 2005 and 2007, the polar vortex was strong. In 2005, Eureka spent most of the campaign on the edge of the vortex, while in 2007, Eureka spent a large amount of time continuously inside the vortex.

In 2005, the ozone and NO_2 columns are negatively correlated when Eureka is on the edge of the vortex, and positively correlated when Eureka is outside the vortex. In 2004 and 2006, the correlation is generally negative, while in 2007 the relation is generally positive. During the springtime campaigns, the negative correlation is a reflection of transport of relatively NO_2-rich and ozone-poor air from lower latitudes. In 2007, Eureka was inside the polar vortex for the bulk of the campaign. The vortex was strong that year, with chlorine activation occurring. The positive correlation may be the result of nitrogen converting active chlorine into reservoir species, discussed in Chapter 1. As seen with the PEARL-GBS, the two species are negatively correlated in the summer and fall, when there is no polar vortex, a reflection of the nitrogen-driven catalytic cycles discussed in Chapter 1. Ozone and BrO columns generally follow the same trends in the 2005–2007 campaigns, with the exception of the beginning of the 2005 campaign when Eureka was inside or on the edge of the polar vortex. This indicates the occurrence of the BrO/ClO-driven catalytic destruction cycle. In all years, BrO and NO_2 are negatively correlated at the end of the campaign, which is consistent with the formation of $BrONO_2$, as NO_2 concentrations increase in the spring. Table 6.3 gives the correlation coefficients (r) calculated for the three species over the four campaigns.

The BrO DSCDs observed in all three winters are larger than the DSCDs observed by similar instruments at similar latitudes, however this variation could be due to differing amounts of BrO in the stratosphere during these winters. The OClO DSCDs are comparable to similar measurements made in the Arctic springtime.

BrO measurements were not possible outside of the spring and early summer with

Table 6.3: Correlation coefficients (r) calculated for ozone, NO_2, and BrO for the four springtime campaigns from the UT-GBS and from August 2006 to October 2007 for the PEARL-GBS. For the PEARL-GBS, the ozone/NO_2 correlation is for August to October in 2006 and May to October in 2007 thus both exclude polar springtime values. The PEARL-GBS correlations for BrO are for BrO DSCDs from February to May. In 2005, two values are given for the ozone correlations for the two different régimes observed (inside and outside the vortex).

Year	O_3/NO_2	O_3/BrO	NO_2/BrO
Spring 2004	-0.60	-	-
Spring 2005	-0.76/0.85	-0.90/0.67	-0.55
Spring 2006	-0.65	0.61	-0.85
Spring 2007	0.59	0.32	-0.61
PEARL-GBS 2006	-0.56	-	-
PEARL-GBS 2007	-0.58	0.41	-0.39

the PEARL-GBS, due to the coarser resolution of the grating used outside of this period and the smaller amount of BrO present in the atmosphere.

Two methods of finding the ozone and NO_2 VCDs from the DSCDs were compared. The averaging method and Langley plot method for ozone are found to produce similar results when observing homogeneous ozone fields. When the field is not homogeneous, such as the case during the beginning of the Eureka 2005 campaign, the results can be very different. The averaging and 90° method for NO_2 are found to agree, regardless of the homogeneity of the NO_2 field.

Chapter 7

The Eureka Campaigns 2004–2007: Comparison of Measurements

The four Eureka campaigns involved a suite of six to nine ground-based instruments, including three to five zenith-viewing UV-visible grating spectrometers. Detailed NDACC-style comparisons of the ozone and NO_2 DSCDs and VCDs from these instruments are discussed in this chapter, following the methods presented in Chapter 4. The ozone and NO_2 VCDs are also compared to the ACE-FTS and ACE-MAESTRO instruments on board the ACE satellite. The results of the 2004–2006 campaigns presented in this chapter have been published in Fraser et al. (2008).

7.1 Instrumentation and Data Analysis

In 2004, three UV-visible instruments were operated during the intensive phase, until March 8: the UT-GBS, MAESTRO, and SPS. Only the UT-GBS remained for the extended phase of the campaign. In 2005, the SAOZ was added to the instrument suite. The four instruments were operated during the intensive phase, with measurements beginning February 18 and continuing until March 8. During the extended phase, from March 9 to March 31, only SAOZ and the UT-GBS remained in Eureka. In 2006, the same four UV-visible instruments were operated during both the intensive and extended phases of the campaign. In 2007, the PEARL-GBS joined the instrument suite. All five instruments took part in the both the intensive and extended phases of the campaign. The data from the SPS and MAESTRO are not yet available for 2007, and so cannot be included here.

Ozonesondes are launched weekly at the Eureka weather station. During the intensive phase of all four campaigns, ozonesondes were launched daily. Generally the ozonesondes are launched at 23:15 UT (18:15 LT), however, on occasion, the launch time is altered to match a satellite overpass.

As described in Chapter 3, the programme WinDOAS is used for the analysis of the five ground-based instruments. The details of the WinDOAS analysis are given in Table 7.1. These settings were chosen to optimize the fits from all the instruments. Daily reference spectra were used, with SZAs varying from 90.8° for the earliest day of the campaign (February 20) to 70.3° for the last day of the campaign (April 14). If the reference spectra of the two instruments differ by more than 0.5°, that day was not included in the comparisons. This eliminated fewer than five comparisons from each campaign.

Figure 7.1 shows typical ozone and NO_2 spectral fits from the four instruments operating on March 4, 2005, and from February 28, 2007 for the PEARL-GBS. Fits from all years are comparable for all instruments. For both species, the MAESTRO spectral fits are noisier than those from the other instruments. This is because the other instruments average spectra before they are analysed. For the UT-GBS, PEARL-GBS, and SAOZ, the number of spectra that are averaged is variable (4–300 for the GBSs, 1–115 for SAOZ), and is limited by the maximum time taken to record the spectra, to avoid smearing over a large SZA range. SPS averages two spectra before they are analysed. MAESTRO records individual spectra. In this work, MAESTRO DSCDs are averaged over 0.25° intervals. Individual integration times range between 13 ms and 30 s for the

Table 7.1: Details of the WinDOAS retrievals for the five UV-visible instruments. The same settings are used for the UT-GBS and PEARL-GBS. The same settings are used for each year of analysis. The same polynomial degree is used in the calibration for both the wavelength shift and slit function parameters, and is given in the column CPD (calibration polynomial degree). CWL (calibration window limit) is the range used for the wavelength calibration. The continuous function (CF) is the degree of the polynomial fit to the optical depth in the DOAS analysis. The offset is the term fit to correct for stray light, discussed in Chapter 3.

Instrument	Species	CPD	CWL (nm)	# of Subwindows	CF	Offset
UT-GBS	Ozone	3	400–550	5	0,1,2,3	none
UT-GBS	NO_2	3	400–550	5	0,1,2,3	none
SAOZ	Ozone	3	400–550	4	0,1,2,5	linear
SAOZ	NO_2	3	400–550	4	0,1,2,5	none
MAESTRO	Ozone	3	400–550	5	0,1,2,3	none
MAESTRO	NO_2	2	400–450	3	0,1,2,3,4,5	none
SPS	Ozone	3	400–550	4	0,1,2,3,4,5	linear
SPS	NO_2	2	400–450	3	0,1,2,3,4,5	linear

GBSs, between 0.5 s and 19 s for SAOZ, and between 50 ms and 10 s for MAESTRO and SPS. The NO_2 DOD fits for SPS and MAESTRO are poorer than the fits from the UT-GBS and SAOZ. The Eureka campaigns take place just after polar sunrise, when the NO_2 column is very small. The NO_2 is near the limits of detection of SPS and MAESTRO. The NO_2 fit from the PEARL-GBS is also noisier than those from the UT-GBS and SAOZ. This is a result of the fit being from a day earlier in the year, with a smaller NO_2 column, and the noon-time reference spectrum is from a lower angle, so the differential absorption of NO_2 is smaller.

7.1.1 ACE

The ACE satellite, also known as SCIentific SATellite (SCISAT), is a solar occultation satellite launched by the Canadian Space Agency in August 2003 (Bernath et al., 2005). The goal of the ACE mission is to improve the understanding of the chemical and dynamical processes that control the concentrations of ozone in the middle atmosphere. Two instruments make up the payload: the ACE-FTS and ACE-MAESTRO. ACE-FTS is

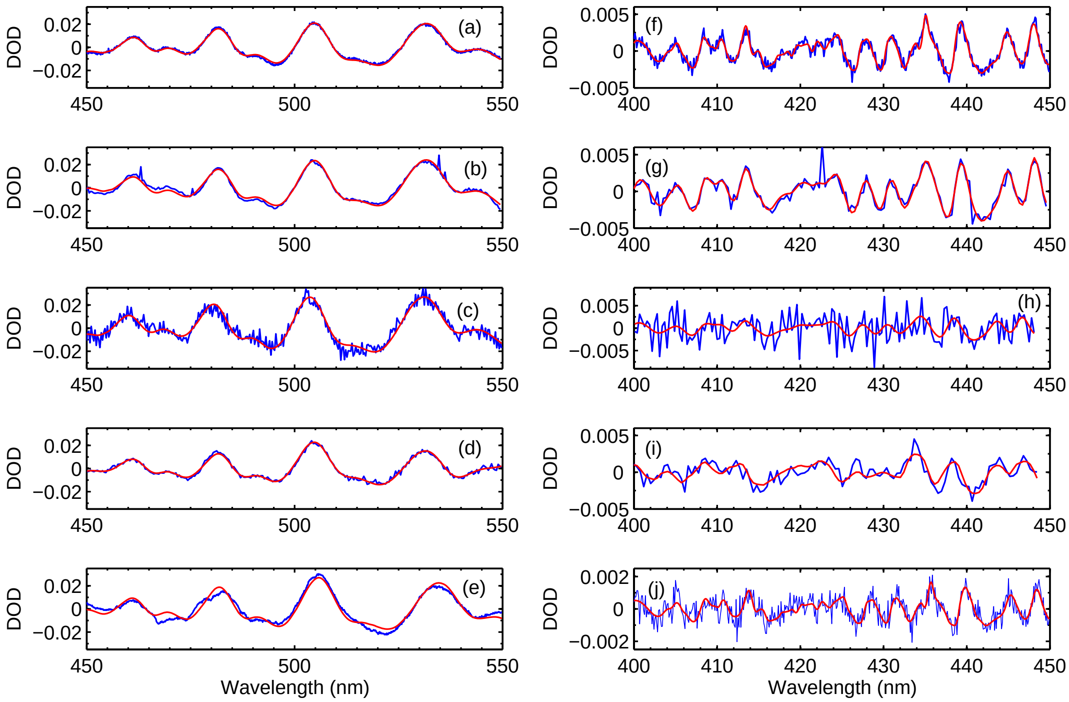

Figure 7.1: Typical differential optical depth ozone fits for (a) UT-GBS, (b) SAOZ, (c) MAESTRO, (d) SPS, and (e) PEARL-GBS. Typical NO_2 fits for (f) UT-GBS, (g) SAOZ, (h) MAESTRO, (i) SPS, and (j) PEARL-GBS. The fits for the first four instruments are for the afternoon of March 4, 2005 at a SZA of approximately 90°. The PEARL-GBS fit is from the afternoon of February 28, 2007 at a SZA of approximately 90°. In all plots, the blue line is the data, while the red line is the fit to the data. Note the different scales for MAESTRO and PEARL-GBS NO_2 fits.

an infrared Fourier transform spectrometer, with high resolution (0.02 cm^{-1}), operating from 750–4400 cm^{-1} (Bernath et al., 2005). The version 2.2 data set including updates for ozone, HDO, and N_2O_5 is used here (Boone et al., 2005). ACE-MAESTRO is a UV-visible-near-IR double spectrometer, with a resolution of 1.5–2.5 nm, and a wavelength range of 270–1040 nm. Version 1.2 is used here (McElroy et al., 2007). Only overpasses within 500 km of Eureka are considered; the distance is determined using the location of the occultation at the 30 km tangent point. Figure 7.2 shows the location of the satellite overpasses used in the comparisons. All of the overpasses are sunset occultations.

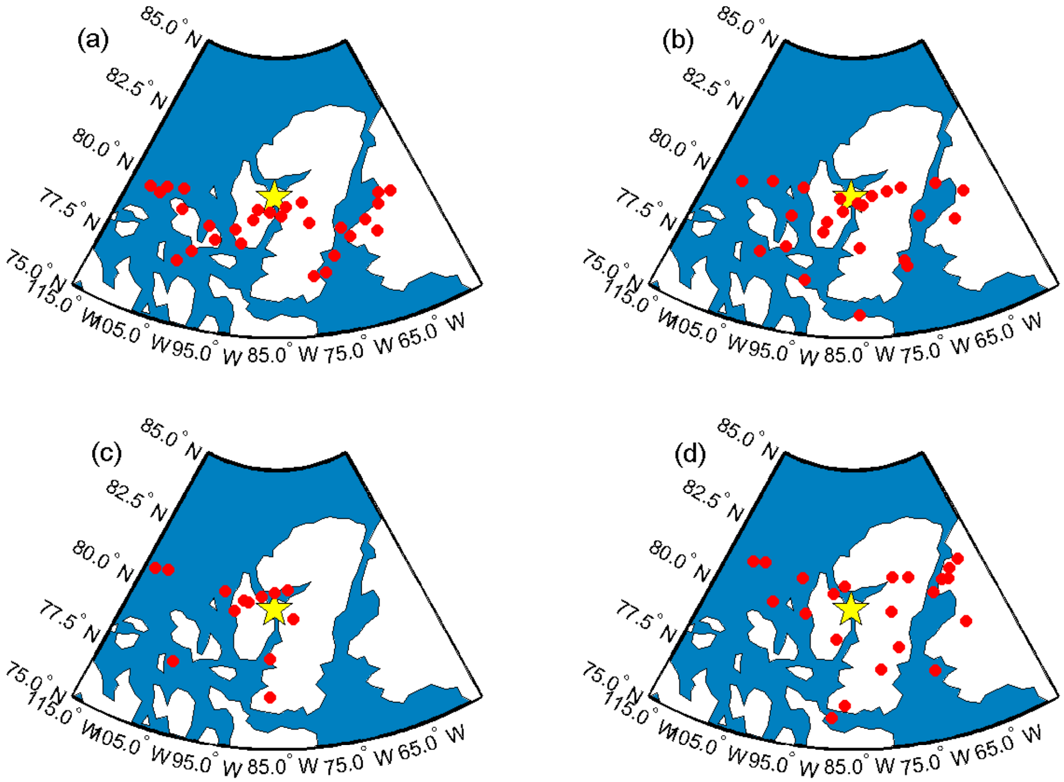

Figure 7.2: Location of ACE occultations at 30 km tangent altitude within 500 km of PEARL in February and March (a) 2004, (b) 2005, (c) 2006, and (d) 2007. The yellow star indicates the location of PEARL.

7.2 Differential Slant Column Density Comparisons

In this section, the DSCDs and VCDs are compared following the methods of the NDACC, which are described in Chapter 4. Figure 7.3 shows an example of the Type 1 regression analysis for March 4, 2005 between the UT-GBS and SAOZ. The increasing residuals with SZA seen in Figure 7.3(b) are typical of DSCDs that were analysed in different wavelength regions. This is not the case for this comparison, and this feature is common to all UT-GBS vs. SAOZ comparisons performed for Eureka. This is possibly due to the differing fields-of-view of the instruments, the effect of which is further discussed in Section 7.2.1. Figure 7.4 shows an example of the Type 2 comparisons for the same instruments and twilight period. The small ratio for ozone is consistent with the increasing residuals

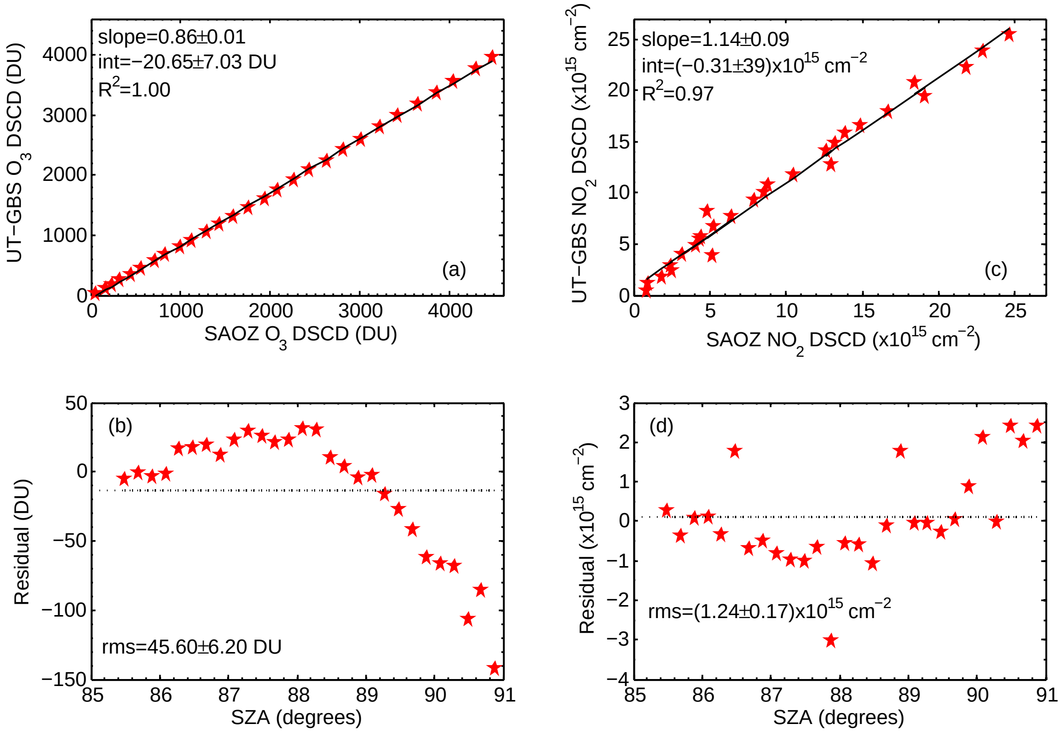

Figure 7.3: (a) Type 1 regression analysis for ozone between the UT-GBS and SAOZ for the afternoon of March 4, 2005, (b) residuals of the fit in (a), (c) same as (a) but for NO_2, and (d) same as (b) but for NO_2. In (a) and (c) the solid lines are the results of the regression fit. In (b) and (d) the dashed lines are the average residuals of the regression fit.

seen in the Type 1 comparisons, and is also due to the different fields-of-view of the two instruments.

The offset of the Type 2 comparisons is not included in the analysis. For polar measurements, the amount of sunlight varies significantly from day to day, meaning that the diurnal variation is not constant, and the offset between morning and afternoon columns is not expected to be constant.

7.2.1 Ozone

Figure 7.5 shows the ozone DSCDs for the UT-GBS, SAOZ, SPS, and MAESTRO for the afternoon of March 4, 2004–2006. The UT-GBS, PEARL-GBS, and SAOZ are shown for the afternoon of February 28, 2007. The general agreement between all the instruments

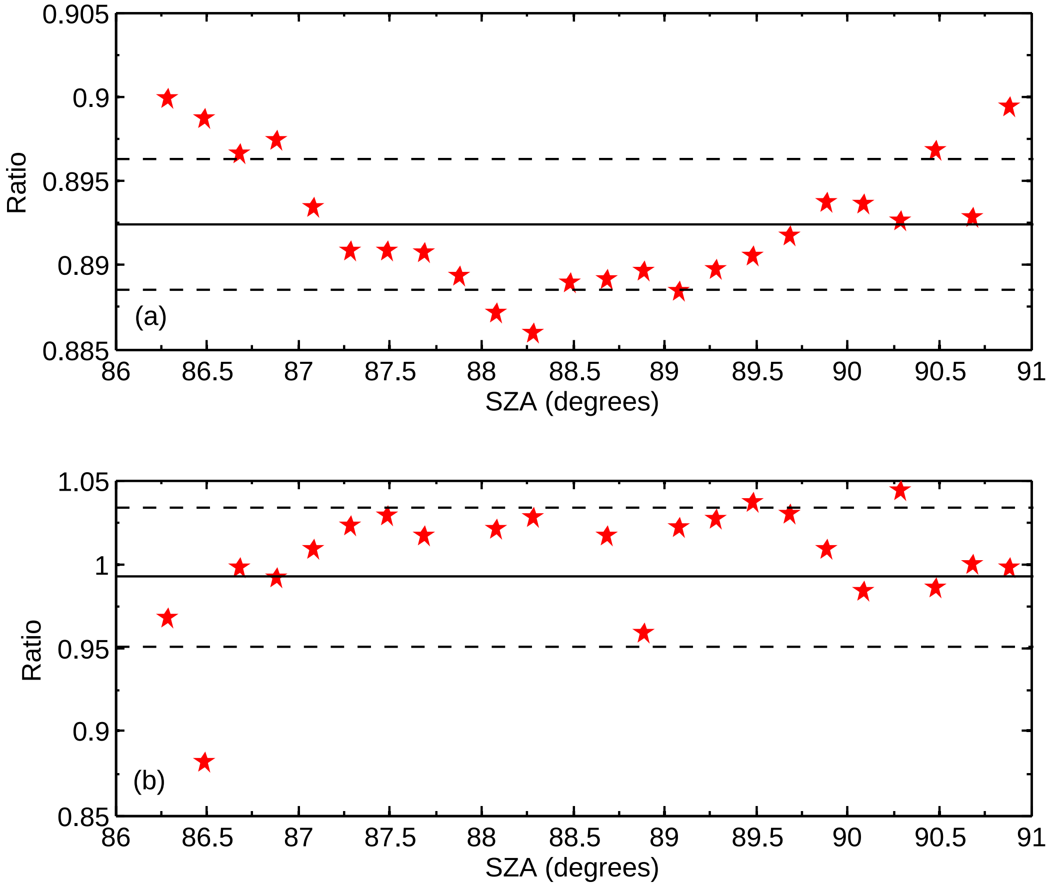

Figure 7.4: (a) Type 2 comparisons for ozone between UT-GBS and SAOZ for the afternoon of March 4, 2005. The solid line indicates the mean of the ratio between the two instruments, while the dashed lines show the extent of the standard deviation. (b) Same as (a) but for NO_2.

is good up to 92°. At this point the MAESTRO and SAOZ DSCDs begin to diverge from the other instruments. In the case of SAOZ, the divergence is always to lower DSCDs. This divergence is due to the consistently warm temperatures (25-30°C) inside the viewing hatch of the instrument. The data beyond 92° is unreliable due to the dark signal (which includes thermal noise) making up a larger percentage of the total signal. The MAESTRO DSCDs diverge to both lower and higher DSCDs, depending on the twilight period. There seems to be no relation between which way the DSCDs diverge and the outside temperature or cloudiness of the day. As only SZAs up to 91° are used in the DSCD comparisons and in the calculation of VCDs, these divergences will not affect

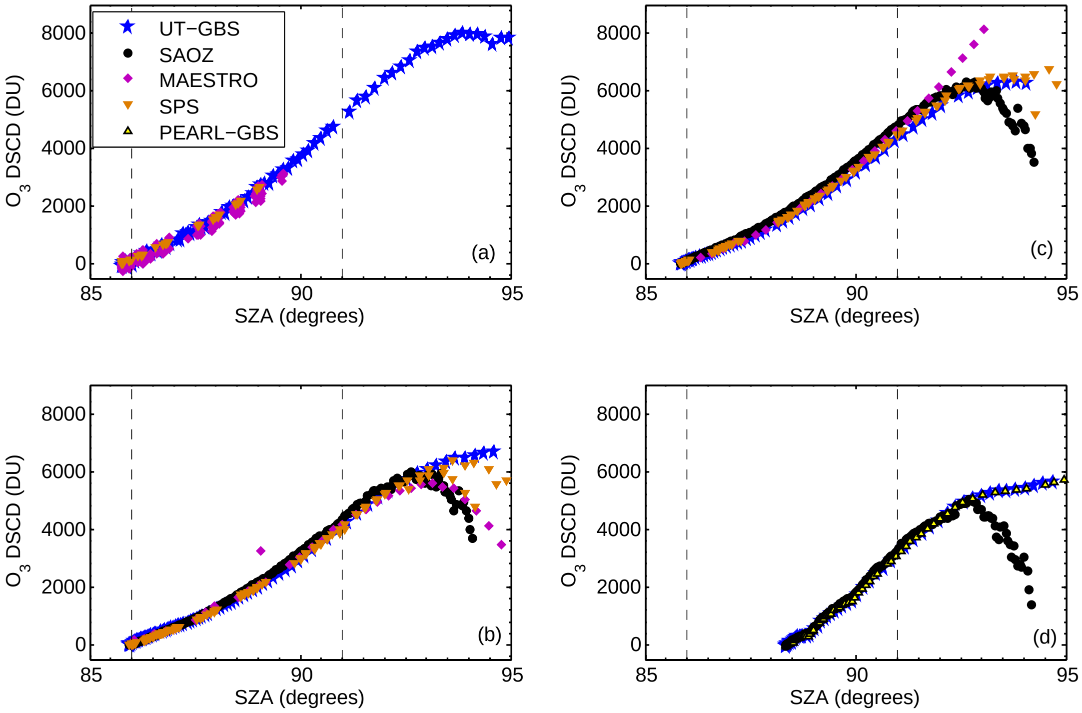

Figure 7.5: Ozone differential slant column densities for the afternoon of March 4 (a) 2004, (b) 2005, (c) 2006, and (d) February 28, 2007. The dashed lines at 86° and 91° indicate the range of DSCDs used in the calculation of VCDs. For the Type 2 comparisons, DSCDs between 85° and 91° are used. For the Type 1 comparisons, all DSCDs up to 91° are used.

the comparisons to be discussed. The UT-GBS and PEARL-GBS DSCDs are in very good agreement.

Figure 7.6 shows the results of the Type 1 ozone DSCD comparisons. In all figures, the campaign-averaged parameter is given, with the standard error represented as the error bars. Table 7.2 gives the number of twilight periods averaged in each of the comparisons. No MAESTRO vs. SPS comparison is given for the 2004 campaign due to the small number of twilight periods available for comparison (less than three).

Examining the slopes first, 18 of the 34 values (seen in Figure 7.6(a),(d),(g), and (j)) meet the NDACC standards, and a further four meet the standards within error bars. The comparisons in 2004, 2006, and 2007 are similar, with the exception of the UT-GBS vs. SPS afternoon comparisons. It should be noted that the 2004 comparison

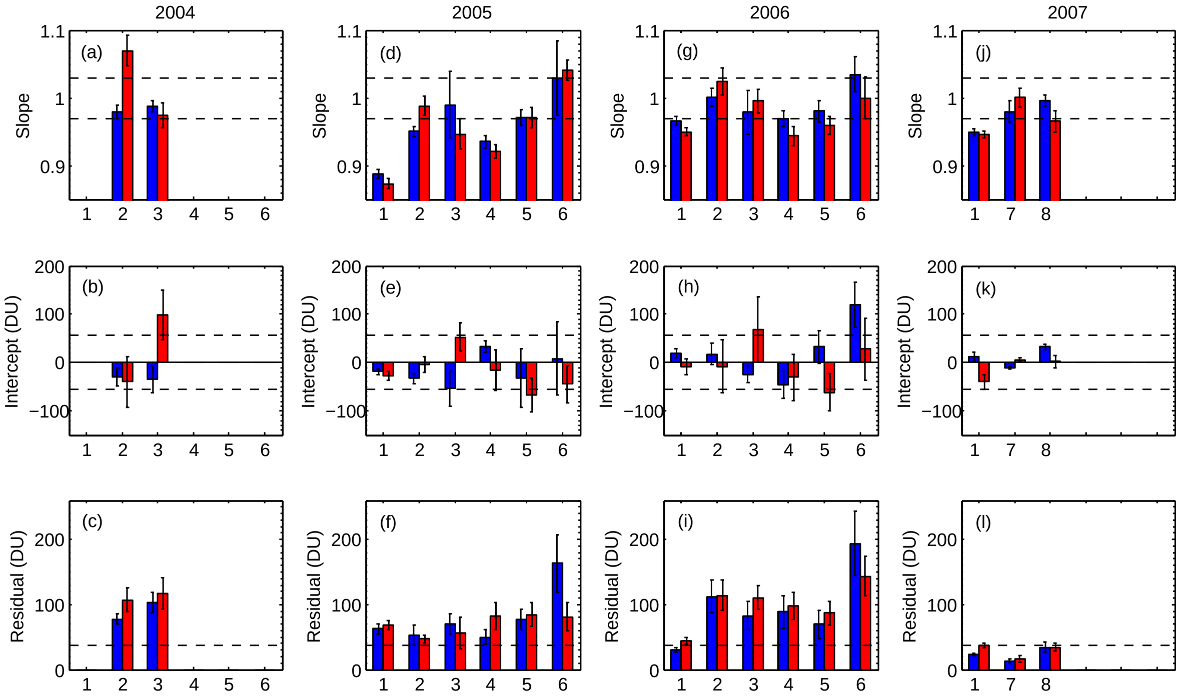

Figure 7.6: Ozone DSCD Type 1 results for (a-c) 2004, (d-f) 2005, (g-i) 2006, and (j-l) 2007. In all figures, blue represents the morning comparisons, while red represents the afternoon. Error bars indicate the standard error. Dashed lines indicate the NDACC standards. The numbers represent the comparisons between the different instruments: 1 – UT-GBS vs. SAOZ, 2 – UT-GBS vs. SPS, 3 – UT-GBS vs. MAESTRO, 4 – SPS vs. SAOZ, 5 – MAESTRO vs. SAOZ, 6 – MAESTRO vs. SPS, 7 – UT-GBS vs. PEARL-GBS, 8 – PEARL-GBS vs. SAOZ.

has only three data points. The NDACC requires at least ten days of comparisons to ensure proper statistics. The slope comparisons tend to be worse in 2005, especially the UT-GBS vs. SAOZ (1) comparison. As discussed in Chapter 6, Eureka was on the edge of the polar vortex throughout most of the campaign. SAOZ has a significantly larger field-of-view than the UT-GBS (10° vs. 2°). Because of this, SAOZ will view more of the atmosphere than the UT-GBS. With the heterogeneous ozone field expected due to Eureka's position on the edge of the vortex, the discrepancy in the DSCDs is likely a result of the instruments sampling different portions of the atmosphere. The sizes of the fields-of-view of MAESTRO and SPS are between those of the UT-GBS and SAOZ, so the effect is not expected to be as large. The UT-GBS and PEARL-GBS (7) meet the NDACC slope standard, however no other pairs of instruments consistently meet the standard.

Table 7.2: Number of twilight periods used in the campaign averages for ozone and NO_2 for both Type 1 and 2 comparisons.

		O_3		NO_2	
Comparison	Year	AM	PM	AM	PM
UT-GBS vs. SAOZ	2005	29	30	29	30
	2006	30	34	29	29
	2007	34	37	28	32
UT-GBS vs. SPS	2004	5	3		
	2005	9	9	8	8
	2006	17	23	10	18
UT-GBS vs. MAESTRO	2004	3	3		
	2005	6	7		
	2006	17	14	10	10
SPS vs. SAOZ	2005	8	10	6	7
	2006	16	23	13	22
MAESTRO vs. SAOZ	2005	7	9		
	2006	15	17	10	9
MAESTRO vs. SPS	2005	6	8		
	2006	11	10	8	10
UT-GBS vs. PEARL-GBS	2007	6	5	4	3
PEARL-GBS vs. SAOZ	2007	6	6	3	5

The UT-GBS and SAOZ consistently do not meet the slope standards. The UT-GBS and MAESTRO (3) meet the NDACC standard within error bars each year; the only twilight period that does not meet the standards is the 2005 afternoon, where there are just seven days to compare. Generally, comparisons with SPS and MAESTRO improve in 2006 when these instruments participated in the extended phase of the campaign.

For the average intercepts, in Figure 7.6(b), (e), (h), and (k), 30 of the 34 comparisons meet the NDACC standards, and a further four comparisons agree within the error bars. For comparisons involving SPS and MAESTRO, the standard errors are large compared to the average intercepts. The UT-GBS vs. PEARL-GBS (7), UT-GBS vs. SAOZ (1), UT-GBS vs. SPS (3), and SPS vs. SAOZ (4) comparisons consistently meet the NDACC standard for both twilight periods for all years of comparison.

The average residuals (Figure 7.6(c), (f), (i), and (l)) are all much larger than the

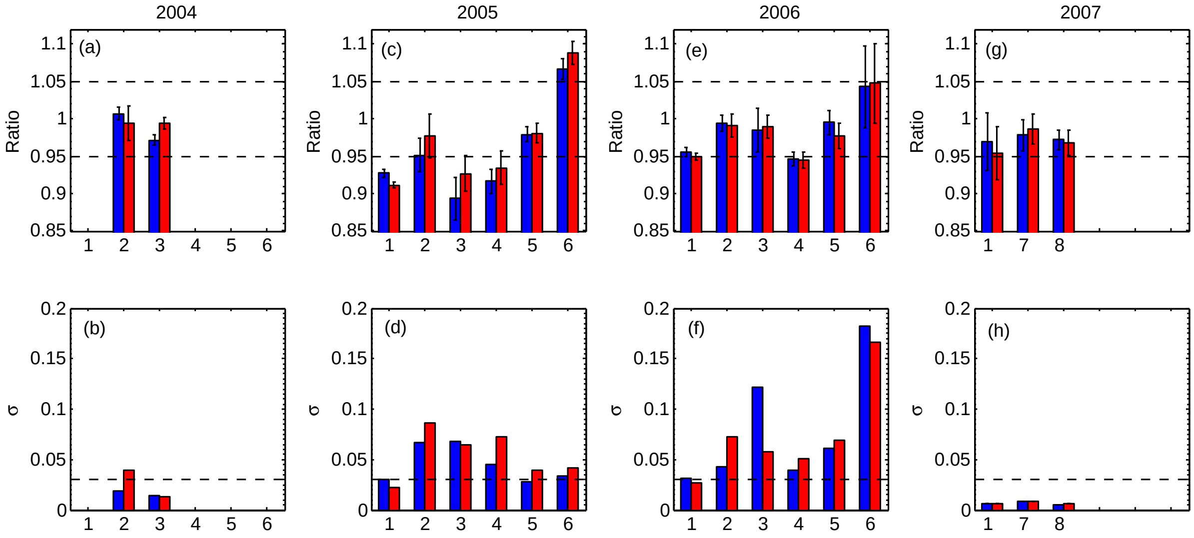

Figure 7.7: Ozone Type 2 ratio results for (a) 2004, (c) 2005, (e) 2006, and (g) 2007. The error bars represent the standard error. The standard deviation results for (b) 2004, (d) 2005, (f) 2006, and (h) 2007. The dashed lines indicate the NDACC standards. Colours and numbers represent the same comparisons as Figure 7.6.

NDACC standard, with large standard error, with the exception of the UT-GBS vs. SAOZ (1) 2006 comparison and all comparisons in 2007. As discussed in Chapter 4, large residuals are an indication of scatter in at least one of the data sets.

The campaign-averaged results of the Type 2 ozone comparisons are shown in Figure 7.7. In 2004, 2006, and 2007, most of the ratios agree within the NDACC standards, or are slightly outside the range (e.g., the SPS vs. SAOZ (4) 2006 comparisons). In 2005, the UT-GBS vs. SAOZ (1), UT-GBS vs. MAESTRO (3), SPS vs. SAOZ (4), and MAESTRO vs. SPS (6) comparisons are all outside the range, although some of these comparisons agree within the error bars. In Figure 7.6, the corresponding comparisons generally have slopes that do not meet the NDACC standards, and intercepts that do. As discussed above, this discrepancy may be due to Eureka's position on the edge of the polar vortex during much of the campaign, and the difference in fields-of-view of the instruments.

The standard deviation of the ratios for the campaign are also shown in Figure 7.7.

Most of the standard deviations are larger than the requirement, the exceptions being the UT-GBS vs. SAOZ (1) comparisons for all years, the UT-GBS vs. MAESTRO (3) 2004 comparison, the morning of the UT-GBS vs. SPS (2) 2004 comparison, the morning of the SPS vs. SAOZ (4) 2005 comparison, and all the comparisons in 2007. This is an indication of the consistency of the ratio comparisons – small standard deviations mean that the ratio has a smaller spread of values. The standard deviations for comparisons involving SPS and MAESTRO are, in general, larger in 2006 than in 2005. This is likely a result of these instruments participating in the extended campaign. As the light levels increased towards the end of March, both instruments recorded many more saturated spectra than during the intensive phase. As a result there are fewer DSCDs for each twilight for these instruments. The regression parameters for comparisons involving MAESTRO and SPS during the extended phase are more scattered than during the intensive phase. If only the intensive phase is considered, the standard deviations are smaller.

7.2.2 NO_2

Figure 7.8 shows the NO_2 DSCDs from the five ground-based instruments for March 4, 2004–2006 and February 28, 2007 (the same days as in Figure 7.5). The UT-GBS DSCDs from 2004 are much more scattered than those from the other years, as a result of the low signal-to-noise ratio caused by the error in the data acquisition code, discussed in Section 2.4.1. In all years, there is more scatter in the data, and a greater discrepancy is seen between the instruments than for the ozone DSCDs. In 2004, the SPS and MAESTRO DSCDs are roughly the same at noon, and are within the large scattered range of the UT-GBS. At high SZAs, the DSCDs from the three instruments diverge. In 2005–2006, the agreement between all instruments is good at lower SZAs, and the DSCDs begin to diverge at higher SZAs. The MAESTRO and SPS DSCDs are more scattered than those of the other instruments at all SZAs. In 2005, the UT-GBS and SAOZ DSCDs agree, while the SPS and MAESTRO DSCDs are smaller. In 2006, the DSCDs from the

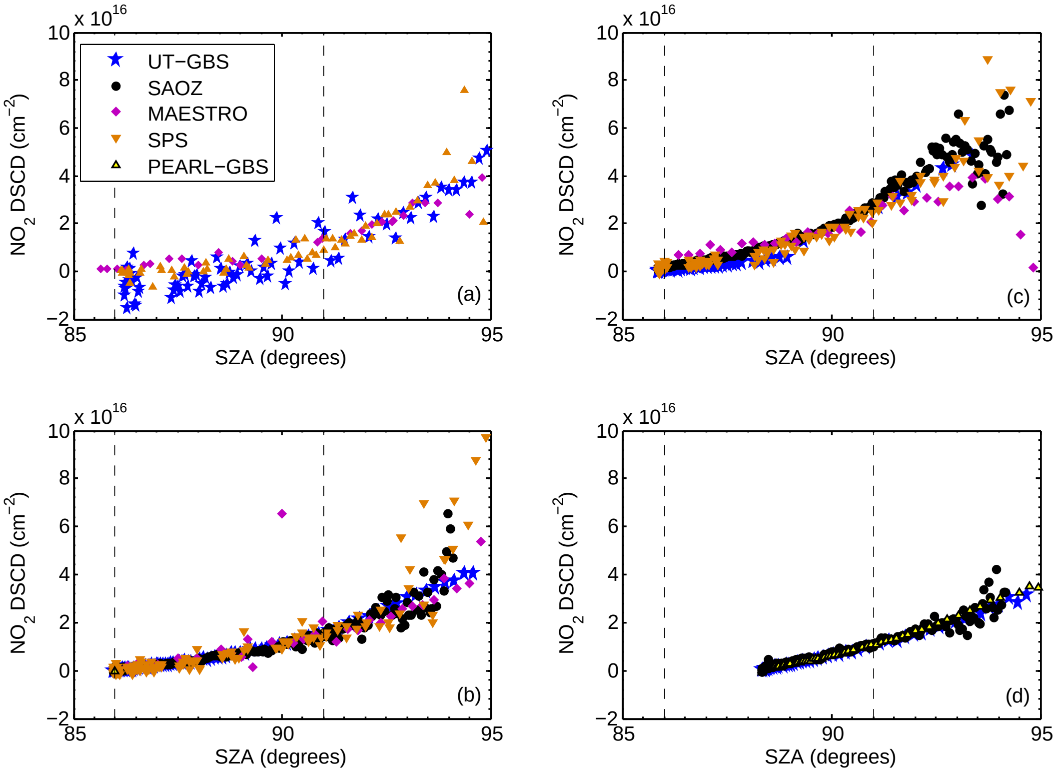

Figure 7.8: NO_2 differential slant column densities for the afternoon of March 4 (a) 2004, (b) 2005, (c) 2006, and (d) February 28, 2007. The dashed lines at 86° and 91° indicate the range of DSCDs used in the calculation of VCDs. For the Type 2 comparisons, DSCDs between 85° and 91° are used. For the Type 1 comparisons, all DSCDs up to 91° are used.

SPS and MAESTRO are scattered about the DSCDs from the other instruments. The SAOZ DSCDs become scattered above 92°, a result of the larger dark signal contribution discussed in Section 7.2.1. Only SZAs up to 91° are used in the comparisons. In 2007, the SAOZ behaves as in other years, while the UT-GBS and PEARL-GBS DSCDs are in good agreement at all SZAs.

Figure 7.9 shows the Type 1 comparisons for NO_2 for the 2005–2007 campaigns. The error bars represent the standard errors. No comparisons are shown in 2004 due to the small number of comparisons for this year (less than three), as well as the large amount of scatter on the DSCDs from the UT-GBS. No NO_2 comparisons from MAESTRO are shown in 2005 due to the small number of twilight periods available for comparison. The

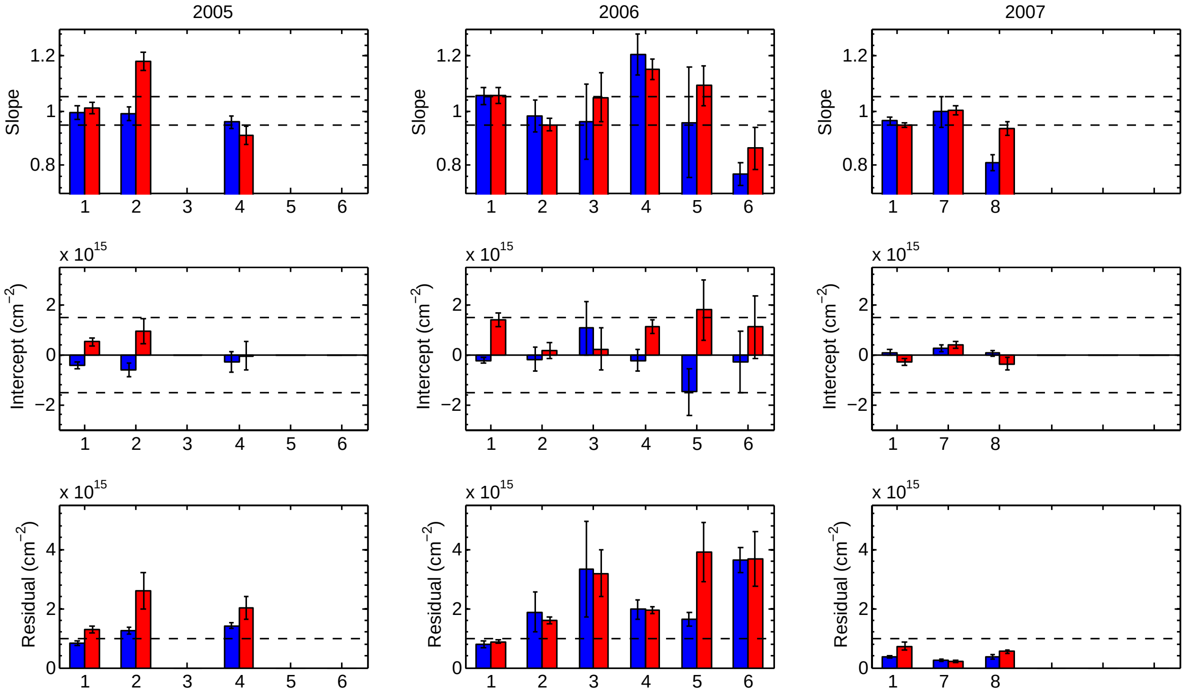

Figure 7.9: NO_2 DSCD Type 1 results for (a-c) 2005, (d-f) 2006, and (g-i) 2007. In all figures, blue represents the morning comparisons, while red represents the afternoon. Error bars indicate the standard error. Dashed lines indicate the NDACC standards. The numbers represent the comparisons between the different instruments: 1 – UT-GBS vs. SAOZ, 2 – UT-GBS vs. SPS, 3 – UT-GBS vs. MAESTRO, 4 – SPS vs. SAOZ, 5 – MAESTRO vs. SAOZ, 6 – MAESTRO vs. SPS, 7 – UT-GBS vs. PEARL-GBS, 8 – PEARL-GBS vs. SAOZ.

number of twilight periods used in the averages is given in Table 7.2.

Fifteen of the 24 campaign-averaged slopes agree within the NDACC standards, and an additional two agree within error bars. The UT-GBS and SAOZ (1) comparison meets the standard for both twilight periods for all three years of comparison. The UT-GBS and PEARL-GBS (7) also meet the standards. No other pairs of instruments consistently meet or fail to meet the NDACC standards. In general, the standard errors of the morning slopes are larger than the those of the afternoon slopes, a result of the smaller amount of NO_2 in the morning versus the afternoon.

For the campaign-averaged intercepts, 23 of the 24 comparisons meet the NDACC standards, while the remaining comparison meets the standard within the error bars. As

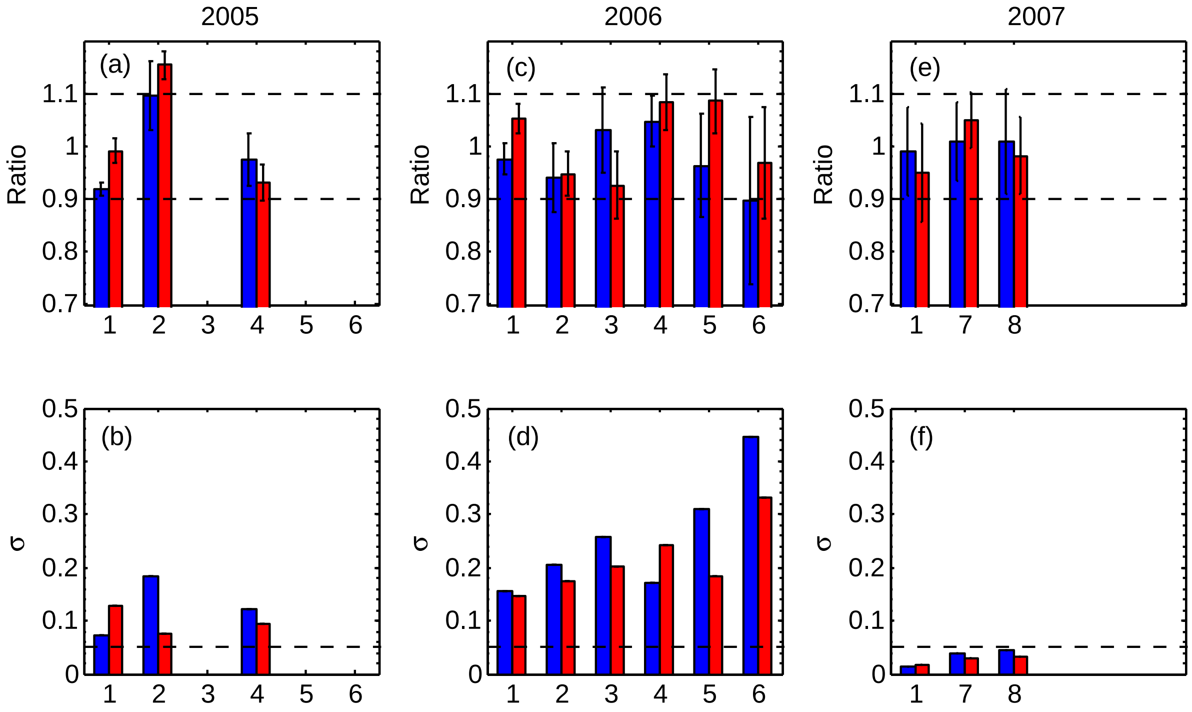

Figure 7.10: NO_2 Type 2 ratio results for (a) 2005, (c) 2006, and (e) 2007. The error bars represent the standard error. The standard deviation results for (b) 2005, (d) 2006, and (f) 2007. The dashed lines indicate the NDACC standards. Colours and numbers represent the same comparisons as Figure 7.9.

with the slope values, the standard errors are generally larger in the morning than in the afternoon. The campaign-averaged residuals for the UT-GBS vs. SAOZ (1) meet or are close to the NDACC standards for all years. In 2007, all the residuals meet the NDACC standards. The other residuals, however, are up to four times larger than the standard. This is a reflection of the scatter in the DSCDs discussed above.

The results of the Type 2 NO_2 comparisons are shown in Figure 7.10. All but two of the ratio results meet the NDACC standard. One of these, the MAESTRO vs. SPS (6) 2005 morning comparison, is very close with a large error bar. The other, the UT-GBS vs. SPS (2) 2005 afternoon comparison is large and does not agree within the error bars. The slope for this pair in the Type 1 comparisons shown in Figure 7.9 is also large.

The standard deviations of the ratios for the campaign are also shown in Figure 7.10.

In 2005–2006, all the standard deviations are up to nine times the NDACC standard. This is a reflection of the scatter in the DSCDs, and hence the VCDs. In 2007, all the standard deviations agree within the NDACC standard. The NDACC standards were established after a summer-time midlatitude intercomparison campaign (Roscoe et al., 1999), when NO_2 is at its annual peak. There is significantly less NO_2 in the polar springtime Arctic stratosphere, making it more difficult to detect, and therefore increasing the random noise (scatter) on the DSCDs.

7.2.3 Relation to the Previous MANTRA 2004 Comparison

The UT-GBS, SAOZ, MAESTRO, and SPS instruments all took part in the MANTRA 2004 campaign, discussed in Chapter 4. For the MANTRA Type 1 ozone comparison, the slopes were found to agree with the NDACC standards for the MAESTRO vs. SPS comparisons. The morning slopes for the UT-GBS vs. SPS and MAESTRO vs. SAOZ comparisons also met the NDACC standards. The UT-GBS vs. SPS afternoon and both UT-GBS vs. MAESTRO comparisons agreed with the standards within the standard error. The intercepts were universally large, two to four times the NDACC standards, with large standard error, and the residuals were large: up to three times the NDACC standard.

For the ozone Type 1 analysis for the Eureka campaigns, the slopes and residuals found here are consistent with the slopes and residuals found during the MANTRA campaign. The intercepts for the Eureka campaigns are much smaller than those found during MANTRA. A daily reference spectrum was used for the DOAS analysis in the Eureka campaigns, while a single reference spectrum was chosen for the MANTRA campaign. Daily reference spectra may cause more consistent intercepts since shifts in the wavelength calibration can occur over the course of a campaign for an instrument due to changes in the temperature. Since the diurnal changes in the wavelength calibration are in general smaller than the changes over a campaign, using a daily reference spectrum can result in better calibration for the DOAS analysis, and thus more accurate DSCDs at lower SZAs. As discussed in Chapter 3, the wavelength shifts relative to the reference spectrum determined by WinDOAS for the Eureka spectra are generally small, between 0 and 0.2 pixels through one twilight period, while the shifts determined by WinDOAS for the MANTRA spectra vary between 0 and 3 pixels, depending on the day. Over one twilight period during MANTRA, the variation can be as high as 0.8 pixels.

The MANTRA Type 2 ozone comparisons had the morning UT-GBS vs. SAOZ, UT-GBS vs. MAESTRO, and morning MAESTRO vs. SAOZ results all meeting the NDACC standards, while the other comparisons were close to the desired range. The SPS vs. SAOZ ratios were significantly smaller than the standards. The standard deviations for all comparisons, with the exception of the UT-GBS vs. SAOZ morning, were within the standards. The ozone Type 2 ratios presented here are better than those found during the MANTRA campaign: the ratios mostly meet the NDACC standards. The standard deviations are larger than during MANTRA, most likely due to the larger spatial and diurnal variability in the spring polar ozone field versus the summer midlatitude ozone field.

Only NO_2 data from the UT-GBS and SAOZ were presented in Chapter 4. For the Type 1 comparisons, the slopes met the NDACC standards. The morning intercept was 3.5 times larger than the required, while the afternoon intercept was 1.25 times larger than the standard. The residuals were three to four times larger. In the comparisons for Eureka for the UT-GBS and SAOZ, all three parameters meet the NDACC standards in 2006 and 2007. In 2005, only the afternoon residual does not meet the standard. The improved comparisons are a result of the improved signal-to-noise ratio of the UT-GBS after the MANTRA 2004 campaign, when the error in the data acquisition code was discovered and a new CCD was obtained.

For the Type 2 NO_2 comparisons, the NDACC standards were met in the MANTRA comparison, with the exception of the morning standard deviation. In the Eureka comparison, the ratios meet the NDACC standard, while the standard deviations do not. This is likely due to low NO_2 concentrations and atmospheric variability of the springtime polar atmosphere.

7.3 Vertical Column Density Comparisons

7.3.1 Comparisons Between Ground-Based Instruments

2004

The ozone vertical column densities calculated using the averaging method from all the ground-based instruments for the Eureka 2004 campaign are shown in Figure 7.11(a) and (b). Also shown in Figure 7.11(b) are integrated ozonesonde profiles. A correction has been added to the ozonesonde columns to account for ozone above the balloon burst height. Errors on the ozonesonde total columns are 5% (Tarasick et al., 2005).

In the following discussions, the average percentage difference is calculated using Equation 7.1:

$$PD = 100 \times \sum_{i=1}^{n} \frac{data_{1,i} - data_{2,i}}{average_i} \tag{7.1}$$

PD is the percentage difference, $data_1$ and $data_2$ are the two data sets being compared, $average$ is the average of the two data sets, n is the number of days of comparison, and i is the day index.

The campaign-averaged absolute and percentage differences for the ground-based instruments and the ozonesondes are given in Table 7.3. Also shown in this table is the combined percentage error in the VCDs from each pair of instruments compared. All the compared instruments agree within the combined random and systematic errors. In Figure 7.11(a) and (b), the ozone VCDs of all three instruments (UT-GBS, SPS, and MAESTRO) agree within error bars (representing both random and systematic errors) on most days. The campaign-averaged differences between the pairs of instruments range

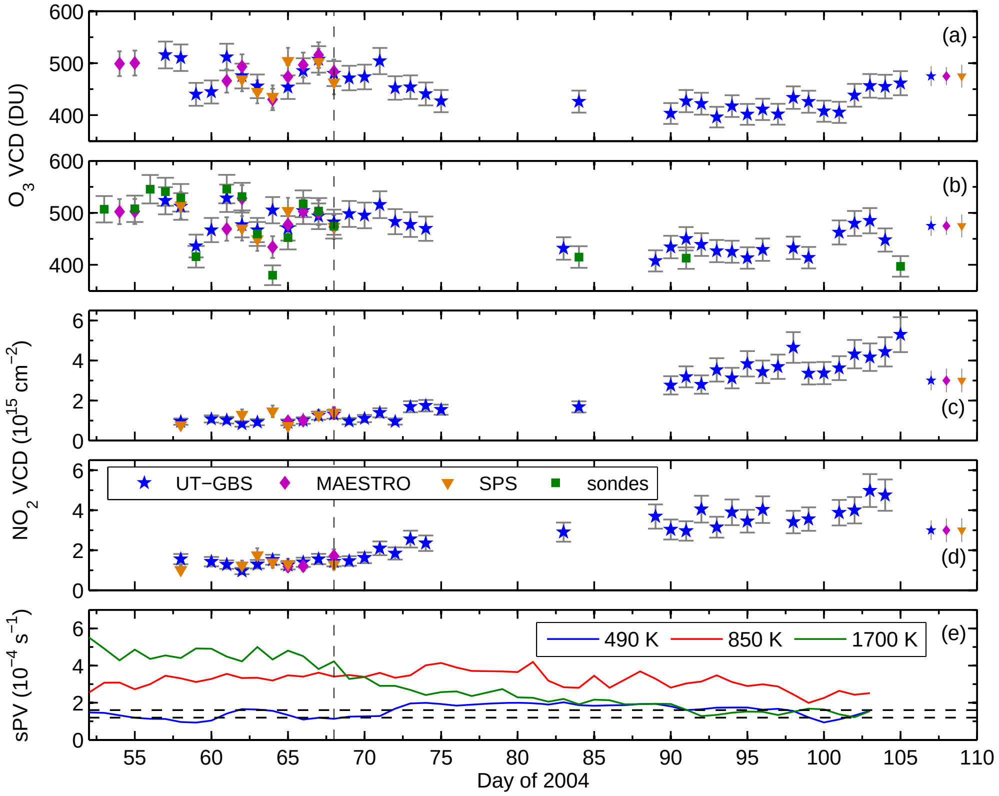

Figure 7.11: Ozone (a) AM and (b) PM and NO_2 (c) AM and (d) PM vertical column densities from the campaign instruments and ozonesondes for 2004. Error bars are the percentage errors given in Chapter 2. For the ozonesondes, the errors are ±5%. For the UV-visible instruments, representative systematic error bars are shown at the right of the figure. (e) The scaled potential vorticity calculated from GEOS-4 reanalysis for Eureka. The potential temperatures correspond to altitudes of approximately 18 km, 30 km, and 50 km. The horizontal dashed lines indicate $1.2\times10^{-4}s^{-1}$ and $1.6\times10^{-4}s^{-1}$, approximately demarking the edges of the polar vortex region. In all figures, the vertical dashed lines indicate the end of the intensive phase of the campaign.

from 0.7 DU (0.1%) to 10.7 DU (2.3%). During the entire campaign, the ozonesonde columns agree with the ground-based instruments within error on most days. The sonde columns agree within an average of 3.1 DU (0.2%) to 7.2 DU (2.0%) with the ground-based columns and tend to be slightly higher.

The ground-based NO_2 VCDs found using the averaging method for the 2004 campaign are shown in Figure 7.11(c) and (d). The columns from the ground-based instruments generally agree within their combined random and systematic error bars. The three instruments agree on average between 0.01×10^{14} molecules/cm^2 (0.01%) and 1.4×10^{14}

Table 7.3: Campaign-averaged absolute and percentage differences for ozone VCDs between the four ground-based instruments and the ozonesondes for the four Eureka campaigns. Ozone absolute differences are in DU. Also shown is the combined percentage error for the two instruments that are compared (the sum in quadrature of the random and systematic errors for the relevant instruments.)

Comparison	Year	AM/PM	Absolute (DU)	PD (%)	Combined error (%)
SAOZ minus UT-GBS	2005	AM	20.7	5.3	5.8
		PM	29.0	6.9	5.8
	2006	AM	16.7	4.0	5.8
		PM	16.1	3.7	5.8
	2007	AM	0.9	0.2	5.8
		PM	14.0	2.9	5.8
SPS minus UT-GBS	2004	AM	2.4	0.5	7.1
		PM	0.7	0.1	7.1
	2005	AM	10.2	2.6	6.5
		PM	12.6	2.6	6.5
	2006	AM	6.5	1.5	6.5
		PM	4.5	1.0	6.5
MAESTRO minus UT-GBS	2004	AM	2.6	0.6	6.9
		PM	−10.7	−2.3	6.9
	2005	AM	62.6	14.6	6.3
		PM	53.7	11.7	6.3
	2006	AM	14.5	3.3	6.3
		PM	2.3	0.5	6.3
SAOZ minus SPS	2005	AM	18.1	4.9	6.5
		PM	14.9	4.0	6.5
	2006	AM	13.9	3.3	6.5
		PM	−15.1	−3.5	6.5
SAOZ minus MAESTRO	2005	AM	-34.7	-7.4	6.3
		PM	−29.6	-5.8	6.3
	2006	AM	−7.2	−1.5	6.3
		PM	11.8	2.7	6.3
SPS minus MAESTRO	2004	AM	−4.4	−0.9	6.9
		PM	−10.3	-2.0	6.9
	2005	AM	−32.5	−7.8	6.9
		PM	−34.8	−7.4	6.9
	2006	AM	−13.1	−3.1	6.9
		PM	−2.6	−0.5	6.9
PEARL-GBS minus UT-GBS	2007	AM	16.4	3.4	5.8
		PM	14.2	3.0	5.8
PEARL-GBS minus SAOZ	2007	AM	7.4	1.5	5.8
		PM	17.4	3.3	5.8
Sondes minus UT-GBS	2004	PM	-7.2	-2.0	7.1
	2005	PM	38.9	8.7	6.5
	2006	PM	2.8	0.5	6.5
	2007	PM	25.6	5.7	6.5
Sondes minus SAOZ	2005	PM	20.0	4.2	6.5
	2006	PM	−11.9	−2.8	6.5
	2007	PM	6.3	1.3	6.5
Sondes minus MAESTRO	2004	PM	3.1	0.2	6.9
	2005	PM	0.47	0.5	6.9
	2006	PM	−7.2	−1.7	6.9
Sondes minus SPS	2004	PM	6.9	1.3	7.1
	2005	PM	35.6	8.3	7.1
	2006	PM	−8.4	−2.0	7.1
Sondes minus PEARL-GBS	2007	PM	-4.1	1.2	6.5

molecules/cm^2 (8.5%). Table 7.4 gives the NO_2 absolute and percentage differences for the ground-based instruments.

2005

Figure 7.12(a) and (b) show the morning and afternoon ozone VCDs from the ground-based instruments for the Eureka 2005 campaign. The columns from the UT-GBS, SAOZ, and SPS all mostly agree within error bars, which represent both random and systematic error. The MAESTRO columns are larger than those from the other instruments, with the exception of day 65 (6 March). Generally, the MAESTRO columns do not agree with the other instruments within error bars. The UT-GBS, SAOZ, and SPS agree within 10.2 DU (2.6%) to 29.0 DU (5.8%), and these three instruments agree with MAESTRO within 29.6 DU (5.8%) to 62.6 DU (14.6%). The UT-GBS columns are the smallest of the four instruments.

The ozonesonde columns are higher than the ground-based columns, with the exception of MAESTRO, and mostly agree within error bars with SAOZ and the SPS. Half the individual comparisons with the UT-GBS, and two-thirds of the individual comparisons with MAESTRO do not agree within error bars. The sondes agree with the ground-based instruments between 0.5 DU (0.5%) and 38.9 DU (8.7%). In Table 7.3, the individual comparisons are seen to agree within combined error, with the exception of the comparisons with MAESTRO, the SAOZ–UT-GBS afternoon, and the sondes–UT-GBS comparisons.

Figure 7.12(c) and (d) show the morning and afternoon NO_2 VCDs from the ground-based instruments. The UT-GBS, SAOZ, and SPS columns all agree within combined random and systematic error bars on most days. The SAOZ columns tend to be larger than those of the other instruments. On average, the ground-based columns agree to within 1.0×10^{14} molecules/cm^2 (2.2%) to 3.7×10^{14} molecules/cm^2 (24.6%).

Table 7.4: Campaign-averaged absolute and percentage differences for NO_2 VCDs between the four ground-based instruments for the four Eureka campaigns. NO_2 absolute differences are in 10^{14} molecules/cm^{-2}. Also shown is the combined percentage error for the two instruments that are compared (the sum in quadrature of the random and systematic errors for the relevant instruments.)

Comparison	Year	AM/PM	Absolute (10^{14} cm^{-2})	PD (%)	Combined error (%)
SAOZ minus UT-GBS	2005	AM	2.08	12.3	23.2
		PM	1.03	2.2	23.2
	2006	AM	0.66	3.2	23.2
		PM	0.62	2.2	23.2
	2007	AM	-0.55	-4.2	23.2
		PM	0.38	2.2	23.3
SPS minus UT-GBS	2004	AM	0.48	2.4	26.1
		PM	0.01	0.01	26.1
	2005	AM	−1.67	−16.3	25.9
		PM	−2.81	−20.8	25.9
	2006	AM	0.70	2.3	25.9
		PM	1.80	12.3	25.9
MAESTRO minus UT-GBS	2004	AM	0.32	2.9	26.1
		PM	−0.12	−0.4	26.1
	2005	AM	−1.98	−17.3	25.9
		PM	−3.72	−24.6	25.9
	2006	AM	−0.09	−4.5	25.9
		PM	−0.05	−1.8	25.9
SAOZ minus SPS	2005	AM	-1.87	-16.3	25.9
		PM	2.19	17.3	25.9
	2006	AM	−0.37	−0.3	25.9
		PM	−2.36	−16.3	25.9
SAOZ minus MAESTRO	2005	AM	2.08	18.6	25.9
		PM	2.70	18.9	25.9
	2006	AM	−0.16	−2.0	25.9
		PM	0.40	3.6	25.9
SPS minus MAESTRO	2004	AM	−0.90	−11.7	28.3
		PM	−1.40	−8.5	28.3
	2005	AM	−0.16	−1.0	28.3
		PM	0.52	5.5	28.3
	2006	AM	0.51	2.8	28.3
		PM	1.87	14.0	28.3
PEARL-GBS minus UT-GBS	2007	AM	0.85	5.4	23.2
		PM	1.09	6.3	23.2
PEARL-GBS minus SAOZ	2007	AM	−1.72	−12.2	23.2
		PM	−0.71	−3.9	23.2

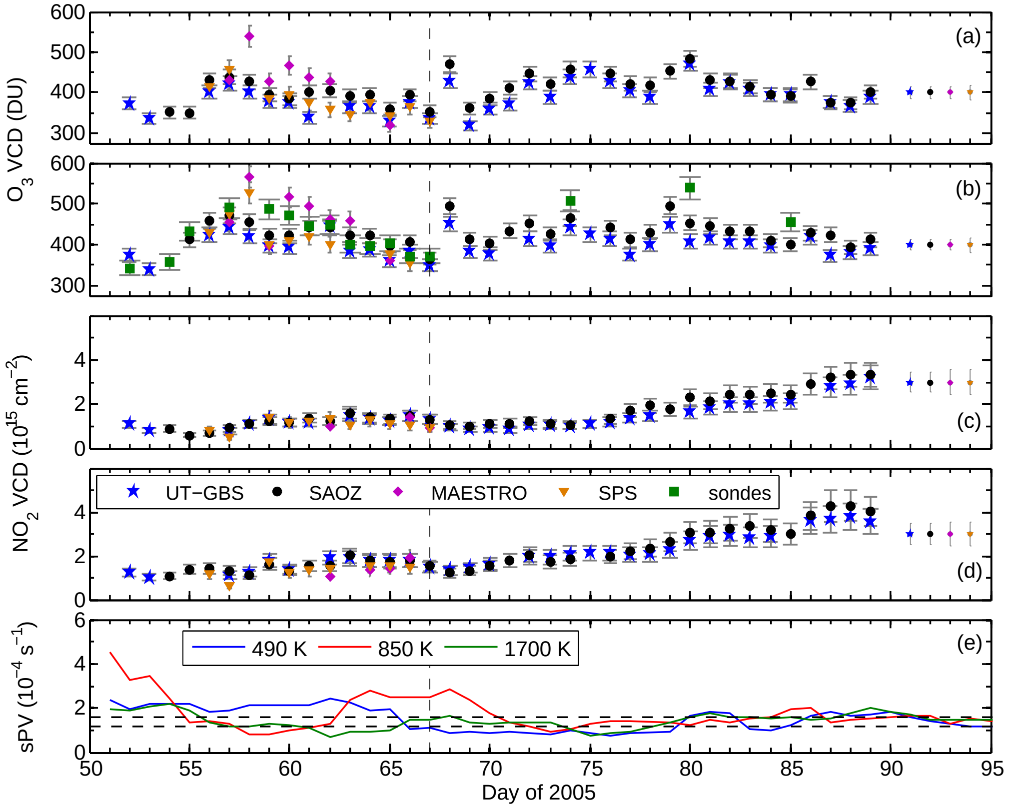

Figure 7.12: Same as Figure 7.11, but for 2005.

2006

The morning and afternoon ozone VCDs for the Eureka 2006 campaign are shown in Figure 7.13(a) and (b). The ground-based instruments agree within combined random and systematic error bars on most days. The MAESTRO and SPS columns are scattered about the SAOZ and UT-GBS columns, while the SAOZ columns are universally larger than those from the UT-GBS. On average, the instruments agree within 2.3 DU (0.5%) to 16.7 DU (4.0%). The agreement between the ozonesonde columns and the ground-based VCDs is also good, with the sonde columns being, on average, within 2.8 DU (0.5%) to 11.9 DU (2.8%). In Table 7.3, all the instrument comparisons agree within the combined percentage error.

The morning and afternoon NO$_2$ columns are shown in Figure 7.13(c) and (d). The

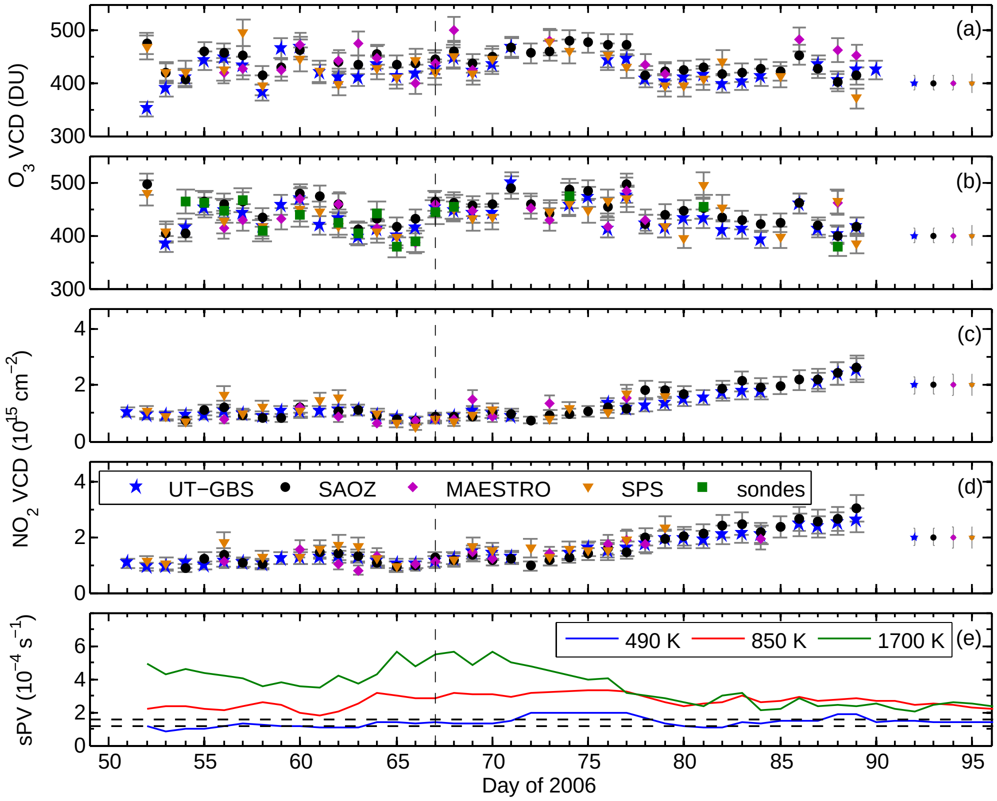

Figure 7.13: Same as Figure 7.11, but for 2006.

UT-GBS and SAOZ are again in good agreement, with the SAOZ columns being larger than the UT-GBS columns. The SPS and MAESTRO are scattered about the UT-GBS and SAOZ columns. The columns are within 0.05×10^{14} molecules/cm^2 (1.8%) to 2.4×10^{14} molecules/cm^2 (16.3%) on average.

2007

Figure 7.14(a) and (b) show the morning and afternoon VCDs for the 2007 campaign. With a few exceptions, the ground-based instruments and the ozonesondes agree within combined random and systematic error bars on most days. On average, the ground-based instruments agree within 0.9 DU (0.2%) to 16.4 DU (3.4%). The ozonesondes and the ground-based instruments agree within 4.1 DU (1.2%) to 25.6 DU (5.7%). All the

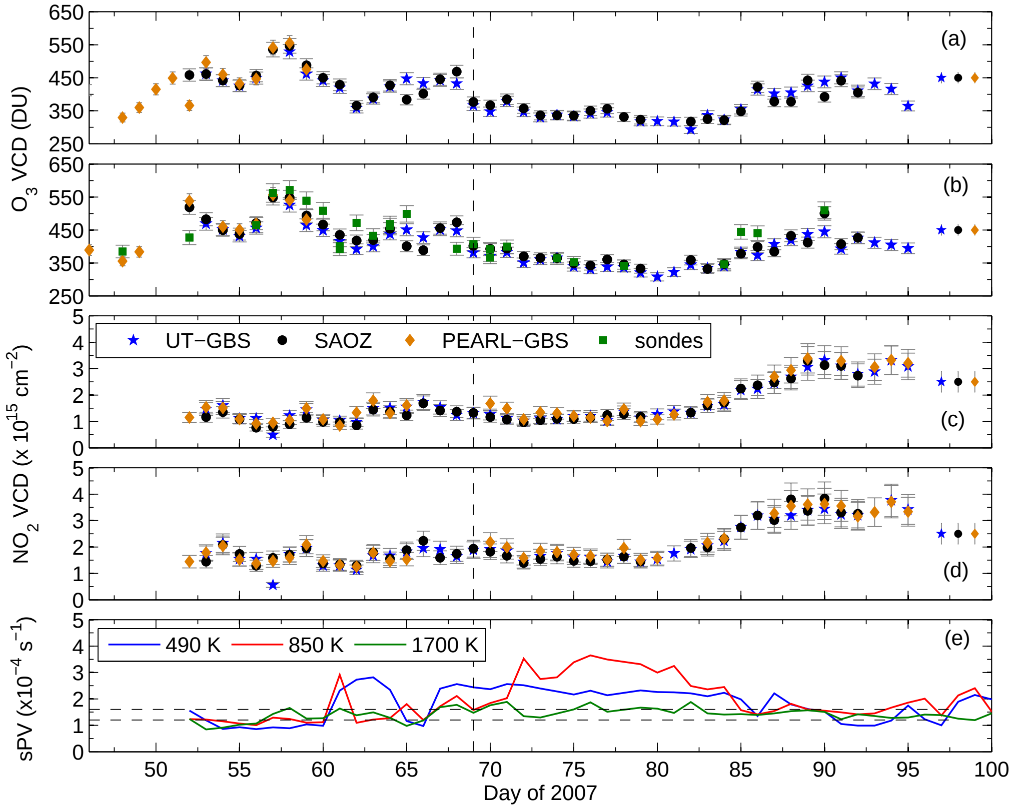

Figure 7.14: Same as Figure 7.11, but for 2007.

instrument comparisons agree within the combined percentage error.

The NO_2 morning and afternoon columns are shown in Figure 7.14(c) and (d). As for ozone, the instruments agree within the combined random and systematic error bars on most days of the campaign. The columns are within 0.4×10^{14} molecules/cm^2 (2.2%) to 1.7×10^{14} molecules/cm^2 (12.2%) on average.

7.3.2 Comparisons with Satellite Instruments

2004

Integrated partial columns of ozone and NO_2 from the ACE-FTS and ACE-MAESTRO profiles taken within 500 km of Eureka are shown in Figure 7.15, along with the average VCDs from the ground-based instruments. The partial columns were calculated by using the volume mixing ratio from the ACE-FTS and ACE-MAESTRO and the density from the ACE-FTS profiles. The ACE satellite overpasses are all in the afternoon, falling between 15:00 LT and 17:42 LT. All the overpasses correspond to SZAs of 89.5°. For ozone, the partial column is calculated between 15 and 40 km. Kar et al. (2007) found these altitudes to be the region where ACE-MAESTRO data is appropriate for scientific analysis. The same altitude range is chosen for ACE-FTS to facilitate comparisons, especially with ACE-MAESTRO. For the ACE-FTS ozone, Dupuy et al. (2008) use a similar altitude region for validation: 16–44 km. To account for the tropospheric ozone contribution below 15 km, the daily ozonesonde data below this altitude have been added to the satellite columns. The column below 15 km is between 98 DU and 207 DU, or about 30% of the total. No correction is made for the ozone above 40 km. The ozonesondes launched during the three campaigns have total columns ranging between 350 DU and 560 DU. Assuming an exponential decay in the ozone column above the burst height of the balloon, the contribution to the total column from 40 to 100 km is between 1 DU and 16 DU. On average, the column above 40 km is 2% of the total column. Since the error on all the columns is greater than 2%, the ground-based total columns and satellite partial columns are expected to agree within error bars. A similar approach is used in Randall et al. (2002) for Polar Ozone and Aerosol Measurement (POAM) III NO_2 validation.

The average afternoon ozone VCDs from the three ground-based instruments (UT-GBS, SPS, and MAESTRO) are shown in Figure 7.15(a), along with the total columns from the ozonesondes and the partial columns from 0 to 40 km (ozonesonde data used from 0 to 15 km) from the satellite instruments. Only the period with satellite overpasses is shown. The ACE-FTS partial columns in Figure 7.15(a) agree with the ground-based columns and sondes for most days. On average, the ACE-FTS partial columns agree with the four sets of ground-based and sonde VCDs within 9.0 DU (1.8%) to 30.8 DU (6.1%) (see column 4 of Table 7.5). The ACE-MAESTRO partial columns are generally smaller than those from the ground-based instruments and sondes, and for the most

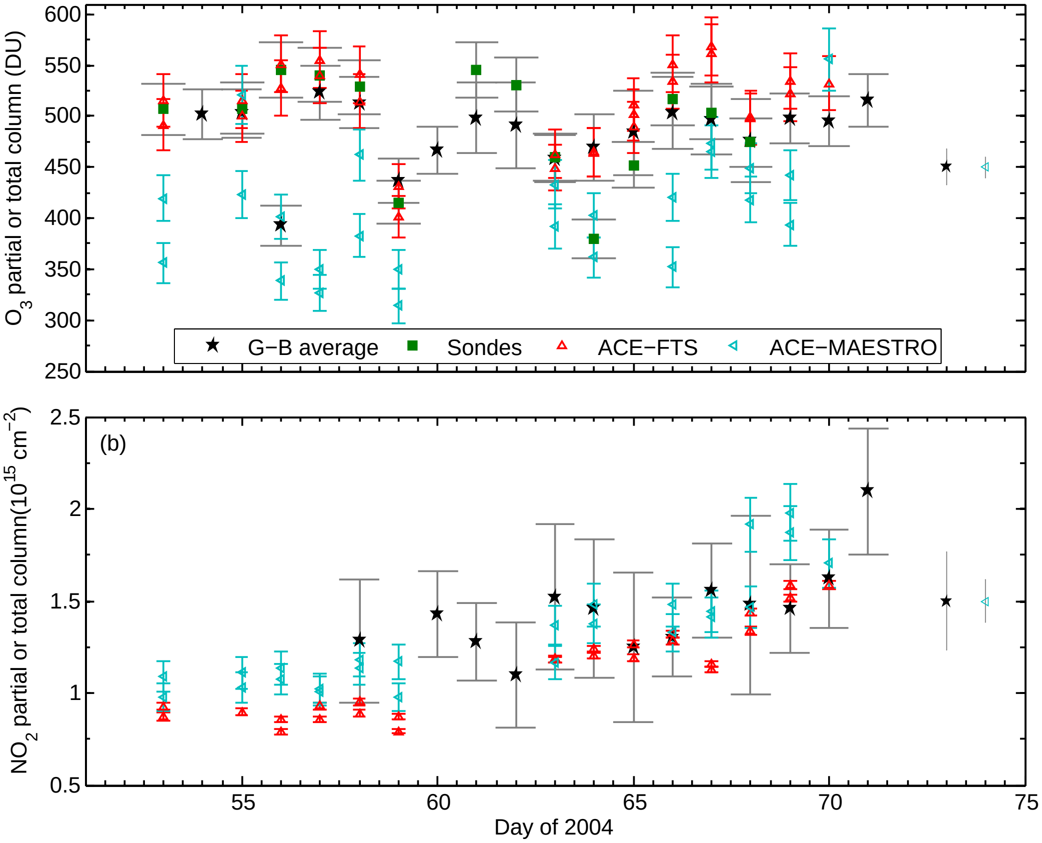

Figure 7.15: Afternoon (a) ozone and (b) NO_2 vertical column densities from the campaign instruments and ozonesondes, and partial columns from ACE-FTS and ACE-MAESTRO for 2004. For both species, the ground-based measurements from the UT-GBS, SPS, and MAESTRO have been averaged. Error bars for the ground-based VCDs are the sum in quadrature of the relevant percentage errors. For the ozonesondes, the errors are ±5%. For ACE-FTS, the error bars represent only the random spectral fitting error, while for ACE-MAESTRO, the error bars are a combination of fitting error, errors in the cross sections, and errors arising from unaccounted-for temperature effects in the cross sections. The error bars to the right of the plot indicate representative systematic error for the ground-based average and the ACE-MAESTRO. For the satellite measurements, the partial columns are taken between 0 and 40 km for ozone and between 22 and 40 km for NO_2.

part do not agree within error bars, which represent both the random and systematic errors. On average, the ACE-MAESTRO partial columns agree within 53.8 DU (12.3%) to 88.5 DU (20.1%) with the ground-based and sonde columns. The ACE-FTS partial columns are larger than those of the ACE-MAESTRO, with the exception of days 55 and 70. The ACE-FTS columns are an average of 100.9 DU (22.5%) larger than the ACE-MAESTRO columns. The absolute and percentage differences for the individual instrument comparisons with the satellite instruments are shown in Table 7.5, as well as the combined percentage error of each pair of instruments compared. For comparisons with ACE-FTS, all of the individual comparisons agree within the combined error of the two instruments. For comparisons with ACE-MAESTRO, the individual comparisons do not agree within the combined error of the two instruments.

The altitude range recommended by Kar et al. (2007) for ACE-MAESTRO is used for the NO_2 partial columns: 22 to 40 km. The same region is used for both ACE-FTS and ACE-MAESTRO. Kerzenmacher et al. (2008) use a larger region for the ACE-FTS validation: 13–58 km. No correction is made to the NO_2 satellite partial columns to account for the NO_2 below 22 km and above 40 km. To quantify the contribution of the column above and below the partial column, NO_2 profiles for late February and early March at 80° N have been generated by the UCI photochemical box model (Prather, 1997; McLinden et al., 2000). The total column of NO_2 during this time is between 1.29×10^{14} molecules/cm^2 and 8.51×10^{14} molecules/cm^2, with the column steadily increasing over the time period. The contribution below 22 km is 0.09×10^{14} molecules/cm^2 (7.34%) in mid-February and 1.04×10^{14} molecules/cm^2 (12.22%) in mid-March. The NO_2 below 22 km is steadily increasing over the time period. The contribution from above 40 km is 0.11×10^{14} molecules/cm^2 (7.20%) in mid-February and 0.09×10^{14} molecules/cm^2 (1.03%) in mid-March. The NO_2 above 40 km is steadily decreasing over the time period. The total contribution from these two regions is between 12.4% and 14.6%. As a result, the satellite partial columns are expected to be roughly 13% smaller than the ground-based

Table 7.5: Campaign-averaged absolute and percentage differences for ozone between the ACE-FTS and ACE-MAESTRO and the four ground-based instruments and the ozonesondes for the four Eureka campaigns. Ozone absolute differences are in DU. The combined percentage error for the two compared instruments is also given, and is the sum in quadrature of the individual percentage errors.

Comparison	Year	Absolute (DU)	PD (%)	Combined error (%)
ACE-FTS minus UT-GBS	2004	17.3	3.2	7.1
	2005	27.2	6.3	6.5
	2006	27.6	6.3	6.5
	2007	11.8	1.7	6.5
ACE-FTS minus SAOZ	2005	1.5	0.1	6.5
	2006	19.5	4.3	6.5
	2007	6.6	0.7	6.5
ACE-FTS minus MAESTRO	2004	30.8	6.1	6.7
	2005	−17.8	-3.1	7.0
	2006	31.8	7.2	7.0
ACE-FTS minus SPS	2004	9.0	1.8	7.1
	2005	17.4	4.4	7.1
	2006	38.9	9.0	7.1
ACE-FTS minus PEARL-GBS	2007	−5.5	−0.8	6.5
ACE-FTS minus sondes	2004	21.0	4.4	7.1
	2005	−4.4	−1.0	7.1
	2006	20.0	4.7	7.1
	2007	−9.7	−3.3	7.1
ACE-MAESTRO minus UT-GBS	2004	−83.8	−19.4	7.4
	2005	−4.7	−2.6	6.8
	2006	−4.4	−1.2	6.9
	2007	−6.1	−2.6	6.9
ACE-MAESTRO minus SAOZ	2005	−45.1	−12.9	6.8
	2006	−7.1	−1.9	6.9
	2007	−20.5	−5.5	6.9
ACE-MAESTRO minus MAESTRO	2004	-53.8	-12.3	7.3
	2005	-84.4	−20.6	7.3
	2006	5.0	1.1	7.3
ACE-MAESTRO minus SPS	2004	-56.3	−12.5	7.4
	2005	−29.2	−7.9	7.4
	2006	-7.5	−2.2	7.4
ACE-MAESTRO minus PEARL-GBS	2007	−41.8	−8.1	
ACE-MAESTRO minus sondes	2004	−88.5	-20.1	7.4
	2005	−45.7	−12.6	7.4
	2006	6.2	1.4	7.4
	2007	−44.0	−10.6	7.4
ACE-FTS minus ACE-MAESTRO	2004	100.9	22.5	7.5
	2005	26.6	7.8	7.5
	2006	23.4	5.5	7.5
	2007	27.8	6.2	7.5

total columns.

The average afternoon columns of NO_2 from the ground-based instruments and the partial columns from the satellite instruments are shown in Figure 7.15(b). Table 7.6 gives the absolute and percentage differences between the satellite and ground-based instruments. Both the ACE-FTS and ACE-MAESTRO partial column measurements follow the general trend of the ground-based total column measurements and agree within error bars, which represent both random and systematic error. The ACE-FTS partial columns are within an average of 0.6×10^{14} molecules/cm^2 (3.3%) to 1.8×10^{14} molecules/cm^2 (13.9%) of the ground-based instruments. The ACE-MAESTRO columns are within an average of 0.2×10^{14} molecules/cm^2 (0.1%) to 0.9×10^{14} molecules/cm^2 (6.4%) of the ground-based instruments. The ACE-FTS and ACE-MAESTRO partial columns generally agree within their error bars, with the ACE-FTS columns being 2.0×10^{14} molecules/cm^2 (17.1%) smaller than the ACE-MAESTRO columns. The difference between the ACE-FTS and the UT-GBS and SPS total columns is approximately the expected percent difference, given the expected vertical distribution of NO_2.

2005

The average afternoon ozone VCDs from the ground-based instruments (UT-GBS, SAOZ, SPS, and MAESTRO) are shown in Figure 7.16(a), along with the total columns from the ozonesondes, and the partial columns from the satellite instruments. The ACE-FTS partial columns agree with the ground-based instruments and the sondes on most days of the campaign. On average, the ACE-FTS columns agree with the ground-based instruments and ozonesondes within 1.5 DU (0.1%) to 27.2 DU (6.3%). The agreement between the ACE-MAESTRO and the other instruments is improved this year. On average, the ACE-MAESTRO partial columns agree with the UT-GBS, SAOZ, SPS, and ozonesondes between 4.7 DU (2.6%) and 45.7 DU (12.6%), and with the MAESTRO within 84.4 DU (20.6%). The ACE-FTS ozone columns are 26.6 DU (7.8%) larger than

Table 7.6: Campaign-averaged absolute and percentage differences between the ACE-FTS and ACE-MAESTRO and the four ground-based instruments for NO_2 for the four Eureka campaigns. Ground-based columns are the total columns. For the satellite instruments, partial columns between 22 and 40 km are used. NO_2 absolute differences are in 10^{14} molecules/cm^2. The combined percentage error for the two compared instruments is also given, and is the sum in quadrature of the individual percentage errors.

Comparison	Year	Absolute (10^{14} cm^{-2})	PD (%)	Combined error (%)
ACE-FTS minus UT-GBS	2004	−1.80	−13.9	16.9
	2005	−1.59	−10.7	16.5
	2006	−1.93	−19.7	16.5
	2007	−2.31	−13.1	16.5
ACE-FTS minus SAOZ	2005	−1.75	−11.9	16.5
	2006	−1.39	−13.6	16.5
	2007	−3.35	−23.2	16.5
ACE-FTS minus MAESTRO	2004	−0.61	−3.3	20.1
	2005	−0.98	−4.6	20.1
	2006	−2.94	−27.2	20.1
ACE-FTS minus SPS	2004	−1.66	−12.3	20.1
	2005	0.12	0.78	20.1
	2006	−2.80	−24.2	20.1
ACE-FTS minus PEARL-GBS	2007	−2.97	−22.0	16.5
ACE-MAESTRO minus G-B avg	2004	0.36	1.3	34.5
	2005	−0.37	−3.3	37.4
	2006	2.00	16.7	37.4
	2007			
ACE-MAESTRO minus UT-GBS	2004	0.18	−0.1	19.7
	2005	−0.84	−5.8	18.2
	2006	1.91	15.6	18.2
	2007	2.56	12.2	18.2
ACE-MAESTRO minus SAOZ	2005	−0.81	−5.5	18.2
	2006	3.21	27.4	18.2
	2007	1.60	2.1	18.2
ACE-MAESTRO minus MAESTRO	2004	0.88	6.4	22.5
	2005	0.86	6.7	21.5
	2006	1.05	9.8	21.5
ACE-MAESTRO minus SPS	2004	0.19	1.9	22.5
	2005	1.24	7.9	21.5
	2006	1.51	13.5	21.5
ACE-MAESTRO minus PEARL-GBS	2007	−1.19	−10.2	18.2
ACE-FTS minus ACE-MAESTRO	2004	−2.06	−17.1	10.4
	2005	−0.80	−5.7	8.0
	2006	−3.92	−35.0	8.1
	2007	−2.35	−15.5	8.1

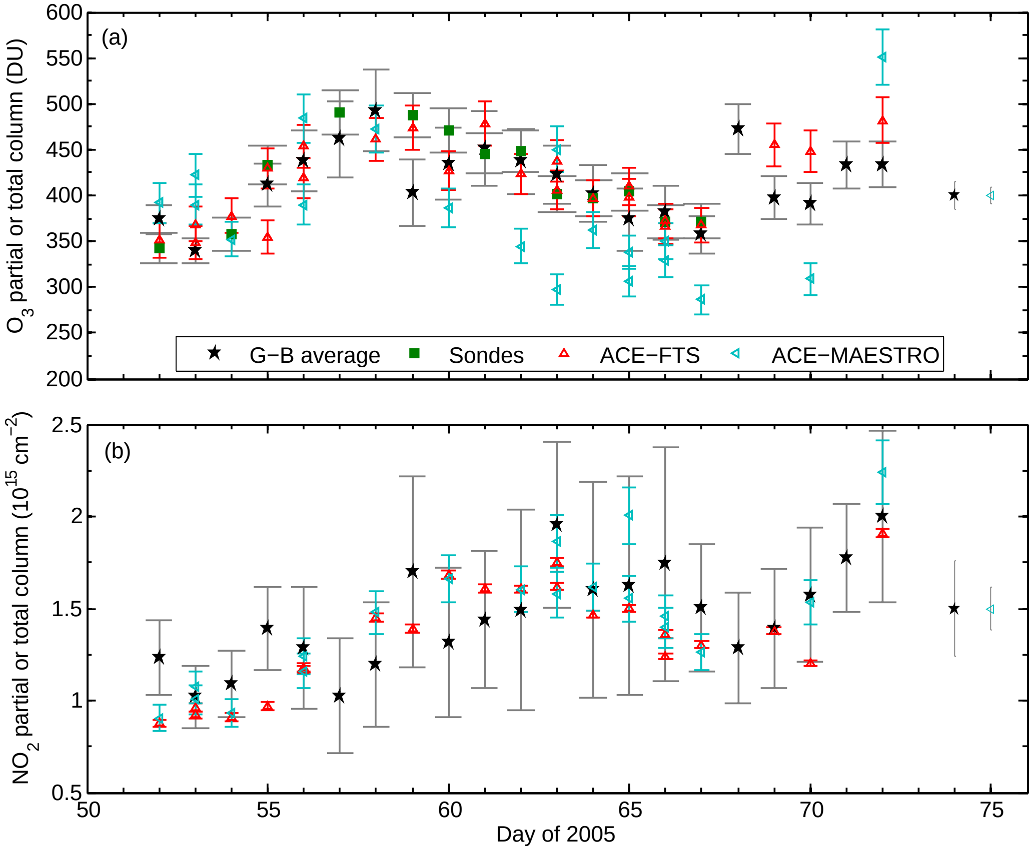

Figure 7.16: Same as Figure 7.15, but for 2005. The ground-based average is the average of the UT-GBS, SAOZ, SPS, and MAESTRO.

the ACE-MAESTRO columns. In Table 7.5, all the comparisons with ACE-FTS are within the combined percentage error of the individual instruments. The comparisons with ACE-MAESTRO are generally not within the combined percentage error.

Figure 7.16(b) shows the average total NO_2 columns from the ground-based instruments and the partial columns from the satellite instruments. As in 2004, the ACE-FTS and ACE-MAESTRO partial columns follow the trend of the ground-based instruments and agree with these instruments within error bars, which represent both random and systematic error. The ACE-FTS partial columns are within 0.12×10^{14} molecules/cm^2 (0.8%) to 1.8×10^{14} molecules/cm^2 (11.9%) of the ground-based total columns. The ACE-MAESTRO columns agree with the ground-based instruments within 0.8×10^{14}

molecules/cm^2 (5.5%) to 1.2×10^{14} molecules/cm^2 (7.9%). The ACE-FTS and ACE-MAESTRO NO$_2$ columns are again in good agreement, with the ACE-FTS columns 0.8×10^{14} molecules/cm^2 (5.7%) smaller than the ACE-MAESTRO columns. The ACE-FTS NO$_2$ partial columns and the UT-GBS and SAOZ total columns differ by the expected percentage difference.

2006

The average total ozone columns from the ground-based instruments (UT-GBS, SAOZ, SPS, and MAESTRO), the total columns from the ozonesondes, and the partial columns from the satellite instruments, are shown in Figure 7.17(a). As in 2004 and 2005, the ACE-FTS partial columns mostly agree within the combined random and systematic error bars with the total columns from the ground-based instruments and the ozonesondes. The agreement is, on average, between 19.5 DU (4.3%) and 38.9 DU (9.0%). There is again an improvement in the comparison of the ACE-MAESTRO columns with the other instruments. The satellite partial columns are within 4.4 DU (1.2%) to 7.5 DU (2.2%) of the ground-based instruments and the ozonesondes. The ACE-FTS and ACE-MAESTRO columns are within 23.4 DU (5.5%) of each other.

The average total NO$_2$ columns from the ground-based instruments and the satellite partial columns are shown in Figure 7.17(b). As in the other campaigns, the ACE-FTS and ACE-MAESTRO partial columns follow the same general trend as the ground-based instruments. The ACE-FTS partial columns are within 1.4×10^{14} molecules/cm^2 (13.6%) to 2.9×10^{14} molecules/cm^2 (27.2%) of the four sets of ground-based total columns. The ACE-MAESTRO columns are within 1.1×10^{14} molecules/cm^2 (9.8%) to 3.2×10^{14} molecules/cm^2 (27.4%) of the ground-based columns. The ACE-FTS columns are an average of 3.9×10^{14} molecules/cm^2 (35.0%) smaller than the ACE-MAESTRO columns. The ACE-FTS NO$_2$ partial columns are smaller than the SAOZ total columns by the expected percentage difference.

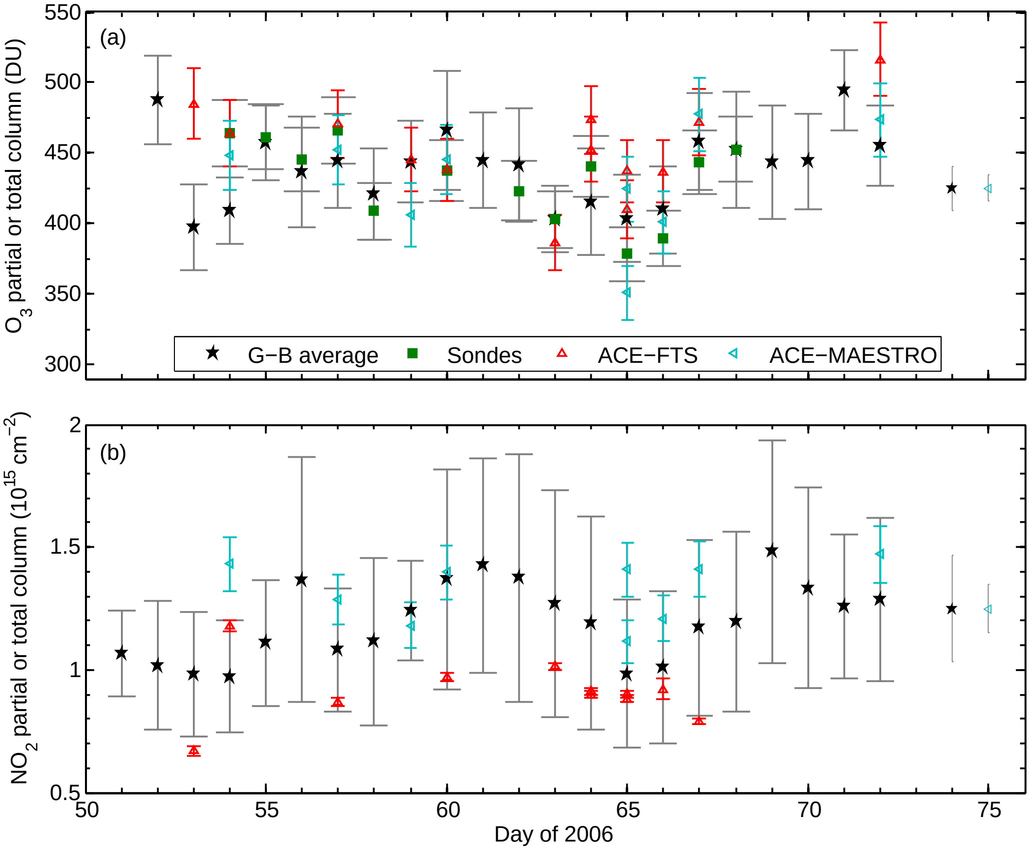

Figure 7.17: Same as Figure 7.15, but for 2006. The ground-based average is the average of the UT-GBS, SAOZ, SPS, and MAESTRO.

2007

Figure 7.18(a) shows the total ozone columns from the ground-based instruments (UT-GBS, SAOZ, and PEARL-GBS) and the ozonesondes and the partial columns from the satellite instruments. Both the ACE-FTS and ACE-MAESTRO columns agree within the combined random and systematic error bars of the total columns from the ground-based instruments and ozonesondes. For the ACE-FTS the agreement is between 5.5 DU (-0.9%) and 11.8 DU (1.7%) on average. The ACE-MAESTRO columns are within 6.1 DU (2.6%) to 44.0 DU (10.6%) on average. All of the ACE-FTS comparisons and most of the ACE-MAESTRO comparisons are within the combined error bars of the instruments. The ACE-FTS and ACE-MAESTRO agree to 27.8 DU (6.2%).

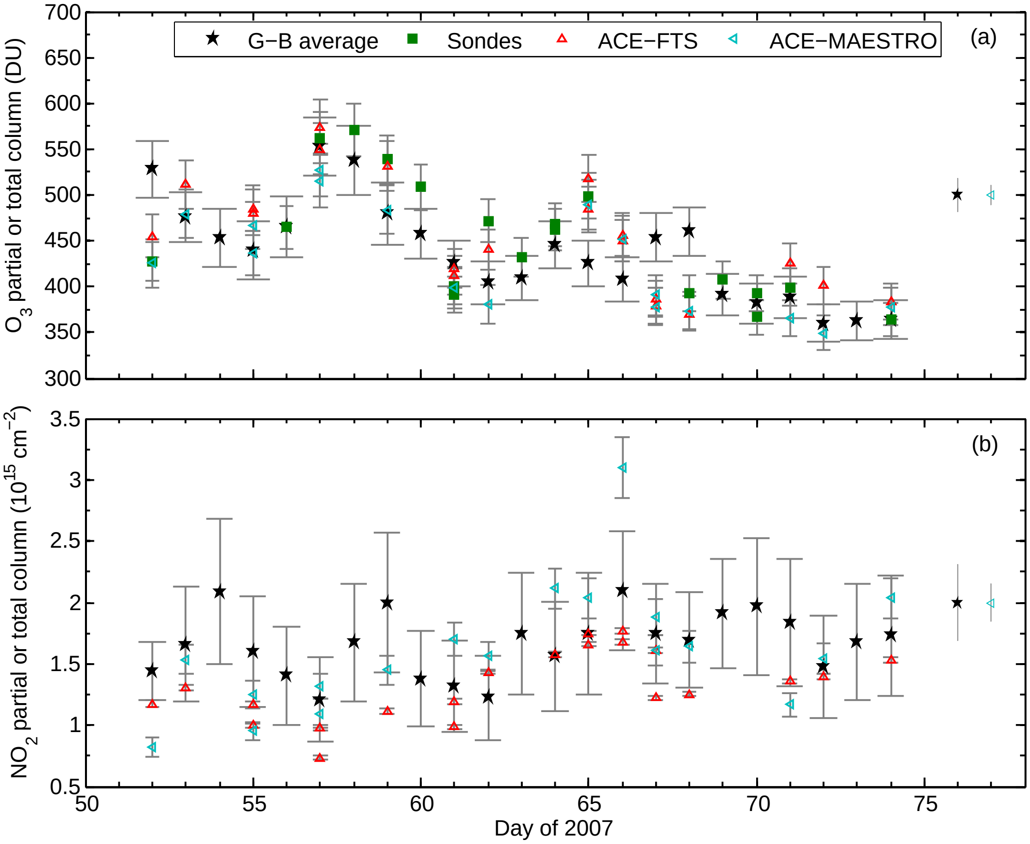

Figure 7.18: Same as Figure 7.15, but for 2007. The ground-based average is the average of the UT-GBS, SAOZ, and PEARL-GBS.

The average total NO_2 columns from the ground-based instruments and the satellite partial columns are shown in Figure 7.18(b). The satellite partial columns follow the same general trend as the ground-based instruments. The ACE-FTS partial columns are between 2.3×10^{14} molecules/cm^2 (13.1%) to 3.4×10^{14} molecules/cm^2 (23.2%) smaller than the ground-based columns, which is the expected percentage agreement. The ACE-MAESTRO columns are within an average of 1.2×10^{14} molecules/cm^2 (10.2%) and 2.6×10^{14} molecules/cm^2 (12.2%) of the ground-based columns. The ACE-MAESTRO partial columns tend to be larger than the columns from the ground-based instruments. The ACE-FTS columns are 2.4×10^{14} molecules/cm^2 (15.5%) smaller than the ACE-MAESTRO columns.

7.3.3 Summary of Satellite Comparisons

Figure 7.19(a-d) shows scatter plots of the ACE-FTS and ACE-MAESTRO partial columns versus the ground-based and ozonesonde total columns for both species. Also shown are the linear fits to the ensembles of data points. For ozone, the expected slope is one and the expected intercept is zero. For NO_2, the expected slope is one and the expected intercept is on the order of -10^{14} molecules/cm^2, which accounts for the difference between the total and partial columns compared. The ACE-FTS vs. ground-based instrument scatter plots for ozone (Figure 7.19(a)) and NO_2 (Figure 7.19(b)) are compact, with the data scattered evenly about the fitted line. The ozone slope is larger than expected, while the NO_2 slope is close to one and includes one in the error of the slope. The ozone intercept is small, while the NO_2 intercept is of the expected order of magnitude. This reflects the agreement seen in Tables 7.5 and 7.6.

The ACE-MAESTRO versus ground-based instrument scatter plots for ozone (Figure 7.19(c)) and NO_2 (Figure 7.19(d)) show significantly more scatter than the ACE-FTS comparisons. Neither slope is close to unity. This reflects the larger scatter in the ACE-MAESTRO partial columns compared to the ground-based instruments. The ozone intercept is large, while the NO_2 intercept is of the expected order of magnitude.

Figures 7.19(e) and (f) show the scatter plots for ACE-FTS and ACE-MAESTRO for ozone and NO_2. In this case, the expected slope is one and the expected intercept is zero for both species. For both ozone and NO_2, the slope is not close to unity, and the intercepts are large. This reflects the large differences between the instruments seen in Table 7.5 and 7.6.

7.4 Summary

The ozone and NO_2 DSCDs and VCDs from the five UV-visible zenith-sky instruments have been compared following the techniques adopted by the UV-visible Working Group

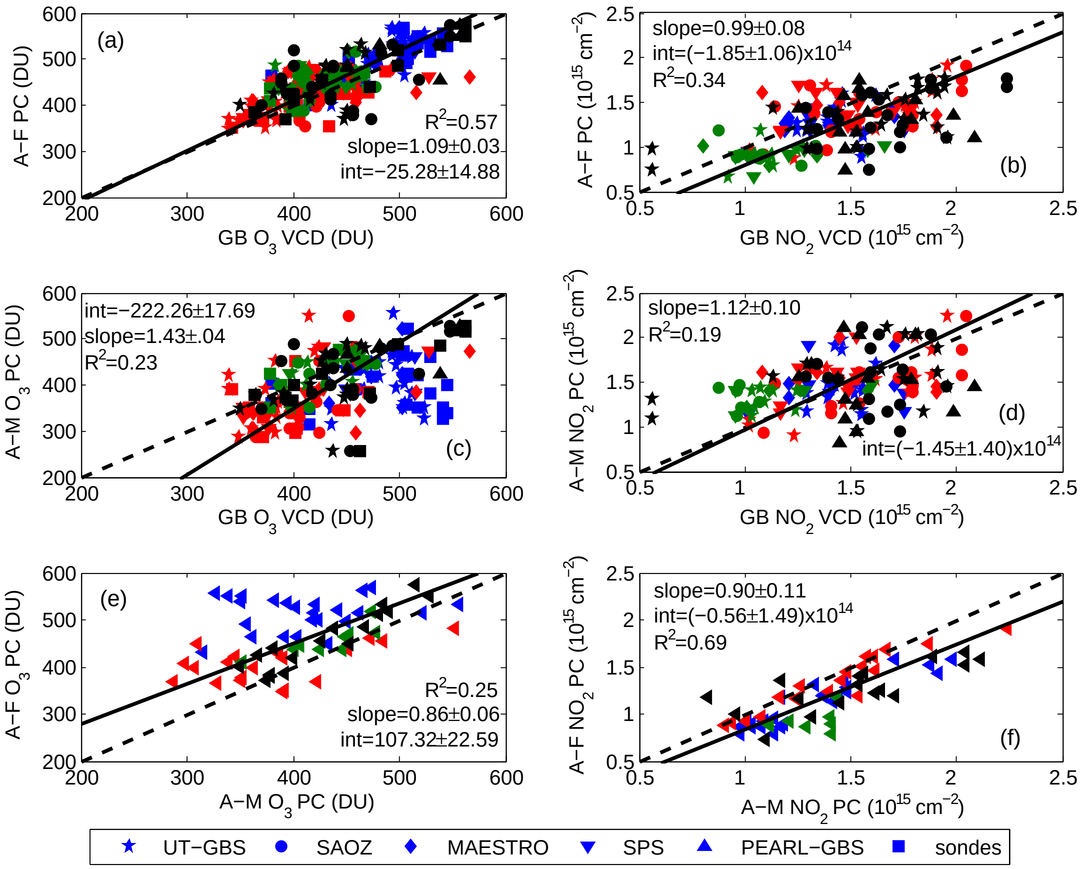

Figure 7.19: Scatter plot of (a) ACE-FTS (A-F) ozone partial columns (PC) vs. ground-based (G-B) total columns and total columns from the ozonesondes. (b) Same as (a), but for NO_2. (c-d) Same as (a-b), but for ACE-MAESTRO (A-M) partial columns. (e-f) Same as (a-b) but for ACE-FTS vs. ACE-MAESTRO. In all figures, the solid line shows the fitted relationship between the two data sets being compared. The slope, intercept, and R^2 for the comparisons are given on the figure. The dotted line shows the one-to-one line relationship for comparison. The blue points are for 2004, the red points are for 2005, the green points are for 2006, and the black points are for 2007. The satellite partial columns are between 0 and 40 km for ozone and between 22 and 40 km for NO_2.

of the NDACC. The ozone DSCDs Type 1 comparisons are found to partially meet the NDACC standards: approximately 53% of the slopes meet the standard. Those comparisons that do not meet the standard are within the standard error, with the exception of comparisons with a small number (less than ten) of twilight periods to compare: the UT-GBS vs. SAOZ (1) comparisons in 2005, and the SPS vs. SAOZ (4) afternoon comparisons in 2006. These comparisons are thought to disagree due to the different fields-of-view of the instruments, as well as Eureka's position on the edge of the polar vortex in 2005. While the comparisons that meet the standards within the standard error (which represents the random error) fail to meet the NDACC standards, their range of possible values includes part of the NDACC range. Not meeting the NDACC standards within the standard error implies that there is a systematic bias between the instruments. The ozone intercepts meet the NDACC standards, with large standard errors. The residuals are generally larger than the standards, indicating scatter in the DSCDs. The ozone Type 2 comparisons are also found to partially agree with the NDACC standards, with the ratios mostly meeting the requirements in 2006 and 2007, but the standard deviations being larger than the requirements in 2005 and 2006.

The NO_2 Type 1 comparisons also partially meet the NDACC standards. The UT-GBS vs. SAOZ comparisons meet all three standards in 2006, and all but one in 2005. About 63% of the slopes meet the NDACC standards. The intercepts meet the NDACC standards, with large standard errors. The residuals are much larger than the standards, except for in 2007. The Type 2 comparisons for NO_2 are better, with most of the ratios meeting the NDACC standards. The standard deviations are large, which could be a result of the small NO_2 columns in the polar springtime.

These comparisons are generally an improvement over comparisons between the UT-GBS, SAOZ, MAESTRO, and SPS during the MANTRA 2004 campaign discussed in Chapter 4.

The UT-GBS and the new PEARL-GBS universally meet both the Type 1 and Type

2 comparisons for both ozone and NO_2.

For ozone, in all the campaigns, the ground-based instruments, ozonesondes, and ACE satellite instruments generally agree within the combined random and systematic error bars of the instruments. The ground-based instruments agree within 62.6 DU (14.6%) for all campaigns. For all but six of the 36 possible instrument pair comparisons, the average difference between the ground-based VCDs is less than the combined error bars of the instruments. The six comparisons that do not agree are all from 2005, when Eureka was on the edge of the polar vortex, which has the greatest horizontal gradient in the ozone field. The ozonesondes and the ground-based instruments agree within 38.9 DU (8.7%) for all campaigns. Generally, the sonde columns fall within the range of VCDs from the ground-based instruments. Twelve of the 14 ground-based instrument vs. sonde comparisons agree within the combined error bars of the instruments. The two comparisons that fall outside this range are from 2005.

For the ACE-FTS, 16 of the 18 comparisons to the ground-based instruments and the ozonesondes agree within the combined random and systematic error bars of the instruments. For ACE-MAESTRO, only seven of 18 comparisons agree to within the combined error bars of the instruments.

For NO_2, during all the campaigns, the ground-based data mostly agree within error bars, which represent both random and systematic errors. The five instruments agree within 3.7×10^{14} molecules/cm^2 (24.6%) for all the campaigns. All of the 36 possible instrument pair comparisons agree to within the combined error bars of the instruments. Both the ACE-FTS and ACE-MAESTRO partial columns follow the trend in NO_2 VCDs as seen by the ground-based instruments. The NO_2 partial columns from the satellite instruments are expected to be roughly 13% smaller than the total columns from the ground-based instruments.

The average differences between the satellite instruments and the average of the ground-based instruments and, in the case of ozone, ozonesondes, is given in Table 7.7.

Table 7.7: Average differences between the satellite instruments and the average of the ground-based instruments and, in the case of ozone, ozonesondes (G-B avg.). Also shown is the average difference between ACE-FTS and ACE-MAESTRO. For the ground-based instruments and the ozonesondes these are total vertical columns. For the satellite instruments these are partial columns: between 0 and 40 km for ozone and between 22 and 40 km for NO_2.

Comparison	O_3	NO_2
ACE-FTS minus G-B avg.	3.4%	−15.9%
ACE-MAESTRO minus G-B avg.	−9.1%	1.2%
ACE-FTS minus ACE-MAESTRO	12.4%	−15.5%

The ACE-FTS ozone partial columns agree within the combined random and systematic error bars of the total columns from the ground-based instruments, while the NO_2 partial columns differ by the expected percentage. The ACE-MAESTRO ozone partial columns are smaller than the total columns from the ground-based instruments, while the NO_2 partial columns are larger than those of the ground-based instruments. For ozone, these results are consistent with Dupuy et al. (2008), who found that profiles and partial columns from satellite-, aircraft-, balloon-, and ground-based instruments agree to within ±10% (generally +5%) of the ACE-FTS measurements, and to within ±10% (generally better than ±5%) of the ACE-MAESTRO measurements. For NO_2, these results are consistent with Kerzenmacher et al. (2008), who found that partial columns from five ground-based Fourier transform infrared spectrometers agree to within 10.1% of the ACE-FTS partial columns and to within 17.6% of the ACE-MAESTRO partial columns.

Table 7.7 also shows the average difference between ACE-FTS and ACE-MAESTRO. For ozone, the partial columns from the ACE-FTS are 12.4% larger than those from ACE-MAESTRO. For NO_2, the partial columns from the ACE-FTS are 15.5% smaller than those from the ACE-MAESTRO. The agreement between the two satellite instruments varies significantly between the different years.

Kar et al. (2007) found that for ozone the two satellite instruments agree to within

5 to 15% between 16 and 50 km, with ACE-MAESTRO showing a low bias of roughly 5% in the Northern Hemisphere. The results found here are consistent with this finding, with the ACE-MAESTRO partial columns being smaller than the ACE-FTS columns. Kar et al. (2007) found that for NO_2 the two instruments agree within 10% between 22 and 40 km in the Northern Hemisphere. Kerzenmacher et al. (2008), using a slightly longer time period and for both hemispheres, found that the two instruments agree to within 20% between 25 and 40 km, with ACE-MAESTRO showing a slight high bias compared to ACE-FTS. Again, the results found here are consistent with these findings, with ACE-FTS columns being smaller than the ACE-MAESTRO columns.

Chapter 8

Conclusions

8.1 Summary of Thesis

Ground-based zenith-sky measurements of solar spectra were made at PEARL in the Canadian High Arctic during polar springtime from 2004 to 2007 as part of the Canadian Arctic ACE validation campaigns. From these spectra, ozone, NO_2, and BrO VCDs have been retrieved using the DOAS technique. These are the first measurements of BrO to be obtained at Eureka. The UT-GBS was also deployed as part of the fourth MANTRA campaign in Vanscoy, Saskatchewan in August and September 2004.

The PEARL-GBS was permanently installed at PEARL in August 2006 and has since been making continuous measurements, with the exception of polar night. During the 2007 springtime campaign, the PEARL-GBS was operated with a finer grating, and measurements of OClO DSCDs were possible. Characterization tests for both instruments have been developed, and are performed regularly to monitor their performance.

The ozone and NO_2 measurements made during the MANTRA campaign have been compared to the measurements from the SAOZ, MAESTRO, and SPS instruments, following the methods established by the UV-visible Working Group of the NDACC. The Type 1 standards, which certify instruments for trend studies, are not met by any of the instrument pairs. The Type 2 standards, which certify instruments for satellite validation, are partially met. Vertical column densities of ozone from the zenith-sky UV-visible instruments, three FTSs, a Brewer spectrophotometer, and ozonesondes were also compared, and found to agree within the combined error estimates of the instruments (15%). NO_2 vertical column densities from the UT-GBS and SAOZ were compared, and are also found to agree within combined error (15%).

During MANTRA, and once while the UT-GBS was operating in Toronto at TAO, thunderstorms passed over the measurement site and enhanced columns of ozone and NO_2 were observed. During MANTRA, SAOZ was also operating during the thunderstorm. The enhanced ozone differential slant columns were primarily due to the longer path traversed by the solar radiation caused by multiple scattering inside the thick cloud layer associated with the thunderstorm. The enhanced NO_2 columns were partly attributed to NO_x production by lightning. Two new methods were developed to separate the NO_2 enhancements into contributions from the longer path length and production by lightning. Combining the observed excess NO_2 with lightning flash data from the Canadian Lightning Detection Network and Environment Canada Doppler radar measurements, the production of NO_2 molecules per lightning flash was determined.

The DSCDs and VCDs of ozone and NO_2 from the five UV-visible instruments that participated in the Eureka campaigns were also compared following the NDACC methods. The instruments were found to partially agree within the required accuracies for both species, although both the vertical and slant column densities were more scattered than required. This might be expected given the spatial and temporal variability of the Arctic stratosphere in spring. The comparisons were worse during the 2005 campaign, when Eureka spent a significant amount of time on the edge of the polar vortex. The discrepancies are thought to be due to the differences in fields-of-view of the instruments. The Eureka comparisons were generally an improvement over the MANTRA comparisons: for the UT-GBS this is a result of the loaner detector used during the MANTRA campaign, and, in 2005-2007, the error in the data acquisition code had been removed. For the MAESTRO and SPS, this is a result of the more favourable operating environment. In 2007, the UT-GBS and PEARL-GBS were found to agree within both sets of NDACC standards for both species.

Two methods of calculating the ozone and NO_2 VCDs from the DSCDs were compared. The averaging and Langley plot methods for ozone were found to agree, generally within 6% of the total column, when observing a homogeneous ozone field, as during MANTRA and most of the Eureka campaigns. When the field is not homogeneous, as was the case during the Eureka 2005 campaign, the results were found to differ significantly, by as much as 15% of the total column. The averaging and 90° methods for NO_2 were found to agree in all cases, generally within 5%.

The vertical column densities from the ground-based instruments during the Eureka campaigns were also compared to integrated total columns from ozonesondes and integrated partial columns from the ACE-FTS and ACE-MAESTRO instruments on board ACE. For both species, the columns from the ground-based instruments and the ozonesondes were found to generally agree within their combined error bars. The ACE-FTS ozone partial columns and the ground-based total columns agree within 3.4%, averaged over the four campaigns. The ACE-MAESTRO ozone partial columns were generally smaller than those of the ground-based instruments, by an average of 9.1%, and were smaller than the ACE-FTS columns by an average of 12.4%. The ACE-FTS NO_2 partial columns were an average of 15.9% smaller than the total columns from the ground-based instruments, as expected. The ACE-MAESTRO NO_2 partial columns were larger than the total columns of the ground-based instruments by an average of 1.2% and larger than the partial columns of the ACE-FTS by an average of 15.5%.

8.2 Suggested Future Work

BrO DSCDs and VCDs were successfully retrieved from both the UT-GBS and PEARL-GBS during the polar springtime campaigns using the 600 gr/mm grating, which is the standard grating used in both instruments. The quality of the spectral fits is significantly improved using a higher density grating, as observed with the PEARL-GBS during the spring of 2007. BrO could not be retrieved from the PEARL-GBS using the 600 gr/mm grating outside of the springtime campaign. To allow for measurements of BrO year-round, the UT-GBS could be permanently installed at PEARL as well. With the UT-GBS using the 600 gr/mm grating and the PEARL-GBS using the 1200 gr/mm grating, columns of ozone, NO_2, and BrO could be retrieved year-round. If this is not possible, the PEARL-GBS could be modified to take spectra alternating between the 600 and 1200 gr/mm gratings. This situation is not ideal, because of the difficulties of sequencing these measurements through twilight, and the shifts in wavelength calibration due to moving the gratings.

The ambient temperature of the GBSs, both when installed in the hatches at PEARL and in the weatherproof box, should be improved upon. The quality of the retrievals of all the species, especially BrO, are sensitive to changing wavelength calibration, which is minimized when the instruments remain at a constant temperature.

The zenith-sky measurements from both instruments can be used to derive low-resolution vertical profiles of NO_2 using an optimal estimation method (Melo et al., 2005; Farahani, 2006).

Both the UT-GBS and the PEARL-GBS have been compared to SAOZ, the only instrument of the MANTRA or Eureka campaign suites to have participated in the NDACC intercomparison campaigns. While SAOZ has compared favourably with other UV-visible instruments during these campaigns, the results of these comparisons have been somewhat similar to the agreement between the UT-GBS and SAOZ presented here. One of the GBSs should participate in the next NDACC intercomparison campaign, to allow comparison with one of the "reference instruments" which are classified as "very high quality". If BrO comparisons are performed as well, such as the case during the campaigns at the Observatoire de Haute Provence (Aliwell et al., 2002) and the Andøya Rocket Range (Vandaele et al., 2005, BrO and OClO columns will be compared in future papers), this will undoubtedly help to improve the quality of the BrO measurements made with the UT-GBS and PEARL-GBS.

The PEARL-GBS can also be coupled to a suntracker, allowing for direct Sun observations. With the two instruments operating at PEARL, the direct Sun and zenith-sky DSCDs can be combined. Using an optimal estimation method, the BrO column can be separated into tropospheric and stratospheric components (Schofield et al., 2003, 2004, 2006). The suntracker could also be used to perform Multi-AXis DOAS (MAX-DOAS) measurements (e.g., Hönninger and Platt, 2002; Hönninger et al., 2004), which are more complicated to interpret than the direct Sun measurements, but can also yield low-resolution profiles of BrO. Either of these configurations would allow for the observation of "bromine explosions", which occur in the Arctic troposphere in the late spring (McElroy et al., 1999), and tropospheric IO (Schönhardt et al., 2008). The suntracker could also be configured to track the Moon, which could extend measurements through the polar night.

Through the use of a split liquid light guide, the two GBSs could be coupled to the suntracker. With one instrument operating with the 600 gr/mm grating and one with the 1200 gr/mm grating, all four species could be retrieved with the same viewing geometry. The suntracker can alternate between direct Sun, zenith-sky, and MAX-DOAS measurements during twilight.

The PEARL-GBS will continue to operate at PEARL as part of CANDAC. This long-term dataset will allow for more detailed comparisons of the interannual and interseasonal variability of the retrieved species. As most notably evidenced by the discovery of the ozone hole, initiated from examination of the long-term dataset of ozone at Halley

Bay, dating back to the International Geophysical Year in 1957 (Farman et al., 1985), long-term measurements of atmospheric species can lead to unexpected and important information about the atmosphere.

Bibliography

S. R. Aliwell, M. Van Roozendael, P. V. Johnston, A. Richter, T. Wagner, D. W. Arlander, J. P. Burrows, D. J. Fish, R. L. Jones, K. K. Tørnkvist, J. C. Lambert, K. Pfeilsticker, and I. Pundt. Analysis for BrO in zenith-sky spectra: An intercomparison exercise for analysis improvement. *J. Geophys. Res.*, 107(doi:10.1029/2001JD000329), 2002.

J. Austin, D. Shindell, S. R. Beagley, C. Brühl, M. Dameris, E. Manzini, T. Nagashima, P. Newman, S. Pawson, G. Pitari, E. Rozanov, C. Schnadt, and T. G. Shepherd. Uncertainties and assessments of chemistry-climate models of the stratosphere. *Atmos. Chem. Phys.*, 3:1–27, 2003.

M. R. Bassford, K. Strong, and C. A. McLinden. Zenith-sky observations of stratospheric gases: The sensitivity of air mass factors to geophysical parameters and the influence of tropospheric clouds. *J. Quant. Spectrosc. Radiat. Transfer*, 68:657–677, 2001.

M. R. Bassford, K. Strong, C. A. McLinden, and C. T. McElroy. Ground-based measurements of ozone and NO_2 during MANTRA 1998 using a zenith-sky spectrometer. *Atmos.-Ocean*, 43:325–338, 2005.

D. R. Bates and M. Nicolet. Atmospheric hydrogen. *Publ. Astron. Soc. Pac.*, 62:106–110, 1950.

S. Beirle, N. Sprichtinger, A. Stohl, K. L. Cummins, T. Turner, D. Boccippio, O. R. Cooper, M. Wenig, M. Grzegorski, U. Platt, and T. Wagner. Estimating the NO_x produced by lightning from GOME and NLDN data: a case study in the Gulf of Mexico. *Atmos. Chem. Phys.*, 6:1075–1089, 2006.

P. F. Bernath et al. Atmospheric Chemistry Experiment (ACE): mission overview. *Geophys. Res. Lett.*, 32(doi:10.1029/2005GL022386), 2005.

P. R. Bevington. *Data reduction and error analysis for the physical sciences.* McGraw Hill Book Company, 1992.

J. Biele, A. Tsias, B. P. Luo, K. S. Carslaw, R. Neuber, G. Beyerle, and T. Peter. Nonequilibrium coexistence of solid and liquid particles in arctic stratospheric clouds. *J. Geophys. Res.*, 106:22 991–23 007, 2002.

R. D. Blatherwick, F. H. Murcray, F. J. Murcray, A. Murcray, A. Goldman, G. A. Vanasse, S. T. Massie, and R. J. Cicerone. Infrared emission measurements of morning N_2O_5. *J. Geophys. Res.*, 94:18 337–18 340, 1989.

S. C. Bloom, A. de Silva, D. Dee, M. Bosilovich, J. D. Chern, S. Pawson, S. Schubert, M. Sienkiewicz, I. Stajner, W. W. Tan, and M. L. Wu. The Goddard Earth Observing Data Assimilation System, GEOS DAS Version 4.0.3: Documentation and Validation. Technical Report 104606 V26, NASA, 2005.

K. F. Boersma, H. J. Eskes, E. W. Meijer, and H. M. Kelder. Estimate of lightning NO_x production from GOME satellite observations. *Atmos. Chem. Phys.*, 5:2311–2331, 2005.

C. D. Boone, R. Nassar, K. A. Walker, Y. Rochon, S. D. McLeod, C. P. Rinsland, and P. F. Bernath. Retrievals for the Atmospheric Chemistry Experiment Fourier-Transform Spectrometer. *Appl. Opt.*, 44:7218–7231, 2005.

G. P. Brasseur and S. Solomon. *Aeronomy of the Middle Atmosphere.* Springer, Dorndrecht, the Netherlands, 2005.

J. P. Burrows, A. Richter, A. Dehn, B. Deters, S. Himmelmann, S. Voight, and J. Orphal. Atmospheric remote-sensing reference data from GOME – 2. Temperature dependent absorption cross-sections of O_3 in the 231–794 nm range. *J. Quant. Spectrosc. Radiat. Transfer*, 61:509–517, 1999.

W. R. Burrows, P. J. Lewis, B. Kochtubajda, B. Snyder, and V. Turcotte. Lightning occurence patterns over Canada and adjacent United States from lightning detection network observations. *Atmos.-Ocean*, 40:59–80, 2002.

K. S. Carslaw, M. Wirth, A. Tsias, B. P. Luo, A. Dörnbrack, M. Leutbecher, H. Volkert, W. Renger, J. T. Backmeister, E. Reimer, and T. Peter. Increased stratospheric ozone depletion due to mountain-induced atmospheric waves. *Nature*, 391:675–678, 1998.

K. V. Chance and R. J. D. Spurr. Ring effect studies: Rayleigh scattering, including molecular parameters for rotational Raman scattering, and the Fraunhofer spectrum. *Appl. Opt.*, 36:5224–5230, 1997.

S. Chapman. On ozone and atomic oxygen in the upper atmosphere. *Philos. Mag.*, 10: 369383, 1930.

H. J. Christian, R. J. Blakeslee, D. J. Boccippio, W. L. Boeck, D. E. Buechler, K. T. Driscoll, S. J. Goodman, J. M. Hall, W. J. Koshak, D. M. Mach, and M. F. Stewart. Global frequency and distribution of lightning as observed from space by the Optical Transient Detector. *J. Geophys. Res.*, 108(doi:10.1029/2002JD002347), 2003.

P. J. Crutzen. The influence of nitrogen oxides on the atmospheric ozone content. *Quart. J. Roy. Meteorol. Soc.*, 96:320–325, 1970.

M. Y. Danilin and J. C. McConnell. Stratospheric effects of bromine activation on/in sulfate aerosol. *J. Geophys. Res.*, 100:11 237–11 243, 1995.

A. Dessler. *The Chemistry and Physics of Stratospheric Ozone.* Academic Press, New York, 2000.

E. Dupuy et al. Validation of ozone measurements from the Atmospheric Chemistry Experiment (ACE). *Atmos. Chem. Phys. Disc.*, 8:2513–2656, 2008.

F. Erle, K. Pfeilsticker, and U. Platt. On the influence of tropospheric clouds on zenith-scattered-light measurements of stratospheric species. *Geophys. Res. Lett.*, 22:2725–2728, 1995.

E. Farahani. *Stratospheric composition measurements in the Arctic and at mid-latitudes and comparison with chemical fields from atmospheric models.* PhD thesis, University of Toronto, 2006.

E. Farahani, K. Strong, R. L. Mittermeier, and H. Fast. Ground-based UV-visible spectroscopy of O_3, NO_2, and OClO at Eureka: Part I - Evaluation of the analysis method and comparison with infrared measurements. *Atmos. Chem. Phys.*, 2008. in preparation.

J. C. Farman, B. G. Gardiner, and J. D. Shanklin. Large loses of total ozone in Antarctica reveal seasonal ClO_x/NO_x interaction. *Nature*, 315:207–210, 1985.

C. B. Farmer, G. C. Toon, P. W. Schaper, J. F.Blavier, and L. L. Lowes. Stratospheric trace gases in the spring 1986 Antarctic atmosphere. *Nature*, 329:126–130, 1987.

C. Fayt and M. Van Roozendael. *WinDOAS 2.1 – Software user manual.* Uccle, Belgium, 2001.

T. Fehr, H. Höller, and H. Huntrieser. Model study on production and transport of lightning-produced NO_x in a EULINOX supercell storm. *J. Geophys. Res.*, 109 (doi:10.1029/2003JD003935), 2004.

D. J. Fish. *Measurements of stratospheric composition using ultraviolet and visible spectroscopy.* PhD thesis, University of Cambridge, 1994.

D. J. Fish and R. L. Jones. Rotational Raman scattering and the Ring effect in zenith-sky spectra. *Geophys. Res. Lett.*, 22:811–814, 1995.

D. J. Fish, R. L. Jones, and E. K. Strong. Mid-latitude observations of the diurnal variation of stratospheric BrO. *J. Geophys. Res.*, 100:18 863–18 871, 1995.

P. F. Fogal. *The determination of atmospheric constituent vertical distribution information from ground-based, high-resolution, infra-red spectra.* PhD thesis, University of Denver, 1994.

P. F. Fogal, R. D. Blatherwick, F. J. Murcray, and J. R. Olson. Infra-red FTS measurements of CH_4, N_2O, O_3, HNO_3, HCl, CFC-11 and CFC-12 from the MANTRA balloon campaign. *Atmos.-Ocean*, 43:351–359, 2005.

E. Franzblau and C. J. Popp. Nitrogen oxides produced from lightning. *J. Geophys. Res.*, 94:11 089–11 104, 1989.

A. Fraser, P. F. Bernath, R. D. Blatherwick, J. R. Drummond, P. F. Fogal, D. Fu, F. Goutail, T. E. Kerzenmacher, C. T. McElroy, C. Midwinter, J. R. Olson, K. Strong, K. A. Walker, D. Wunch, and I. J. Young. Intercomparison of ground-based ozone and NO_2 measurements during the MANTRA 2004 campaign. *Atmos. Chem. Phys.*, 7:5489–5499, 2007a.

A. Fraser, F. Goutail, C. A. McLinden, S. M. L. Melo, and K. Strong. Lightning-produced NO_2 observed by two ground-based UV-visible spectrometers at Vanscoy, Saskatchewan in August 2004. *Atmos. Chem. Phys.*, 7:1683–1692, 2007b.

A. Fraser, F. Goutail, K. Strong, P. F. Bernath, C. Boone, W. H. Daffer, J. R. Drummond, D. G. Dufour, T.E. Kerzenmacher, G. L. Manney, C. T. McElroy, C. Midwinter, C. A. McLinden, F. Nichitiu, C. R. Nowlan, J. Walker, K. A. Walker, H. Wu, and J. Zou. Intercomparison of UV-visible measurements of ozone and NO_2 during the Canadian Arctic ACE Validation Campaigns: 2004-2006. *Atmos. Chem. Phys.*, 8:1763–1788, 2008.

D. Fu, K. A. Walker, K. Sung, C. D. Boone, M.-A. Soucy, and P. F. Bernath. The Portable Atmospheric Research Interferometric Spectrometer for the Infrared, PARIS-IR. *J. Quant. Spectrosc. Radiat. Transfer*, 103:362–370, 2007.

J. F. Grainger and J. Ring. Anomalous Fraunhofer line profiles. *Nature*, 193:762, 1962.

G. F. Greenblatt, J. J. Orlando, J. B. Burkholder, and A. R. Ravishankara. Absorption measurements of oxygen between 330 and 1140 nm. *J. Geophys. Res.*, 95:18 577–18 582, 1990.

A. Grund, T. Klüpfel, A. Grendel, B. Krug, and D. Perner. Ozone depletion potential from statospheric OClO and BrO observations during Arctic winters 1992–96 and the comparison with observed ozone columns. In R. D. Bojkov and G. Viscounti, editors, *Proc. of the XVIII WQuadrennial Ozone Symposium*, volume 1, pages 209–212, L'Aquila, Italy, 12–21 September 1996, 1998.

H. Harder, H. Bösch, C. Camy-Peyret, M. P. Chipperfield, R. Fitzenberger, S. Payan, D. Perner, U. Platt, B. M. Sinnhuber, and K. Pfeilsticker. Comparison of measured and modeled stratospheric BrO: Implications for the total amount of stratospheric bromine. *Geophys. Res. Lett.*, 27:3695–3698, 2000.

D. Hofmann et al. Intercomparison of UV/Visible spectrometers for measurements of stratospheric NO_2 for the Network for the Detection of Stratospheric Change. *J. Geophys. Res.*, 100:16 765–16 791, 1995.

G. Hönninger and U. Platt. Observations of BrO and its vertical distribution during surface ozone depletion at Alert. *Atmos. Env.*, 36:2481–2489, 2002.

G. Hönninger, C. von Friedeberg, and U. Platt. Multi axis differential optical absorption spectroscopy (MAX-DOAS). *Atmos. Chem. Phys.*, 4:231–254, 2004.

H. Huntrieser, C. Feigl, H. Schlager, G. C. Schröder, P. van Velthoven, F. Flatøy, C. Théry, A. Petzold, H. Höller, and U. Schumann. Airborne measurements of NO_x, tracer species and small particles during the European Lightning Nitrogen Oxides Experiment. *J. Geophys. Res.*, 107(doi:10.1029/2000JD000209), 2002.

D. Jacob. *Introduction to Atmospheric Chemistry.* Princeton University Press, Princeton, NJ, 1999.

P. V. Johnston, J. P. Pommereau, and H. K. Roscoe. Appendix II - UV/Vis instruments. http://www.ndacc.org, 1999.

J. Kar, C. T. McElroy, J. R. Drummond, J. Zou, F. Nichitiu, K. A. Walker, C. E. Randall, C. R. Nowlan, D. G. Dufour, C. D. Boone, P. F. Bernath, C. R. Trepte, L. W. Thomason, and C. McLinden. Initial comparison of ozone and NO_2 profiles from ACE-MAESTRO with balloon and satellite data. *J. Geophys. Res.*, (doi:10.1029/2006JD008242), 2007.

T. E. Kerzenmacher et al. Validation of NO and NO_2 from ACE-FTS and MAESTRO. *Atmos. Chem. Phys. Discuss.*, 8:3027–3142, 2008.

T. E. Kerzenmacher, K. A. Walker, K. Strong, R. Berman, P. F. Bernath, C. D. Boone, J. R. Drummond, H. Fast, A. Fraser, K. MacQuarrie, C. Midwinter, K. Sung, C. T. McElroy, R. L. Mittermeier, J. Walker, and H. Wu. Measurements of O_3, NO_2 and temperature during the 2004 Canadian Arctic ACE Validation Campaign. *Geophys. Res. Lett.*, 32(doi:10.1029/2005GL023032), 2005.

M. Koike, Y. Kondo, W. A. Matthews, P. V. Johnston, H. Nakajima, A. Kawahuchi, H. Nakane, I. Murata, A. Budiyono, M. Kanada, and N. Toriyama. Assessment of the uncertainties in the NO_2 and O_3 measurements by visible spectrometers. *J. Atmos. Chem.*, 32:121–145, 1999.

W. D. Komhyr and R. D. Grass. Total ozone decrease at South Pole, Antarctica, 1964–1985. *Geophys. Res. Lett.*, 13:1248–1251, 1986.

T. Koop, B. P. Luo, U. M. Biermann, P. J. Crutzen, and T. Peter. Freezing of $HNO_3/H_2SO_4/H_2O$ solutions at stratospheric temperatures: Nucleation statistics and experiments. *J. Phys. Chem. A.*, 101:1117–1133, 1997.

M. J. Kurylo and R. J. Zander. The NDSC – Its status after ten years of operation. In R. D. Bojikov and S. Kazuo, editors, *Proceedings of the Quadrennial Ozone Symposium*, pages 137 – 138, Sapporo, Japan, 3 – 8 July 2000, 2000.

A. O. Langford, R. W. Portmann, J. S. Daniel, H. L. Miller, and S. Solomon. Spectroscopic measurements of NO_2 in a Colorado thunderstorm: Determination of the mean production by cloud-to-ground lightning flashes. *J. Geophys. Res.*, 109 (doi:10.1029/2003JD004158), 2004.

D. J. Lary. Gas phase atmospheric bromine chemistry. *J. Geophys. Res.*, 101:1505–1516, 1996.

D. J. Lary. Catalytic destruction of stratospheric ozone. *J. Geophys. Res.*, 102:21 515–21 526, 1997.

K. N. Liou. *An Introduction to Atmospheric Radiation.* Academic Press, New York, 2002.

J. E. Lovelock, R. J. Maggs, and R. J. Wade. Halogenated hydrocarbons in and over the Atlantic. *Nature*, 241:194196, 1973.

C. Mackay. Charge-coupled devices in astronomy. *Annual Review of Astronomy and Astrophysics*, 24:255–283, 1986.

P. L. MacKeen, H. E. Brooks, and K. L. Elmore. Radar reflectivity-derived thunderstorm parameters applied to storm longevity forecasting. *Weather and Forecasting*, 14:289–295, 1999.

A. Makhijani and K. R. Gurney. *Mending the Ozone Hole: Science, Technology, Policy.* MIT Press, Cambridge, MA, 1995.

G. L. Manney, W. H. Daffer, K. B. Strawbridge, K. A.Walker, C. D. Boone, P. F. Bernath, T. E. Kerzenmacher, M. J. Schwartz, K. Strong, R. J. Sica, K. Krüger, H. C. Pumphrey, L. Froidevaux, A. Lambert, M. L. Santee, N. J. Livesey, E. E. Remsberg, M. G. Mlynczak, and J. R. Russell III. The High Arctic in extreme winters: vortex, temperature, and MLS and ACE-FTS trace gas evolution. *Atmos. Phys. Chem.*, 8: 505–522, 2008.

G. L. Manney et al. Solar occultation satellite data and derived meteorological products: Samping issues and comparisons with Aura MLS. *J. Geophys. Res.*, 112 (doi:10.1029/2007JD008709), 2007.

G. L. Manney, K. Krüger, J. L. Sabutis, S. A. Sena, and S. Pawson. The remarkable 2003–2004 winter and other recent warm winters in the Arctic stratosphere since the late 1990s. *J. Geophys. Res.*, 110(doi:10.1029/2004JD005367), 2005.

G. L. Manney, R. W. Zurek, A. O'Neill, and R. Swinbank. On the motion of air through the stratospheric polar vortex. *J. Atmos. Sci.*, 51:2973–2994, 1994.

R. V. Martin, B. Sauvage, I. Folkins, C. E. Sioris, C. Boone, P. Bernath, and J. R. Ziemke. Space-based constraints on the production of nitric oxide by lightning. *J. Geophys. Res.*, 112(doi:10.1029/2006JD007831), 2007.

C. T. McElroy. A spectroradiometer for the measurement of direct and scattered solar irradiance from on-board the NASA ER-2 high-altitude research aircraft. *Geophys. Res. Lett.*, 22:1361–1364, 1995.

C. T. McElroy, C. A. McLinden, and J. C. McConnell. Evidence for bromine monoxide in the free troposphere during the Arctic polar sunrise. *Nature*, 397:338–341, 1999.

C. T. McElroy, C. R. Nowlan, J. R. Drummond, P. F. Bernath, D. V. Barton, D. G. Dufour, C. Midwinter, R. B. Hall, A. Ogyu, A. Ullberg, D. I. Wardle, J. Kar, J. Zou, F. Nichitiu, C. D. Boone, K. A. Walker, and N. Rowlands. The ACE-MAESTRO instrument on SCISAT: description, performance, and preliminary results. *Applied Optics*, 46:4341–4356, 2007.

C. A. McLinden, J. C. McConnell, E. Griffioen, and C. T. McElroy. A vector radiative-transfer model for the Odin/OSIRIS project. *Can. J. Phys.*, 80:375–393, 2002.

C. A. McLinden, S. C. Olsen, B. Hannegan, O. Wild, M. J. Prather, and J. Sundet. Stratospheric ozone in 3-D models: A simple chemistry and the cross-tropopause flux. *J. Geophys. Res.*, 105:14653–14665, 2000.

R. D. McPherson. The national centers for environmental prediction: operational climate, ocean, and weather prediction for the 21st century. *Bull. Am. Meteor. of Soc.*, 75:363–373, 1994.

S. M. L. Melo, K. Strong, M. R. Bassford, K. E. Preston, C. T. McElroy, E. V. Rezanov, and T. Egorova. Retrieval of stratospheric NO_2 vertical profiles from ground-based zenith-sky DOAS measurements: results for the MANTRA 1998 field campaign. *Atmos.-Ocean*, 43:339–350, 2005.

L. J. Mickley, J. P. D. Abbatt, J. E. Frederick, and J. M. Russell III. Response of summertime odd nitrogen and ozone at 17 mbar to Mount Pinatubo aerosol over the southern midlatitudes: Observations from the Halogen Occultation Experiment. *J. Geophys. Res.*, 102:23 573–23 582, 1997.

M. Molina and F. S. Rowland. Stratospheric sink for chlorofluoromethanes: Chlorine atomic-catalysed destruction of ozone. *Nature*, 249:810–812, 1974.

G. H. Mount, R. W. Sanders, A. L. Schmeltekopf, and S. Solomon. Visible spectroscopy at McMurdo station, Antarctica,1, overview and daily variations of NO_2 and O_3 during austral spring, 1986. *J. Geophys. Res.*, 92:8320–8328, 1987.

J. F. Noxon. Nitrogen dioxide in the stratosphere and troposphere measured by ground-based absorption spectroscopy. *Science*, 189:547, 1975.

J. F. Noxon. Atmospheric nitrogen fixation by lightning. *Geophys. Res. Lett.*, 3:463–465, 1976.

J. F. Noxon, E. C. Whipple, and R. S. Hyde. Stratospheric NO_2 1. Observational method and behavior at mid-latitude. *J. Geophys. Res.*, 84:5047–5065, 1979.

F. H. Perrin. Whose absorption law? *J. Opt. Soc. America*, 38:72–74, 1948.

K. Pfeilsticker, D. W. Arlander, J. P. Burrows, F. Erle, M. Gil, F. Goutail, C. Hermans, J.-C. Lambert, U. Platt, J.-P. Pommereau, A. Richter, A. Sarkissian, M. Van Roozendael, T. Wagner, and T. Winterrath. Intercomparison of the influence of tropospheric clouds on UV-visible absorptions detected during the NDSC intercomparison campaign at OHP in June 1996. *Geophys. Res. Lett.*, 26:1169–1172, 1999a.

K. Pfeilsticker, F. Erle, O. Funk, L. Marquand, T. Wagner, and U. Platt. Optical path modifications for zenith-sky measurements of stratospheric gases. *J. Geophys. Res.*, 103:25 323–25 335, 1998.

K. Pfeilsticker, F. Erle, and U. Platt. Observation of the stratospheric NO_2 latitudinal distribution in the northern winter hemisphere. *J. Atmsop. Chem.*, 32:101–120, 1999b.

J. M. Picone, A. E. Hedin, D. P. Drob, and A. C. Aikin. NRLMSISE-00 empirical model of the atmosphere: statistical comparison and scientific issues. *J. Geophys. Res.*, 107: 1468–1483, 2002.

M. Piot and R. von Glasgow. The potential importance of frost flowers, recycling on snow, and open leads for ozone depletion events. *Atmos. Chem. Phys.*, 8:2437–2467, 2008.

U. Platt. *Air monitoring by spectroscopic techniques*, chapter Differential Optical Absorption Spectroscopy (DOAS), pages 27–84. John Wiley, Hoboken, NJ, 1994.

U. Platt, D. Penner, and H. W. Pätz. Simultaneous measurements of atmospheric CH_2O, O_3, and NO_2 by differential optical absorption. *J. Geophys. Res.*, 84:6329–6335, 1979.

J. P. Pommereau and F. Goutail. O_3 and NO_2 ground-based measurements by visible spectrometry during Arctic winter and spring 1988. *Geophys. Res. Lett.*, 15:891–894, 1988.

N. S. Pougatchev, B. J. Connor, and C. P. Rinsland. Infrared measurements of the ozone vertical distribution above Kitt Peak. *J. Geophys. Res.*, 100:16 689 – 16 698, 1995.

M. J. Prather. Catastrophic loss of stratospheric ozone in dense volcanic clouds. *J. Geophys. Res.*, 97:10187–10191, 1997.

C. Price, J. Penner, and M. Prather. NO_x from lightning 1. Global distribution based on lightning physics. *J. Geophys. Res.*, 102:5929–5941, 1997.

C. E. Randall, J. D. Lumpe, R. M. Bevilacqua, K. W. Hoppel, E. P. Shettle, D. W. Rusch, L. L. Gordley, K. Kreher, K. Pfeilsticker, H. Boesch, G. Toon, F. Goutail, and J. P. Pommereau. Validation of POAM III NO_2 measurements. *J. Geophys. Res.*, 107 (doi:10.1029/2001JD001520), 2002.

A. Richter, M. Eisinger, A. Ladstätter-Weißenmayer, and J. P. Burrows. DOAS zenith sky observations: 2. Seasonal variations of BrO over Bremen (53°N) 1994–1995. *J. Atmos. Chem.*, 32:83–99, 1999.

B. A. Ridley, J. E. Dye, J. G. Walega, J. Zheng, F. E. Grahek, and W. Rison. On the production of active nitrogen by thunderstorms over new mexico. *J. Geophys. Res.*, 101:20 985–21 005, 1996.

R. A. Ridley, L. Ott, K. Pickering, L. Emmons, D. Montzka, A. Weinheimer, D. Knapp, F. Grahek, L. Li, G. Heymsfield, M. McGill, P. Kucera, M. J. Mahoney, D. Baumgardner, M. Schultz, and G. Brasseur. Florida thunderstorms: A faucet of reactive nitrogen to the upper troposphere. *J. Geophys. Res.*, 107(doi:10.1029/2004JD004769), 2004.

R. A. Ridley, K. E. Pickering, and J. E. Dye. Comments on the parameterization of lightning-produced NO in global chemistry-transport models. *Atmos. Environ.*, 39: 6184 – 6187, 2005.

C. P. Rinsland, N. B. Jones, B. J. Connor, J. A. Logan, N. S. Pougatchev, A. Goldman, F. J. Murcray, T. M. Stephen, A. S. Pine, R. Zander, E. Mahieu, and P. Dumoulin. Northern and southern hemisphere ground-based infrared spectroscopic measurements of tropospheric carbon monoxide and ethane. *Geophys. Res. Lett.*, doi:10.1029/98JD02515, 1998.

C. D. Rodgers. *Inverse methods for atmospheric sounding: theory and practice*, volume 2 of *Series on atmospheric, oceanic and planetary physics*. World Scientific Co. Pte. Ltd., 2000.

C. D. Rodgers and B. J. Connor. Intercomparison of remote sounding instruments. *J. Geophys. Res.*, 108(doi:10.1029/2002JD002299), 2003.

H. K. Roscoe et al. Slant column measurements of O_3 and NO_2 during the NDSC intercomparison of zenith-sky UV-Visible spectrometers in June 1996. *J. Atmosp. Chem.*, 32:281–314, 1999.

H. K. Roscoe, D. J. Fish, and R. L. Jones. Interpolation errors in UV-visible spectroscopy for stratospheric sensing: implications for sensitivity, spectral resolution, and spectral range. *Applied Optics*, 35:427–432, 1996.

L. S. Rothman et al. The HITRAN molecular spectroscopic database: edition of 2000 including updates through 2001. *J. Quant. Spectrosc. Radiat. Transfer*, 82:5–44, 2003.

L. S. Rothman et al. The HITRAN 2004 molecular spectroscopic database. *J. Quant. Spectrosc. Radiat. Transfer*, 96:139–204, 2005a.

L. S. Rothman, N. Jacquinet-Husson, C. Boulet, and A. M. Perrin. History and future of the molecular spectroscopic databases. *C. R. Physique*, 6:897–907, 2005b.

F. S. Rowland. Stratospheric ozone depletion. *Phil. Trans. R. Soc. B*, 361:769–790, 2006.

A. Rozanov, V.-V. Rozanov, M. Buchwitz, A. Kokhanovsky, and J. P. Burrows. SCIATRAN 2.0: A new radiative transfer model for geophysical applications in the 175–2400 nm spectra region. *Adv. Space Res.*, 36:1015–1019, 2005.

R. J. Salawitch, G. P. Gobbi, S. C. Wofsy, and M. B. McElroy. Denitrification in the Antarctic stratosphere. *Nature*, 339:525–527, 1989.

A. Sarkissian, G. Vaughan, H. K. Roscoe, L. M. Bartlett, F. M. O'Connor, D. G. Drew, P. A. Hughes, and D. M. Moore. Accuracy of measurements of total ozone by a SAOZ ground-based zenith sky visible spectrometer. *J. Geophys. Res.*, 107:1379–1390, 1997.

V. Savastiouk and C. T. McElroy. Brewer spectrophotometer total ozone measurements made during the 1998 Middle Atmosphere Nitrogen Trend Assessment (MANTRA) campaign. *Atmos.-Ocean*, 43:315–324, 2005.

M. R. Schoeberl and D. L. Hartmann. The dynamics of the stratospheric polar vortex and its relation to springtime ozone depletions. *Science*, 251:46–52, 1991.

R. Schofield, B. J. Connor, K. Kreher, P. V. Johnston, and C.D. Rodgers. The retrieval of profile and chemical information from ground-based UV-visible spectroscopic measurements. *J. Quant. Spectrosc. Radiat. Transfer*, 86:115–131, 2003.

R. Schofield, P. V. Johnston, A. Thomas, K. Kreher, B. J. Connor, S. Wood, D. Shooter, M. P. Chipperfield, A. Richter, R. von Glasow, , and C. D. Rodgers. Tropospheric and stratospheric BrO columns over Arrival Heights, Antarctica, 2002. *J. Geophys. Res.*, 111(doi:10.1029/2005JD007022), 2006.

R. Schofield, K. Kreher, B. J. Connor, P. V. Johnston, A. Thomas, D. Shooter, M. P. Chipperfield, C. D. Rodgers, and G. H. Mount. Retrieved tropospheric and stratospheric BrO columns over Lauder, New Zealand. *J. Geophys. Res.*, 109 (doi:10.1029/2003JD004463), 2004.

A. Schönhardt, A. Richter, F. Wittrock, H. Kirk, H. Oetjen, H. K. Roscoe, and J. P. Burrows. Observations of iodine monoxide columns from satellite. *Atmospheric Chemistry and Physics*, 8:637–653, 2008.

U. Schumann and H. Huntrieser. The global lightning-related nitrogen oxides source. *Atmos. Chem. Phys.*, 7:3823–3907, 2007.

J. H. Seinfeld and S. N. Pandis. *Atmospheric Chemistry and Physics: From Air Pollution to Climate Change*. John Wiley and Sons, Toronto, 1998.

B. M. Sinnhuber et al. Comparison of measurements and model calculatios of stratospheric bromine monoxide. *J. Geophys. Res.*, 107(doi:10.1029/2002JD000940), 2002.

S. Solomon. On the role of iodine in ozone depletion. *J. Geophys. Res.*, 99:20 491 – 20 499, 1994.

S. Solomon. Stratospheric ozone depletion: a review of concepts and history. *Rev. Geophys.*, 37:275–316, 1999.

R. S. Stolarski and R. J. Cicerone. Stratospheric chlorine: a possible sink for ozone. *Can. J. Chem.*, 52:1610–1615, 1974.

R. S. Stolarski, A. J. Krueger, M. R. Schoeberl, R. D. McPeters, P. A. Newman, and J. C. Alpert. Nimbus 7 satellite measurements of the springtime Antarctic ozone decrease. *Nature*, 322:808–811, 1986.

K. Strong et al. MANTRA – A balloon mission to study the odd-nitrogen budget of the stratosphere. *Atmos.-Ocean*, 43:283–299, 2005.

A. Tabazadeh, E. J. Jensen, O. B. Toon, K. Drdla, and M. R. Schoeberl. Role of the stratospheric polar freezing belt in denitrification. *Science*, 291:2591–2594, 2001.

A. Tabazadeh, M. L. Santee, M. Y. Danilin, H. C. Pumphrey, P. A. Newman, P. J. Hamill, and J. L. Mergenthaler. Quantifying denitrification and its effect on ozone recovery. *Science*, 288:1407–1411, 2000.

D.W. Tarasick, V. E. Fioletov, D. I. Wardle, J. B. Kerr, and J. Davies. Changes in the vertical distribution of ozone over Canada from ozonesondes: 1980-2001. *J. Geophys. Res.*, 110(doi:10.1029/2004JD004643), 2005.

L. W. Thomason, L. R. Poole, and T. Deshler. A global climatology of stratospheric aerosol surface area density deduced from Stratospheric Aerosol and Gas Experiment II measurements: 1984–1994. *J. Geophys. Res.*, 102:8967–8976, 1997.

X. Tie, R. Zhang, G. Brasseur, and W. Lei. Global NO_x production by lightning. *J. Atmos. Chem.*, 43:61–74, 2002.

O. B. Toon, E. V. Browell, S. Kinne, and J. Jordan. An analysis of lidar observations of polar stratospheric clouds. *Geophys. Res. Lett.*, 17:393–396, 1990.

O. B. Toon, A. Tabazadeh, E. V. Browell, and J. Jordan. Analysis of lidar observations of Arctic polar stratospheric clouds during January 1989. *J. Geophys. Res.*, 103:20 589–20 615, 2000.

K. K. Tørnkvist, D. W. Arlander, and B. M. Sinnhuber. Ground-based UV measurements of BrO and OClO over Ny-Ålesund during winter 1996 and 1997 and Andøya during winter 1998/99. *J. Atmosp. Chem.*, 43:75–106, 2002.

A. Tsias, M. Wirth, K. S. Carslaw, J. Biele, H. Mehrtens, J. Reichardt, C. Wedekind, V. Weiss, W. Renger, R. Neuber, U. von Zahn, B. Stein, V. Santacesaria, L. Stefanutti, F. Fierle, J. Bacmeister, and T. Peter. Aircraft lidar observations of and enchanced type Ia polar stratospheric clouds during APE POLECAT. *J. Geophys. Res.*, 104:23 961 – 23 696, 1998.

A. C. Vandaele et al. An intercomparison campaign of ground-based UV-Visible measurements of NO_2, BrO, and OClO slant columns: Methods of analysis and results for NO_2. *J. Geophys. Res.*, 110(doi:10.1029/2004JD005423), 2005.

A. C. Vandaele, C. Hermans, P. C. Simon, M. Carleer, R. Colin, S. Fally, M. F. Mérienne, A. Jenouvrier, and B. Coquart. Measurements of the NO_2 absorption cross-section from 42 000cm^{-1} to 10 000cm^{-1} (238–1000nm) at 220K and 294K. *J. Quant. Spectrosc. Radiat. Transfer*, 59:171–184, 1998.

G. Vaughan et al. An intercomparison of ground-based UV-visible sensors of ozone and NO_2. *J. Geophys. Res.*, 102:1411–1422, 1997.

C. Voigt, J. Schreiner, A. Kohlmann, P. Zink, K. Mauersberger, N. Larsen, T. Deshler, C. Kröger, J. Rosen, A. Adriani, F. Cairo, G. Di Donfrancesco, M. Viterbini, J. Ovarlez, H. Ovarlez, C. David, and A. Dörnbrack. Nitric acid trihydrate (NAT) in polar stratospheric clouds. *Science*, 290:1756–1758, 2000.

T. Wagner, F. Erle, C. Marquard, C. Otten, K. Pfeilsticker, T. Senne, J. Stutz, and U. Platt. Cloudy sky optical paths as derived from Differential Optical Absorption Spectroscopy observations. *J. Geophys. Res.*, 103:25 307–25 321, 1998.

T. Wagner et al. Comparison of box-air-mass-factors and radiances for Multiple-Axis Differential Optical Absorption Spectroscopy (MAX-DOAS) geometries calculated from different UV/visible radiative transfer models. *Atmos. Chem. Phys.*, 7:1809–1833, 2007.

T. Wagner, C. vonFriedeburg, M. Wenig, C. Otten, and U. Platt. UV-Visible observations of atmospheric O_4 absorptions using direct moonlight and zenith-scattered sunlight for clear-sky and cloudy sky conditions. *J. Geophys. Res.*, 107 (doi:10.1029/2001JD001026), 2002.

A. Wahner, G. S. Tyndall, and A. R. Ravishankara. Absorption cross sections for symmetric chlorine dioxide as a function of temperature in the wavelength range 240 – 480 nm. *J. of Phys. Chem.*, 91:2734–2738, 1987.

D. M. Wilmouth, T. F. Hanisco, N. M. Donahue, and J. G. Anderson. Fourier transform ultraviolet spectroscopy of the A $^2\pi_{3/2} \longleftarrow X^2\pi_{3/2}$ transition of BrO. *J. Phys. Chem. A*, 103:8935–8945, 1999.

T. Winterrath, T. P. Kurosu, A. Richter, and J. P. Burrows. Enhanced O_3 and NO_2 in thunderstorm clouds: convection or production? *Geophys. Res. Lett.*, 26:1291–1294, 1999.

F. Wittrock, M. Eisinger, A. Ladstätter-Weißenmayer, A. Richter, and J. P. Burrows. Ground-based UV-VIS measurements of O_3, NO_2, OClO, and BrO over Ny-Ålesund (79° N, 12° E). In R. D. Bojkov and G. Viscounti, editors, *Proc. of the XVIII Quadrennial Ozone Symposium*, volume 1, pages 623–626, L'Aquila, Italy, 12–21 September 1996, 1998.

WMO. *Scientific Assessment of Ozone Depletion: 2006, Rep. 50.* Global Ozone Research and Monitoring Project, World Meteorological Organization, Geneva, Switzerland, 2007.

S. C. Wofsy, M. B. McElroy, and Y. L. Yung. The chemistry of atmospheric bromine. *Geophys. Res. Lett.*, 2:215–218, 1975.

W. L. Wolfe. *Introduction to Radiometry.* SPIE Optical Engineering Press, Bellingham, WA, 1998.

D. Wunch, C. Midwinter, J. R. Drummond, C. T. McElroy, and A.F. Bagès. The University of Toronto's balloon-borne Fourier Transform Spectrometer. *Rev. Sci. Inst.*, 77:93–104, 2006.

D. Wunch, M. P. Tingley, T. G. Shepherd, J. R. Drummond, G. W. K. Moore, and K. Strong. Climatology and predictability of the late summer stratospheric zonal wind turnaround over Vanscoy, Saskatchewan. *Atmos.-Ocean*, 43:301–313, 2005.

D. York, N. M. Evensen, M. López Martínez, and J. De Basabe Delgado. Unified equations for the slope, intercept, and standard errors of the best straight line. *Am. J. Phys.*, 72:367–375, 2004.

Y. L. Yung, J. P. Pinot, R. T. Watson, and S. P. Sander. Atmospheric bromine and ozone perturbations in the lower stratosphere. *J. Atmos. Sci.*, 37:339–353, 1980.

Y. B. Zel'dovitch and Y. P. Raizer. *Physics of shock waves and high-temperature hydrodynamic phenomena*. Academic, San Diego, CA, 1966.